ULPGC
Universidad de
Las Palmas de
Gran Canaria

IUMA
Instituto Universitario de
Microelectrónica Aplicada

IUMA

Contributions to the development of hyperspectral imaging instrumentation and algorithms for medical applications targeting real-time performance

Doctorado en Tecnologías de Telecomunicación e Ingeniería Computacional

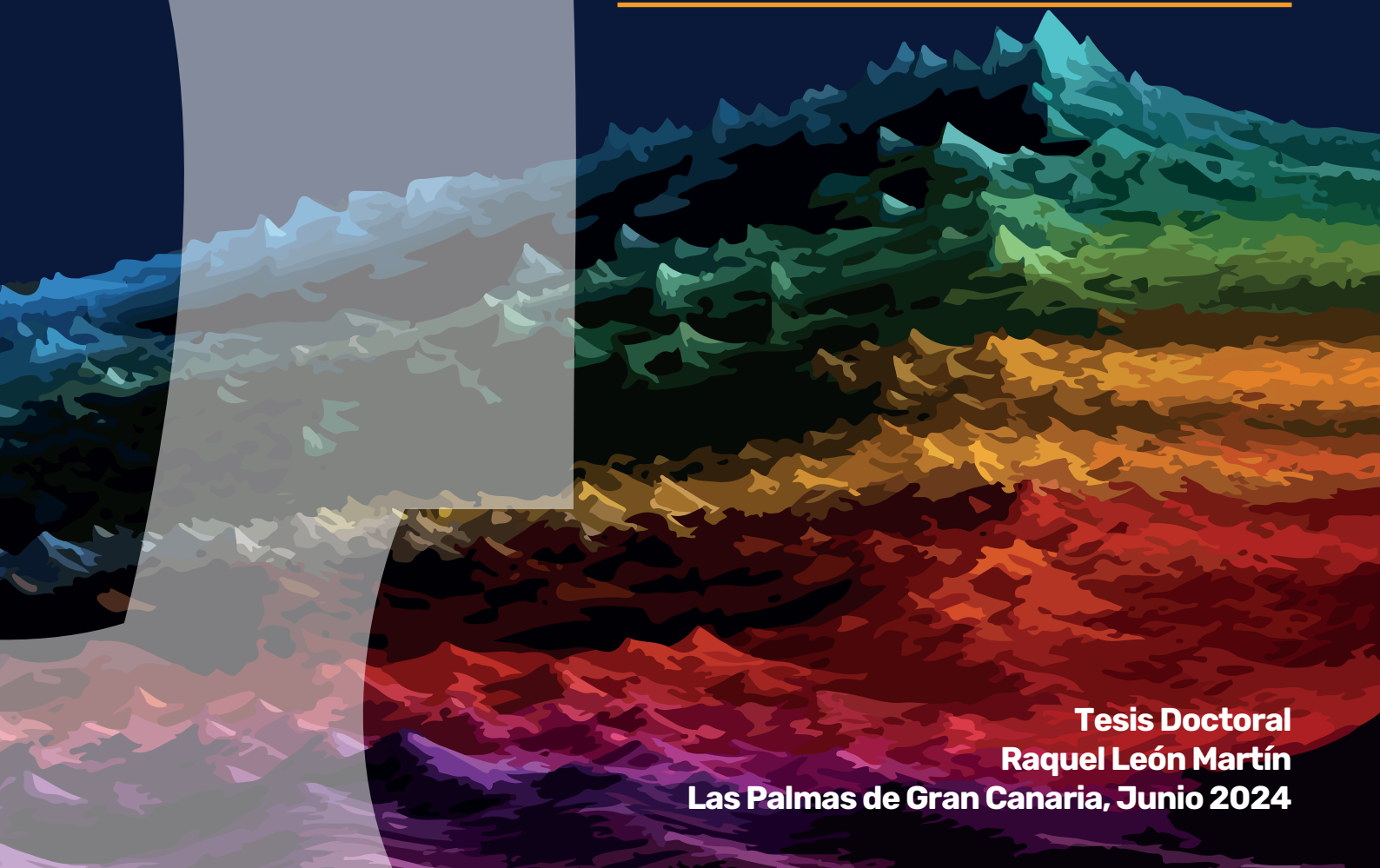

Tesis Doctoral
Raquel León Martín
Las Palmas de Gran Canaria, Junio 2024

ULPGC
Universidad de
Las Palmas de
Gran Canaria

IUMA
Instituto Universitario de
Microelectrónica Aplicada

DIVISIÓN DE DISEÑO DE SISTEMAS INTEGRADOS

TESIS DOCTORAL

CONTRIBUTIONS TO THE DEVELOPMENT OF HYPERSPECTRAL IMAGING INSTRUMENTATION AND ALGORITHMS FOR MEDICAL APPLICATIONS TARGETING REAL-TIME PERFORMANCE

Raquel León Martín

Gobierno de Canarias
Consejería de Economía, Conocimiento y Empleo
Agencia Canaria de Investigación, Innovación y Sociedad de la Información

Unión Europea
Fondo Social Europeo

Canarias avanza con Europa

Abstract

Hyperspectral imaging is an emerging imaging modality originated in the remote sensing field that has expanded its application to other research and industrial areas in the past years. Hyperspectral images are composed by spatial and spectral information, conforming a three-dimensional matrix, where each spatial pixel is related to a vector of intensity light values that spans hundreds of different spectral wavelengths, conforming an almost continuous spectrum. In medical applications, hyperspectral imaging technology has been widely investigated to measure different tissue properties such as oxygen saturation, perfusion, water, melanin, etc. It has also used to discriminate between tumor and normal tissue in different organs, or for early disease detection. One major benefit of this technology is its potential use as a diagnostic and guidance tool in various medical applications, being a non-contact, non-ionizing and label-free imaging technique. This PhD dissertation explores the use of hyperspectral imaging to advance beyond the current state-of-the-art and demonstrates its feasibility in three different medical applications.

First, an intraoperative hyperspectral acquisition system for brain surgical diagnostics and guidance was optimized to extend its capabilities and study the use of a wider spectral range to discriminate between tumor and normal brain tissue. Using this system, an in-vivo hyperspectral human brain image database was generated, and a new approach was proposed to perform spectral fusion of data obtained from two different hyperspectral cameras, covering the spectral range between 400 and 1,700 nm. Furthermore, using this database and the one acquired before the optimization in a previous research project, vascular enhanced maps were generated, and different analyses using spectral and spatial information were performed to detect and delineate brain tumors with a robust validation methodology using machine learning algorithms. The intraoperative system was validated using 61 hyperspectral images. Additionally, the identification of the blood vessels could help to reduce the number of classes to be differentiated by a classifier. The fusion approach led to classification maps that were more detailed and had fewer false positives than the maps prior to the fusion.

Second, a customized dermatoscopic hyperspectral imaging prototype was developed to capture real-time data of in-vivo pigmented skin lesions, with the main goal of proposing a novel classification framework based on hyperspectral image segmentation and supervised classification. This study aimed to demonstrate, as a proof-of-concept, the potential use of hyperspectral imaging technology to assist dermatologists in the discrimination of benign and malignant pigmented skin lesions (including both melanoma and non-melanoma lesions) in routine clinical practice. The dermatoscopic prototype was validated on 76 hyperspectral images and it was able to segment the pigmented lesion, extract and classify the associated pixels to reduce the computational cost. In addition, a risk threshold was applied to discriminate malignant lesions.

Finally, the third application involved the use of a hyperspectral acquisition system capable of capturing spectral information from 900 to 1700 nm, targeting the analysis of blood plasma using pixel-wise supervised classifiers to discriminate between subjects

affected by major neurocognitive disorder and healthy controls. The methodology included subject selection, blood plasma samples preparation, and their subsequent capture and analysis through machine learning methods. The study was conducted using 83 hyperspectral images and showed promising results for the potential identification of spectral biomarkers in blood plasma samples.

These studies showed that combining hyperspectral imaging with machine learning algorithms can provide promising results in the identification and discrimination of diseases in the three medical applications proposed.

Resumen

Las imágenes hiperespectrales son una modalidad de imagen emergente originada en el campo de la teledetección que ha ampliado su aplicación a otras áreas de la investigación y la industria en los últimos años. Las imágenes hiperespectrales están compuestas por información espacial y espectral, conformando una matriz tridimensional, donde cada píxel espacial está relacionado con un vector de valores de intensidad en el rango de cientos de longitudes de onda espectrales diferentes, formando un espectro casi continuo. En aplicaciones médicas, la tecnología de imágenes hiperespectrales se ha investigado ampliamente para medir distintas propiedades de los tejidos, como por ejemplo, la saturación de oxígeno, la perfusión, el agua, la melanina, etc. También se ha utilizado para discriminar entre tejido tumoral y normal en distintos órganos, o para la detección precoz de ciertas enfermedades. Una de las principales ventajas de esta tecnología es que puede utilizarse como herramienta de ayuda al diagnóstico en distintas aplicaciones médicas. En esta Tesis doctoral, el uso de las imágenes hiperespectrales se empleó en tres aplicaciones médicas diferentes.

En primer lugar, se optimizó un sistema de adquisición hiperespectral intraoperatorio para el diagnóstico durante operaciones de neurocirugía, con el fin de ampliar las capacidades del sistema y estudiar el uso de un rango espectral más amplio para discriminar entre tejido cerebral tumoral y normal. Utilizando este sistema, se generó una base de datos de imágenes hiperespectrales *in vivo* de cerebro humano y se propuso un nuevo enfoque para realizar la fusión espectral de los datos obtenidos con dos cámaras hiperespectrales diferentes, cubriendo el rango espectral entre 400 y 1700 nm. Además, utilizando esta base de datos y la adquirida en un proyecto de investigación anterior, se generaron mapas vasculares mejorados, y se realizaron diferentes análisis utilizando información espectral y espacial para detectar y delinear tumores cerebrales con una metodología de validación robusta utilizando algoritmos de aprendizaje automático. El sistema intraoperatorio se validó utilizando 61 imágenes hiperespectrales. Adicionalmente, la identificación de los vasos sanguíneos podría ayudar a reducir el número de clases a diferenciar por un clasificador. Los mapas de clasificación obtenidos utilizando el enfoque de fusión revelan que los mapas presentan más detalles, eliminando los falsos positivos que estaban presentes en los mapas antes de realizar la fusión.

En segundo lugar, se desarrolló un prototipo de imagen hiperespectral dermatoscópica personalizado capaz de capturar datos en tiempo real de lesiones cutáneas pigmentadas *in vivo* con el objetivo principal de proponer un novedoso marco de clasificación basado en la segmentación de imágenes hiperespectrales y la clasificación supervisada. Este estudio pretendía demostrar, como prueba de concepto, el uso potencial de la tecnología de imágenes hiperespectrales en la práctica clínica habitual para ayudar a los dermatólogos en la discriminación de lesiones cutáneas pigmentadas benignas y malignas (incluyendo tanto las lesiones de melanomas como las de no-melanomas). El prototipo dermatoscópico se validó en 76 imágenes hiperespectrales y fue capaz de segmentar las lesiones pigmentadas, así como de extraer y clasificar los píxeles asociados para reducir de esta forma el coste computacional. Además, se aplicó un umbral de riesgo para discriminar las lesiones malignas.

Finalmente, la tercera aplicación consistió en el uso de un sistema de adquisición hiperespectral capaz de capturar información espectral en el rango de 900 a 1700 nm,

dirigido al análisis de plasma sanguíneo mediante clasificadores supervisados por píxeles para discriminar entre sujetos afectados por trastorno neurocognitivo mayor y controles sanos. La metodología incluyó la selección de sujetos, la preparación de muestras de plasma sanguíneo y su posterior captura y análisis mediante métodos de aprendizaje automático. El estudio se realizó utilizando 83 imágenes hiperespectrales y mostró resultados prometedores para la identificación potencial de biomarcadores espectrales en muestras de plasma sanguíneo.

Todos estos estudios han revelado que el uso de imágenes hiperespectrales combinadas con algoritmos de aprendizaje automático son capaces de proporcionar resultados prometedores en la identificación y discriminación de distintas enfermedades en las tres aplicaciones médicas propuestas.

Acknowledgements

Developing this PhD Thesis has been a challenging journey, but I am grateful for the invaluable support of the many individuals who have played integral roles in both my professional and personal life over the years. Your contributions have been instrumental in my success, and I sincerely appreciate your help.

First, I my deepest gratitude to my supervisor, Prof. Gustavo M. Callico, for giving me the invaluable opportunity to join the ITHaCA project and immerse myself in the research field. I sincerely thank you for your confidence in me and for entrusting me with significant responsibilities throughout this journey. His belief in my abilities has not only boosted my self-confidence, but has also pushed me to do my best. I am truly grateful for the opportunities you have given me to grow and contribute to our common goals. Secondly, I would like to express my heartfelt appreciation to my co-supervisor, Dr. Himar Fabelo, whose unwavering support and endless motivation have been pivotal in guiding me through each stage of my research journey. I am deeply grateful for the privilege of having been under his supervision, and I greatly appreciate the wealth of knowledge and wisdom that I have acquired under your guidance. Your insights have shaped not only my academic journey, but also my personal and professional growth. Thank you for imparting invaluable lessons and insights that will undoubtedly resonate throughout my career, and for trusting in me, even in moments of self-doubt.

In addition to my supervisors, I would like to express my gratitude to Pedro P. Carballo, for his exceptional mentorship and for laying the foundation of my research journey during my bachelor and master's studies. His guidance and encouragement have been fundamental in achieving this goal. Thank you for the opportunity to co-supervise several undergraduate theses alongside you, which provided me with invaluable first-hand experience of effective mentorship and exemplary leadership.

I extend my thanks to my colleagues of research team. I am happy to see how much the team has grown since I started the PhD Thesis. Thanks to Samuel Ortega, Abián Hernández, Beatriz Martinez-Vega, Laura Quintana-Quintana, Antonio J. Rodríguez-Almeida, Carlos Vega, Maria Castro, and Guillermo V. Socorro-Marrero, for making the last part of my journey more enjoyable. I would like to make a special mention to Laura, who has helped me to reduce my workload and for always being on the same page. Thank you for suggesting transgressive ideas, for being the head of marketing and communications department and, most importantly, for counting on me both inside and outside the lab. Antonio, thank you for our discussions. I would also like to acknowledge the effort and dedication that Samuel has dedicated to each result of my thesis, your comments have been very valuable to improve my research. I would also like to thank my colleagues at DSI Lab: Yubal Barrios, Antonio Sanchez, Felipe Machado, and Samuel Torres. Having them as lab partners has been the best part of this phase. Thank you for sharing great moments with me both in and out of the lab.

This PhD Thesis was possible thanks to the different collaboration between medical doctors. I would like to thank the Department of Neurosurgery of the University Hospital of Gran Canaria Doctor Negrin (Jesús Morera, Adam Szolna, Juan F. Piñeiro, Carlos Espino, María Hernández, Aruma J. O'Shanahan, Sara Bisshopp, Coralia Sosa,

and David Carrera) for their notable collaboration during the ITHaCA project. Additionally, I would like to thank the Department of Dermatology at the University Hospital of Gran Canaria Doctor Negrín (Dr. Gregorio Carretero and Dr. Irene Castaño) and at the Complejo Hospitalario Universitario Insular-Materno Infantil (Dr. Javier A Hernandez and Dr. Pablo Almeida) for their support during the creation of the skin lesion dataset. I extend my gratitude to Dr. Francisco J. Balea-Fernandez, who always helped me with medical terminology and provided the plasma samples for this thesis. Furthermore, I would like to thank Dr. Bernardino Clavo from the Research Unit of the University Hospital of Gran Canaria Doctor Negrín, for his valuable comments during my research.

Additionally, I would like to thank the following researchers who made this dissertation possible. First, Dr. Alejandro Cruz-Guerrero and Prof. Daniel Ulises Campos-Delgado from the Universidad Autónoma de San Luis Potosí, for their valuable collaboration in spectral unmixing. Second, Dr. Marco La Salvia, Dr. Emanuele Torti, and Prof. Francesco Leporati from the University of Pavia, for their valuable support and collaboration during my research stay in their laboratory. Finally, MSc. Sofia H. Gelado for her curiosity and efforts in this field. Additionally, I would like to thank the other researchers that we have shared moments and conferences, and also project, Dr. Eduardo Juárez, Dr. Jaime Sancho, and Dr. Miguel Chavarrías from the Universidad Politécnica de Madrid.

My sincere thanks to the Network Infrastructure Service of the University Institute of Applied Microelectronics, Agustín Quintana and Enrique Montesdeoca, for their exceptional assistance. Their professionalism and dedication have ensured the smooth progression of my research activities. I would also like to thank Fátima Melián and Cruci Melián for often being the first people I greeted in the morning and always responding with a smile.

Finally, but not less important, I am extremely grateful to my parents, Lourdes and Pablo, and my sister Sara, who were always enthusiastic about my research, even though they did not understand what I was doing. They tirelessly listened to my problems and doubts, strongly encouraged me to pursue my aspirations and remained a constant source of support despite the physical distance between us. I owe the successful completion of this journey to their unwavering support and love.

To those who were here, to those who were not, too.

Contents

List of Figures

List of Tables

List of Acronyms

Acronym	Meaning
ABCDE	Asymmetry of the mole, Border irregularity, Color uniformity, Diameter and Evolving size, shape or color
ABS	Acrylonitrile butadiene styrene
ANN	Artificial Neural Network
AOTF	Acousto-Optic Tunable Filter
AUC	Area Under the Curve
BCC	Basal Cell Carcinoma
BG	Background
BIL	Band-Interleaved-by-Line
BIP	Band-Interleaved-by-Pixel
BOR	Band Outlier Removal
BSQ	Band Sequential
BV	Blood Vessel
CCD	Charge-Coupled Device
CDR	Clinical Dementia Rating
CMOS	Complementary Metal-Oxide-Semiconductor
CNN	Convolutional Neural Network
CNS	Central Nervous System
CSF	Cerebrospinal Fluid
CT	Computed Tomography
DL	Deep Learning
DNN	Deep Neural Network
DSM-5	Diagnostic and Statistical Manual of Mental Disorders, 5th Edition
EBEAE	Extended Blind End-member and Abundance Extraction
FAST	Functional Assessment Staging
FAST	Features from Accelerated Segment Test
FN	False Negative
FNRc	False Negative Rate per class
FoM	Figure of Merit
FOV	Field of View
FP	False Positive
G1	Grade 1 of Tumor Malignancy
G2	Grade 2 of Tumor Malignancy
G3	Grade 3 of Tumor Malignancy
G4	Grade 4 of Tumor Malignancy
GA	Genetic Algorithm
GDS	Global Deterioration Scale
GT	Ground Truth
HG	High-Grade
HIV	Human Immunodeficiency Virus
HKM	Hierarchical K-means
HS	Hyperspectral
HSI	Hyperspectral Imaging
IFOV	Instantaneous Field of View
IGS	Image Guided Stereotactic
InGaAs	Indium Gallium Arsenide
IQR	Interquartile Range
IUMA	Instituto Universitario de Microelectrónica Aplicada
KNN	K-Nearest Neighbors
LCTF	Liquid Crystal Tunable Filter
LED	Light-Emitting Diode
LG	Low-Grade
LiDAR	Light Detection and Ranging
MCT	Mercury Cadmium Telluride
MI	Mutual Information
ML	Machine Learning
MM	Malignant Melanoma
MMI	Mattes Mutual Information

MNCD	Major Neurocognitive Disorder
MRI	Magnetic Resonance Imaging
MS	Multispectral
MSAC	M-estimator SAmple Consensus
MSER	Maximally Stable Extremal Regions
MSI	Multispectral Imaging
MV	Majority Voting
NCD	Neurocognitive Disorder
NEBEAE	Nonlinear Extended Blind End-member and Abundance Extraction
NIR	Near-Infrared
NMSC	Non-Melanoma Skin Cancer
NOR	No Outlier Removal
NT	Normal Tissue
OA	Overall Accuracy
PCA	Principal Component Analysis
PCC	Pearson Correlation Coefficient
PET	Positron Emission Tomography
PETG	Polyethylene Terephthalate Glycol
PLA	Polylactic Acid
PSL	Pigmented Skin Lesion
QoL	Quality of Life
QTH	Quartz-Tungsten-Halogen
RBF	Radial Basis Function
RD	Relative Diference
ReLU	Rectified Linear Unit
RF	Random Forest
RGB	Red Green Blue
ROC	Receiver Operating Characteristic
ROI	Region of Interest
SAM	Spectral Angle Mapper
SCC	Squamous Cell Carcinoma
SDK	Software Development Kit
SG	Squared Gradient
SGD	Stochastic Gradient Descent
SIFT	Scale-Invariant Feature Transform
SOR	Signature Outlier Removal
SSIM	Structural Similarity Index
SU	Spectral Unmixing
SURF	Speeded Up Robust Features
SVM	Support Vector Machine
SWIR	Short-Wave Infrared
TMD	Three Maximum Density
TN	True Negative
TP	True Positive
TT	Tumor Tissue
ULPGC	Universidad de Las Palmas de Gran Canaria
UV	Ultraviolet
VIS	Visible
VNIR	Visual and Near-Infrared

Chapter 1: Introduction

1.1 Motivations

Hyperspectral (HS) Imaging (HSI) is an emerging technique capable of providing label-free, non-contact, near real-time, and minimally-invasive intraoperative guidance by using non-ionizing illumination and without employing any contrast agent [1], hence being totally harmless for the patient. HS images are formed by hundreds of narrow spectral channels within and beyond the visual spectral range. This technique provides, for each pixel, an almost continuous spectrum that allows the identification of the tissue, material or substance present in the captured scene based on its chemical composition [2].

In recent years, medical HSI has started to achieve promising results in many different specialties (e.g., oncology [3], [4], digital and computational pathology [5], ophthalmology [6], dermatology [7], [8] or gastroenterology [9], [10]) through the utilization of cutting-edge Artificial Intelligence (AI) algorithms and thanks to the increased modern computational power [11], [12]. Promising results are being achieved in the automatic identification of different types of cancer using HSI [3]. Particularly, HSI has been widely studied in the literature for gastrointestinal cancer in both in-vivo and ex-vivo tissue samples, including stomach, liver, esophagus, pancreas, and colorectal cancer [10]. Additionally, HSI is becoming a tool not only for cancer detection, but also for the diagnosis of other diseases, such as biomarker discoveries and validation [13] or tissue perfusion measurements [14].

The research group where this PhD Thesis has been carried out has previously utilized HSI technology in neurosurgery, as a proof-of-concept, to distinguish between brain tumors and healthy tissue during surgical procedures. However, the potential of HSI extends beyond neurosurgery applications. In this sense, this PhD Thesis evaluate the potential of HSI as a diagnostic tool for three different medical applications:

1) *Neurosurgery:* by optimizing the acquisition system, increasing the in-vivo HS brain database and evaluating a wider spectral range for intraoperative brain tumor diagnostics and enhanced vascularization.

2) *Dermatology:* by developing a proof-of-concept system for the acquisition and processing of dermatological HS data for *in-situ* diagnosis of skin cancer.

3) *Neurogeriatrics:* by evaluating the spectral properties of blood plasma samples using near-infrared information targeting the identification of neurocognitive disorders (NCDs).

1.1.1 Neurosurgery

Surgical resection is the most common treatment for primary brain tumors, especially for diffuse gliomas, since the early and total resection of the tumor increase the overall survival rate (e.g., 5-year survival rate of 50% for diffuse astrocytoma and 81% for oligodendroglioma [15]). In this sense, the extent of resection increases the survival rates of patients with all types of gliomas. However, to achieve maximal resection, neurosurgeons need to determine the precise limits of the tumor during surgery using imaging-guiding techniques [16]. Additionally, neurosurgeons must avoid damaging normal tissue, which can lead to neurological deficits in patients and thus affect their quality of life (QoL) [17]. Current intraoperative imaging guidance techniques have several limitations [16], being necessary to develop new image acquisition and visualization systems to provide quick, detailed, accurate and highly personalized diagnostics for optimal decision-making during neurosurgical procedures, improving the outcomes in the QoL of the patient and reducing the errors, surgical times, and costs.

1.1.2 Dermatology

The process of diagnosing skin cancer is accomplished by a dermatologist who performs a preliminary diagnosis by visually examining the Pigmented Skin Lesion (PSL) normally following the ABCDE (Asymmetry of the mole, Border irregularity, Color uniformity, Diameter and Evolving size, shape or color) rule [18]. After this examination, a biopsy is performed if the dermatologist suspects that the lesion is malignant. Then, a pathological analysis of the sample is carried out to assess the definitive diagnosis. There are several tools based on dermoscopic images and algorithms that implement the ABCD rule (without taking into account the evolving characteristic, which would imply a monitoring over time of the PSL) to assist dermatologist in their clinical routine practice for PSL evaluation and classification [19], [20]. Nevertheless, the current methodologies are not accurate enough, giving as a result high false positive and negative rates. To avoid unnecessary biopsies and surgical procedures, because of the uncertainty in the current diagnoses, and to achieve cost-effective early diagnosis, new methods to improve skin cancer diagnosis should be investigated.

1.1.3 Neurogeriatrics

The diagnosis of NCD establishes, as a main goal, identifying cognitive impairment and NCD from secondary etiology, therefore, potentially treatable patients [21]. Current diagnostic criteria to determine the degree of functional impairment is based on scales that evaluate the subject's cognitive ability. The evolution of neurodegenerative diseases, especially Alzheimer's disease, is slow and both cognitive and behavioral symptoms appear simultaneously. The disease presents and progresses differently in each subject, which may mislead the diagnosis of another disease. For this reason, it is necessary to find effective diagnostic techniques that could help in the early detection of this disease. Biomarkers allow an early biological diagnosis (preclinical phase) and

improve the etiological study of NCDs. The common clinical tests to diagnose a possible Alzheimer's disease are based on *in-vivo* neuroimaging biomarkers and body fluid biomarkers [22], [23]. However, the use of these procedures is expensive, highly invasive, and has a restricted availability for verifying the diagnosis [24]. For this reason, other biomarkers related to blood samples are being investigated. This alternative is less invasive and cost-effective for early detection, especially in the identification of patients both in the clinical and preclinical phases of Alzheimer's disease.

1.1.4 Research Hypotheses

The research carried out in this PhD Thesis is based on two main hypotheses:

1) HS instrumentation can detect subtle spectral variations in biological samples and can be adapted to different medical applications.

2) A methodology based on supervised and unsupervised Machine Learning (ML) algorithms can be employed for processing spectral information, performing disease diagnosis regardless of the type or origin of the disease.

In summary, this dissertation aims to explore the potential of HSI technology as a diagnostic tool in different medical applications. The hypotheses are examined and validated to advance our understanding of the role of HSI in modern medical diagnosis and to facilitate its integration into clinical practice on a larger scale.

1.2 Objectives

The main objective of this PhD Thesis is to demonstrate the capabilities of HSI in the medical field by analyzing its use in different medical applications, such as *neurosurgery* (intraoperative brain cancer diagnostics and delineation), *dermatology* (*in-situ* diagnostics of skin cancer), and *neurogeriatrics* (early diagnosis of major NCDs (MNCDs) through blood plasma samples). In order to achieve this main goal, several specific objectives have been raised at the beginning of this dissertation. These specific objectives have been subdivided by primary and secondary specific objectives:

1) **To acquire the necessary knowledge** about the different HS instrumentation for medical applications currently employed in the state-of-the-art:

    a) **Medical HS instrumentation for intraoperative environments and surgical guidance and diagnostics**, especially for neurosurgery.

    b) **Medical HS instrumentation for in-situ diagnostics using portable devices**, especially for dermatology.

    c) **Laboratory HS instrumentation for data acquisition of liquid biological samples**.

2) **To obtain the necessary knowledge** about the different algorithms based on ML and Deep Learning (DL) commonly used in the literature for pre and post-processing HS images.

3) **To design and develop HS acquisition systems** for different medical applications that will allow the generation of **HS databases**, which will be used for the development of algorithms based on ML/DL for disease identification and diagnosis:

    a) **To optimize an intraoperative HS-based acquisition system** developed in a previous project, enhancing its capabilities for capturing data in a wide spectral range for the use case of neurosurgery.

    b) **To develop a dermatologic HS-based acquisition system** for capturing in-situ pigmented skin cancer lesions during clinical routine practice.

    c) **To prepare an HS-based acquisition framework** for capturing blood plasma samples in a laboratory environment.

4) **To design and develop HS classification frameworks** capable of identifying different diseases depending on the clinical application:

    a) **To generate a methodology to provide vascular enhanced maps** of in-vivo brain during neurosurgical operations.

    b) **To create a benchmark for intraoperative brain tumor detection and delineation** using an enhanced in-vivo human HS database.

    c) **To propose a processing framework to fuse data from two different HS cameras** and evaluate its performance in the use case of neurosurgery.

    d) **To design and evaluate a classification framework to discriminate between benign, malignant, and atypical PSLs**, targeting a hand-held clinical device for dermatology.

    e) **To design and evaluate a classification framework for MNCD detection** through processing blood plasma samples.

1.3 Collaborations and acknowledgments

This PhD Thesis presents the outcomes achieved during the close collaboration between the Institute for Applied Microelectronics (IUMA) of the University of Las Palmas de Gran Canaria (ULPGC) and several research institutions:

- University of Pavia (Italy).
- Autonomous University of San Luis Potosí (Mexico).
- Department of Neurosurgery of the University Hospital of Gran Canaria Doctor Negrin of Las Palmas de Gran Canaria (Spain).
- Department of Dermatology of the University Hospital of Gran Canaria Doctor Negrin of Las Palmas de Gran Canaria (Spain).

- Department of Dermatology of the Complejo Hospitalario Universitario Insular-Materno Infantil of Las Palmas de Gran Canaria (Spain)
- Research Unit of the University Hospital of Gran Canaria Doctor Negrín (Spain).

In addition, this research was conducted as part of the ITHaCA (Hyperspectral Identification of Brain Tumors) project, funded by the Canary Islands Government under Grant Agreement ProID2017010164.

Finally, this PhD Thesis was developed while the candidate was beneficiary of a predoctoral grant given by the "Agencia Canaria de Investigacion, Innovacion y Sociedad de la Información (ACIISI)" of the "Consejería de Economía, Conocimiento y Empleo" of the "Gobierno de Canarias", which is part-financed by the European Social Fund (FSE) (POC 2014-2020, Eje 3 Tema Prioritario 74 (85%)).

1.4 Document organization

This document has been structured in 6 chapters. A brief explanation of each chapter is presented next.

Chapter 1: Introduction. In the present chapter, the main motivations and objectives that have led to the development of this dissertation are described. In addition, the structure of the document is presented.

Chapter 2: Background on hyperspectral imaging instrumentation, algorithms, and applications. In this chapter, the concept of the HSI and the description of the main algorithms employed are presented. In addition, the current state-of-the-art in different medical applications using HSI is detailed.

Chapter 3: Intraoperative HS acquisition system for brain surgical diagnostics and guidance. This chapter presents an overview of the HS system developed and the modifications applied to the previous intraoperative demonstrator for brain cancer detection. In addition, brain cancer detection algorithms are evaluated using an extensive HS database. Finally, VNIR-NIR fusion algorithm are evaluated using the reference database and the *in-vivo* HS human brain database.

Chapter 4: Dermatoscopic HS system for skin cancer detection. The feasibility of the developed system for brain cancer detection was the basis for the exploration of its application in other medical contexts, such as the specific case of skin cancer detection using a similar approach. In this chapter, the HS system employed for skin cancer detection and the HS database are presented. A dermatologic framework based on automatic segmentation and classification is explained. Finally, the framework is evaluated using a three-way partition.

Chapter 5: SWIR-based acquisition system targeting early detection of major neurocognitive disorders. Previous applications evaluated the VNIR and NIR spectral ranges for its application in different medical applications. This chapter evaluates a different spectral range in a different application context but using the same methodology for processing the spectral data. A SWIR-based system was developed to generate a HS plasma database. A framework based on

supervised classification using ML and DL approaches was used to detect major neurocognitive disorders.

Chapter 6: Conclusions & future lines. This chapter concludes the work presented in this dissertation by summarizing the advantages, disadvantages and main contributions of the methods developed as well as presenting future research lines of this dissertation. Finally, the academic production developed in the context of this PhD Thesis is presented.

Annex A: Sinopsis en español. In this annex, a brief summary of the dissertation is presented in Spanish.

Bibliography: This PhD Thesis manuscript concludes with the list of references employed during the elaboration of this document.

Chapter 2: Background on Hyperspectral Imaging Instrumentation, Algorithms, and Applications

2.1 Introduction

This chapter presents a comprehensive review of the current research in the different medical fields relevant to the development of this PhD Thesis. First, the basic concepts of HSI and the common HSI instrumentation are introduced. Second, a brief description of the basic pre-processing techniques used to analyze HS images and the different algorithms commonly used are described, as well as the performance metrics for their evaluation. Finally, a brief state-of-the-art related to the use of HSI in the medical field is presented, with special emphasis on brain cancer, skin cancer and MNCD diseases, which are the areas studied in this dissertation.

2.2 Basic Concepts of HSI

HSI is an emerging imaging modality originated in the remote sensing field [25] that has expanded its application to other research and industrial areas in the past years [26], such as food quality inspection [27], quality control of pharmaceutical products [28], marine ecosystems monitoring [29], soil pollution monitoring [30], petrochemical industry [31] or defense and security [32]. HS images are composed by spatial and spectral information, conforming a three-dimensional matrix, also called *HS cube* (Figure 2-1.a), where each spatial pixel is related to a vector of intensity light values that belong to hundreds of different spectral wavelengths, also called *channels* or *bands*. This vector conforms a continuous spectrum that is commonly named *spectral signature*. On the contrary, Multispectral (MS) sensors have lower spectral resolution than HS sensors, where a spectral band can integrate between tens to hundreds of nanometers. This MS sensors usually include spectral bands related to blue, green, red, red edge, and near infrared, while maintaining gaps among different bands [33] (Figure 2-1.a). Unlike standard digital color cameras, that captures RGB (red, green and blue) images, using only three wavelengths (Figure 2-1.a), MS and HS cameras are able to

cover broadband spectral ranges (Figure 2-1.b), such as Visible (VIS), between 400 and 700 nm, Visual and Near Infrared (VNIR) between 400 and 1000 nm, Near Infrared (NIR) from 900 to 1700 nm or near Short-Wave Infrared (SWIR) from 900 to 2500 nm [34]. RGB images can be seen as a specific and very reduced case of MS Imaging. The spectral signature allows the differentiation, at pixel level, of the materials presented in the captured scene based on their chemical composition [35].

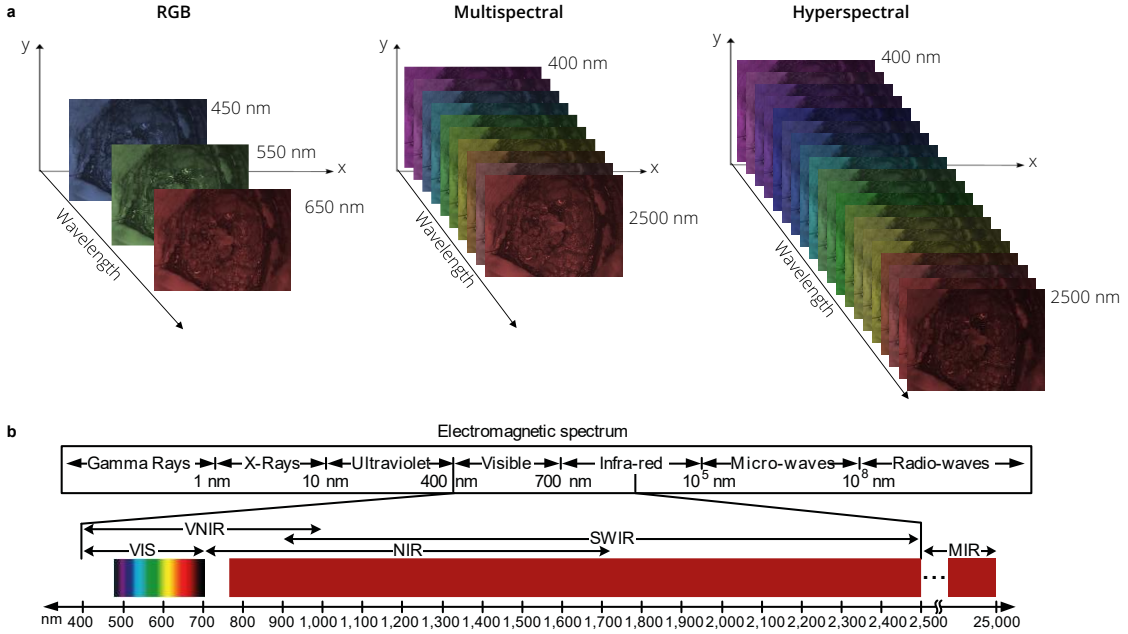

Figure 2-1: Principles of hyperspectral imaging technology. a) Comparison of the different image modalities. **b**) Electromagnetic spectrum.

Many studies in the literature have demonstrated the high potential of HSI for improving remote and non-destructive detection of chemical compositions in different applications, obtaining promising results. In remote sensing, vegetation indices are commonly used to enhance vegetation information and suppress background information [36]. These indices are based on RGB color and new indices have emerged employing several spectral bands. HSI can be useful for differentiating plants depending on the pigments or distinguishing crop types, analyzing their quality by using the water absorption peak present in the plant leaf within the NIR range at 1400 and 1900 nm [37]. Chlorophyll is the primary photosynthetic pigment in green vegetation and can be identify using the chlorophyll absorption peaks at 450 nm and 680 nm, related with the blue and red regions, respectively. Plant stress can be detected by reducing the growth of chlorophyll [38]. Marine ecosystem has been study using underwater HSI system showing its potential to monitor pigmentation in benthic and sympagic phototrophic organisms at small spatial scales [29]. For example, in-vivo chlorophyll pigments of warm-water corals achieve a maximum absorption at 670 nm applying the second derivative. Chlorophyll absorption at 700 nm is employed to discriminate coral from sand and algae [29].

The food industry employs visual inspection, microscopy, polymerase chain reaction, fluorescence, etc. for detecting the presence of contaminants in monitoring process [27]. HSI technology has been tested as non-invasive monitoring of food quality, achieving to detect parasites at a depth of 8 mm using wavelengths between 350 and 950 nm [39]. Apart of contaminants, visual features have also been analyzed,

such as color, to determinate the physical, chemical, or microbiological quality of food products. Another examples of the use of HSI in this field are the detection of chilling injuries produced by low-temperature storage or bruises in fruits and vegetables during packing and transporting [40]. Fraud detection in meat is another application which employ HSI technology to discriminate pure and mixed meat in minced meat. Six wavelengths (957, 1071, 1121, 1144, 1368, and 1394 nm) were employed to identify minced beef adulterated with horse, pork, or chicken [41]. In addition, detection of adulterated chocolate powder with peanut flour was achieving using NIR HSI by Laborde *et al.* [42]. The main ingredients of chocolate powder, sucrose and cocoa, and the peanut flour were analyzed. The study found that cocoa has peak absorption at 1208, 1491, and 1935 nm, related with cocoa proteins. Sucrose has absorption peaks at 1435 and 2072 nm associated with the carbon-hydrogen and oxygen-hydrogen stretching. Peanut flour has two main absorption peaks at 1200 and 1942 nm, representative of the water absorption, and two peaks at 1474 and 1735 nm related with proteins.

HSI technology has been also employed during quality control of pharmaceutical products [28]. Al Ktash *et al.* [43] analyzed the active pharmaceutical ingredients in tablets, as ibuprofen, acetylsalicylic acid, and paracetamol employing Ultra-Violet (UV) region from 225 to 400 nm. Ibuprofen present an absorbance peak at 223 nm, while acetylsalicylic acid achieves a maximum peak at 228 nm. Finally, paracetamol present a distinct band at 244 nm.

In medical applications, HSI technology has been widely researched to measure deoxyhemoglobin and oxyhemoglobin, employing isosbestic points of the hemoglobin absorption spectra in the spectral region 510-590 nm or absorbance at the oxygen-sensitive wavelength at 600 nm [44]. These points have been employed to visualize and highlight the arteries and veins in forearm to assist in phlebotomy [45]. In addition, skin lesions can be identified using the HSI systems, analyzing the spectral properties of the skin, which are caused by groups of chromophores, such as melanin, hemoglobin, water, beta-carotene, collagen, and bilirubin. These chromophores concentrations have been analyzed in the epidermis and dermis in the spectral range from 500 to 1000 nm [46]. The reflected light provides information of these chromophores [47]. Kubelka-Munk is a theorical model employed to create skin models using two layers (epidermis and dermis) and two chromophores (melanin and hemoglobin) [48]. Another emerging application is organ quality assessment during perfusion. HSI was evaluated to predict tissue water index in kidneys, allowing to analyze tissue-related damage during ex vivo preservation. This index was computed analyzing two water absorption peaks 760 and 970 nm [49]. Alzheimer's disease has been investigated by amyloid-beta protein analysis in the retina and the combination of HSI system due to does not require the use of contrast agents. The presence of amyloid-beta protein can increase the reflectance at 550 nm [50].

2.3 HSI Instrumentation

In HSI, the instrumentation is a crucial element to have a reliable, efficient, and high-quality spectral data acquisition. Usually, an HSI platform consists of a HS camera, a light source, a computer with the acquisition software, and, in some instances, a motorized mobile station, which depends on the scanning mode employed

by the HS camera [51]. HSI systems can be classified based on the measurement mode (*reflectance*, *transmittance*, or *interactance*), the image acquisition mode (*point*, *line*, or *area scanning*), or the spectral ranges that can be captured (*VIS*, *VNIR*, *NIR*, or *SWIR*).

The three most commonly used measurement modes depend on the lighting configuration [2]. In reflectance mode, the light source and the HS camera are on the same side regarding the sample and the light reflected from the sample is captured. (Figure 2-3.b). In the transmittance mode, the HS camera is located on the opposite side of the light source, capturing the transmitted light that penetrates through the sample (Figure 2-3.b). The interactance mode combines the reflectance and transmittance modes. In this case, the light source and the HS camera are on the same side, parallel to each other and separated by a light barrier. The light barrier ensures that the light received by the HS camera is transmitted through the sample with a minimal penetration depth, depending on the system employed. This is achieved by sealing the light from the environment to prevent any interference (Figure 2-3.c). Reflectance mode may not be as effective for detecting internal quality because of limited light penetration but provides rich amount of information of regarding the surface of the sample. Transmittance mode provides valuable information from inside the sample but requires a high-intensity light source or the sample to be thin enough to allow light transmission. Interactance mode is useful for evaluating the properties of sublayer tissues. It works by transmitting light into the sample and then measuring the amount of light that is backscattered to the surface [2]. A similar strategy to interactance is light scattering, which quantifies the optical scattering coefficients of the sample using a light source that can be a continuous wave, temporally modulated or pulsed, or spatially modulated [52].

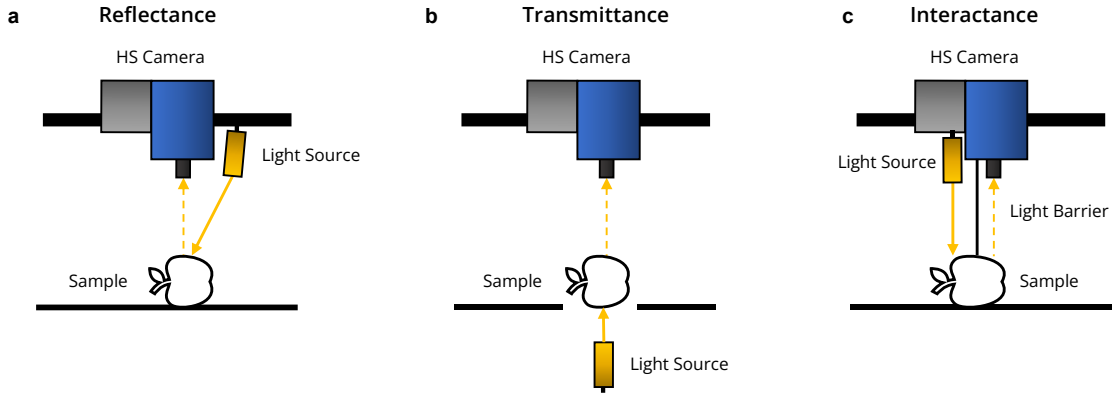

Figure 2-2: Hyperspectral imaging measurement modes. a) Reflectance mode. **b**) Transmittance mode. **c**) Interactance mode.

The HS camera is the main component of the acquisition system, which consists of two main structures: spectrographs or spectrometers and a detector or array of photo-sensitive detectors [53]. Spectrographs allow dispersing of polychromatic incident light into light beams with specific wavelengths, there being three types of devices [54]: monochromator, optical bandpass filter, and single-shot imager. The scattering devices focus the narrow wavelength light toward each of the detectors. In this sense, the photosensors most used in HSI are Charge-Coupled Devices (CCDs) and Complementary Metal-Oxide Semiconductors (CMOS) [55]. The principal difference between these two sensors lies in the transmission scheme of the incoming signals. On the one hand, CCD sensors focus on measuring the luminous intensity, transferring the

resulting multi-sensor signal to a digital/analog converter. On the other hand, CMOS sensors incorporate the photodetector and the digital/analog converter together, thus the information from each sensor is independent of the rest. Because of this difference, CMOS sensors are faster in measuring and capturing photons, but these sensors are susceptible to the presence of non-linear noise and are mostly affected by dark currents [55]. This situation is compensated by CCD sensors, since by digitizing the signals outside the photodiode allows the inclusion of components with different characteristics that mitigate noise, and dark current, but at the cost of a reduced acquisition speed. In addition, CCDs and CMOS have better sensitivity for the spectral range between 400 and 1000 nm (VNIR), while indium gallium arsenide (InGaAs) and mercury cadmium telluride (MCT) sensors are used to cover the NIR range from 900 to 1700 nm and SWIR range, from 900 to 2500 nm (Figure 2-6) [2].

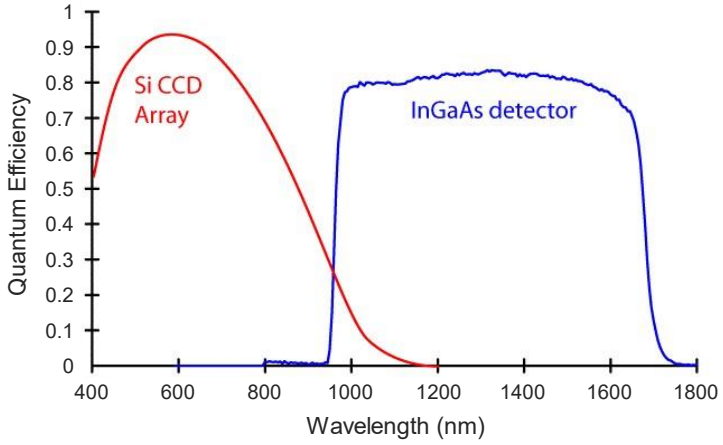

Figure 2-3: Quantum efficiency of CCD and InGaAs sensors [56]**.**

In general, HSI cameras are classified depending on the scanning method used to generate the HS cubes, with four main types of scanning: *whiskbroom*, *pushbroom*, *focal plane*, and *snapshot* [55], as indicated in Figure 2-4.

Whiskbroom or *point-scanning* cameras are characterized by capturing the spectral information of one pixel per time (Figure 2-4.a); this means that to scan a particular region, it is necessary to have a scanning platform that is moved through the scanning area of the camera at each location in the *X* and *Y* spatial dimensions. Because of this, whiskbroom cameras require considerable time to acquire an image, so spatial resolution is often limited. Nevertheless, the main strength of these cameras is their high spectral resolution which permits to capture a large amount of spectral information.

Pushbroom or *line-scanning* cameras (Figure 2-4.b) acquire the complete spectra of several pixels of one spatial dimension in one shot, hence, the area of interest is scanned line by line until the entire HS image is composed. This scanning mode requires also a scanning platform to cover the second spatial dimension, and for that reason motion artifacts may occur. Pushbroom cameras provide relatively high spatial and spectral resolution and for this reason it is the most used technique in several applications.

Focal plane cameras (also known as *spectral* or *area scanning*) (Figure 2-4.c) acquire a 2D monochromatic image at a given wavelength, i.e., each wavelength is captured independently until completing the HS cube. Usually, this acquisition mode

allows to capture different wavelengths using adjustable filters such as Liquid Crystal Tunable Filter (LCTF) or Acousto-Optic Tunable Filter (AOTF). The main advantage of these cameras is that they can capture a single wavelength or several wavelengths, making them highly configurable, but they are susceptible to the presence of motion artifacts. In addition, they are notable for their capacity to acquire detailed spatial information in a relatively reduced amount of time.

Snapshot cameras (Figure 2-4.d) acquire spatial and spectral information simultaneously, but unlike focal plane cameras, this type of cameras produces the HS cube in a single shot, which results in a significative reduction of the acquisition time. However, currently snapshot cameras can capture only a limited number of spectral bands, so the spectral resolution is lower than with other camera types. The same applies to the spatial resolution: to fit pixels in the sensor at different wavelengths the spatial resolution is usually reduced.

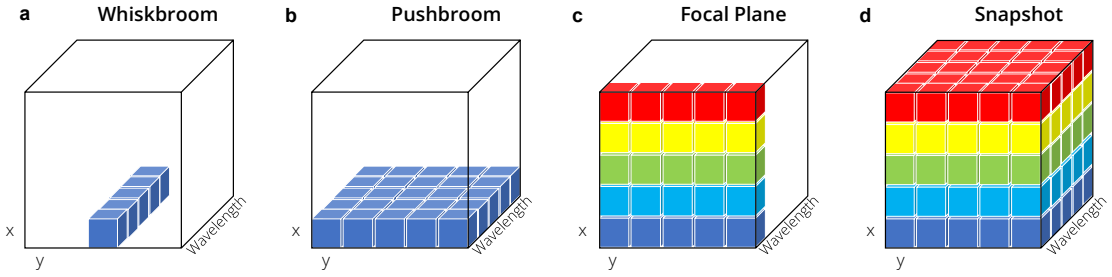

Figure 2-4: Hyperspectral imaging acquisition methods. a) Whishbroom. **b**) Pushbroom. **c**) Focal Plane. **d**) Snapshot.

After acquisition, the HS images must be stored in a logically organized file to allow reconstruction of the HS cubes in any software. The most common formats are the *Band-Interleaved-by-Pixel* (BIP), *Band-Interleaved-by-Line* (BIL), and *Band Sequential* (BSQ). In BSQ format (Figure 2-5.a), each line of data is immediately followed by the next line in the same spectral band. BIL format stores the first line of the first band followed by the first line of the second band, and so forth (Figure 2-5.b). In BIP format, the first pixel of all bands is placed in sequential order, followed by the second pixel of all bands, and so on (Figure 2-5.c). Whiskbroom sensors typically store HS images in BIP format, whereas pushbroom sensors use BIL format, and focal plane and snapshot sensors typically use BSQ for storage [57].

In this sense, the light source is another crucial component of the HSI acquisition system, since light is the medium that provides information about the objects under study. Currently, halogen lamps are the most widely used because of their broad-spectrum, which is continuous, soft, and without sharp peaks [53]. However, this type of illumination has certain disadvantages, such as temperature rise in the sample, short lifetime of the bulb, and spectral peak change due to variations in temperature, voltage, and time of use. On the other hand, Light-Emitting Diodes (LEDs) have started to be used as light sources due to their long lifetime, fast response, compact size, low power consumption, and low heat generation [53]. LEDs can produce broad and short spectra in the ultraviolet, visible, and infrared regions. However, they are not very efficient in dissipating heat, which reduces their lifetime and affects their spectrum. Finally, lasers are light sources with a narrow bandwidth, linearly directed, and used mainly in fluorescence and photoluminescence applications.

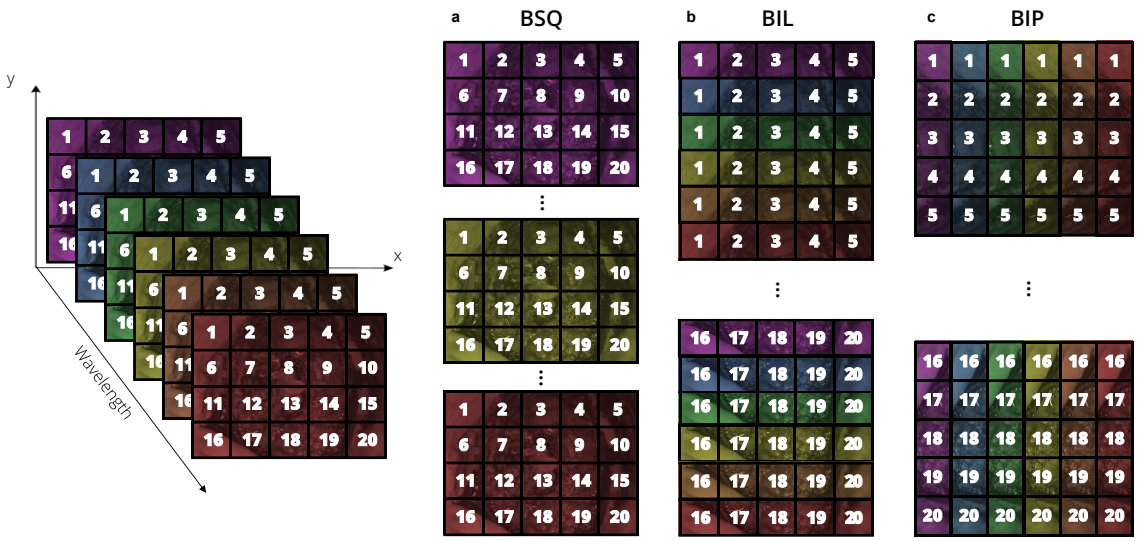

Figure 2-5: HS data storage structure types. a) Band Sequential (BSQ) format. **b**) Band-Interleaved-by-Line (BIL) format. **c**) Band-Interleaved-by-Pixel (BIP) format.

2.4 Processing Algorithms for HSI

Many studies in the literature have demonstrated the high potential of HSI for remote, non-invasive and non-destructive detection of the tissue chemical composition in different applications, obtaining promising results [46]. However, a proper analysis of HS images is not an easy task, considering that the key idea relies on the analysis of spectral and spatial information presented in the HS image to identify the spectral signatures of the basic components [58]. To achieve this proper spectral analysis, pre-processing techniques could be applied to reduce the effects of temperature and illumination changes and light source aging. After that, the HS images are processed following different approaches that could be grouped as Spectral Unmixing (SU) and ML, among the most relevant ones. The ML group can be subdivided into supervised, unsupervised, and semi-supervised methods according to the prior labeling information used for training. However, only supervised, and unsupervised methods were evaluated in this dissertation. Figure 2-6 represents the most common processing steps and algorithms that have been employed in the work presented in this dissertation and will be presented in the following sections.

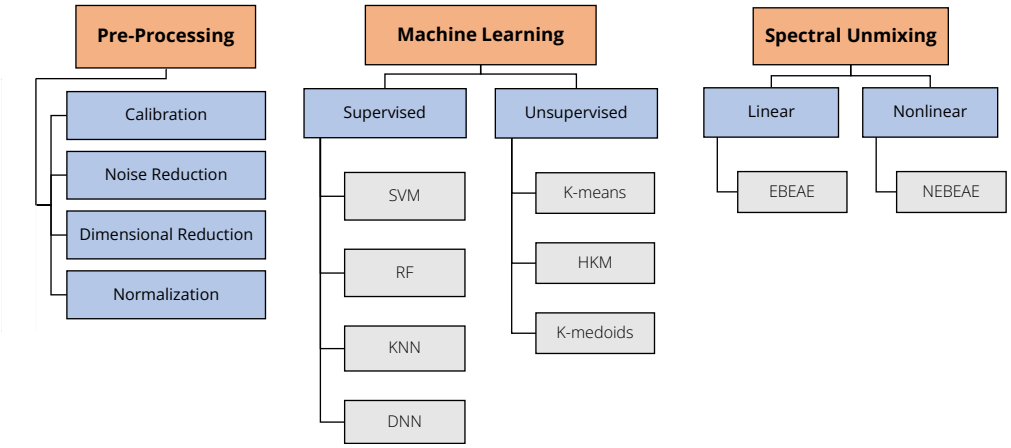

Figure 2-6: Summary of the pre-processing techniques and algorithms used in this dissertation.

2.4.1 Basic Pre-processing Techniques

HS images are composed of a large number of pixels with a high correlation of information between the bands. The accuracy and reliability of the results obtained from these HS images may be compromised by the presence of erroneous data values or outliers [59]. The instrumentation employed in the HS cameras can affect the acquired data due to environmental factors. Temperature can cause fluctuations in the dark currents of the sensors, introducing spectral noise, especially in the extreme bands of the sensor. Additionally, the interaction of light with the object can generate artifacts that affect the overall quality of the HS image. For these reasons, it is necessary to apply various pre-processing techniques before analyzing HS images, such as, black-and-white correction to reduce dark currents and the influence of illumination irregularities, denoising methods using filters to reduce spatial and spectral noise or even methods to reduce the redundant information [59], [60].

In general, once a raw HS image (I_0) is acquired by the sensor, it is necessary to perform a first pre-processing to eliminate the effects of temperature and illumination changes and aging of the light source. This pre-processing is known as spectral calibration and is a widely used method for correcting dark current noise [61], [62]. The raw image is modified based on a dark (D) and white (W) reference images. Commonly, D is captured by closing the camera shutter, while W is obtained from an image of a highly reflective and uniform white surface. These two reference images are used to calculate the HS corrected image (I) by Eq. (1), which represents the relative reflectance of each pixel [63]. Figure 2-7 shows an example of how the spectral signatures of different pixels are calibrated. The spectral signatures of the dark and white references are shown in Figure 2-7.a, and two random pixels before (Figure 2-7.b), and after calibration (Figure 2-7.c).

$$I = \frac{I_0 - D}{W - D} \tag{1}$$

The HS corrected image I can also be expressed in terms of absorbance (A) by evaluating Eq. (2) [63]. In addition, Figure 2-7.d shows the absorbance spectral signature after applying Eq. (2).

$$A = -\log_{10}\left(\frac{I_0 - D}{W - D}\right) \tag{2}$$

In this PhD Thesis, all datasets employed were pre-processed applying spectral calibration. In addition, other methods have been used depending on the type of analysis to be performed. For example, to minimize the spectral noise caused by the low response of the HS sensor in the lower and higher spectral bands, some bands can be removed, and, hence, reducing the number of bands in the pre-processed HS cube. Moreover, the HS data can be filtered using a smooth filter for reducing the spectral noise in the remaining spectral bands. This filter can be based on several methods, but the one employed in this works is based on a moving average filter, being applied to each point of the spectral signature. The new smooth value $(y_k)_s$ of a certain wavelength (k) is computed using Eq. (3), where $2n + 1$ is defined as *span* or *window* of the moving average filter, y_i is the original value at the wavelength i, and n is the number of neighboring data points on either side of y_i.

$$(y_k)_s = \frac{1}{2n+1}\sum_{i=k-n}^{k+n} y_i \tag{3}$$

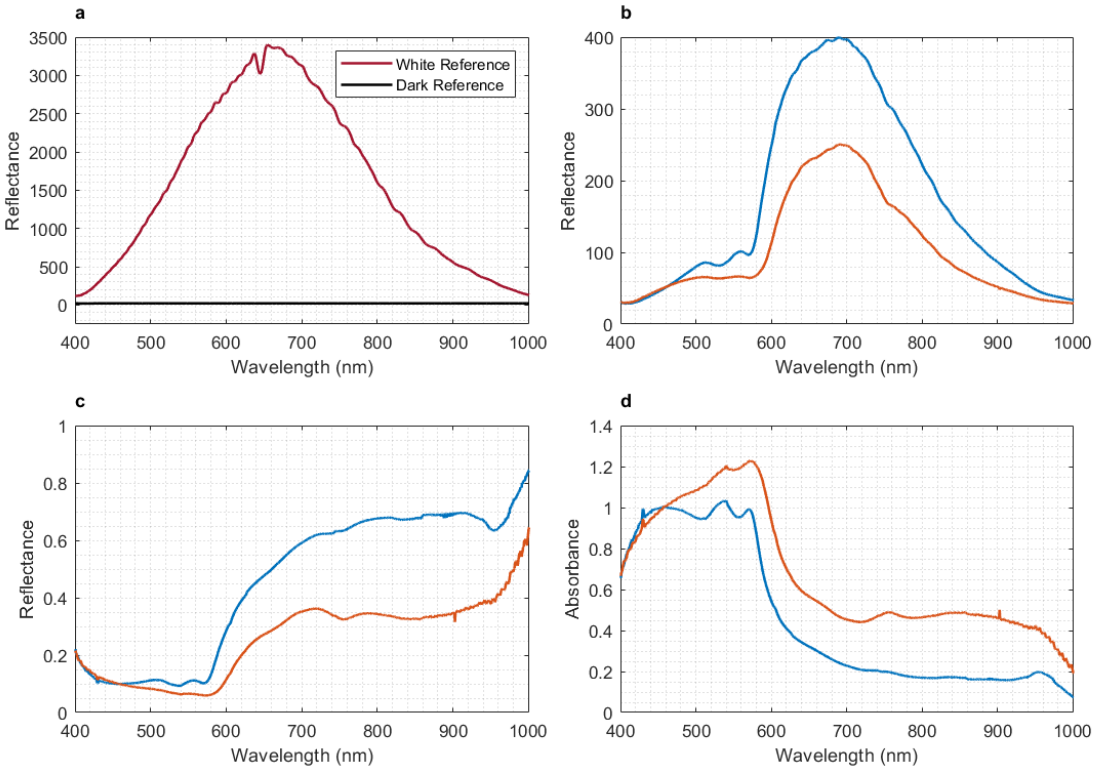

Figure 2-7: Effect of calibration in the spectral signatures. **a**) White and dark reference spectral signatures. **b**) Two examples of uncalibrated spectral signatures. **c**) Two examples of calibrated spectral signatures. **d**) Calibrated spectral signatures converted to absorbance.

Additionally, pushbroom HS sensors (as the one employed in some of our studies) typically have high spectral resolution, providing redundant information in consecutive bands. In some cases, in order to reduce this redundancy and to speed up the processing algorithms execution, different dimensional reduction algorithms or methods can be applied to reduce the number of bands. In this dissertation, we decimated the number of bands in some experiments and also employed PCA algorithms. PCA is a technique that performs a linear transformation of the HS image by using orthogonal projections to minimize the covariance matrix of the original HS image [64].

Finally, normalization can be applied to each spectral signature to range the data between 0 and 1 with the goal of homogenizing its amplitude, thus avoiding the subsequent processing methods to be affected by the amplitude differences caused by non-uniform illumination conditions. In this sense, only the shape of the spectral signature will be considered. Eq. (4) shows the min-max normalization that was employed in this dissertation, where $\min(z_k)$ and $\max(z_k)$ are the minimum and maximum value, respectively, in a certain pixel (z_k).

$$(z_k)_n = \frac{z_k - \min(z_k)}{\max(z_k) - \min(z_k)} \tag{4}$$

In the following chapters, the different pre-processing methods applied to the database will be explained in detail, depending on the HS camera used in each targeted application.

2.4.2 Algorithms based on Machine Learning

The analysis of HSI by means of ML techniques allows the identification and classification of different spectral signatures, recognizing of features or patterns, mainly in a supervised or unsupervised manner.

2.4.2.1 Supervised ML algorithms

Supervised ML-based classifiers allow the automatic identification of substances or tissue types at pixel level in a HS image relying on prior labeled data to train the classification models. In this subsection, the supervised ML algorithms employed in this dissertation are presented.

The Support Vector Machine (SVM) classifier finds out the best hyperplane to separate data from different classes with a maximum margin, being used for classification and regression purposes [65]. This classifier finds out the best hyperplane to separate data from different classes with a maximum margin. The boundary hyperplane is calculated using a training dataset. A linear hyperplane sometimes is not enough to separate data in some classification problems. For this reason, it is necessary to transform the dimensional space. This transformation is performed using different kernel functions. Linear, Gaussian Radial Basis Function (RBF), sigmoid, and polynomial kernel are the most used. Table 2-1 presents the mathematical expressions of each kernel and the hyperparameters, where x and y are observation vectors and the superscript T refers to transpose operation. The hyperparameter cost (C) is common to all kernels and controls the trade-off between achieving a low training error and minimizing the complexity of the decision boundary. The hyperparameter gamma (γ) influences individual training samples at the decision boundary. The (d) hyperparameter is the degree of the polynomial kernel function. The higher the hyperparameter value d, the more curved the resulting hyperplane line. cf is the intercept constant hyperparameter. These hyperparameters can be tuned to improve the outcomes of the classification. The LIBSVM library [66] was used in the different experiments performed in this dissertation.

Table 2-1: Mathematical expressions of the Support Vector Machine (SVM) kernels and control hyperparameters.

Kernel	Formula	Hyperparameters
Linear	$k(x,y) = x^T \cdot y$	C
RBF	$k(x,y) = exp(-\gamma \cdot \|x-y\|^2)$	C, γ
Sigmoid	$k(x,y) = tanh(\gamma \cdot x^T \cdot y + cf)$	C, γ, cf
Polynomial	$k(x,y) = (\gamma \cdot x^T \cdot y + cf)^d$	C, γ, cf, d

K-Nearest Neighbor (KNN) is a pixel-wise classifier focused on finding and classifying data based on the majority class of the number of nearest neighbors (K_{NN}) [67]. The neighborhood is formed by the training dataset, and each incoming sample is compared with all neighbors (using a distance metric) to find the K_{NN} closest neighbors. Then, the label of the incoming sample is assigned to the majority class of the K_{NN} nearest neighbors. Different distance metrics can be computed to find the nearest

neighbors, such as Euclidean, Chebyshev, Cosine, or Mahalanobis metrics. Table 2-2 presents the mathematical expressions of each distance metric, where x and y are observation vectors to determine the distance, and C is the covariance matrix. For the KNN classifier, the number of nearest neighbors is the hyperparameter to be optimized to obtain the best model. The MATLAB® Statistics and Machine Learning Toolbox was employed for the KNN implementation used in the different experiments performed in this dissertation.

Table 2-2: Mathematical expressions of the K-Nearest Neighbors (KNN) distance.

Distance	Formula
Euclidean	$d_E = \sqrt{(x-\mathrm{y})(x-\mathrm{y})^T}$
Chebychev	$d_{Ch} = max_j\{\lvert x_j - y_j \rvert\}$
Cosine	$d_C = 1 - \frac{xy^T}{\sqrt{(xx^T)(yy^T)}}$
Mahalanobis	$d_M = \sqrt{(x-y)C^{-1}(x-y)^T}$

Random Forest (RF) is a supervised learning method that can be applied to solve classification or regression problems [68]. It is composed by a combination of predictor trees where each tree depends on the values of a random vector. The RF algorithm identifies a new data class by obtaining a vote of the predictions of the new data from a multitude of decision trees. The training data are hierarchically partitioned into smaller homogeneous groups in each decision trees. Compared with other algorithms, RF offers a reduced training time [69]. The optimization of a RF model can be performed by establishing the most suitable number of trees (N) in the model. The MATLAB® Statistics and Machine Learning Toolbox was employed for the RF implementation used in the different experiments performed in this dissertation.

Deep Neural Networks (DNN) architecture is a system of interconnected neurons composed of several layers, including input and output layers, and at least one hidden layer in between (Figure 2-8). In DL models, neurons represent a linear function followed by a nonlinear mapping function Φ. In this way, the optimal solution provided is a nonlinear solution spanned by the inputs. Let $y = f(x)$ be a continuous function from $\mathbb{R}^B$ to $\mathbb{R}^{NC}$, where B represents the spectral resolution and NC the number of classes. As a classification problem, the goal is to approximate y by a function $\hat{f}(x;\theta)$, where the training weights (θ) are the parameters of the DL model that minimize a loss function. In this dissertation, the Cross-Entropy Loss function was employed, where the function controls the value of the parameters θ:

$$\min_{\theta} \; -\sum_{i}^{NC} y_i \log\left[\hat{f}(x;\theta)_i\right], \tag{5}$$

where the i subscript enumerates the different classes. The MATLAB® Deep Learning Toolbox was used for the DNN implementation used in the different experiments performed in this dissertation.

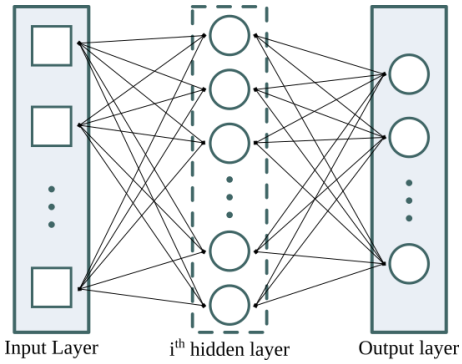

Figure 2-8: DNN Architecture with expandable hidden layers. Each neuron is a circle. Input layer size is defined by dimension B, output size by number of classes NC.

2.4.2.2 Unsupervised ML algorithms

Unlike supervised ML algorithms, unsupervised algorithms do not have access to target labels, discovering patterns, structures, or relationships in unlabeled data. These algorithms are commonly used for tasks such as clustering, anomaly detection, dimensionality reduction, and data visualization.

Clustering algorithms group similar data points in different groups or clusters. Data are grouped together on the basis of feature similarity. K-means and K-medoids are similar clustering algorithms widely used to segment HS images into K different clusters [70]. K-medoids is robust to outliers and the centroid of each cluster is an actual spectrum found in the cluster set, while in the K-means algorithm, the cluster centroid is the average value of all spectra in the cluster set [71]. Hierarchical clustering organizes the data into a tree structure, being the number of trees defined by the K value. Hierarchical K-means (HKM) uses K-means to split the clusters [72].

The optimal number of clusters (K) can be determined employing clustering evaluation methods, such as Silhouette [73], Calinski Harabasz [74] and Davies Bouldin [75]. Silhouette value for the ith point is computed using Eq. (6), where a_i is the average distance between each point within a cluster, and b_i is the average distance between all clusters. Silhouette values range from -1 to 1, with high values indicating that the points match their clusters well. The Calinski Harabasz value is computed using Eq. (7), where SS_B is the inter-cluster variance, SS_W is the overall within-cluster variance, K is the number of clusters, and N is the number of observations. Davies Bouldin value is computed using Eq. (8), where $\bar{d}_i$ is the average distance between each point in the i_{th} cluster and the centroid of the i_{th} cluster, $\bar{d}_j$ is the average distance between each point in the j_{th} cluster and the centroid of the j_{th} cluster, and $d_{i,j}$ is the Euclidean distance between the centroids of the i_{th} and j_{th} clusters. The MATLAB® Statistics and Machine Learning Toolbox was employed for the K-means and K-medoids implementations used in the different experiments performed in this dissertation.

$$S_i = \frac{b_i - a_i}{\max(a_i, b_i)} \tag{6}$$

$$CH_k = \frac{SS_B}{SS_W} \times \frac{(N-K)}{(K-1)} \tag{7}$$

$$DB_k = \frac{1}{K}\sum_{i=1}^{K} \max_{i \neq j}\left\{\frac{\bar{d}_i + \bar{d}_j}{d_{i,j}}\right\} \tag{8}$$

2.4.3 Algorithms based on Spectral Unmixing

In the literature, several approaches have been proposed to identify and classify endmembers present in an HS image, but the main two strategies are based on Spectral Unmixing (SU) and ML [58], [76]. First, in SU, the physical relation between endmembers and their abundances is represented by a mathematical model, which describes the optical paths and interactions of the reflected light by the objects in the scene [77]. The simplest approach in SU assumes that photons interact with only one material before reaching the sensor, meaning that a linear mixing model might solve the problem; however, this approach is only suitable for simple and not realistic scenarios, because the light captured by the sensor may present scattering and nonuniform reflection patterns. Therefore, a nonlinear mixture model, that considers multiple reflections of photons, should be considered to pursue a SU for more realistic scenarios [77], [78].

Nonlinear mixture model can be divided in terms of the order of the model into two main categories: *bilinear mixing models* and *high-order mixing models*. On the one hand, the generalized bilinear model proposed by Fan *et al.*, and the linear quadratic mixing model are one of the most representative approaches of the first category. On the other hand, the p-linear model, the polynomial post-nonlinear model, and the multilinear mixing model are examples of higher-order mixing models [79]. Despite of the order of the nonlinear mixture model, all models are conformed by a linear component and a nonlinear term depending on the assumed optical interactions.

Proper analysis of HSI under a SU approach requires not only the estimation of endmembers and their abundances, but also the estimation of the specific nonlinear mixture model parameters [80]. If early studies of materials or tissue elements with their respective spectral signatures are available, a supervised strategy could be considered, where the endmembers are assumed to be known. However, in many real scenarios, including the medical application of HSI, it is very difficult to have prior studies and the endmembers spectral information. Therefore, for cases where endmembers are unknown, an unsupervised approach, also known as blind unmixing methodology, could be considered where the information have to be jointly estimated [81].

In this dissertation, two SU algorithms have been employed: linear Extended Blind End-member and Abundance Extraction (EBEAE) and Nonlinear Extended Blind End-member and Abundance Extraction (NEBEAE). The EBEAE is employed in non-negative datasets using a linear mixing model to perform the estimation of characteristic spectral endmembers and their abundances [81]. The NEBEAE is a nonlinear version of EBEAE, capable of quantifying non-linear optical interactions during the acquisition process, which is also robust against noise [77]. In both cases, different hyperparameters can be modified such as the similarity between endmembers (ρ) or the entropy of the abundances (γ). The MATLAB® implementations for EBEAE and NEBEAE [77], [81] were used in the different experiments performed in this dissertation.

2.4.4 Performance Evaluation Metrics

To assess the effectiveness and efficiency of HSI instrumentation and the outcomes of the processing algorithms, performance metrics play a crucial role to provide quantitative results for comparing different developments. In the following sections, the evaluation metrics employed in the evaluation of the different works carried out in this dissertation are briefly explained. Figure 2-9 shows a summary of theses metrics.

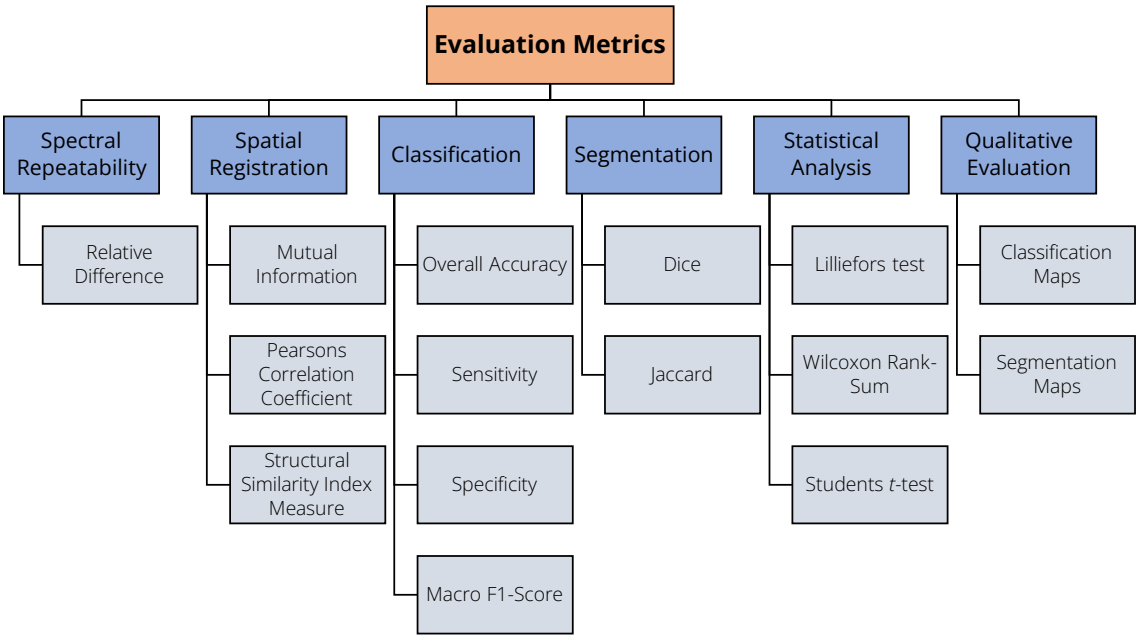

Figure 2-9: Summary of the evaluation metrics used in this dissertation to evaluate the effectiveness and efficiency of the HSI instrumentation and the results of the processing algorithms.

2.4.4.1 Spectral Repeatability Metrics

In order to measure the spectral repeatability of the HS acquisition systems and to evaluate the signal-to-noise ratio in each spectral band, the absolute Relative Difference percentage (RD) metric can be employed. This metric computes the relation between the absolute difference and the mean values of two vectors following Eq. (9), where x and y represent the data from a HS image pair. A lower RD value in a certain spectral band implies lower differences between the two bands of the same scene (i.e., better repeatability of the acquisition system and higher signal-to-noise ratio).

$$RD(\%) = \frac{|x - y|}{(\bar{x} + \bar{y})/2} \cdot 100 \tag{9}$$

2.4.4.2 Spatial Registration Metrics

Algorithms developed to spatially register images captured with different imaging systems can be evaluated using image-based similarity and overlap-based metrics. Mutual Information (MI) measures the dependency between two images X and Y [82]. This can be expressed as in Eq. (10), where $p_X(x)$ and $p_Y(y)$ are the marginal probability distributions of X and Y, respectively, and $p_{XY}(x, y)$ denotes the joint probability distribution of X and Y. When the optimal alignment occurs, the MI is maximized. The Pearson's Correlation Coefficient (PCC) is widely used for comparing images [83]. This

coefficient measures the degree of linear correlation or anti-correlation between two sets of data in the range [-1,1], where $PCC = -1$ indicates perfectly anti-correlated images, $PCC = 1$ indicates perfectly linearly correlated images, and $PCC = 0$ indicates linearly uncorrelated images. The PCC can be expressed as the covariance between two images by the product of their standard deviations (Eq. (11)). The Structural Similarity Index Measure (SSIM) is a metric commonly used in image compression to evaluate the compressed image against the original uncompressed image [84]. SSIM metric is computed considering the luminance, contrast and structure terms as shown in Eq. (12-14), where μ and σ represent the mean and standard deviations for x and y, σ_{xy} represents the cross-covariance for x, y, and C_1, C_2, and C_3represent the regularization constants for luminance, contrast, and structural terms, respectively. Combining the three terms, SSIM can be expressed as show in Eq. (15), where α, β, and γ represent the weight of each term. The SSIM result is a value in the range [-1,1], where $SSIM = -1$ indicates uncorrelated images and $SSIM = 1$ indicates correlated images.

$$MI(X;Y) = \sum_{x,y} p_{X,Y}(x,y) \log \frac{p_{XY}(x,y)}{p_X(x)p_Y(y)} \tag{10}$$

$$PCC = \frac{cov(X,Y)}{\sigma_X \sigma_Y} \tag{11}$$

$$l(x,y) = \frac{2\mu_x\mu_y + C_1}{\mu_x^2 + \mu_y^2 + C_1} \tag{12}$$

$$c(x,y) = \frac{2\sigma_x\sigma_y + C_2}{\sigma_x^2 + \sigma_y^2 + C_2} \tag{13}$$

$$s(x,y) = \frac{\sigma_{xy} + C_3}{2\sigma_x\sigma_y + C_3} \tag{14}$$

$$SSIM(x,y) = [l(x,y)]^{\alpha} \cdot [c(x,y)]^{\beta} \cdot [s(x,y)]^{\gamma} \tag{15}$$

2.4.4.3 Classification Metrics

The performance of the algorithms is evaluated using the confusion matrix, which compares the actual values using the ground-truth, with the values predicted by the algorithm. The confusion matrix is an $N \times N$ matrix, where N is the number of classes evaluated. Each row represents the instance in an actual class, while each column represents the instances in a predicted class, taking positive or negative values. Using the matrix values, different performance metrics can be obtained, such as overall accuracy (OA), macro F1-score, sensitivity, or specificity metrics. Each of the values of the confusion matrix (Figure 2-10) are defined as follows:

- **True Positives (TP):** the actual value is positive, and the predicted value is also positive.
- **True Negatives (TN):** the actual value is negative, and the prediction is also negative.
- **False Positives (FP):** the actual value is negative, but the prediction is positive.
- **False Negatives (FN):** the actual is positive, but the prediction is negative.

		Predicted Condition	
	Total Population (P+N)	**Positive** (PP)	**Negative** (PN)
Actual Condition	**Positive** (P)	True Positive(TP)	False Negative(FN)
	Negative (N)	False Positive(FP)	True Negative(TN)

Figure 2-10: Example of a confusion matrix.

OA measures the frequency of correct predictions made by the classifier, calculating the ratio of correct predictions and the total number of predictions (Eq. (16)). This metric is used in balanced datasets; for unbalanced datasets, the model can achieve high accuracy in predicting that each point belongs to the majority class label. However, the model could be not accurate.

Sensitivity evaluates the model's ability to predict correctly positive instances (Eq. (17)). High sensitivity is essential in situations where a positive case cannot be missed, particularly in medicine. A high sensitivity score indicates that the model is capable of reducing false negatives, thereby accurately detecting most true positive cases.

Specificity metric evaluates the model's ability to predict correctly negative instances (Eq. (18)). High specificity means that the model has the ability to minimize the occurrence of incorrect positive predictions among the actual negatives.

F1-score metric (Eq. (20)) is used in imbalanced datasets, computing the harmonic mean of the sensitivity and precision (Eq. (19)). In multi-class case, different average scores can be employed. The macro F1-Score (Eq. (21)) is computed by the unweighted mean of F1-Score per class, where i is the class index and N the number of classes. The micro F1-Score (Eq.(22)) computes a global average F1-Score by counting the total TP, FP, and FN. The weighted F1-Score (Eq. (23)) is computed with the mean of F1-Score per class considering the weight of each class. This weight (w_i) refers to the number of actual occurrences of the class. Weight F1-Score assigns greater contribution to the class with more samples; however, macro F1-Score assigns equal importance to each class while micro F1-Score assigns equal importance to each individual sample.

The Receiver Operating characteristic (ROC) curve is commonly employed to find the optimal hyperparameters of the supervised classifiers, finding the best performance using the Area Under the Curve (AUC) metric. The ROC curve shows the relationship between the sensitivity for the model and the false positive rate ($1 - specificity$) and is used in binary classifications to determine whether one variable is more predictive than another [85].

$$OA = \frac{TP + TN}{TP + TN + FP + FN} \tag{16}$$

$$Sensitivity = \frac{TP}{TP + FN} \tag{17}$$

$$Specificity = \frac{TN}{TN + FP} \tag{18}$$

$$Precision = \frac{TP}{TP + FP} \tag{19}$$

$$F1\text{-}Score = 2 \cdot \frac{Sensitivity \cdot Precision}{Sensitivity + Precision} = \frac{2 \cdot TP}{2 \cdot TP + FP + FN} \tag{20}$$

$$Macro\ F1\text{-}Score = \frac{1}{N}\sum_{i=1}^{N} F1\text{-}Score_i \tag{21}$$

$$Micro\ F1\text{-}Score = \frac{2 \cdot \sum_{i=1}^{N} TP_i}{2 \cdot \sum_{i=1}^{N} TP_i + \sum_{i=1}^{N} FP_i + \sum_{i=1}^{N} FN_i} \tag{22}$$

$$Weight\ F1\text{-}Score = \sum_{i=1}^{N} F1\text{-}Score_i \cdot w_i \tag{23}$$

2.4.4.4 Segmentation Metrics

Overlap-based metrics are employed to evaluate the segmentation quality achieved by clustering algorithms, comparing the segmented image (*SI*) against the ground-truth (*GT*). The Dice similarity coefficient measures the match between two images and is equal to twice the intersection divided by the sum of the two images as can be seen in Eq. (24) [86]. Jaccard similarity coefficient measures the similarity between the *GT* and *SI*, being defined as the intersection over the union of the two images, as shown in Eq. (25) [87]. These metrics are the most used in image segmentation evaluation and can be expressed using the definition of TP, FP, and FN. Dice and Jaccard coefficients are similar metrics and both measurements have a value range in [0, 1], where 0 indicates no similarity, there are no common elements between the *SI* and the *GT,* while 1 indicates complete similarity, indicating that the *SI* and the *GT* are identical. However, Jaccard coefficient penalizes misclassifications more than Dice coefficient.

$$Dice = \frac{2 \cdot |SI \cap GT|}{|SI| + |GT|} = \frac{2 \cdot TP}{2 \cdot TP + FP + FN} \tag{24}$$

$$Jaccard = \frac{|SI \cap GT|}{|SI \cup GT|} = \frac{TP}{TP + FP + FN} \tag{25}$$

2.4.4.5 Statistical Analysis

Segmentation and classification results can be statistically analyzed using paired data. In addition, statistical analyses can be computed using reflectance and absorbance spectral signatures to evaluate pairs of spectral signatures at each wavelength.

In this dissertation, data normality was evaluated using the Lilliefors test [88], which is a two-sided goodness-of-fit statistical procedure used to estimate the distribution when they are unknown. In the case where the data had a non-normal distribution, the two-tailed Wilcoxon Rank-Sum test was used to compute the statistical analysis [89]. This test calculates the p-value for testing the null hypothesis that two data vectors are samples from continuous distributions with equal medians against the alternative hypothesis that they are not. In the other case, Student's *t*-test was employed when data had normal distribution [90]. Student's *t*-test is a method of testing hypotheses about the mean of a small sample drawn from a normally distributed population when the population standard deviation is unknown. In both cases, tests were performed at a 5% significance level.

2.4.4.6 Qualitative Evaluation

After evaluating quantitative results, qualitative analysis plays a crucial role in evaluating the performance of the HS processing algorithms in order to identify different structures or patterns in the resulting color maps where each pixel corresponds to a certain class or cluster. An RGB image (Figure 2-11.a) can be used to generate a ground-truth map with predefined labels or classes (Figure 2-11.b). Classification maps (Figure 2-11.c), generated by supervised algorithms, assign predefined labels or classes to each pixel or region in an image. Segmentation maps, generated by unsupervised algorithms, group pixels or regions based on their spectral similarity and according to the number of previously defined clusters (Figure 2-11.d).

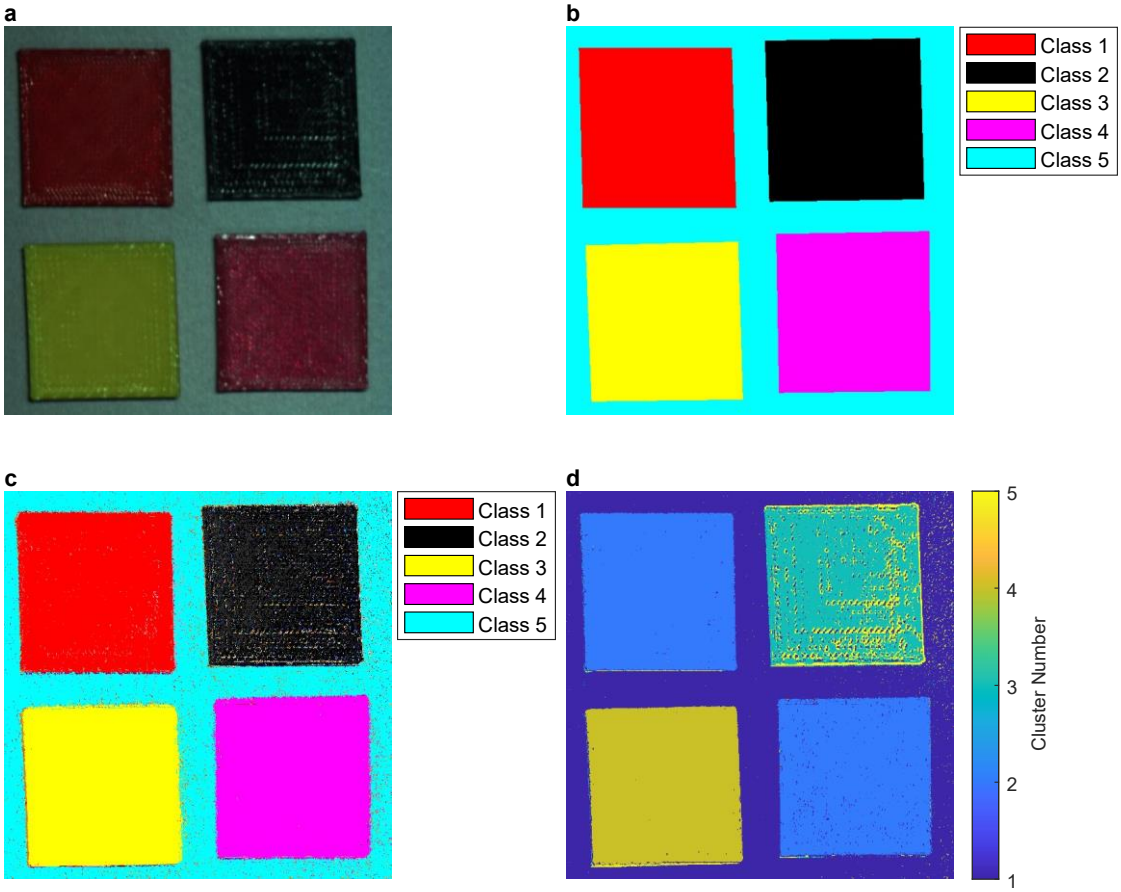

Figure 2-11: Examples of classification and segmentation maps. a) RGB image. **b**) Ground-truth map where each color represents a specific class. **c**) Classification map generated by a supervised ML algorithm where each color represents a specific class. **d**) Segmentation map generated by an unsupervised ML algorithm using 5 clusters where each color represents a cluster.

2.5 HSI Applications for Disease Detection

In recent years, HSI and MS Imaging (MSI) have emerged as powerful tools in medicine. These imaging techniques provide non-invasive and non-destructive approaches that allow real-time visualization and analysis of tissue [91]. In the context of cancer, HSI and MSI have shown great potential for improving tumor detection and delineation, differentiating between benign and malignant lesions, and could help to reduce unnecessary biopsies and improve patient outcomes [1], [8]. These technologies

allow monitoring various parameters such as tissue oxygenation, collagen, melanin, etc., useful in fields like cancer detection, wound assessment, and tissue viability monitoring [92], [93].

Gastrointestinal cancers represent 26% of global incidence and 35% of mortality in 2018 and include cancers of the stomach, liver, esophagus, pancreas, and colorectum [94]. Endoscopic tools are employed to detect gastrointestinal cancers and other abnormalities. These tools include gastroscopy, colonoscopy and wireless capsule endoscopy, which employs mainly RGB cameras [95]. With the aim of increasing the diagnostic performance of endoscopic systems, HSI has been employed to exploit the spectral properties of the different tissue types. In 2018, Lin *et al.* developed a system named ICL SLHSI (Structured Light and Hyperspectral Imager), which employed a pushbroom HS camera able to capture 640 pixels, covering the spectral range between 400-1,000 nm with 270 spectral bands [96]. Wu *et al.* proposed a method for identifying early esophageal cancerous lesions by an HS endoscopic imaging system based on a spectrometer, analyzing the spectral range between 350-800 nm [97]. In the work by Yoon *et al.*, a line-scanning HS endoscopic system able to capture 100 spectral bands covering the spectral range of 400-800 nm was developed with a spatial resolution of 120 μm at a working distance of 5 mm [98]. The HSI system was employed to enhance polyp discrimination for detection and resection in 7 patients undergoing routine colonoscopy screening. The KNN algorithm was employed as a classifier to discriminate into patients with and without polyps [99]. Köhler *et al.* developed a HSI laparoscope able to capture 500 spectral bands covering the spectral range from 500 to 1,000 nm. Resulting HS cubes had a spatial dimension of 640×480 with 100 spectral channels after performing spectral and spatial reduction, testing the system with resected (ex-vivo) human tissue [100]. Meanwhile, Sato *et al.* employed a pushbroom NIR HS camera in the range 1,000–2,350 nm with 256 spectral bands and capturing 320 pixels [101]. In this study, 12 ex-vivo gastrointestinal stromal tumors were imaged. The SVM algorithm was employed to predict normal and tumor regions, achieving specificity, sensitivity, and accuracy of 73.0%, 91.3%, and 86.1%, respectively. Additionally, a commercial HSI system, TIVITA® Tissue System (Diaspective Vision GmbH, Am Salzhaff, Germany) has been employed in several works to capture spectral information of gastrointestinal tissue [102], [103]. This system was able to capture images in the spectral range within 500-1,000 nm, with a spatial resolution of 640×480 pixels. This tool was evaluated for the determination of the resection margin during colorectal surgery in 24 patients [102] and to detect colorectal carcinoma with a database of ex-vivo HS images from 54 patients [103]. In this last work, using an Artificial Neural Networks (ANN) classifier, tumor and healthy mucosa in colorectal carcinoma was classified with a sensitivity of 86% and a specificity of 95% [103] .

Head and neck cancer includes the tumors that appear in the oral cavity, nasopharynx, pharynx, and larynx [104]. The diagnosis strategies are quite diverse: (i) oral cavity tumors are often detected by patient self-identification, (ii) laryngeal tumors are diagnosed at early stage by presenting voice changes or florid hoarseness, (iii) nasopharyngeal carcinoma can present hearing loss or cranial nerve palsies [104]. Halicek *et al.* proposed a method to use HSI and Convolutional Neural Network (CNN) to perform an optical biopsy of ex-vivo head and neck cancer [105]. The data were acquired employing the commercial CRI Maestro imaging system (Perkin Elmer Inc., Waltham, Massachusetts), which is composed of a xenon white-light illumination

source, a LCTF system, and a 16-bit CCD camera with a spatial resolution of 1,040×1,392 pixels able to capture 91 spectral bands, ranging from 450 to 900 nm. Brouwer de Koning *et al.* developed an HSI system to acquire ex-vivo samples of tongue squamous cell carcinoma [106]. The system was based on two pushbroom HS cameras operating from 400 to 1,700 nm. The VNIR camera worked from 400-950 nm, capturing 384 spectral bands and a spatial resolution of 1,312 pixels. The NIR camera captured 256 spectral bands from 950-1,700 nm with a spatial resolution of 320 pixels. The HS system distinguished between tumor and muscle with a sensitivity of 84% in the VNIR range, 77% in the NIR range, and 83% when both spectral ranges were combined. Recently, Eggert *et al.* performed a prospective clinical observational study to classify the tissue into healthy and tumor of laryngeal, hypopharyngeal and oropharyngeal mucosa [107]. The HSI system was able to capture 30 spectral bands from 390 to 680 nm. In this work, 98 patients were examined due to suspicious lesions of the mucosal membrane before surgery in-vivo. DL methods were employed to achieve an average accuracy of 81%, a sensitivity of 83% and a specificity of 79%.

Histological samples are examined by an expert physician using the naked eye and, in some cases, using digital pathology to identify several diseases. In the latter case, the samples are digitalized employing microscopy, so that partial or complete (whole-slide) images are captured at different magnifications (e.g., 5×, 10×, 50×, etc.) [108]. HSI has been employed in different works for histological analysis using microscopy [5]. Ortega *et al.* presented a methodology to correctly set-up a pushbroom HS microscope to acquire high-quality HS images [109]. The pushbroom HS camera worked in the spectral range from 400 to 1,000 nm, capturing 826 spectral bands and 1,004 spatial pixels. The HS camera was directly coupled to a conventional light microscope. However, although the spectral range of the HS camera covered from 400 to 1,000 nm, the optics of the microscope limited the effective spectral range to approximately 400–800 nm. Employing this system, a dataset of 83 HS images was obtained at 5× and 10× magnifications from 13 pathology slides from biopsies of human brain tissue resected during surgery to patients affected by grade 4 Glioblastoma tumor [110]. The HS images, captured using a 5× magnification, were classified using three different supervised classification algorithms: SVM, ANN and RF. Competitive results in the discrimination between normal and tumor tissue were obtained employing two different approaches, intra-patient and inter-patient, with results above 80% accuracy in both cases using 10-fold cross-validation. [111]. In a recent work, the pushbroom HS microscope system was modified to remove the limitation of the effective spectral range (400–800 nm). To achieve this goal, the microscope was replaced, obtaining an effective spectral range of 400–1,000 nm. A new database was collected with 527 HS images, where 337 were non-tumor brain samples and 190 were diagnosed as Glioblastoma [112]. A CNN was employed to detect glioblastoma samples, achieving average sensitivity and specificity values of 88% and 77%, respectively. In addition, the same HS system was also used to discriminate between normal and tumor breast cancer cells [113]. In this way, 112 HS images were captured from histology samples of breast tumor from human patients using a 20× magnification. In order to discriminate between tumor cells from normal breast cells, a CNN was used, which obtained results with an AUC higher than 0.89 for all the experiments.

In another work, Ma *et al.* developed a HS microscopic imaging system employing a SnapScan HS camera covering a spectral range from 460 to 750 nm with 87 spectral bands [114]. A total of 15 histology slides of larynx and hypopharynx tissue from 15

head and neck cancer patients were collected at a 40× magnification. The authors proposed a nuclei segmentation method based on Principal Component Analysis (PCA). After that, spectral-based SVM and patch-based CNN were used for nuclei classification. The average accuracy results were 68% and 82% for the SVM and of CNN classification, respectively. Finally, Souza *et al.* presented a system to acquire HS images using a LCTF-based system and a conventional microscope [115]. The system captured spectral information in the range of 400-720 nm based on light polarization. This system was tested employing hematoxylin-eosin-stained slides of a rat skin treated with Aminolevulinic Acid (ALA)-mediated photodynamic therapy. Four different algorithms were employed (KNN, SVM Linear, SVM RBF, and RF) obtaining an overall accuracy result between 96% and 98% in the discrimination of epidermis, dermis, and necrotic area.

Next, a more detailed analysis of the state-of-the-art in the use of HSI for the analysis of brain cancer, skin cancer, and major neurocognitive disorders is presented, since these particular areas have been the primary focus of this dissertation.

2.5.1 Brain cancer

In 2020, brain and Central Nervous System (CNS) cancer was the twelfth most common cancer in terms of mortality, with an estimated 308,102 incident cases, associated to 251,329 deaths worldwide for both sexes and all ages [116]. These numbers are expected to increase by 38.5% and 43.7% for incidences and mortality, respectively, for 2040 [117]. In the young population under 35 years of age, it was the second most common cancer in terms of mortality (31,181 deaths) after leukemia [116], while in children under 14 years old, it was the second most common cancer in terms of both morbidity and mortality (24,388 incident cases/11,889 deaths) worldwide [116]. Particularly, brain tumors account for more than 90% of occurrence within CNS cancers, linked to high mortality and morbidity, especially in pediatric cases [118], [119].

Treatment consists of biopsy or aggressive surgical resection with postoperative radiation and chemotherapy [118]. However, successful tumor resection is associated with prolonged survival, which requires accurate identification of the boundaries between tumor and normal tissue [17]. Different intraoperative guidance tools are employed during surgery, such as intraoperative Image Guided Stereotactic (IGS) neuronavigation, intraoperative Magnetic Resonance Imaging (MRI), or fluorescent tumor markers like 5-ALA [120].

In addition, HSI has emerged as a new intraoperative guidance tool. First works employ HSI system for monitoring brain oxygenation and hemodynamic using animals [121], [122]. Recently works employ HSI system to identify human brain cancer. Fabelo *et al.* developed a HS intraoperative system for the identification of cancer tissue during in-vivo brain surgery [123]. The system was based on two push broom HS cameras, an illumination system, and a scanning platform. The HS cameras covered the VNIR spectral range between 400 and 1,000 nm and was able to capture 826 spectral bands and 1004 spatial pixels. Another HS camera covered the NIR range between 900 and 1,700 nm, capturing 172 spectral bands and 320 spatial pixels. The illumination system was based on a Quartz Tungsten Halogen (QTH) lamp of 150 W with a broadband emission between 400 and 2,200 nm. The lamp was connected to an optical fiber that transmits the light to a cold light emitter, isolating the high temperature

produced by the QTH lamp from the brain surface. To provide the necessary movement to generate the HS cubes, the HS cameras and the illumination system were coupled to a scanning platform.

Employing this system, a HS human brain database was obtained from 22 patients with both primary and secondary tumors [124]. The data acquisition was performed in two different campaigns: one at the University Hospital of Southampton, UK, and the other one at the University Hospital of Gran Canaria Doctor Negrin of Las Palmas de Gran Canaria, Spain. Several works have employed this database to perform brain cancer classification and boundary delimitation. A hybrid framework that combined supervised and unsupervised machine learning methods was proposed to perform a spatio-spectral classification [70]. The SVM was employed as a supervised pixel-wise classification algorithm and the generated classification map was spatially homogenized using a one-band representation of the HS cube and performing a KNN filtering. The information generated in this stage was combined using a Majority Voting (MV) algorithm with the unsupervised stage employing a HKM algorithm to obtain a segmentation map. The results obtained demonstrated that it was possible to accurately discriminate between *normal tissue*, *tumor tissue*, *blood vessels* and *background* with an OA higher than 99% following an intra-patient methodology. Apart from the traditional ML methods, DL approaches were also proposed to identify glioblastoma tumor following an inter-patient approach [125]. The proposed framework was able to identify the parenchymal area, which corresponds to the primary surgical area of the exposed brain and blood vessels, employing a 2D convolution neural network. In addition, a four-class classification map was obtained using 1D-DNN. This framework was able to identify glioblastoma tumor obtaining an OA of 80% following an inter-patient approach. Another research employed blind linear unmixing method to identify glioblastoma as a low computational time cost alternative using the same database [126]. This method was compared with a supervised SVM strategy, which required a higher training time, achieving similar classification results but with a speedup factor of ~429× in the training phase. Using the same database, a method based on the fusion of multiple deep models was proposed by Hao *et al.* to use the spectral and spatial information to identify glioblastoma [127]. This framework included four steps: 1) spectral phasor analysis and data oversampling; 2) 1D-DNN spectral HSI feature extraction and classification; 3) 2D-CNN spectral–spatial HSI feature extraction and classification; 4) edge-preserving filtering-based classification result fusion and optimization, and fully convolutional network-based background segmentation. The proposed method achieved an OA of 96.69% for four-class classification and OA of 96.34% for glioblastoma identification, adopting a leave-one-patient-out cross validation technique.

Mühle *et al.* integrated an HSI camera into a surgical microscope (S100 OPMI Pico, Carl Zeiss Meditec AG, Germany) for neurosurgical brain tumor resection [128]. The HS system was based on the commercial HS camera TIVITA® Tissue System (Diaspective Vision GmbH, Am Salzhaff, Germany), capturing 100 bands in the spectral range from 500 to 1,000 nm, with a spatial image size of 640×480 pixel. In this proof of concept, the authors performed an extensive evaluation of different lamps to assess the effect in different spectral regions. In addition, a spectral characterization of the light was performed and compared between the laboratory setup and the clinical setup. Finally, a single HS image was analyzed using an RF classifier to discriminate between

healthy tissue, malignant tissue, vessels, and background. Using 5-fold stratified cross-validation, the RF classifier achieved an overall accuracy of 99.1%.

Urbanos *et al.* presented a HS acquisition system to acquire and process HS images in the surgical environment [129]. The system was based on a snapshot HS camera able to capture 25 bands along the spectral range from 655 to 975 nm. The illumination system was based on 150 W halogen light source connected to two fiber-optic cables. In this study, a HS database was generated, composed by more than 50 images of different pathologies, and labeled into five different classes: *healthy tissue*, *tumor*, *venous blood vessel*, *arterial blood vessel* and *dura mater*. Finally, 13 images corresponding to grade 3 tumors and glioblastoma (grade 4) were employed to train SVM, RF, and CNN classifiers achieving an OA result between 60 to 95% using an intra-patient approach. Using the same HS database, Martín-Pérez *et al.* performed a comparison between non-optimized models with optimized models [130]. This comparison was performed using SVM and RF algorithms and three different optimization methods: *grid search*, *random search*, and *Bayesian optimization*. The study showed that the RF results did not improve significantly when the model was optimized with any of the three optimization methods. However, the optimized SVM model improved the tumor identification. Sancho *et al.* presented SLIMBRAIN [131], a modification of the HS system presented by Urbanos *et al.* that incorporated augmented reality using a LiDAR (Light Detection and Ranging) camera. The classification results obtained from the HS images were overlapped with the RGB point cloud captured by a LiDAR camera and presented in an augmented reality visualization.

Puustinen *et al.* developed an operating microscope-integrated HSI system for microneurosurgery as a monitoring tool during neurosurgical operations [132]. The system was based on an operating microscope (OPMI Pentero 900, Carl Zeiss Meditec AG, Germany) coupled to a snapshot HS camera with a spectral range of 500 to 900 nm, and a spatial resolution of 1,024×1,024 pixels. The illumination system was based on a tunable LED source with 10 different channels. As a proof of concept, two HS images were labeled and used to train and test different algorithms, with the best overall accuracy of 98.3% for all tissue classes (compact bone, high-grade glioma, blood, dura internal leaf, cortical vein, and intact cortex with pia matter) and 97.7% for the glioma class using the light gradient boosting machine algorithm. In [133] the HS system was used to generate a microneurosurgical HSI database with 11 HS images obtained from two patients.

Giannantonio *et al.* presented an intraoperative HS system based on a surgical microscope (OPMI Pentero 900, Carl Zeiss Meditec AG, Germany) coupled to an IMEC Snapscan VNIR (IMEC, Leuven, Belgium) [134]. The HS camera covered the spectral range of 470 - 900 nm in 150 spectral bands, however, due to the limitation of the infrared filter in the microscope, only the spectral range from 470 to 780 nm with 104 spectral bands was considered. In this study, the authors presented a dataset of low-grade gliomas (grade 1 and 2) composed of 18 HS images from 5 patients with a spatial resolution of 1,600×1,600 pixels. Different algorithms were used (RF, SVM, and DNN) and an OA of more than 90% was obtained when HS images were classified into healthy and tumor using an intra-patient approach.

Additionally, HSI systems have been employed during neurosurgical procedures to monitor the oxygenated and deoxygenated hemoglobin concentration changes occurring in the brain [92]. The system was based on a HS camera able to capture 25

spectral bands covering the spectral range between 675 and 975 nm. Another HSI system employed the spectral range between 400 and 800 nm for monitoring intraoperative changes in brain surface hemodynamics to identify postoperative cerebral hyperperfusion syndrome [93].

The following Table 2-3 provides a comprehensive summary of the different HSI systems used in the literature for the identification of brain tumor, highlighting the specification of the system and the objective of the study.

Table 2-3: Summary of the HSI systems used to identify brain tumor.

Ref.	Year	HSI System Type	Wavelength (nm)	Bands	Spatial Resolution	Patients	HS Images	Study Objective
[70]	2018	Pushbroom	400 – 1,000	826	1004×1787 pixels	5	5	Primary (G4)
[123]	2018					26	43	Primary (G1, G2, G3, and G4) and Secondary
[125]	2019					16	26	Primary (G4)
[126]	2020					16	26	Primary (G4)
[127]	2021					5	7	Primary (G4)
[128]	2020	Pushbroom - Surgical Microscope	500 – 1,000	100	1280×960 pixels	1	1	Primary (G3)
[129]	2021	Snapshot	655 - 975	25	217×409 pixels	12	13	Primary (G3 and G4)
[130]	2022					9	10	Primary (G3 and G4)
[131]	2023					12	13	Primary (G3 and G4)
[132]	2022	Snapshot - Surgical Microscope	500 - 900	n/a	1024×1024 pixels	2	11	Primary (G1 and G3)
[133]	2023					1	2	Primary (G3)
[134]	2023	Snapscan - Surgical Microscope	470 - 780	104	1600×1600 pixels	5	18	Primary (G1 and G2)

G1: Grade 1; **G2**: Grade 2; **G3**: Grade 3; **G4**: Grade 4; **n/a**: not available

2.5.2 Skin cancer

The incidence of skin cancer has increased in the last years, being one of the most common cancers [135]. Skin cancer includes Malignant Melanoma (MM) and Non-Melanoma Skin Cancer (NMSC), which comprises Basal Cell Carcinoma (BCC), Squamous Cell Carcinoma (SCC) and other types of cancer with minor incidence. MM is the 17th most common cancer worldwide with 325,000 new cases in 2020, while NMSC is the 5th most common cancer worldwide with 1,200,000 new cases in 2020 [135]. BCC is the most frequent skin cancer, involving 80-85% of NMSC, followed by SCC (15-20%) [136].

Traditionally, skin cancer is detected during visual inspection by the naked eye and a dermatoscopic system, which contains a magnifying lens and polarized light [137], [138]. A preliminary diagnosis is performed following the ABCDE rule, which require to study and measure such properties of the mole: asymmetry of the mole, border irregularity, color uniformity, diameter and evolving size, shape or color [18]. Nowadays different novel imaging techniques are employed in clinical practice: confocal microcopy, polarized imaging, three-dimensional topography, thermal imaging, MSI and HSI, etc. [47]. The combination of these technologies and ML

algorithms allows the development of tools aiming the automatic discrimination and detection of skin cancer [139], [140]. Compared to the traditional dermatoscope, HSI is able to provide information beyond the human visual range, capturing information related of chromophores, such as melanin, hemoglobin, water, beta-carotene, collagen, and bilirubin [141].

MSI technology has been widely employed to identify skin cancer, while HSI has been employed to a lesser extent. In both cases, snapshot imaging systems have been employed to capture skin lesions, as they provide fast acquisition of spatial and spectral information in a single capture. Commercial MS systems have been developed to assist in the detection of melanoma. MelaFind is a MS system able to capture 10 spectral bands in the spectral rage comprised between 430 and 950 nm with spatial resolution of 1,280×1,024 pixels [142]. This tool provides a recommendation to perform or not a biopsy of a skin lesion. The lowest wavelength was used to create a mask for segmentation of the spatial information in the remaining wavelengths. After that, lesion parameters (asymmetry, blotchiness, texture, etc.) were computed from each segmented image. Linear and nonlinear classifiers were employed to classify the lesion as malignant or benign. Finally, a threshold was applied to determine whether the malignant lesion was a melanoma or non-melanoma [142]. This system has been used in different studies to identify melanoma. In 2001, Elbaum *et al.* achieved 100% and 84% of sensitivity and specificity, respectively, to identify melanomas using a dataset of 63 melanomas and 183 melanocytic nevus [143]. In 2011, Monheit *et al.* performed a prospective multicenter study to evaluate the effectiveness of MelaFind [144]. Seven clinical sites participated in the study obtaining 1,831 PSLs from 1,383 patients. Finally, 1,632 lesions were eligible, where 127 were melanoma, reporting a sensitivity and specificity of 98.4% and 9.9%, respectively. In 2017, Fink *et al.* performed an analysis of this tool in a real-life clinical setting [145]. In this study, 360 PSLs were analyzed from 111 patients (but only 3 melanomas), achieving a melanoma sensitivity and specificity values of 100% and 68.5%, respectively. Finally, in 2020, a study with 150 non-melanomas and 59 melanomas was performed obtaining a sensitivity and specificity of 82.5%, 52.4%, respectively [146]. The results were compared with the diagnosis using teledermoscopy, obtaining a sensitivity and specificity of 84.5% and 82.6%, respectively, and the criteria of a local dermatologist (96.6% and 32.2%, respectively).

Another commercial MS system is Spectrophotometric Intracutaneous Analysis (SIAscopy) [147]. This tool can capture 8 bands in the 400–1,000 nm spectral range of a spatial area of 24×24 mm or 12×12 mm. The input MS images were calibrated and the infrared spectral bands were subsequently used in combination with logistic regression to determine different parameters, such as the quantity of collagen and hemoglobin in the papillary dermis and the total melanin in epidermis and papillary dermis [147]. A clinical evaluation of the system was performed in 2001 using a dataset of 348 pigmented lesions including 52 melanomas, achieving a melanoma sensitivity of 82.7% and a specificity of 80.1% [147]. In 2007, Govindan *et al.* examined 886 patients obtaining a sensitivity of 94.4% with a false negative rate of 3.7% for malignant melanoma [148]. In 2010, Emery *et al.* performed a study with 858 patients and 1,211 lesions, developing a Primary Care Scoring Algorithm (PCSA), which modified the logistic regression used in the tool to improve the diagnosis of suspicious lesions [149]. Using the PCSA, the authors obtained a sensitivity of 50% and a specificity of 84%. PCSA was later integrated to SIAscopy. In 2013, the MoleMate system was integrated to SIAscopy using PCSA to improve the management of PSLs in primary care [150]. In

2014, Sgouros *et al.* analyzed the use of this tool in the detection of melanoma and non-melanoma skin cancers [151]. In this study, 188 lesions of 180 patients were examined, obtaining sensitivity and specificity values of 85.7% and 65.4% respectively.

Different non-commercial acquisition systems have been employed in the literature. Tomatis *et al.* employed a MS acquisition system called SpectroShade (MHT, Verona, Italy) able to capture MS images of 15 spectral bands between 483 and 950 nm, with a spatial resolution of 640×480 pixels [152]. The illumination system was based on a light source, a concave mirror incorporating a diffraction grating (monochromator), and a bundle of optical fibers which provided homogeneous illumination. The mirror was moved by a stepping motor allowing to select 15 different spectral bands. The system included a digital color CCD camera and a digital Black & White CCD camera. A calibration step was performed followed by a lesion segmentation obtained using a hybrid algorithm, combining a region-oriented and a thresholding method. Later, parameter extraction and data reduction were performed. Finally, an ANN classifier was employed to perform an automatic diagnosis to discriminate between melanomas and non-melanoma lesions, achieving a sensitivity of 80.4% and a specificity of 75.6% in 1,391 in-vivo lesions. In 2007, Carrara *et al.* employed the same system in a study that involved 1,784 patients. Using ANN achieved a sensitivity of 88% and a specificity of 80%, using a dataset composed by 1,966 PSLs [153]. In 2010, Ascierto *et al.* used the SpectroShade system to analyze 54 PSLs, obtaining sensitivity and specificity to detect melanoma of 66.6% and 76.2%, respectively [154].

In 2012, Diebele *et al.* employed a MS camera that captured information in the spectral range 450–950 nm [155]. The skin area was illuminated by a ring of halogen lamps with a diffuser and a polarizing film. The system was able to distinguish melanoma from pigmented nevi obtaining a sensitivity and specificity of 94% and 89%, respectively. The diagnostic criterion was based on skin optical density differences at three wavelengths: 540, 650 and 950 nm. In 2017, Stamnes *et al.* employed a spectral radiometer able to capture 10 different wavelengths (365–1,000 nm), where, in each wavelength, three images were captured simultaneously at different detection angles [156]. The sensor head contained an illuminating system of 12 fixed LED lamps. Different maps of physiology properties and morphometric parameters were obtained. A classification method based on clustering was proposed using a dataset of 712 PSLs, obtaining sensitivity and specificity results of 99% and 93%, respectively. Delpueyo *et al.* developed a MS system to improve the detection of skin cancer lesions, specifically melanomas and BCC [157]. The system was based on a CCD monochrome camera with an illumination source based on LED, which allowed capturing 8 wavelengths between 400-1,000 nm with a spatial resolution of 1280×960 pixels. The discrimination was performed between malignant and benign PSLs using the spectral features of the lesions, such as reflectance and color. The study analyzed 429 pigmented and non-pigmented lesions proving a sensitivity of 87.2% and a specificity of 54.5% in melanoma identification. Rey-Barroso *et al.* developed an extended near infrared MSI system based on an InGaAs sensor covering the range from 995 to 1,613 nm and capturing 6 wavelengths with a spatial resolution of 320×256 pixels [158]. This system had the goal of diagnosing skin cancer in an early and non-invasive way. The classification method was based on the analysis of first-order statistic descriptors, PCA, and SVM algorithms. The system was tested in a pilot study with 39 nevi and 14 melanomas from Caucasian patients, providing a sensitivity of 78.6% and a specificity of 84.6%.

In 2019, a novel smartphone-based MSI was reported by Ding *et al.* [159] as a proof of concept of a portable and cost-effectiveness tool. The images were captured by the CMOS sensor of the smartphone, combined with lens and linear variable filter allowed to capture different spectral bands. The system captured 9 spectral bands within the spectral range 400-700 nm. The skin was illuminated with linearly polarized light, with the goal of detecting melanin and hemoglobin. Another smartphone-based dermatoscope using MSI was proposed by Uthoff *et al.* in 2020 [160]. In this work, polarized MSI was employed to obtain deoxyhemoglobin, oxyhemoglobin, and melanin maps. The illumination employed was based on LEDs with different wavelengths covering the range between 450-940 nm and capturing 8 spectral bands.

HSI acquisition systems also have been employed to identify skin cancer. In 2006, a high resolution HSI microscopic system was developed for histopathology to detect abnormalities in skin tissue using hematoxylin-eosin-stained preparations of normal and abnormal skin, benign nevi and melanomas [161]. The system called PARISS (Prism and Reflector Imaging Spectroscopy System) was able to capture the spectral range comprised between 365 and 800 nm. More than 85% of the samples were correctly assigned to the correct class and were able to distinguish between melanoma and normal skin. Nagaoka *et al.* employed a system called MSI-03 (Mitaka Kohki Co., Ltd., Tokyo, Japan) to identify melanoma [162]. This system was able to capture an effective area of 16×20 mm, with 658×489 spatial pixels, and spatial resolution of 32.7 μm, covering the spectral range between 450–750 nm with 124 spectral bands. The illumination system employed was based on a halogen lamp of 150 W. A melanoma discrimination index was proposed by the authors to avoid unnecessary excision of benign PSLs. Nagaoka *et al.* performed also a pilot study in 2011 to evaluate this system, which discriminated melanomas with a sensitivity of 90% and a specificity of 84% [163]. In 2012, this system was employed to discriminate between acral lentiginous melanoma and acral nevus, achieving a sensitivity of 92% and a specificity of 86% [164]. In 2014, a clinical trial was performed in two centers using the MSI-03, obtaining a dataset composed by 24 melanomas and 110 other skin lesions. In this study, sensitivity and specificity results of 96% and 87%, respectively, were obtained [162]. The MSI-03 system was mainly evaluated in Asian populations, however, in 2021, Christensen *et al.* evaluated the system in a Caucasian population [165]. This study involved 186 patients with 202 PSLs. The objective of this study was to evaluate the discrimination between melanoma and benign PSL, obtaining a sensitivity to detect melanoma of 96.7% and a specificity for benign PSL of 42.1%.

In 2015, a HSI system prototype was presented by Neittaanmäki-Perttu *et al.* to delineate the margins of lentigo maligna and MM [166]. The system was able to capture 76 bands in the spectral range of 500–900 nm with a spatial resolution of 240×320 pixels, using an external light source coupled to a fiber optic ring light. The HS images were analyzed employing linear mixture model to obtain the pure spectral malignant lesion and normal skin, producing abundance maps that delineate the lesion borders. The results obtained were compared with histology results obtaining a match of 94.7%. In 2019, this system was employed to delineate BCC in a pilot study, which included 16 lesions, being accurately delineated 75% of them [167]. In 2021, the system was tested to distinguish between BCC and melanoma [168]. In this work, a CNN algorithm was employed to classify 26 pigmented lesions (10 BCCs, 12 melanomas in-situ and 4 invasive melanomas), obtaining a sensitivity of 100% and a specificity of 90%.

In 2016, Zherdeva *et al.* proposed a HSI system to discriminate between different skin cancer types employing 61 bands in the range 450-750 nm, with a spatial resolution of 501×501 pixels [169]. The work evaluated 16 melanomas, 19 BCCs and 10 benign tumors, identifying skin lesions (benign and malignant lesions) from healthy skin with very high sensitivity and specificity of 84% and 87%, respectively. The optical density of hemoglobin and melanin was employed to perform the discrimination.

In 2019, Hosking *et al.* employed the Melanoma Advanced Imaging Dermatoscope (mAID) based on non-polarized LED-driven HS camera [170]. The illumination system illuminated with 21 wavelengths, covering the spectral range between 350-950 nm. The study obtained 70 HS images of skin lesions and performed a classification between nevus and melanoma, achieving a sensibility of 100% and specificity of 36%.

In 2021, Courtenay *et al.* employed a pushbroom HS camera to distinguish between healthy and non-healthy skin [171]. The HS camera was placed on a motorized structure to capture the HS cube and two 60 W halogen light sources were mounted on either side of the HS sensor. The system was able to capture 270 spectral bands with a spectral range of 398–995 nm, generating HS cubes with a spatial dimension of 640×1,785 pixels. A total of 60 patients with 41 confirmed cases of BCC and 19 cases of SCC were employed to perform robust statistical tests to identify the differences between healthy tissue and carcinomas (BCC and SCC), finding differences between 429 and 520 nm. In a later work, the use of a CNN combined with a final SVM activation layer was proposed to classify the same dataset, achieving up to 90% classification in terms of OA [172].

In 2022, the SICSURFIS (Spectral Imaging of Complex Surface Tomographies) system was proposed as a compact hand-held HSI tool for capturing HS data in complex skin surfaces [173]. The system worked in the spectral range between 475–975 nm, capturing 33 spectral bands with a spatial dimension of 1,605×1,640 pixels. In addition, the system had a photometric stereo imaging that provided skin-surface models. A dataset of 42 skin lesions were evaluated to discriminate between malignant and benign pigmented and non-pigmented skin tumors. Classification and delineation methods were proposed using a CNN employing spectral, spatial, and a skin-surface model. The results achieved a sensitivity of 87% and a specificity of 93% in recognizing melanoma from pigmented nevi and healthy skin.

Different works employed HSI systems to analyze skin characteristics or morphology. A multi-mode dermoscope based on HSI was proposed in 2014 by Vasefi *et al.* called SkinSpect [174]. The system was composed by a programmable illumination system based on Xenon arc light source, which allowed a wavelength selection over the range from 468 to 857 nm and captured 33 spectral bands. The images were obtained by two cameras, with polarization filters installed, and oriented orthogonally to each other. However, this system was employed to perform an analytical model to map the distribution of specific skin biomolecules. In subsequent works, the system was used to measured melanin and hemoglobin concentrations skin pigmented nevi [175]. In 2019, He and Wang proposed a HSI system based on a snapshot camera to analyze morphological features [176]. The HS camera was based on a CMOS sensor with 2,048×1,088 pixels able to capture 16 spectral bands in the range between 400-600 nm.

The following Table 2-4 provides a comprehensive summary of the different HSI systems used in the literature to study skin cancer and other skin lesion, highlighting the specification of the system and the objective of the study.

Table 2-4: HSI systems used to study skin cancer and other skin lesion.

Ref.	Year	MSI/HSI System Type	Wavelength (nm)	Bands	Spatial Resolution/FoV	Patients	MS/HS Images	Lesion Type
[143]	2001	MS – Focal Plane (MelaFind)	430–950	10	1280×1024 pixels	n/a	246	MM and N
[144]	2011					1,383	1,831	MM
[145]	2017					111	360	MM
[146]	2020					184	209	MM
[147]	2001	MS – Focal Plane (SIAscopy)	400–1000	8	24×24 mm or 12×12 mm	311	348	MM
[148]	2007					886	886	MM
[149]	2010					858	1,211	MM and B
[151]	2014					180	188	MM and NM
[152]	2005	MS – Focal Plane (SpectroShade)	483–950	15	640×480 pixels	1,359	1,391	MM and NM
[153]	2007					1,784	1,966	MM and NM
[154]	2010					54	54	MM
[155]	2012	MS - Focal Plane	450–950	51	n/a	n/a	82	MM and N
[156]	2017	MS – Focal Plane	365–1,000	10	n/a	n/a	712	M and B
[157]	2017	MS – Focal Plane	400-1000	8	1280×960 pixels	n/s	429	MM and BCC
[158]	2018	MS - Snapshot	900-1,600	6	320×256 pixels	n/a	53	MM and N
[159]	2019	MS – Focal Plane (Smartphone)	400–700	9	n/a	n/a	n/a	N
[160]	2020	MS – Focal Plane (Smartphone)	450-940	8	5312×298 pixels	n/a	n/a	N and SCC
[161]	2006	HS – Pushbroom (PARISS)	365-800	640	2.5×500 µm or 0.4×80 µm	n/a	n/a	NS, B, and MM
[163]	2011	HS – Line scanning (MSI-03)	450–750	124	658×489 pixels	20	28	MM and NM
[164]	2012					20	20	ALM and AN
[162]	2015					97	132	MM and NM
[165]	2021					186	202	MM and B
[174]	2014	HS – Focal Plane (SkinSpect)	468–857	33	11×16 mm	2	n/a	N
[175]	2016					20	20	N
[166]	2015	HS - Snapshot	500-900	76	240×320 pixels	19	19	LM and LMM
[167]	2019					16	16	BCC
[168]	2021					24	26	MM and BCC
[169]	2016	HS – Focal Plane	450-750	61	501×501 pixels	45	45	MM, BCC, and B
[170]	2019	HS – Focal Plane (mAID)	350-950	21	n/a	91	100	MM and NM
[176]	2019	HS - Snapshot	460-600	16	2,048×1,088 pixels	n/a	n/a	N
[171]	2021	HS - Pushbroom	398-995	270	640 × 1785 pixels	60	60	BCC, SCC, and NS
[172]	2022					60	60	BCC and NS
[173]	2022	HS – Focal Plane (SICSURFIS)	475-975	33	1605×1640 pixels	33	42	B and M

ALM: Acral Lentigo Melanoma; **AN**: Acral Nevus; **B**: Benign; **BCC**: Basal Cell Carcinoma; **FoV**: Field of View; **LM**: Lentigo Maligna; **LMM**: Lentigo Maligna Melanoma **M**: Malignant; **MM**: Malignant Melanoma; **n/a**: not available; **N**: Nevus; **NM**: Non-Melanoma; **NS**: Normal Skin; **SCC**: Squamous Cell Carcinoma.

2.5.3 Major Neurocognitive Disorders

The current increment in life expectancy is correlated with an increase in the number of people affected by NCDs, which is the major cause of dependency and disability among the older adult population [177]. Additionally, NCDs are not a natural or unavoidable outcome of aging. These types of disorders are a rapidly growing public health problem with nearly 10 million new cases every year, affecting over 50 million people worldwide in 2019 [178]. The most common form of NCD is Alzheimer's disease, accounting for 60% to 70% of NCD cases [178].

NCD, previously known as dementia and/or mild cognitive impairment, is characterized by a decline from a previously attained level of cognitive functioning. It can be distinguished between minor and major NCD (mNCD and MNCD, respectively) according to the Diagnostic and Statistical Manual of Mental Disorders (DSM-5) criteria defined by the American Psychiatric Association [21]. mNCD is characterized by a noticeable decrement in cognitive functioning [21]. This evidence of a cognitive decline is revealed by the subject, an informant who knows the subject, or the clinician who treats the subject. However, the cognitive deficit does not interfere with daily activities and does not occur exclusively in the context of a confusional state. In contrast, MNCD is characterized by the evidence of considerable deficits acquired in one or more cognitive domains [21] that, as in mNCD, is also reported by the subject, an informant, or the clinician. The evidence results from the fact that there is a considerable decline in cognitive function and a substantial deterioration in cognitive performance. In contrast to mNCD, MNCD cognitive deficits interfere with the individual autonomy in daily routines and activities [21].

Diagnosis of NCD establishes, as a main goal, identifying cognitive impairment and NCD from secondary etiology, therefore, potentially treatable controls, e.g., human immunodeficiency virus (HIV), brain tumors or alcohol abuse [21]. Moreover, the diagnostic process must analyze the personal and family history and the social context. The diagnosis in the asymptomatic phase allows healthcare providers to monitor the disease and define a care protocol. In addition, it offers the opportunity for family members and the patient to make decisions about the patient's future [179]. Current diagnostic criteria to determine the degree of functional impairment is based on scales that evaluate the subject's cognitive ability. On the one hand, the Global Deterioration Scale (GDS) developed by Reisberg *et al.* [180] and the Functional Assessment Staging (FAST) [181] identify seven clinically recognizable stages from normality to the most severe form of Alzheimer's dementia. On the other hand, the Clinical Dementia Rating (CDR) [182] describes five broad stages from normality to severe dementia.

The evolution of neurodegenerative diseases, especially Alzheimer's disease, is slow and both cognitive and behavioral symptoms appear simultaneously. The disease is presented and evolves differently in each subject, which may mislead the diagnosis of another disease. For this reason, it is necessary to find effective diagnostic techniques. Biomarkers allow an early biological diagnosis (preclinical phase) and improve the etiological study of NCDs. A biomarker can serve as an indicator of health or illness and must be sensitive to normal biological process, pathological process, or pharmacological interventions [183]. Several investigations explore the relationship between biomarkers and atrophy in specific brain regions to make an accurate diagnosis, both in the clinical and preclinical phases of Alzheimer's disease [184], [185].

Biomarkers can be divided into body fluid biomarkers, imaging biomarkers (topographic and pathophysiological), and other biomarkers [22].

The common clinical tests to diagnose a possible Alzheimer's disease are based on in-vivo neuroimaging biomarkers using Positron-Emission Tomography (PET) or MRI, both of which are used in a preclinical phase [23]. PET imaging diagnosis allows to detect β-amyloid peptide (Aβ) and tau protein [23]. MRI biomarkers are used to discard specific pathologies, such as tumor or vascular disease. In-vivo neuroimaging biomarkers are widely used to detect Alzheimer's disease in the absence of symptoms, or in cases where neuropathological changes are shown independently of the clinical symptoms [186]. However, the use of these procedures is expensive and has a restricted availability for verifying the diagnosis [24].

Cerebrospinal Fluid (CSF) is the most common body fluid employed to identify Alzheimer's disease biomarkers. Three CSF biomarkers have been studied in the literature: $A\beta_{1\text{-}42}$, total tau protein (t-tau), and phosphorylated tau (p-tau). A decrement of $A\beta_{42}$ in CSF is a predictor of progression from mNCD (Alzheimer's disease) to MNCD (Alzheimer's disease). However, an increment of t-tau represents axonal degeneration at the early stages of Alzheimer's disease. Finally, p-tau increases before the beginning of the prodromal stage of Alzheimer's disease [22]. Nevertheless, the lumbar puncture in CSF collection is a highly invasive procedure that causes discomfort and can cause side effects, such as headache, back pain, swelling, or bruising. For this reason, other body fluid biomarkers related to blood samples have been investigated. This alternative is less-invasive and is cost-effective for early detection, especially in the identification of patients both in the clinical and preclinical phases of Alzheimer's disease. Blood plasma is used to identify proteins related with the disease, such as albumin, fibrinogen, and immunoglobulins [187]. Biomarkers present in CSF have been studied in blood plasma and include $A\beta_{42/40}$, neurofilament light chain (NfL), neurogranin (Ng) and YKL-40 (also known as Chitinase 3-like 1) [184]. Furthermore, the use of blood plasma biomarkers reduces the cost and the risk of adverse effects. In this sense, novel techniques to identify these biomarkers in blood plasma samples should be investigated.

In the field of NCD detection the use of HSI is limited. In 2019, Hadoux *et al.* employed a HS retinal camera, covering the VNIR range from 450 nm to 900 nm, to identify potential biomarkers that represent the accumulation of Aβ in the retina for Alzheimer's disease detection [188]. The HS retinal camera captures images of the retina with a 30-degree field of view and a pixel resolution of ~8.3 μm. This study consisted of 35 participants divided into case group (n = 15) and the control group (n = 20). At wavelengths below 565 nm, reflectance spectra were different between cases and controls. More *et al.* developed a system based on a clinical ophthalmic camera and a spectrographic camera covering the spectral range from 400 to 1000 nm with a resolution of 2.5 nm [189]. However, this study was a proof of concept to translate the HS system from animal models to human Alzheimer's disease subjects. In 2020, Lemmens *et al.* presented an HS retinal imaging based on a snapshot camera able to capture from 460 to 620 nm with 16 spectral bands and 272×512 spatial pixels [190]. The HS data and nerve fiber layer thickness data were used in a linear discriminant classification model to discriminate between Alzheimer's disease patients and controls using a leave-one-out cross-validation technique, achieving an AUC value of 0.74.

Additionally, previous works carried out by our group employed HS microscopy in the VNIR range to propose a novel methodology for identifying potential biomarkers of MNCD in blood plasma samples [191]. The Table 2-5 provides a comprehensive summary of the different HSI systems used in the literature to study MNCD disease, highlighting the specification of the system and the objective of the study.

Table 2-5: HSI systems used to study MNCD disease.

Ref.	Year	HSI System Type	Wavelength (nm)	Bands	Spatial Resolution	Patients (Case/Control)	HS Images	Study Objective
[188]	2019	Whiskbroom (Retinal Imaging)	450-900	90	n/a	15/20	n/a	AD
[189]	2019	Focal Plane (Retinal Imaging)	400-1000	240	n/a	19/16	n/a	AD
[190]	2020	Snapshot (Retinal Imaging)	460-620	16	272×512 pixels	17/22	n/a	AD
[191]	2020	Pushbroom (Microscopy of Blood Plasma)	400-1000	826	400×1004 pixels	5/5	20	AD

AD: Alzheimer's Disease; **n/a**: not available.

2.6 Conclusions

In this chapter, the basic concepts of HSI were presented, exploring the HS instrumentation commonly employed for HS image acquisition. Different processing methods found in the literature were explained, which play a key role in extracting meaningful information from the complex hyperspectral datasets. In this context, common algorithms used to process HS images were detailed, with a particular focus on supervised and unsupervised methods that were employed in this dissertation. These algorithms allow to extract critical results from the data. To ensure the reliability of the results obtained in this dissertation, we discussed the use of various performance evaluation metrics. These metrics provide an objective and quantitative means of assessing the effectiveness and accuracy of the algorithms used, thus providing a solid foundation for drawing meaningful conclusions from the HSI data.

The most recent advances in HSI for medical applications were presented, with special emphasis in skin cancer, brain cancer, and MNCD. These specific medical applications showcase the true potential of HSI image analysis in revolutionizing healthcare due to the advantages of its non-contact, non-ionizing, label-free, and minimally invasive nature. The use of HSI in the medical field can provide a wealth of information that can help with early detection and accurate diagnosis. Skin cancer is one of the most common types of cancer, the use of HSI can benefit in skin detection with non-invasive tool, avoiding many biopsies. The early detection of lesions using HSI can lead to improved patient outcomes and better overall prognosis. Similarly, in the case of brain cancer, HSI can play a crucial role in guiding surgeons during tumor resection surgeries. By providing a real-time tool that delineates between healthy and tumor tissue, it enables effective removal of tumors while preserving vital healthy brain tissue. In addition, the use of HSI in MNCD can potentially identify specific biomarkers associated with neurodegenerative diseases. This advance could revolutionize early diagnosis of Alzheimer's disease and other dementias as a cost-effective tool.

Beyond medical applications, HSI techniques are branching out into various other fields, ranging from agriculture and environmental monitoring to industrial quality control and mineral exploration.

Chapter 3: Intraoperative HS acquisition system for brain surgical diagnostics and guidance

3.1 Introduction

This chapter presents the intraoperative HS acquisition system for brain surgery diagnosis and guidance. The developments in this PhD Thesis build on a system that was previously developed as part of the European HELICoiD project, funded by the Research Executive Agency under Grant Agreement 618080, through the Future and Emerging Technologies (FET-Open) Programme and under the 7th Framework Programme of the European Union [123], [124]. The system that served as a starting point for this research, was designed as a proof of concept with the goal of delineating brain tumors during surgical procedures. By exploiting the existing system, this dissertation aims to extend its capabilities, refine its functionalities, and explore new avenues of application. Part of the research carried out in this dissertation was related to the Regional Project ITHaCA, funded by the Canary Islands Government through the ACIISI (Canarian Agency for Research, Innovation, and the Information Society) under Grant Agreement ProID2017010164[1].

The original intraoperative HS acquisition system consisted of two pushbroom HS cameras covering the VNIR spectral range from 400 to 1000 nm, and the NIR spectral range from 900 to 1700 nm. The HS cameras and the illumination system were mounted on a scanning platform to enable movement. However, only HS images of the VNIR HS camera were used during the HELICoiD project for the algorithm's development. In this dissertation, several optimizations were performed to the original system. Employing the optimized intraoperative HS acquisition system, an in-vivo HS human brain image database was generated. Using this database, a new approach was proposed to perform spectral fusion of two HS cubes obtained with two different HS cameras covering the VNIR and NIR spectral range, aiming to obtain a broadband HS cube. This fusion procedure was investigated targeting an improvement of the previous results in the processing of the intraoperative HS brain tumors including NIR information. Furthermore, combining the VNIR database generated in this dissertation

[1] ithaca.iuma.ulpgc.es

and the one captured with the previous HS system [124], vascular enhanced maps hemoglobin spectral ratios were proposed, and different analyses using spectral and spatial information were performed to detect and delineate brain tumors with a robust validation methodology.

The work related to the HS analysis using SU was performed in collaboration with the research group of Prof. Daniel Ulises Campos-Delgado at the Faculty of Sciences of the Universidad Autónoma de San Luis Potosí (UASLP), Mexico. The work related with the data collection in the operating theater was carried out in a very close collaboration with the neurosurgery department led by Dr. Jesús Morera (having a special role in the research Dr. Adam Szolna and Dr. Juan F. Piñeiro) from the University Hospital of Gran Canaria Doctor Negrin of Las Palmas de Gran Canaria and also with Dr. Bernardino Clavo from the Research Unit of the same hospital.

3.2 Optimization of the Intraoperative HS Acquisition System

The intraoperative HS acquisition system developed in the European Project HELICoiD (Figure 3-1.a and Figure 3-1.b) was modified to optimize the system to evaluate the delineation of brain tumors during surgical operations by using the VNIR and NIR spectral ranges. The original system had several limitations that affected the possible use of the two HS image types and also the real-time performance of the system. Therefore, improvements to the original system were proposed to reduce the acquisition time and increase the quality of the captured images from both HS cameras.

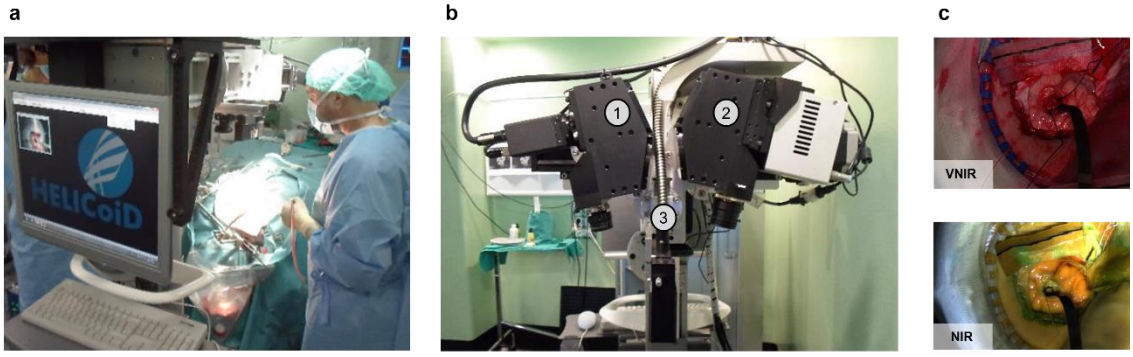

Figure 3-1: Original intraoperative HS acquisition system. a) HS acquisition system being used during a neurosurgical operation at the University Hospital of Gran Canaria Doctor Negrin (Spain). **b**) Original camera position (1) VNIR HS camera, (2) NIR HS camera, (3) cold light emitter. **c**) Example of a VNIR and a NIR HS image captured from the same scene.

This HS acquisition system was composed by two pushbroom HS cameras: the VNIR camera covered the spectral range between 400 and 1000 nm and the NIR camera between the 900 and 1700 nm (1 and 2 in Figure 3-1.b). The illumination system was based on a QTH lamp of 150 W with a broadband emission between 400 and 2200 nm. The light source was connected to a cold light emitter (3 in Figure 3-1.b) through an optical fiber to avoid the high temperatures of the QTH lamp in the exposed brain surface. The HS cameras and the cold light emitter were installed in a scanning platform to provide the necessary movement for the pushbroom technique to generate the complete HS cubes. The working distance between the lens of the cameras and the exposed brain tissue was 40 cm. The field of view of both cameras was oriented and

aligned to the beam of the cold light emitter to obtain the highest reflectance value in the sensors (Figure 3-1.b). As a result, both cameras were tilted to capture the same FOV, but this meant that both HS cubes had different perspectives of the scene and it was not possible to achieve an accurate registration for data fusion (Figure 3-1.c).

3.2.1 Improvements in the HS Cameras Positioning

In this dissertation, different modifications of the intraoperative HS acquisition system were performed to achieve the optimal orientation of the cameras respect to the exposed brain surface. In the original intraoperative HS acquisition system (Figure 3-2.a), both cameras were adjusted at a 15º angle to capture the same FOV, resulting that each HS cube had a different perspective view of the scene.

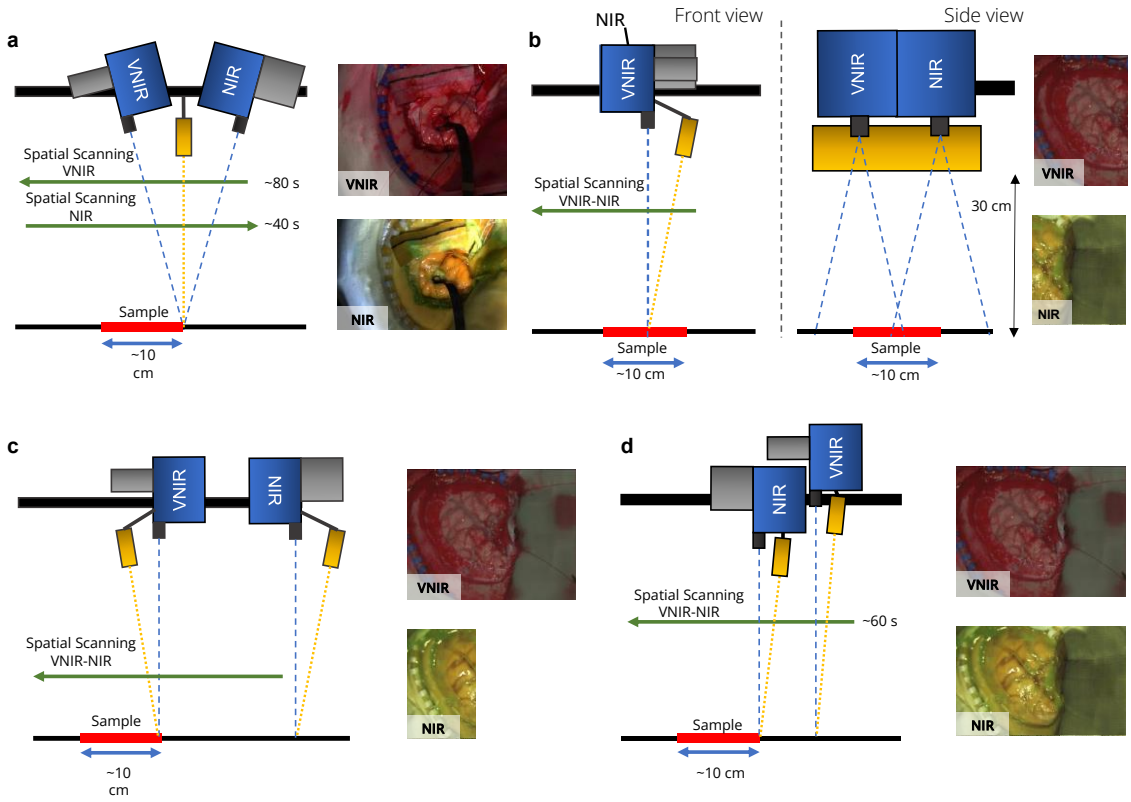

Figure 3-2: The original and the different modifications performed to the intraoperative HS acquisition system. a) Original. **b**) First modification. **c**) Second modification. **d**) Third and selected modification.

The first proposed variation of the intraoperative HS acquisition system was to eliminate the tilt of the original HS camera system (Figure 3-2.b). In this variant, the HS cameras are arranged in a coupled manner, where the line to be acquired coincides for both cameras. This modification was made to avoid the addition of another light source. With this arrangement, the scanning movement for both HS cameras is the same and the HS cubes can be acquired in parallel in the same scan, reducing acquisition times. However, this modification presents a problem. When analyzing the HS images for the area of interest of approximately 10 cm (commonly maximum exposed brain surface after craniotomy) and at the minimum allowed working distance (due to safety restrictions in the operating theater) between the lens and the exposed brain (30 cm), the HS cube formed by both cameras has a common area of less than 1 cm. In order to capture the same area of interest for both HS cameras the working

distance would have to be increased and this would cause a loss of spatial resolution and could affect the accuracy of tumor classification. Therefore, another solution was proposed.

The second proposed variation follows the main objective of the previous variation to avoid tilting of the HS cameras (Figure 3-2.c). This changes from a single point where both HS cameras focus to two different points separated by a certain distance. In this case, it is necessary to add a second light source to provide illumination for each HS camera independently. The acquisition process for this setup starts from idle state and the motor moves the HS cameras, placing the VNIR lens at the beginning of the region of interest (ROI). The VNIR acquisition begins, moving the HS cameras to generate the HS cube. When the VNIR lens leaves the ROI, the acquisition of that HS camera ends. The motor then moves the cameras to bring the NIR into the area of interest and begin acquisition. This configuration has a problem when capturing the HS cube for both cameras. Due to the size of the scanning platform, the acquisition of the second HS camera is interrupted before the acquisition process is complete. The distance between the lenses is too large and insurmountable due to the structure of these cameras, so other alternatives were considered.

Finally, the third option is to place the HS cameras without tilting to ensure that the area of interest coincides in the two HS images (Figure 3-2.d). In this configuration, the goal is to reduce the distance between the lenses to ensure that the scan can be performed completely. To do this, one HS camera is placed on top of the other to reduce the distance between the HS camera housings. This means that one HS camera is further away from the area of interest than the other, but this is compensated for by the fact that the VNIR HS camera has a higher spatial resolution than the NIR HS camera. The acquisition process for this setup starts from an idle state, placing the VNIR lens at the beginning of the ROI. Before the VNIR camera finishes capturing the entire area, the NIR lens enters the area of interest, capturing both HS cameras simultaneously. Subsequently, the VNIR HS camera stops capturing and later the NIR HS camera finishes the capture.

After modifying the intraoperative HS acquisition system, both HS cameras had a similar FOV, allowing an accurate image registration. The working distance between the lens of the cameras and the area to be captured were ~33 and ~42 cm for the NIR and VNIR cameras, respectively, to obtain the sharpest focus. In addition, the acquisition time of the modified system to capture both HS cubes was reduced to ~60 s, performing only a scanning in a single direction. This improvement represented a time reduction of 1 min, due to the original system required ~80 and ~40 s for the VNIR and NIR HS cubes capturing, respectively, involving two scanning movements in both directions as shown in Figure 3-2.a. Finally, the optimized intraoperative HS acquisition system was validated during neurosurgical interventions (Figure 3-3) and after the modifications the system was composed by: a NIR and a VNIR HS camera (1 and 2 in Figure 3-3.b, respectively), and two illumination systems based on a QTH lamp of 150 W (3 and 4 in Figure 3-3.b), one for each HS camera. Each light source was connected to a cold light emitter (5 and 6 in Figure 3-3.b) through an optical fiber to avoid the high temperatures of the QTH lamp in the exposed brain surface.

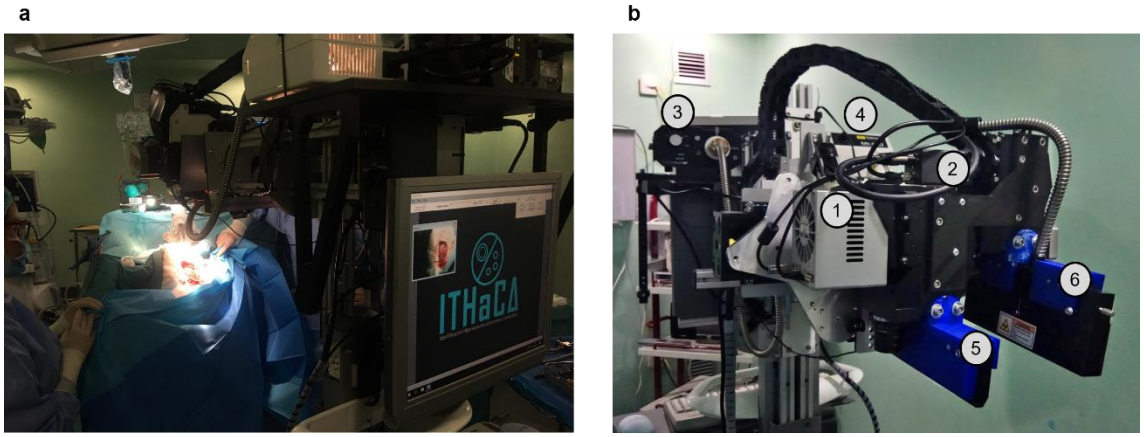

Figure 3-3: Modified intraoperative HS acquisition system. a) HS acquisition system being used during a neurosurgical intervention at the University Hospital of Gran Canaria Doctor Negrin (Spain). **b**) Final HS camera distribution (1) NIR HS camera, (2) VNIR HS camera, (3) VNIR illumination system, (4) NIR illumination system, (5) NIR cold light emitter, (6) VNIR cold light emitter.

3.2.2 Graphical Interface for Control, Acquisition and Processing

The HELICoiD project was not focused on the creation of a single graphical interface to perform the various stages of data acquisition and processing, working in real-time in the operating room. These stages include motor control, image acquisition, image display, image processing and classification, and presentation of classification maps.

In the work presented in this dissertation, a unified graphical interface (Figure 3-4) was developed, integrating different SDKs (Software Development Kits) necessary to control the VNIR and NIR HS cameras, as well as the motor controller for camera movement. The software allowed the acquisition of the black and white reference of both HS cameras, making possible to perform the pre-processing and post-processing of the HS images in the same application. The system had a positioning camera that allowed the visualization of the area to be scanned by the HS cameras, since these cameras only capture a spatial line and, therefore, it is impossible to determine the exact position over the exposed brain surface. For this reason, an RGB camera was included and aligned with the HS cameras to identify the area of the brain to be captured. The software shows the continuous visualization of the RGB image of the positioning camera (1 in Figure 3-4.a) and the synthetic RGB images of the NIR and VNIR cameras after finishing the capturing process (2 and 3 in Figure 3-4.a, respectively). After viewing the HS images, image processing can be performed, which included pre-processing and post-processing using the framework explained in Section 3.5. An advantage of this software is that the HS image can be cropped by adjusting the ROI, thus reducing the processing time. Finally, the presentation of the thematic map (generated using the VNIR data) is displayed together with the synthetic RGB image of the VNIR (2 and 1 in Figure 3-4.b, respectively)

In addition to the aforementioned characteristics, an approach to optimize the focus of the system was developed, guiding the user during this process that required to displace up or down the head were the cameras were mounted. Several focusing algorithms were analyzed, including derivative, statistical, and histogram-based algorithms [192]. The output of an ideal focus algorithm is defined as having a maximum value at the best-focused image. It decreases as defocus increases. However, the choice of the algorithm was determined by its ease of implementation and reduced

computational time, prioritizing simplicity and computational efficiency. For this reason, the Squared Gradient (SG) derivative-based algorithm was selected. This algorithm sums the squared differences, making larger gradients have more influence. Eq. (26) compute the SG where $f(x,y)$ is the luminance or grayscale level at pixel (x,y) in an image of size $M \times N$ pixels.

$$SG = \sum_{x=0}^{M-2} \sum_{y=0}^{N-1} [f(x+1,y) - f(x,y)]^2 \quad (26)$$

$$if\ [f(x+1,y) - f(x,y)]^2 \geq \epsilon$$

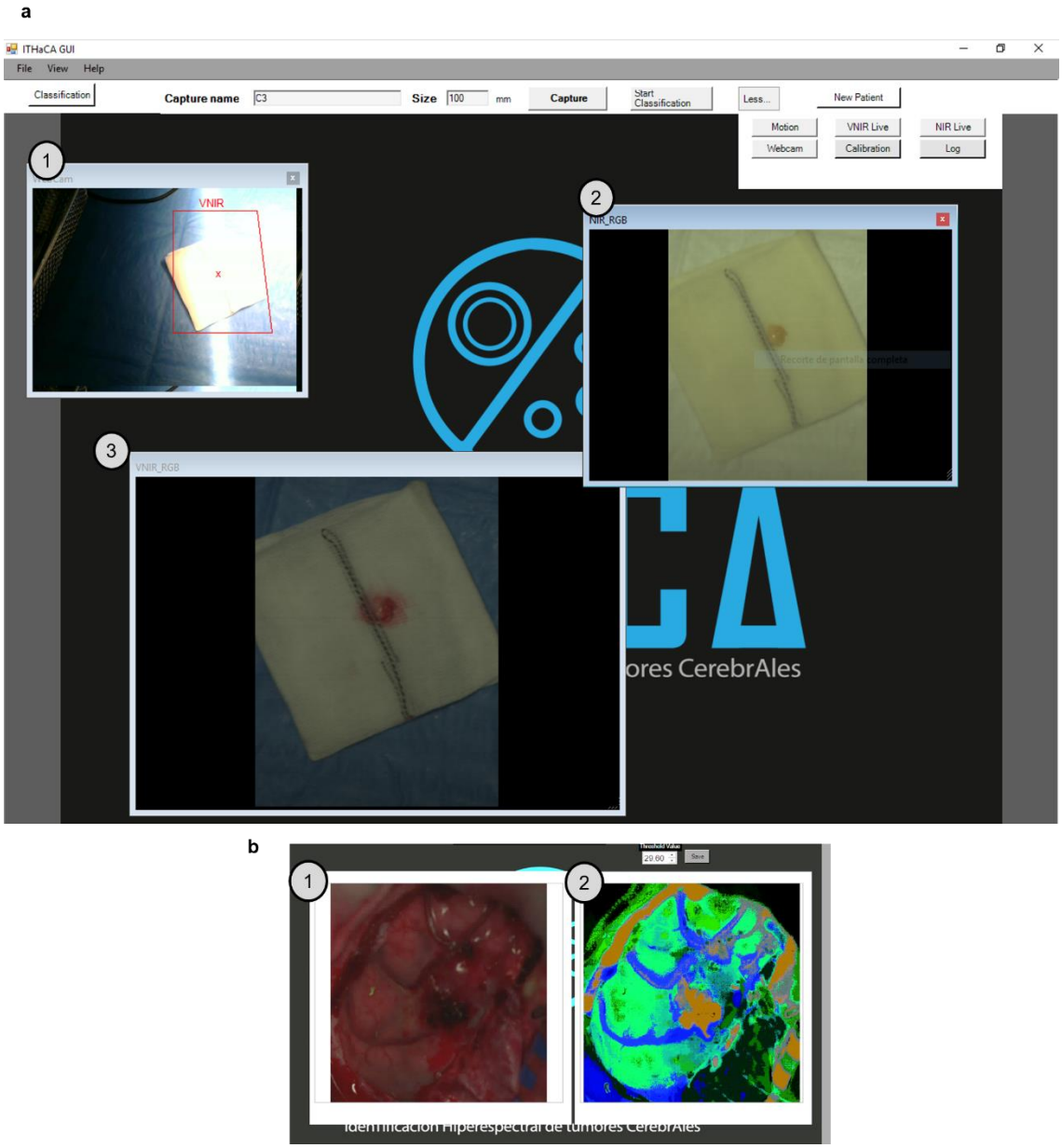

Figure 3-4: Graphical interface for control and acquisition. a) Graphical interface with (1) live positioning camera, (2) synthetic RGB NIR image, (3) synthetic RGB VNIR image. **b**) Classification results after processing the VNIR data, (1) synthetic RGB VNIR image after cropping the region of interest, (2) thematic map.

In our case, the image used is a pushbroom frame (namely Y-lambda image or Yλ image). In pushbroom systems, the Yλ images are employed for focusing the HS

camera. This image is a conventional 2-D grayscale image where the λ-axis represents the spectral dimension, the Y-axis represents the spatial dimension, and the gray level indicates the luminance for a certain pixel. The SG was calculated in real-time in the software and was used to position the intraoperative HS acquisition system over the exposed brain at the correct distance from the exposed brain to the lens to acquire a focused HS image. Every 500 ms, a Yλ frame was captured (Figure 3-5.a) to calculate the SG. The results were plotted on a graph in the graphical user interface (Figure 3-5.b), where the value was updated every 500 ms. At the same time, the intraoperative HS acquisition system was moved in the Y-axes by a 24 VDC motor coupled to a spindle. By observing the SG graph, the optimal position was found to obtain a focused HS image.

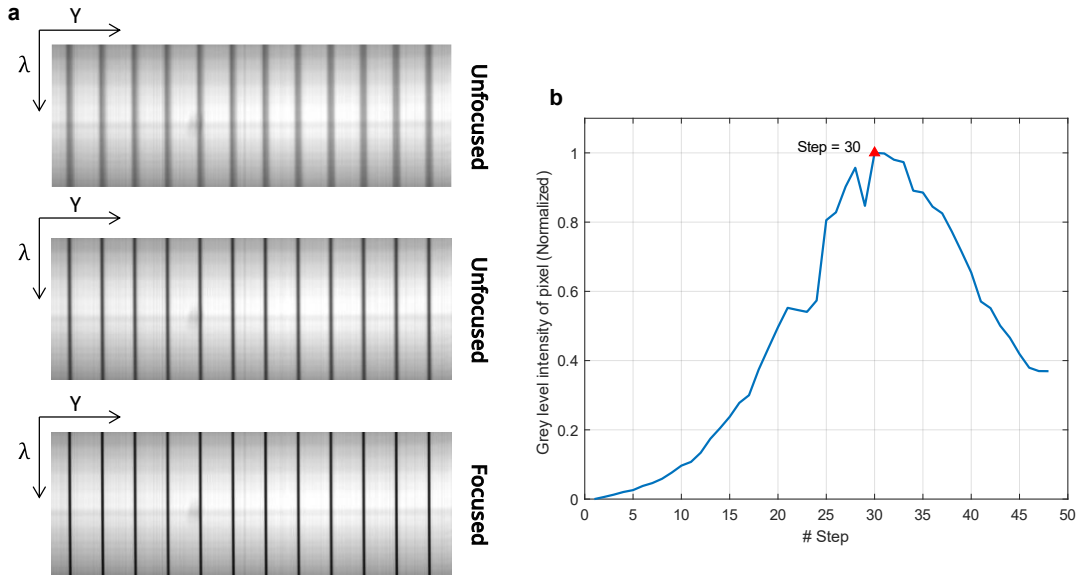

Figure 3-5: Focus procedure using the SG algorithm. a) Y-lambda images. **b**) Grey level intensity computed using squared gradient.

3.2.3 Intraoperative HS Acquisition System Integration

In summary, the HS acquisition system consists of several submodules that communicate directly with the control unit. Figure 3-6 shows how each module communicates with the control unit. The two HS cameras are directly connected to the control unit via USB 2.0 for the NIR camera and Camera Link for the VNIR camera. These HS cameras are mounted on the scanner platform, which communicates directly with the control unit via the RS-232 serial interface. The linear movement of this platform is performed in the graphical interface for control and acquisition, where the user can control its movement. In this interface, the user can start the acquisition of the HS images, visualize its acquisition and subsequent result, and control the system through the display port. The HS images captured by both HS cameras are stored in the control unit's memory, which is accessible by the visualization software. This software is responsible for accelerating the HS image post-processing algorithm. The acceleration is performed by an NVIDIA STRIX-GTX1060 GPU, which communicates directly with the control unit via PCI Express 3.0.

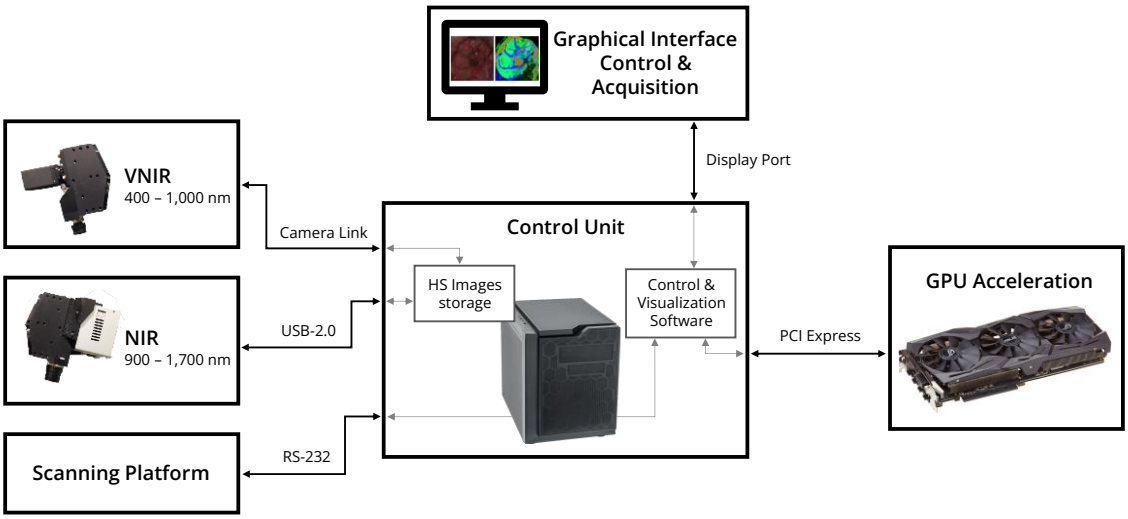

Figure 3-6: Block diagram of the different modules that composed the HS acquisition system.

3.3 Enhanced In-vivo and Ex-vivo Hyperspectral Human Brain Image Database for Brain Cancer Detection

After the optimization of the intraoperative HS acquisition system, this system was used to generate a new HS human brain cancer database, captured during the execution of the ITHaCA project. This new database allowed to augment the database previously collected in the HELICoiD project [124], making possible to perform more robust analyses on the HS images and to validate the ML results for both classification and data fusion methods. The procedure for capturing the HS images is shown in Figure 3-7.

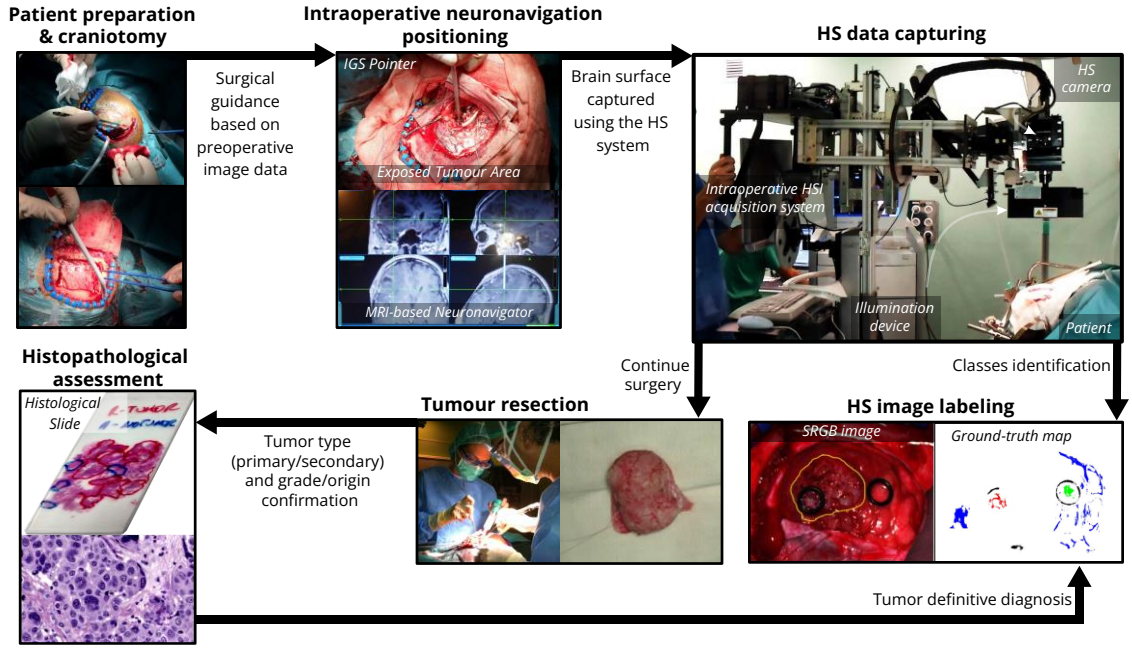

Figure 3-7: HS data acquisition and labelling procedure during surgery. In the ground-truth map, red represents tumor labelled pixels, green normal pixels, blue hypervascularized pixels, and black background pixels. Meanwhile, white represents non-labelled pixels.

First, a craniotomy was performed to the patient by using IGS neuronavigation and then, the durotomy was accomplished to expose the brain surface. Next, the acquisition system was placed over the patient's brain to acquire the HS image. In some questionable cases, rubber ring markers were placed over tumor and normal tissue areas according to the IGS system information to later identify the tissue type. After that, tumor tissue was resected for neuropathological evaluation to achieve the definitive diagnosis of the tumor. When possible, more than one HS image was acquired while the tumor was being resected.

HS images were manually cropped to select the ROI where the parenchymal area was exposed. Afterwards, the data were labelled by using information provided by neuropathologists and the knowledge of the operating surgeons through a semi-automatic labelling tool based on the Spectral Angle Mapper (SAM) algorithm developed to this end [124]. The SAM algorithm is an automated method for comparing the spectra in the pixels of an HS image with a known spectrum obtained from a reference pixel. The procedure to generate the neurosurgeon's ground truth map is as follows:

1) The operating surgeon selects a reference pixel from the synthetic RGB image.
2) Then, the most similar pixels to the selected reference pixel are highlighted, after computing the SAM algorithm.
3) The threshold to indicate if a pixel is considered similar or not the reference pixel is configurable by the user to adjust tolerance levels on selected pixels. This threshold is computed using SAM algorithm. Once only the pixels belonging to a single class are highlighted, they are assigned to that class. Neurosurgeons are advised to only select a few sets of highly reliable pixels rather than a broader set that may be uncertain.

The ground-truth maps were composed by four classes (acronym – pixel color): tumor tissue (TT – red), normal tissue (NT – green), blood vessels (BV – blue) and background (BG – black). White pixels in the ground-truth maps represented the non-labelled pixels, since only pixels with high confidence to belong to a certain class were labelled. Several images in the database do not contain tumor pixels due to the impossibility of performing a reliable labelling or due to the patient underwent surgery for another pathology, such as a blood clot or epilepsy.

The data acquisition campaign was carried out at the University Hospital of Gran Canaria Doctor Negrin, Spain, from July 2019 to October 2019. Written informed consent was obtained from all participant subjects, and the study protocol and consent procedures were approved by the *Comité de Ética de la Investigación / Comité de Ética de la Investigación con Medicamentos* (CEI/CEIM) of the University Hospital Doctor Negrin (2019-001-1). All the research methodologies were performed in accordance with relevant guidelines/regulations. This data campaign was capture using the new configuration of the acquisition system, explained in Section 3.2. During this data campaign, nine neurosurgeries were attended and a total of 15 images were acquired. Finally, this data campaign (called the third data campaign) consists of 10 images from 8 different patients, after excluding some images that were acquired in non-optimal conditions.

During the HELICoiD project, two data acquisition campaigns were carried out at the University Hospital of Gran Canaria Doctor Negrin, Spain [124]. The first data campaign was conducted from March 2015 to June 2016, and the second from October 2016 to April 2017. Written informed consent was obtained from all the participant subjects. The study protocol and consent procedures were approved by the *Comité Ético de Investigación Clínica-Comité de Ética en la Investigación* (*CEIC/CEI*) of the University Hospital Doctor Negrín (130069). All the research methodologies were performed in accordance with relevant guidelines/regulations.

Table 3-1 summarizes the in-vivo HS images (Figure 3-8.a) acquired in HELICoiD and ITHaCA projects, showing the number of patients (identified as Op*x*: operation number) and HS images (identified as C*y*: capture number) captured in each data campaign, the image dimensions, the number of labelled pixels, and the definitive pathological diagnosis. Table 3-2 summarizes the ex-vivo HS images (Figure 3-8.b) captured in HELICoiD and ITHaCA projects. Figure 3-8.c shows the number of patients and HS images of each data acquisition campaign before and after excluding the HS images that were captured in non-optimal conditions.

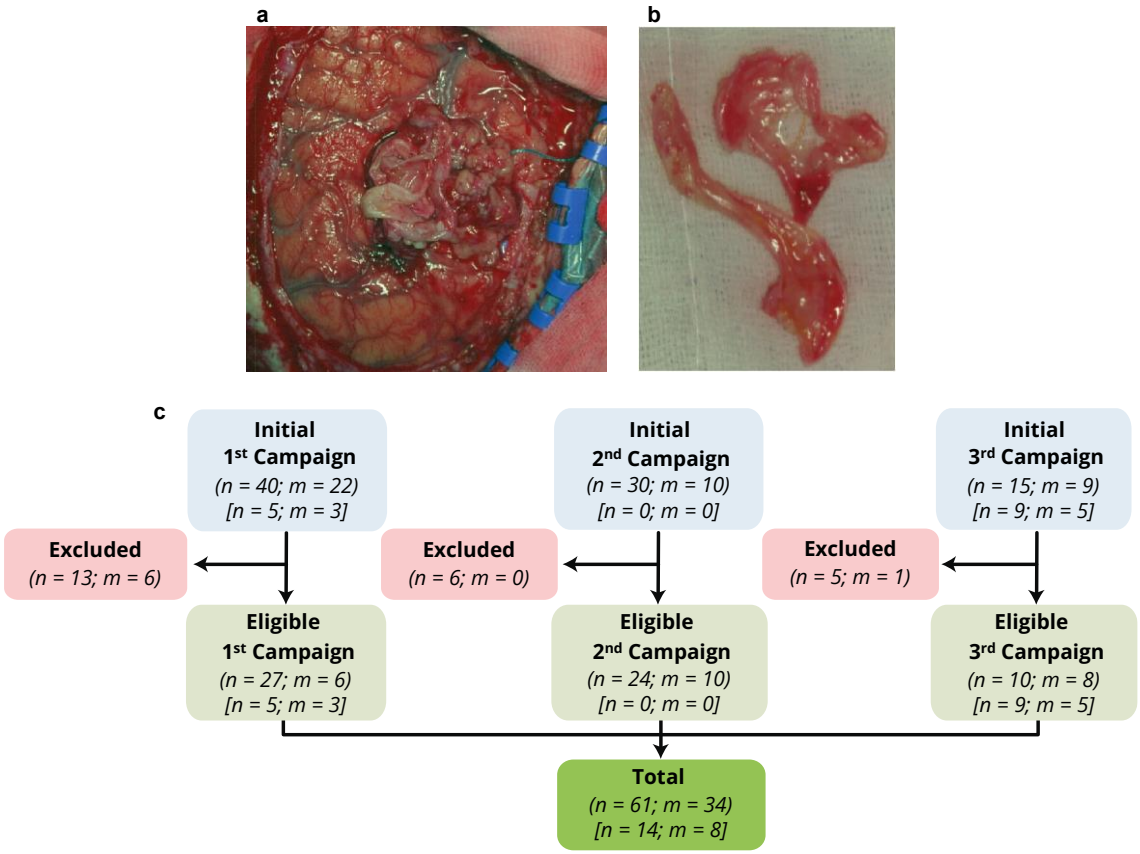

Figure 3-8: HS in-vivo and ex-vivo database. a) Example of HS in-vivo image. **b**) Example of HS ex-vivo image. **c**) Patient/image flow scheme of the enhanced in-vivo (in parentheses) and ex-vivo (in brackets) HS human brain image database. n: number of HS images; m: number of patients.

Table 3-1: Summary of the enhanced in-vivo HS human brain image database.

Campaign	Image ID	Size (H×W)	#Labeled Pixels				Diagnosis
			NT	TT	BV	BG	
First Data Campaign	Op04C2	389×345	5,007	0	965	1,992	Normal Brain
	Op05C1	483×488	6,061	0	1,727	20,483	Renal Carcinoma (S)
	Op07C1	582×400	7,714	0	1,089	0	Normal Brain
	Op08C1	460×549	2,295	1,221	1,331	630	G4 Glioblastoma (P)
	Op08C2	480×553	2,187	138	1,000	7,444	G4 Glioblastoma (P)
	Op10C3	371×461	10,626	0	2,332	3,972	G4 Glioblastoma (P)
	Op12C1	443×497	4,516	855	8,697	1,685	G4 Glioblastoma (P)
	Op12C2	445×498	6,553	3,139	6,041	8,731	G4 Glioblastoma (P)
	Op13C1	298×253	1,827	0	129	589	Lung Carcinoma (S)
	Op14C1	317×244	0	30	64	1,866	G4 Glioblastoma (P)
	Op15C1	376×494	1,251	2,046	4,089	696	G4 Glioblastoma (P)
	Op16C1	335×323	3,970	0	246	12,002	Normal Brain
	Op16C2	335×326	349	0	0	2,767	Normal Brain
	Op16C3	315×321	603	0	234	1,696	Normal Brain
	Op16C4	383×297	1,178	0	1,064	956	G4 Glioblastoma (P)
	Op16C5	414×292	2,643	0	452	5,125	G4 Glioblastoma (P)
	Op17C1	441×399	1,328	0	68	3,069	G4 Glioblastoma (P)
	Op18C1	479×462	13,450	0	488	9,773	G1 Ganglioglioma (P)
	Op18C2	510×434	4,813	0	958	5,895	G1 Ganglioglioma (P)
	Op19C1	601×535	6,499	0	1,350	1,933	G1 Meningioma (P)
	Op20C1	378×330	1,842	3,655	1,513	2,625	G4 Glioblastoma (P)
	Op21C1	452×334	3,405	167	793	5,330	Breast Carcinoma (S)
	Op21C2	448×324	2,353	31	555	2,137	Breast Carcinoma (S)
	Op21C5	433×340	969	0	1,637	1,393	Breast Carcinoma (S)
	Op22C1	597×527	2,806	0	1,064	3,677	G3 Anaplastic Oligodendroglioma (P)
	Op22C2	611×527	8,174	0	680	0	G3 Anaplastic Oligodendroglioma (P)
	Op22C3	592×471	0	96	0	0	G3 Anaplastic Oligodendroglioma (P)
Second Data Campaign	Op34C1	319×356	0	0	0	15,609	G3 Anaplastic Astrocytoma (P)
	Op34C2	300×342	512	145	0	12,979	G3 Anaplastic Astrocytoma (P)
	Op34C3	290×301	0	360	0	10,533	G3 Anaplastic Astrocytoma (P)
	Op35C1	431×503	9,025	0	7,287	485	G2 Oligodendroglioma (P) [DL]
	Op35C2	312×535	0	1,338	629	1,353	G2 Oligodendroglioma (P)
	Op36C1	412×324	11,665	0	4,461	4,621	G4 Glioblastoma (P) [DL]
	Op36C2	432×322	2,940	888	2,980	5,853	G4 Glioblastoma (P)
	Op37C1	434×453	12,719	0	2,524	11,161	G4 Glioblastoma (P) [DL]
	Op37C2	315×526	2,997	0	375	4,166	G4 Glioblastoma (P)
	Op37C3	290×422	3,201	407	0	0	G4 Glioblastoma (P)
	Op37C4	280×444	0	330	0	0	G4 Glioblastoma (P)
	Op38C1	497×490	18,511	2,295	4,229	3,669	G1 Meningioma (P)
	Op39C1	415×446	4,003	244	489	9,829	G4 Glioblastoma (P)
	Op39C2	399×439	7,705	1,629	822	9,867	G4 Glioblastoma (P)
	Op40C1	303×374	2,728	394	1,151	3,492	G1 Meningioma (P)
	Op40C2	294×344	817	700	2,130	902	G1 Meningioma (P)
	Op41C1	449×486	2,359	69	1,047	5,030	G1 Ganglioglioma (P)
	Op41C2	437×488	4,874	158	2,150	4,888	G1 Ganglioglioma (P)
	Op42C1	629×646	20,565	0	10,956	8,991	G2 Astrocytoma (glioma) (P)
	Op42C2	623×584	19,435	428	5,110	3,983	G2 Astrocytoma (glioma) (P)
	Op42C3	650×582	2,385	401	979	716	G2 Astrocytoma (glioma) (P)
	Op43C1	575×543	28,285	1,177	4,012	5,995	G4 Glioblastoma (P)
	Op43C2	554×446	17,236	475	2,103	1,964	G4 Glioblastoma (P)
	Op43C3	522×533	11,798	589	2,727	1,587	G4 Glioblastoma (P)
	Op43C4	538×525	14,160	0	4,749	687	G4 Glioblastoma (P)
Third Data Campaign	Op50C1	565×533	2,116	1,091	620	5,502	G1 Meningioma (P)
	Op51C1	635×617	1,164	0	424	31,247	G4 Glioblastoma (P)
	Op53C1	546×446	361	5,549	0	33,606	Breast Carcinoma (S)
	Op54C1	515×504	2,697	0	3,506	9,535	G4 Glioblastoma (P)
	Op55C1	397×435	3,128	0	901	8,278	G3 Astrocytoma (glioma) (P)
	Op55C2	500×349	0	1,046	545	9,415	G3 Astrocytoma (glioma) (P)
	Op56C1	446×598	1,346	4,081	2,200	28,370	G2 Astrocytoma (glioma) (P)
	Op56C2	467×566	1,326	372	1,116	7,702	G2 Astrocytoma (glioma) (P)
	Op57C1	440×535	1,773	771	1,263	23,415	Breast Carcinoma (S)
	Op58C2	721×752	6,589	1,629	4,565	43,565	G2 Meningioma (P)
Total labeled pixels			**305,449**	**37,944**	**101,305**	**405,401**	

NT: Normal; **TT**: Tumor; **BV**: Blood vessel; **BG**: Background; **S**: Secondary; **P**: Primary; **G1**: Grade 1; **G2**: Grade 2; **G3**: Grade 3; **G4**: Grade 4; **DL**: Deep layer tumor; **H**: Height; **W**: Width.

Table 3-2: Summary of the enhanced ex-vivo HS human brain image database, including spatial and spectral dimension, and the diagnosis.

Campaign	Image ID	Size (H×W)	Diagnosis
First Data Campaign	Op08C3	158×196	G4 Glioblastoma (P)
	Op15C2	146×182	G4 Glioblastoma (P)
	Op15C3	326×270	G4 Glioblastoma (P)
	Op21C3	215×223	Breast Carcinoma (S)
	Op21C4	214×229	Breast Carcinoma (S)
Third Data Campaign	Op50C2	431×412	G1 Meningioma (P)
	Op50C3	518×693	G1 Meningioma (P)
	Op56C3	228×197	G2 Astrocytoma (glioma) (P)
	Op56C4	210×213	G2 Astrocytoma (glioma) (P)
	Op57C3	159×140	Breast Carcinoma (S)
	Op57C4	169×149	Breast Carcinoma (S)
	Op58C3	330×346	G2 Meningioma (P)
	Op58C4	455×338	G2 Meningioma (P)
	Op58C5	390×205	G2 Meningioma (P)

S: Secondary; **P**: Primary; **G1**: Grade 1; **G2**: Grade 2; **G4**: Grade 4; **H**: Height; **W**: Width.

The enhanced in-vivo HS human brain image database was composed by a total of 61 HS images from 34 adult patients with brain tumors. The summary of the patient demographics and clinic data is shown in Table 3-3. Ages ranged from 30 to 73 years, with a median age of 51.5 years. Among these patients, there were 21 males and 13 females. Of these 34 patients, 28 (82.4%) had a primary tumor. The most frequency primary grade was the G4 (44.1%, $n = 15$), followed by G1 and G2 (14.7%, $n = 5$ each one), while the 8.8% ($n = 3$) of the tumors were G3. The remaining 6 (17.6%) tumors were secondary: 3 from breast carcinoma, 2 from lung (one adenocarcinoma and one carcinoma), and 1 from kidney (renal carcinoma). Most of tumors were located in the right temporal lobe (23.5%, $n = 8$), followed by the left frontal and right parietal lobes (20.6%, $n = 7$ each).

Table 3-3: Summary of patient demographic and tumor characteristics.

Variable [patients with no missing values/Total patients]	Characteristic	Total (n)	%
Sex [34/34]	Male	21	61.8
	Female	13	38.2
Age [33/34]	Median	51.5	-
	Range	30-73	-
Tumor Type [34/34]	Primary	28	82.4
	Secondary	6	17.6
Primary Tumor Grade [28/34]	WHO Grade 1	5	14.7
	WHO Grade 2	5	14.7
	WHO Grade 3	3	8.8
	WHO Grade 4	15	44.1
Metastasis [6/34]	Breast	3	8.8
	Lung	2	5.9
	Kidney	1	2.9
Location [34/34]	Right Frontal Lobe	3	8.8
	Left Frontal Lobe	7	20.6
	Right Parietal Lobe	7	20.6
	Left Parietal Lobe	4	11.8
	Right Temporal Lobe	8	23.5
	Left Temporal Lobe	1	2.9
	Right Occipital Lobe	2	5.9
	Left Occipital Lobe	1	2.9
	Cerebellum	1	2.9

3.4 Vascular Enhanced Maps using a Diffuse Absorbance Hemoglobin Spectral Ratio Framework

Spectral ratios have been used in the literature to discriminate between different types of tissues in a variety of imaging methods including diffuse reflectance spectroscopy [193] and HSI [194]. Fu *et al.* proposed the use of the ratio between 545 and 560 nm (named R545/R560) to calculate the degree of cerebral ischemia [194]. The spectral channel of 545 nm is an isosbestic band of oxygenated hemoglobin and deoxygenated hemoglobin, which is independent of changes in saturation. The spectral channel of 560 nm is the spectral band where the largest difference between oxyhemoglobin and deoxyhemoglobin occurs [194]. The R545/R560 ratio reflects a maximized difference between deoxyhemoglobin and oxyhemoglobin, that was studied to help in the identification of brain ischemia using HSI, as well as the application of classification thresholds based on these ratios to distinguish necrosis from normal brain tissue [194].

In the work presented in this section, the R545/R560 spectral ratio was employed to perform an evaluation of in-vivo and ex-vivo tumor tissue samples captured with the optimized HS acquisition system. For this purpose, seven HS images from the in-vivo database and their corresponding ex-vivo samples (presented in Section 3.3) were used, selecting two wavelengths (545 and 560 nm) to compute the absorbance R545/R560 spectral ratio. In addition, the in-vivo HS images were used to generate heat maps and vascular enhanced maps, demonstrating the potential of this framework to be used as intraoperative surgical guidance system in real-time.

The proposed method for computing the absorbance spectral ratio and performing the comparison between the in-vivo and ex-vivo tissue samples is summarized in Figure 3-9.

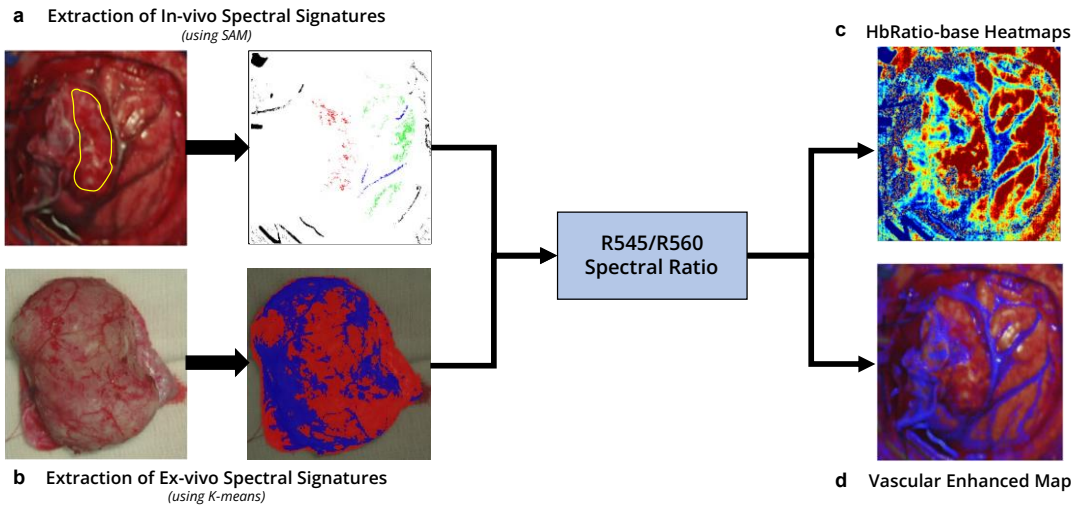

Figure 3-9: Block diagram of the proposed diffuse absorbance spectral ratio processing framework.

First, the raw HS images acquired with the intraoperative acquisition system were pre-processed and the spectral data were converted from reflectance to absorbance values. In the case of the in-vivo HS images, only the labeled pixels were used to perform the spectral analysis (Figure 3-9.a). In the case of ex-vivo HS images, the complete samples were employed, splitting the HS image into different regions using

an unsupervised segmentation method (Figure 3-9.b). Finally, HbRatio-based heatmaps of the in-vivo HS images were generated using the R545/R560 spectral ratio (Figure 3-9.c). A qualitative evaluation of the different tissue structure was performed. In addition, an analysis of the distribution of the R545/R560 ratio in labeled blood vessel pixels was employed to automatically enhance their structures in the in-vivo images (Figure 3-9.d). These vascular enhanced maps were produced using the first and third quartiles of the distribution as limits.

3.4.1 Spectral comparison of in-vivo and ex-vivo samples

Seven in-vivo and fourteen ex-vivo HS images obtained from seven different patients were used in this work, extracted from the database presented in Section 3.3. The in-vivo HS images were previously labeled using the semi-automatic labelling tool based on the SAM algorithm. Table 3-4 summarizes the characteristics of the HS images employed and the labeled pixels, where a total of 44,964 pixels were labeled into three different tissue classes: 10,977 pixels of TT, 17,925 pixels of NT and 16,062 pixels of BV. The ex-vivo images were not labeled at the pixel level, and images captured at different working distances (different focus of the scene that could cause blurred data) were analyzed to determine if the differences in focus could affect the results. The HS images were pre-processed following the different steps presented in Section 2.4.1, applying data calibration, spectral noise reduction, and extreme band removal. Finally, the resulting HS cube, composed of 645 spectral bands, was converted to absorbance following Eq. (2) presented in Section 2.4.1.

Table 3-4: Summary of the labeled dataset employed to perform the diffuse absorbance hemoglobin spectral ratio framework.

Patient ID	Image ID	Sample type	#Labeled Pixels		
			NT	TT	BV
Op08	C2	In-Vivo	2,187	138	1,000
	C3	Ex-Vivo	-	-	-
Op15	C1	In-Vivo	1,251	2,046	4,089
	C2	Ex-Vivo	-	-	-
	C3	Ex-Vivo	-	-	-
Op21	C1	In-Vivo	2,663	1,221	2,325
	C3	Ex-Vivo	-	-	-
	C4	Ex-Vivo	-	-	-
Op50	C1	In-Vivo	2,116	1,091	620
	C2	Ex-Vivo	-	-	-
	C3	Ex-Vivo	-	-	-
Op56	C1	In-Vivo	1,346	4,081	2,200
	C3	Ex-Vivo	-	-	-
	C4	Ex-Vivo	-	-	-
Op57	C1	In-Vivo	1,773	771	1,263
	C3	Ex-Vivo	-	-	-
	C4	Ex-Vivo	-	-	-
Op58	C2	In-Vivo	6,589	1,629	4,565
	C3	Ex-Vivo	-	-	-
	C4	Ex-Vivo	-	-	-
	C5	Ex-Vivo	-	-	-
Total			**17,925**	**10,977**	**16,062**

NT: Normal; **TT**: Tumor; **BV**: Blood vessel.

The K-means algorithm was applied to the ex-vivo HS images in order to segment the tissue samples into different clusters (tissue regions with similar spectral characteristics). The number of clusters was determined by using clustering evaluation methods (Calinski Harabasz, Davies Bouldin, and Silhouette) in each HS image independently, and without taking account the background of the image (mainly

composed by the white gauze where the tissue sample was placed). The background was manually segmented. As shown in Figure 3-10, Op08C3 is composed by three pieces and each piece was consider as an independent image for the analysis. After applying the three cluster evaluation methods, it was found that the optimal number of clusters obtained for almost all HS ex-vivo images was two, except for Op50C3 (six clusters), and Op58C4 and Op58C5 (five clusters, both). Figure 3-10 shows the obtained ex-vivo segmentation maps. Additionally, it is worth noticing that Op21C3 and Op21C4, which were captured with different working distances (and hence different focus), obtained similar segmentation maps.

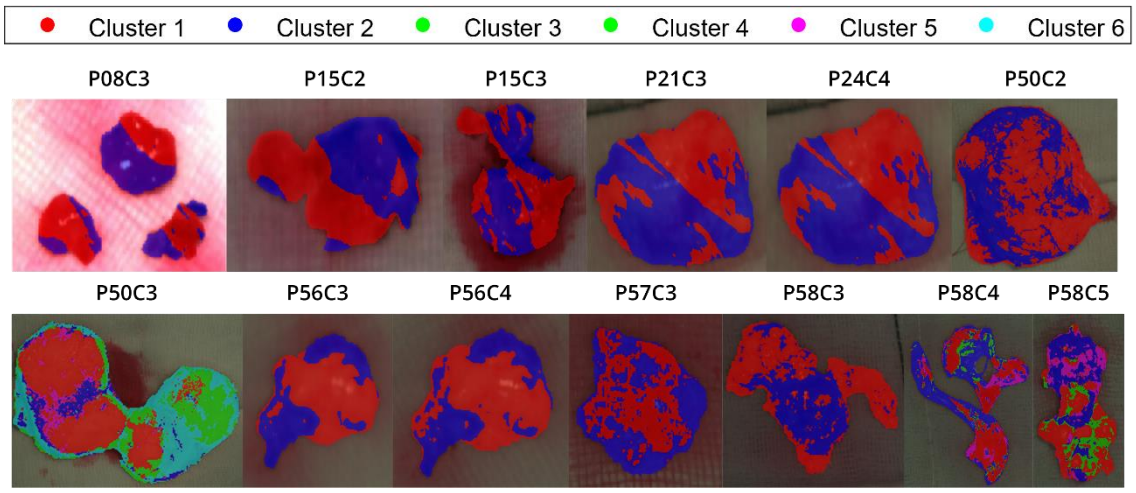

Figure 3-10: Ex-vivo segmentation maps applying K-means algorithm (colors are randomly assigned).

After extracting the spectral signatures from the in-vivo and ex-vivo HS images, these spectral signatures were employed to evaluate the absorbance values in the different tissue samples. Figure 3-11 shows a comparison between in-vivo and ex-vivo spectral signatures. To achieve this comparison, the mean spectral signatures of each class (NT, TT, and BV) was obtained using the in-vivo HS images (solid lines).

After tumor resection, the ex-vivo samples were captured and segmented into different clusters (named CL# in the figure), obtaining the mean spectral signatures from each cluster (dashed lines). It can be observed that in the in-vivo samples the absorbance values of BV pixels between 500 and 600 nm are higher than in tumor and normal tissue, having normal tissue the lowest absorbance values. The ex-vivo spectral signatures have different absorbance values depending on the clusters obtained in the HS images. This can be related to differences between tissue types in the resected sample, which can involve tumor and the surrounding healthy tissue in some cases. Ex-vivo spectral signatures from Op21C3 and Op21C4 (CL1 (C3) - CL1 (C4) and CL2 (C3) – CL2 (C4) in Figure 3-11.c) are overlapping indicating, in this case, that having a slightly different focus does not affect the spectral signature. However, in Op56C3 and Op56C4 (CL1 (C3) - CL1 (C4) and CL2 (C3) – CL2 (C4) in Figure 3-11.e) the amplitudes are similar but not overlapped, this can be produced due to both images have higher differences in focus than Op21.

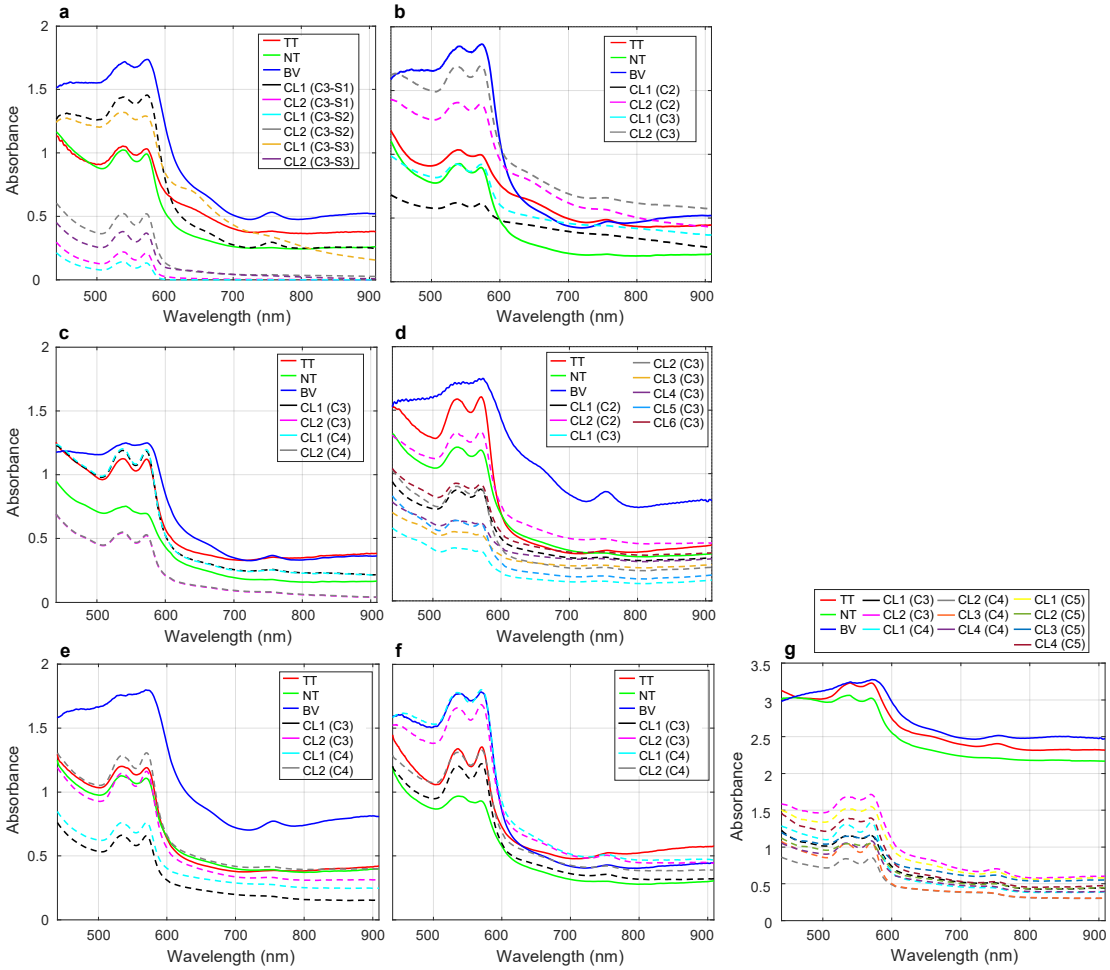

Figure 3-11: Mean spectral signatures of the different classes labelled in the in-vivo samples (solid lines) and the different clusters (dashed lines) obtained from the corresponding resected ex-vivo tissue (from different captures). a) Op08, **b**) Op15, **c**) Op21, **d**) Op50, **e**) Op56, **f**) Op57, and **g**) Op58. TT: Tumor Tissue; NT: Normal Tissue; BV: Blood Vessels; CL#: Cluster; C#: Capture; S#: Segment of capture Op08C3 where there are three pieces of tissue.

3.4.2 Statistical analysis of the R545/R560 spectral ratio between in-vivo and ex-vivo samples

Figure 3-12 shows the boxplots of the R545/R560 spectral ratios obtained in the different tissue types. These results show that, in the in-vivo samples, NT achieved higher ratios followed by TT and BV. Additionally, it can be observed that higher ratio values were obtained in the ex-vivo data respect to the in-vivo data. However, ex-vivo data present high interquartile rages (IQR). Lower values of the R545/R560 spectral ratio involve higher hemoglobin contributions, as the wavelength of 560 nm maximizes the difference between oxyhemoglobin and deoxyhemoglobin. In this sense, it is possible to observe that in the in-vivo samples, as expected, the blood vessel class has the lowest ratio values, while the normal class has the highest. In the case of the tumor class, the ratio values are lower than the normal class due to the hypervascularization produced by the tumor.

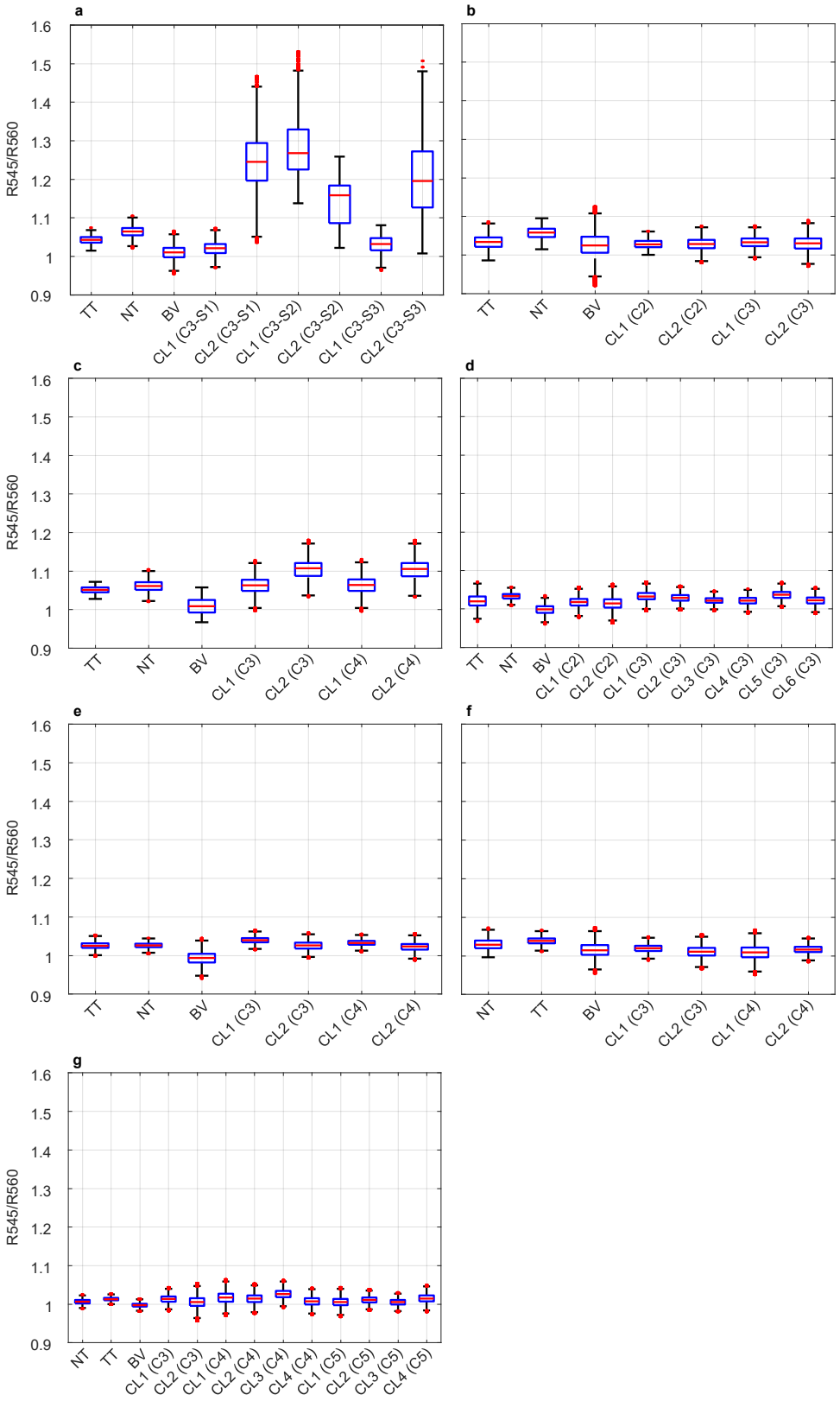

Figure 3-12: Boxplots of the R545/R560 spectral ratios from the different classes labelled in the in-vivo samples and the different clusters obtained from the corresponding resected ex-vivo tissue (from different captures). a) Op08, **b**) Op15, **c**) Op21, **d**) Op50, **e**) Op56, **f**) Op57, and **g**) Op58. TT: Tumor Tissue; NT: Normal Tissue; BV: Blood Vessels; CL#: Cluster; C#: Capture; S#: Segment of capture Op08 where there are three pieces.

3.4.3 In-vivo HbRatio-based heatmaps and vascular enhanced maps

Using the R545/R560 spectral ratios and the first and third quartiles as threshold points, the HbRatio-based heatmaps and vascular enhanced maps were generated as shown in Figure 3-13. A Gaussian smoothing filter was applied to the HbRatio-based heatmaps to reduce the spatial noise in the results. In the vascular enhanced maps, blood vessels were visually, in general, well delimited using such spectral ratios. However, in some cases, background elements were identified as vascular, for example in P15C2 and P57C1. In any case, this background elements can be easily identified by the operating surgeon's naked eye.

3.4.4 Experimental Results Discussion

To the best of our knowledge, the work presented in this section employs, for the first time, a discrimination of different in-vivo human brain tissue structures based on hemoglobin ratios using HSI. The ratio reflects a maximized difference between deoxyhemoglobin and oxyhemoglobin. In addition, HbRatio-based heatmaps and vascular enhanced maps were obtained using the first and third quartiles of R450/R560 spectral ratio. This work analyzes the correlation between ex-vivo and in-vivo samples of human brain tissue that, to the best of our knowledge, has not been carried out in the literature. This correlation was performed after analyzing the optimal cluster values in the ex-vivo samples to extract the spectral signatures.

This work would allow the development of a real-time intraoperative system for enhanced surgical guidance and blood flow monitoring. The system could be based on an HS camera that captures only the spectral bands used to calculate the hemoglobin ratio, reducing the acquisition time and the high computation requirements for processing large number of spectral bands. By reducing the spectral range, the spatial resolution could increase, also improving the definition of the generated maps. In addition, the identification of the blood vessels in the enhanced vascular maps could help to improve the identification of tumor areas during surgical procedures, by reducing the number of classes to be differentiated by a ML classifier. This fact, in addition with the identification of the parenchymal area of the surgical scene could achieve a binary classification between tumor and normal tissue that have been demonstrated to be more precise than a four class-classification [125]. For this reason, future works will involve the use of DL techniques to identify parenchymal areas in the HS images, as well as the use of the proposed enhanced vascular maps to identify blood vessel, allowing a better binary classification of the brain tissue between tumor and normal parenchymal tissue.

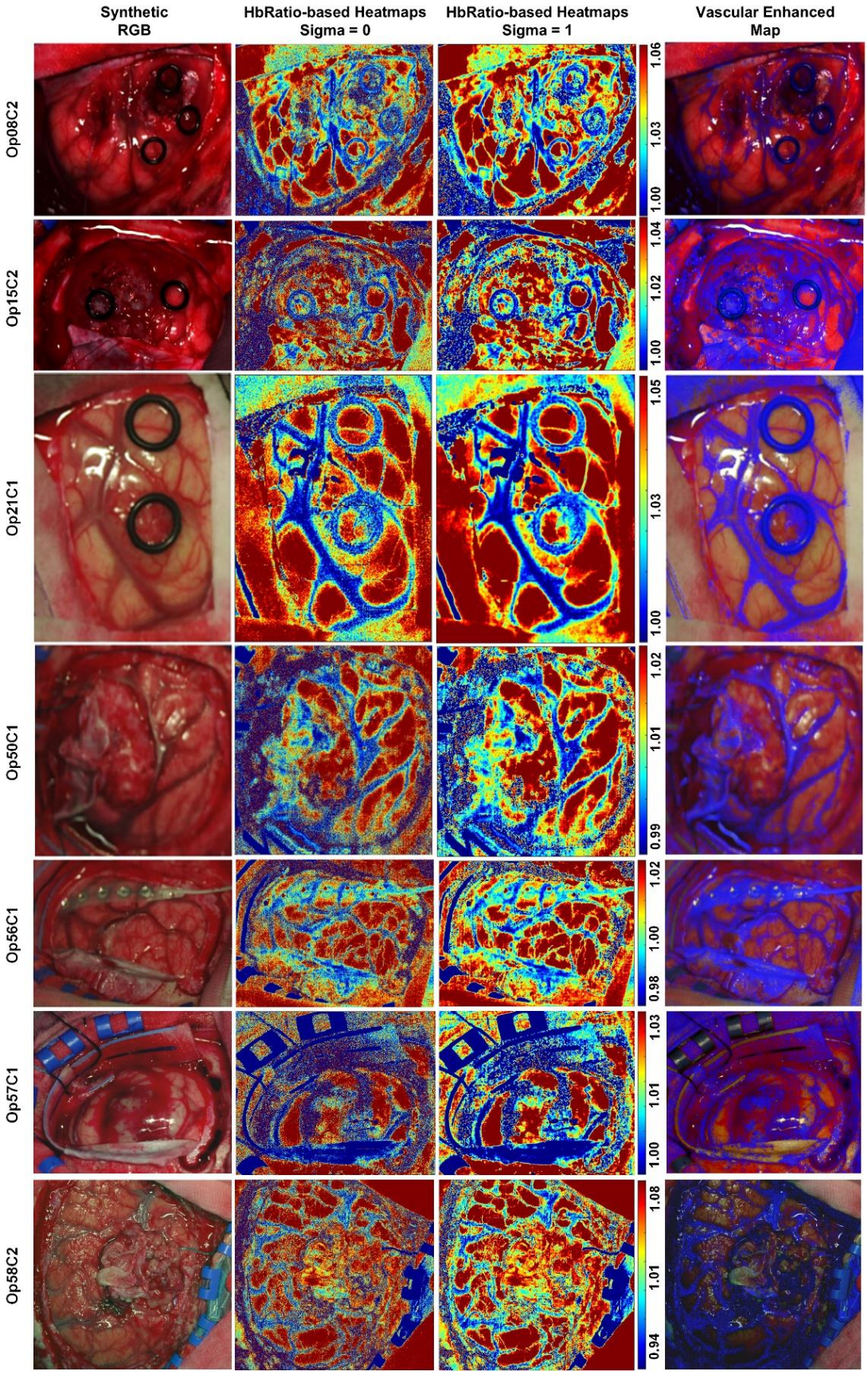

Figure 3-13: HbRatio-based heatmaps and vascular enhanced maps. Synthetic RGB images, HbRatio-based heatmaps (before and after applying Gaussian smoothing filter) and vascular enhanced maps (obtained with first and third quartiles of R545/R560 spectral ratio) from the seven HS in-vivo images from the seven different patients.

3.5 HSI Benchmark for Intraoperative Brain Tumor Detection and Delineation

In this section, we demonstrate with a robust k-fold cross-validation approach that HSI combined with the proposed processing framework is a promising intraoperative tool for in-vivo identification and delineation of brain tumors, including both primary (high-grade - HG and low-grade - LG) and secondary tumors. Using the enhanced in-vivo HS human brain image database, we have analyzed the spectral characteristics of the brain tissue (normal and tumor) and blood vessels, and the different tumor types according to their malignancy grades (G1 to G4) and origin (primary and secondary), performing a statistical analysis between all the medians of each spectral channel when comparing the different classes and tumor grades and origins. Here, we provide a benchmark for further developments in the field of in-vivo brain tumor detection and delineation using hyperspectral imaging to be used as a real-time decision support tool during neurosurgical workflows.

3.5.1 Spectral characterization of brain tissue

To perform the spectral characterization a basic pre-processing was applied to the HS images: calibration, extreme band noise removal, and noise filtering. Statistical differences were found between all the medians of each spectral channel when comparing TT vs NT (Figure 3-14.a) and TT vs BV (Figure 3-14.b) using the Wilcoxon Rank Sum test at 5% of significance level. High standard deviation values were obtained in the spectral signatures due to the interpatient variability and also the different tumor types included in the database. Additionally, the intraoperative HS data acquisition during surgery is a complex procedure that can be affected, in some cases, by the non-flat brain surface. These irregular surfaces can affect the illumination conditions, and, hence, the image focus in certain areas, reducing the reflectance values and increasing the noise of the spectral signature respect to the more focused areas. For this reason, a complete pre-processing chain was applied to the HS data, where each spectral signature was normalized to a minimum of zero and a maximum of one, so that only the shape of the signature was taken into account in the computation of the processing algorithms, avoiding differences due to uneven illumination conditions. Additionally, a decimation process was applied to reduce the dimensionality of the data in the spectral dimension and, hence, the computational cost of the processing algorithms [195].

The mean spectral signatures of TT, NT, BV were converted to absorbance values (Figure 3-15) to be represented and compared with the molar extinction coefficient of oxyhemoglobin and deoxyhemoglobin [196]. Absorbance values of all classes increase between 500 and 600 nm (Figure 3-15.a-c-e), due to the existence of two oxyhemoglobin absorbance peaks (~540 and ~575 nm) and one deoxyhemoglobin absorbance peak (~555 nm) in this spectral range [197]. Particularly, oxyhemoglobin peaks in BV are not detected (Figure 3-15.e), probably because we labelled veins and arteries indistinctly, mixing oxy and deoxyhemoglobin characteristics. Higher absorbance values were found in TT with respect to NT, but lower than BV. Moreover, an absorbance peak was found at ~760 nm (Figure 3-15.b-f) related to deoxyhemoglobin [198], [199]. Our spectral data reveal that the contribution of deoxyhemoglobin is the highest in BV (Figure 3-15.f), having a lower contribution in TT

(Figure 3-15.b). However, this contribution is not found in NT (Figure 3-15.d). This difference between NT and TT could be mainly related to the lack of oxygenation in the brain tissue affected by cancer [200].

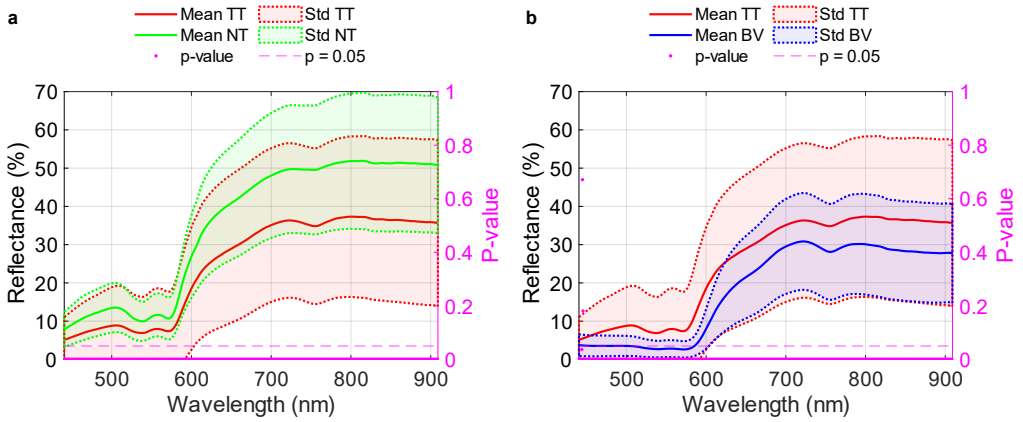

Figure 3-14: Spectral characterization of different brain tissue. Mean and standard deviation (std) of the entire labelled dataset after applying a basic pre-processing (calibration, extreme band noise removal, and noise filtering) and separated by classes, including the corresponding p-value computed for each spectral channel using the Wilcoxon Rank Sum test at 5% of significance level between the two compared classes. **a**) TT vs NT class, **b**) TT vs BV class.

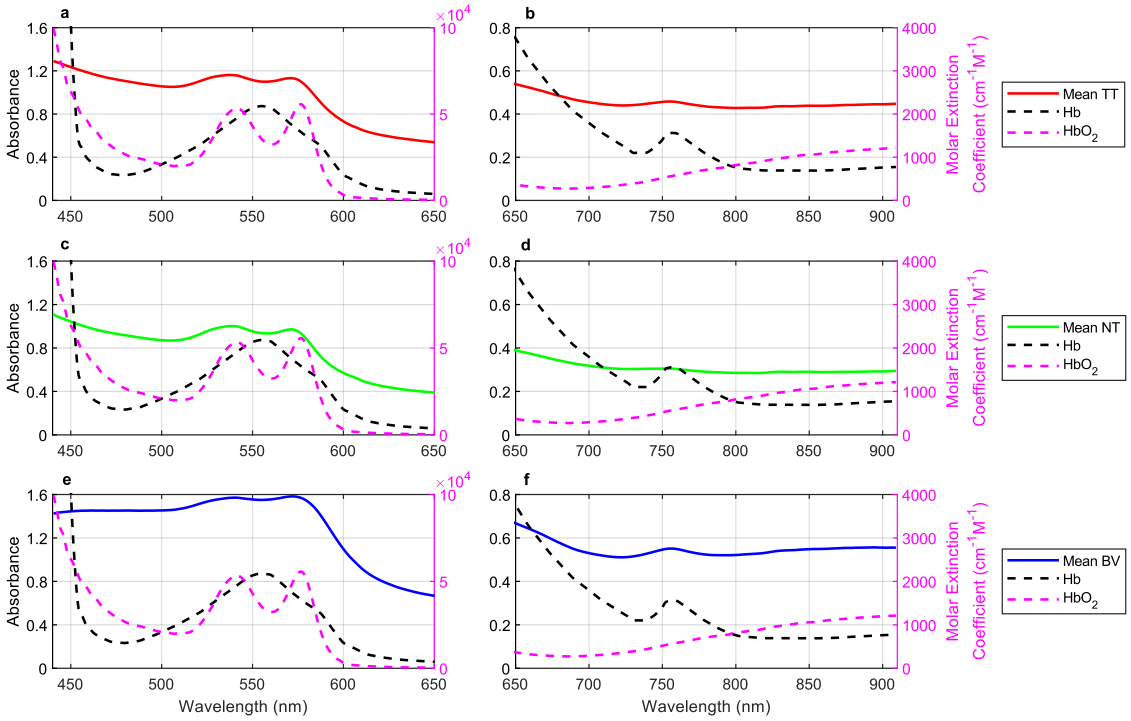

Figure 3-15: Spectral characterization of tumor tissue, normal tissue, and blood vessels classes and their relationship with deoxyhemoglobin (Hb) and oxyhemoglobin (HbO_2). Mean absorbance values of the entire labelled dataset separated by classes (solid) after applying a basic pre-processing (calibration, extreme band noise removal, and noise filtering) and molar extinction spectra (dashed) of Hb and HbO2. **a**) Tumor tissue (TT) between 440 and 650 nm. **b**) TT between 650 and 910 nm. **c**) Normal tissue (NT) between 440 and 650 nm d, NT between 650 and 910 nm. **e**) Blood vessels (BV) between 440 and 650 nm. **f**) BV between 650 and 910 nm.

3.5.2 Spectral characterization of different brain tumor types

As stated in the introduction section, brain tumors can be subdivided into different subtypes depending on their origin (primary/secondary) or the grade of malignity in the case of primary tumors. Regardless of tumor grade and origin, there is an absorbance peak (reflectance valley) around 760 nm (Figure 3-15) related to deoxyhemoglobin [198]. Secondary tumors present lower standard deviation values than primary ones (Figure 3-16.a). However, this fact can be related to the reduced number of patients affected by secondary tumors in our database, and the reduced number of labelled pixels with respect to the primary type. Despite of this, statistical differences between the medians of each spectral channel were found at 440-599, 602-756 and 769-909 nm spectral ranges. HG and LG primary tumors present similar reflectance and standard deviation values (Figure 3-16.b). Nonetheless, statistical differences were found at 466-510, 522-549, 559-572 and 580-909 nm spectral ranges (Figure 3-15.b). Considering the tumor grades of primary tumors, statistical differences were found between the medians of all spectral channels of G1 and G2 tumors (Figure 3-16.c), whereas in the case of G3 and G4 tumors (Figure 3-16.d), only the 440-460, 578-644, 745-764 and 779-909 nm spectral ranges were found to be statistically different.

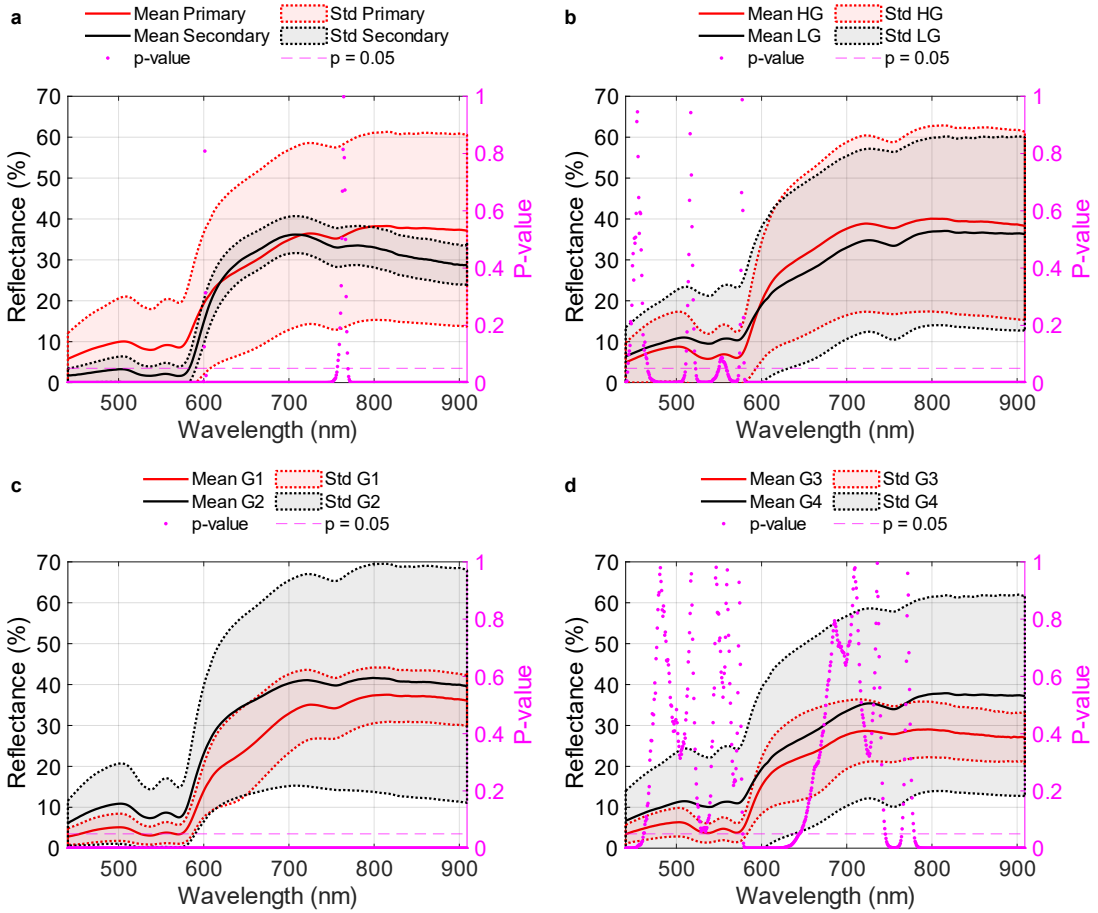

Figure 3-16: Spectral characterization of different tumor types. Mean and standard deviation (std) of the entire labelled dataset after applying a basic pre-processing (calibration, extreme band noise removal, and noise filtering) and separated by classes, including the corresponding p-value computed for each spectral channel using the Wilcoxon Rank Sum test at 5% of significance level between the two compared classes. **a**) Primary vs. secondary tumors. **b**) HG vs. LG primary tumors. **c**) G1 vs. G2 primary tumors. **d**) G3 vs. G4 primary tumors.

3.5.3 Supervised Classification Algorithms

ML algorithms used in this work were based on SVM, RF, and KNN classifiers (Section 2.4.2), while the DL algorithm employed was a two-layer one-dimensional DNN (Section 2.4.2). Moreover, two unmixing-based algorithms were studied (EBEAE and NEBEAE) (Section 2.4.3). Linear and RBF kernels were employed in the case of SVM algorithm and the hyperparameter optimized were cost (C) in both kernel, and gamma (γ) in RBF kernel. The optimization of the RF model was performed by searching for the most appropriate number of trees (T). For the KNN classifier, we employed the Euclidean and Cosine distance metrics and the hyperparameter to be optimized in each case was the number of nearest neighbors (N). The DNN was composed by two hidden layers, followed by a batch normalization layer, using the rectified linear unit as an activation function. The learning rate was established to 0.1, and the network was trained for 300 epochs. The output size (L) of the hidden layers was optimized. This DNN structure was studied in a previous work and compared with a two-dimensional CNN implementation, achieving the DNN the best performance [125]. For the EBEAE and NEBEAE algorithms, the characteristic endmembers were estimated by each algorithm. The estimation process was performed using the labelled pixels from the training set. The representative number of endmembers was two for NT, two for TT, one for BV and three for BG, while the hyperparameter ρ was set to 0.3 for NT, 0.2 for TT, and 0.01 for BG [126]. The endmember of the BV class was obtained by calculating the average of all labelled pixels in that class. In both algorithms the entropy weight (γ) hyperparameter was optimized during the estimation of the complete abundance matrix.

3.5.4 Data Partition and K-Fold Cross-Validation

Due to the high computational cost required to train several of the selected classifiers, a methodology based on the K-Means algorithm was used to reduce the number of pixels in the training set, balancing the classes, avoiding the inclusion of redundant information, and drastically reducing the training execution time [195]. In this approach, K-means clustering is applied independently to each class of labelled pixels in the training set to obtain 100 different clusters ($K = 100$) per class empirically selected (in this work, 400 clusters in total related to the four classes: NT, TT, BV, and BG). Thus, 100 centroids corresponding to a particular class are obtained. To reduce the original training data set, these centroids are used to identify the most representative pixels of each class using the SAM algorithm. For each centroid, only the n most similar pixels are included in the reduced training set. Figure 3-17 shows the block diagram of the proposed training data reduction approach. In this work, three different number of similar pixels were evaluated ($n \in \{10, 20, 40\}$), generating three different training sets composed by 1,000, 2,000, and 4,000 pixels per class (100 centroids × n pixels). The total number of labelled pixels in the HS images from the validation and test sets was used for the quantitative evaluation of the processing framework (Table 3-5). This approach was evaluated in a previous work, where different metrics were compared with respect to the completed training set. The results obtained in such work revealed that the OA did not present a relevant change between using the full and reduced training sets, however, the accuracy of TT class improved by up to ~20% and the execution time when training the classification model was drastically decreased (a speedup of ~48×) when using the reduced training set [195].

Three different training sets were obtained using this methodology composed by 1,000, 2,000, and 4,000 pixels per class. The total number of labelled pixels in the HS images from the validation and test sets was used for the quantitative evaluation.

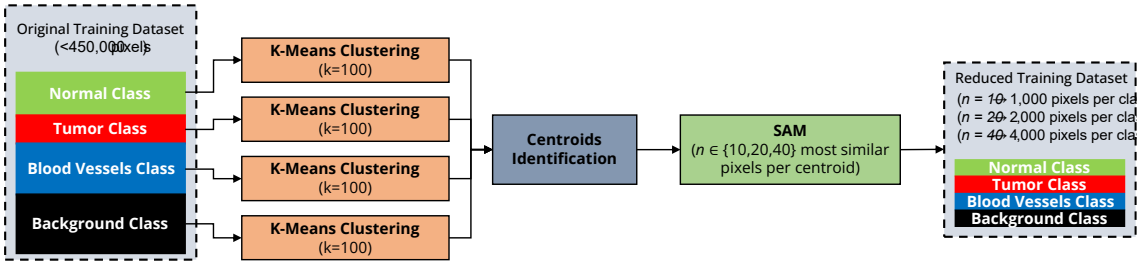

Figure 3-17: Block diagram of the training dataset reduction algorithm that employs K-means and SAM algorithms.

Table 3-5: Summary of the total number of labelled pixels per class and fold divided by training, validation, and test sets.

#Fold	# Labelled Pixels				
	NT	TT	HT	BG	Total
Training Set					
1	179,536	32,006	71,578	316,587	599,707
2	122,166	23,729	48,459	305,504	499,858
3	184,524	20,543	81,757	227,404	514,228
4	231,083	32,143	80,107	332,824	676,157
5	228,518	17,712	70,655	302,677	619,562
Validation Set					
1	39,410	3,555	9,548	43,357	95,870
2	77,240	4,513	28,326	88,002	198,081
3	81,427	8,860	20,533	78,133	188,953
4	48,307	1,979	15,345	45,151	110,782
5	44,229	4,260	17,048	31,033	96,570
Test Set					
1	90,164	1,764	29,713	82,724	204,365
2	109,704	9,083	34,054	49,162	202,003
3	43,159	7,922	8,549	137,131	196,761
4	29,720	3,203	15,387	64,693	113,003
5	36,363	15,353	23,136	108,958	183,810

In contrast to previous works that employed a leave-one-patient-out cross-validation using a reduced database [125], in this study we robustly evaluate the classification performance of the proposed approach by using a three-way data partition performed at patient level, dividing the HS database into *training* (60%), *validation* (20%), and *test* (20%) sets. Additionally, five different folds were created to achieve more robust results due to the limited number of patients. This data partition was performed randomly using the patients' identifiers as instances, where each patient could have more than one HS image (Figure 3-18 and Table 3-6). Labelled data were employed to train the classification models (*training set*), to optimize their hyperparameters (*validation set*), and to quantitatively evaluate the results using unseen HS data (*test set*). The hyperparameter optimization of each algorithm was performed in each fold independently, evaluating the results with their respective validation sets and using the macro F1-Score metric and performing a coarse search. The optimal hyperparameters were selected using the best macro F1-Score result (Section 2.4.4.3) of each fold without considering the BG class.

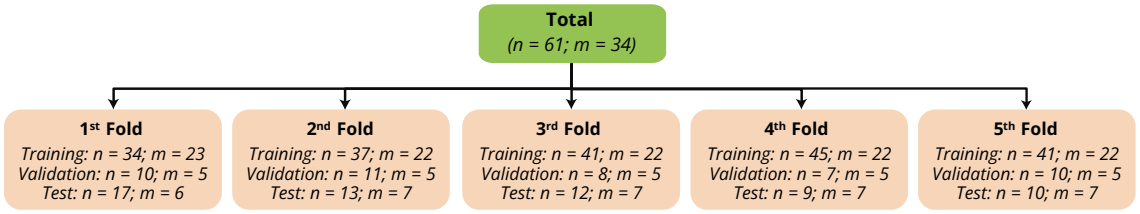

Figure 3-18: Proposed data partition employing the enhanced in-vivo HS human brain image database. The database was split into 5 folds. Each fold contains training, validation, and test sets.

Table 3-6: Data partition detail of the 5 folds, divided into training, validation, and test sets. Different captures from the same patient were included in the same set.

#Fold	Training Patients (#Total Images)	Validation Patients (#Total Images)	Test Patients (#Total Images)
1	Remaining 23 patients (34)	Op4*, Op8, Op22, Op39, Op41 (10)	Op10*, Op16*, Op21, Op37, Op42, Op54* (17)
2	Remaining 22 patients (37)	Op37, O41, Op42, Op50, Op58 (11)	Op4*, Op12, Op17*, Op22, Op38, Op43, Op55 (13)
3	Remaining 22 patients (41)	Op4*, Op36, Op43, Op53, Op57 (8)	Op5*, Op13*, Op18*, Op34, Op39, Op50, Op56 (12)
4	Remaining 22 patients (45)	Op10, Op18, Op36, Op50, Op54 (7)	Op7*, Op14, Op19*, Op35, Op40, Op51*, Op57 (9)
5	Remaining 22 patients (41)	Op10*, Op35, Op37, Op 40, Op50 (10)	Op8, Op15, Op20, Op36, Op41, Op53, Op58 (10)

*indicates patients without tumor samples labelled.

3.5.5 Brain tissue classification based on spectral information.

The enhanced in-vivo HS human brain image database was used to perform classification based on spectral information. The previously presented supervised classification algorithms (Section 3.5.3) were trained using the three training sets and following the previously presented data partition (Section 3.5.4) to achieve this spectral classification capable of distinguishing between the four different classes.

First, three different training sets were evaluated with different number of balanced pixels in each class (1,000, 2,000 and 4,000 pixels per class) as explained before. No statistically significant differences were found between the three training data reductions (Figure 3-19.a). Hence, the use of 1,000 pixels per class allowed to reduce the time required for training the model (particularly for the SVM-based implementations) without compromising the classification performance. For this reason, we selected this training data reduction for the subsequent experiments. Additionally, our results show that statistically significant differences were found between the unmixing-based methods and the ML-based ones, obtaining both the unmixing-based algorithms lower classification performance. The highest median macro F1-Score result was obtained with the SVM-RBF model (78.4±5.1%), but no statistically significant differences were observed between this algorithm and the others (except for EBEAE and NEBEAE). The highest average OA was also reached by the SVM-RBF (91.5±4.7%), but the highest TT sensitivity (65.9±13.1%) was obtained with the Figure 3-19.b. Average specificity results were higher than 90% for the ML and DL-based approaches.

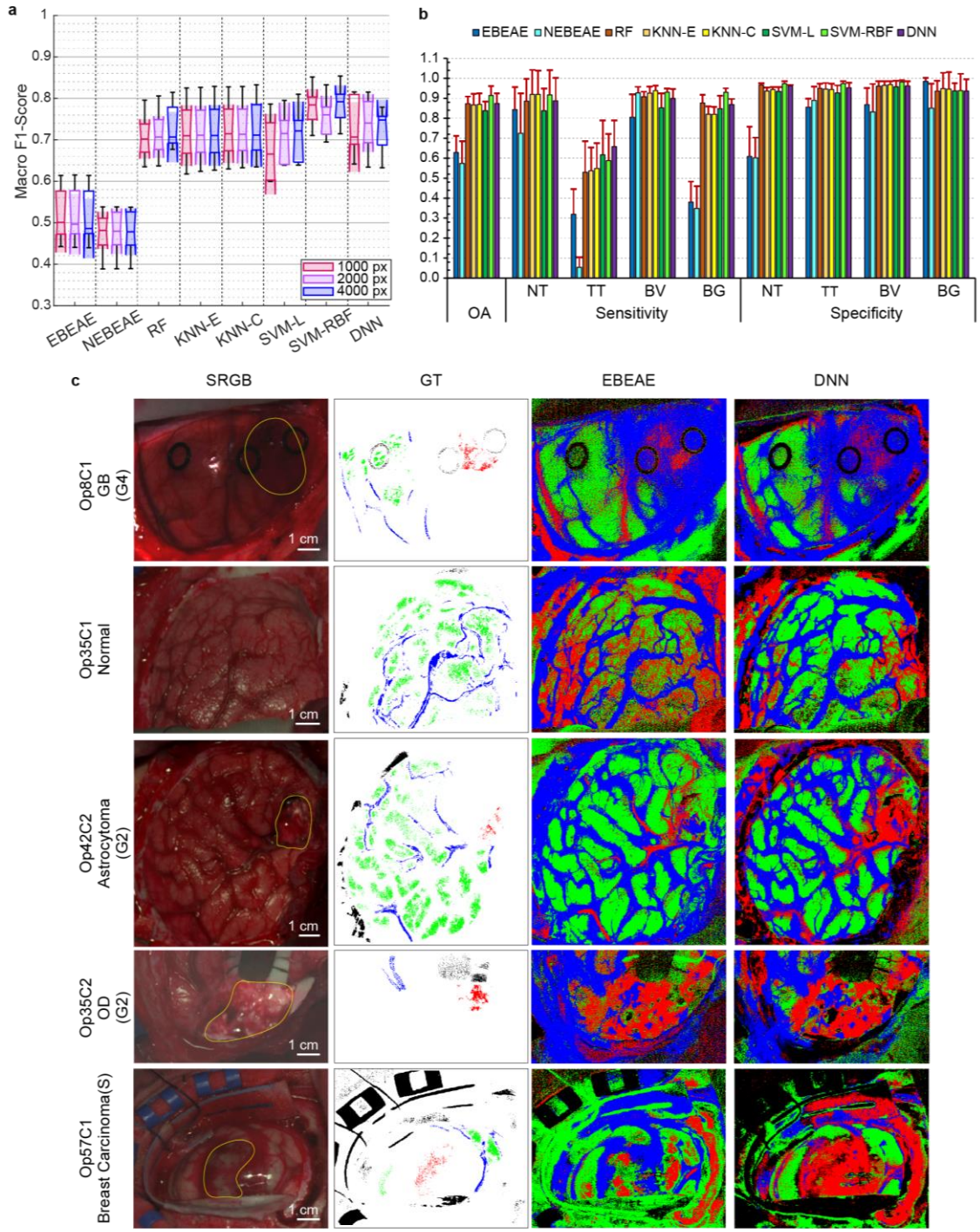

Figure 3-19: Spectral classification results of brain tissue. a) Boxplots of the macro F1-Score results of the validation set for each training data reduction and each classifier, including the five folds using the optimal hyperparameters in each classifier. Two medians are significantly different at the 5% significance level if their intervals (shaded color areas) do not overlap. **b**) Average OA, sensitivity, and specificity results of the validation set from the 5 folds using the data reduction of 1,000 pixels per class. **c**) Examples of synthetic RGB (SRGB) images, ground-truth (GT) maps and supervised classification maps generated using the eight algorithms with the optimal hyperparameters from different tumor types of the validation set. Approximate tumor areas were surrounded in yellow on the SRGB image by the operating surgeon according to the intraoperative neuronavigation and the definitive pathological diagnosis of the resected tissue. Rubber ring markers were employed in some cases (e.g., Op8C1) to indicate the area where the biopsies for pathology were resected. Opx: Operation number; Cy: Capture number.

Qualitative results, extracted from the validation set and obtained after applying the supervised classification model (generated using 1,000 pixels per class and the optimal hyperparameters) to the entire HS image, show the pixel-wise identification of both labelled and non-labelled pixels (Figure 3-19.c). As expected, according to the quantitative results (Figure 3-19.a,b), the unmixing-based methods (EBEAE and NEBEAE) increase the number of false positives and false negatives in the classification maps, particularly in Op35C1 employing EBEAE, where the normal tissue is identified as tumor, and Op57C1 using NEBEAE, where tumor areas are identified as normal tissue. The remaining classifiers achieve more consistent results, although the SVM-based and DNN algorithms improve the identification of the tumor areas in Op42C2 and Op57C1 (only using SVM-L and DNN).

3.5.6 Brain tumor identification and delineation based on spatial-spectral information.

In order to develop this HSI benchmark using the enhanced in-vivo HS brain database, a spatial-spectral approach was employed based on a combination of a dimensionality reduction, a supervised classifier, a spatial filtering, an unsupervised segmentation, and a Majority Voting (MV) algorithm to merge the results from both supervised and unsupervised approaches (Figure 3-20).

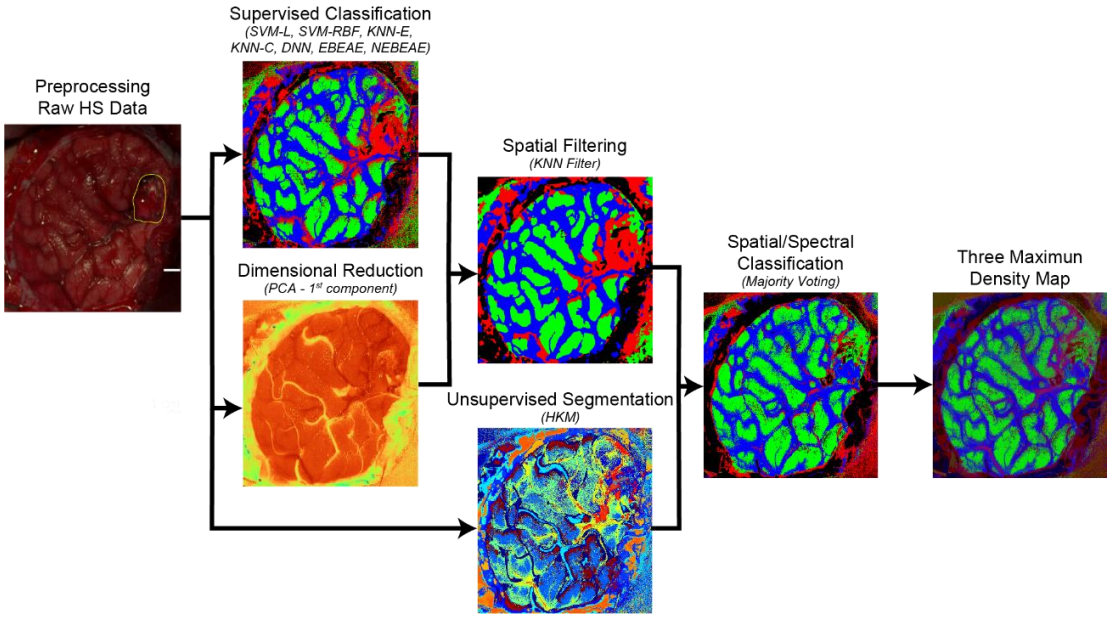

Figure 3-20: Proposed processing framework to generate the density maps for intraoperative pathology-assisted surgery.

This approach has been used in previous works [70], [125] to prove that the use of the spatial information available in the HS images helps to improve the classification results and to reduce the misclassified pixels found in the supervised classification maps created using only the spectral information. In this work, the PCA algorithm was employed for dimensionality reduction [123], obtaining a one-band representation of the pre-processed HS image. The spatial filtering aims to improve the supervised classification including the spatial features. The KNN filtering algorithm was employed using the previously studied parameters ($\lambda = 1$ and $K = 40$) [70] and a window size of 8 rows using the Euclidean distance [201]. The probability maps from the supervised classifier and the one-band representation are the inputs of this algorithm. The K-

means algorithm was used as the unsupervised segmentation method to identify K different clusters into the HS images ($K = 24$ according to a previous work [70]). Finally, the MV algorithm is used to merge the results obtained from the spatial-spectral supervised classification and the unsupervised segmentation, using a color gradient approach to create the Three Maximum Density (TMD) maps [70]. MATLAB® Statistics and Machine Learning Toolbox was employed to implement the K-means, PCA and KNN filtering algorithms.

Following this approach, we have compared the quantitative results of the validation set (Figure 3-21.a) by using only the spectral information (*Spectral*), by applying the KNN filtering to include also the spatial information (*Spatial/Spectral*) and by combining the spatial-spectral supervised classification with an unsupervised segmentation through a MV (*Majority Voting)* approach. Our results reveal that the inclusion of the spatial information increases the median macro F1-Score results (an increment between 0.4 and 7.7%), reducing the standard deviation (an increment between 0.2 and 3.7%), in all algorithms, except for the unmixing-based approaches. However, no statistical differences were found between these results. Additionally, it is worth noticing that the *Majority Voting* results achieved lower median results and increased the standard deviation. Nonetheless, this lower performance could be motivated by the construction of the output classification map in the MV approach, which is obtained by considering only the majority class assigned to each cluster of the unsupervised HKM map. At the *Spatial/Spectral* stage, the SVM-RBF reached the highest average OA (92.3±4.6%), but the DNN obtained the best average TT sensitivity (68.9±14.3%), closely followed by the SVM-L algorithm (67.7±19.3%) (Figure 3-21.b).

The qualitative results of each step of the proposed algorithm have been analyzed, where the supervised map represents, as an example, the classification map generated using only spectral information with the DNN method (Figure 3-21.c). The PCA map represents, in a false color intensity map, the first principal component where the more important information contained in the HS image is relocated in a low dimensional space. For example, in Op8C1, the tumor area is partially highlighted with more intensity values (between the two rubber ring markers on the right of the image). The KNN-Filtered map offers a smoothed version of the supervised map, where the spatial properties of the HS image are used (by combining the information of the probability maps generated by the supervised classifier and the PCA map). This approach reduces the granularity of the supervised map, providing more homogeneous class regions. This *Spatial/Spectral* classification was combined with an unsupervised segmentation (HKM map) that identifies 24 different regions (or clusters) in the HS image according to their similar spectral characteristics, providing a very accurate delineation of different structures but without any identification of the tissue, material, or substance that each cluster represents. For this reason, the information provided by the HKM map was merged with the KNN-Filtered map by means of a MV approach [70], where each cluster is labelled by the majority class within it. In the MV map (Figure 3-21.c), the boundaries between different class regions are determined by the HKM map, while the identification of each cluster class is defined by the KNN-Filtered map. However, in these maps, only the information relative to the class with the majority number of pixels in each cluster is shown. Hence, as a surgical visualization tool, we proposed to combine the information provided by the three maximum probability values (classes NT, TT, and BV) of the MV approach, by mixing the RGB colors in each cluster

according to the percentage of pixels covered by each class in such cluster (i.e., the R channel corresponds to the percentage of TT pixels, the G channel to NT pixels, and the B channel to BV pixels). For example, a cluster represented by a bright red, green or blue color denotes it belongs to only one single class (TT, NT, or BV, respectively). In contrast, any other color represents a combination of classes in a cluster (e.g., purple color represents a mixture between TT and BV classes that commonly happens in certain blood vessels, hypervascularized areas or extravasated blood, see Op42C2, Op35C2 or Op57C1). This resulting map is called TMD map [70] (Figure 3-21.c).

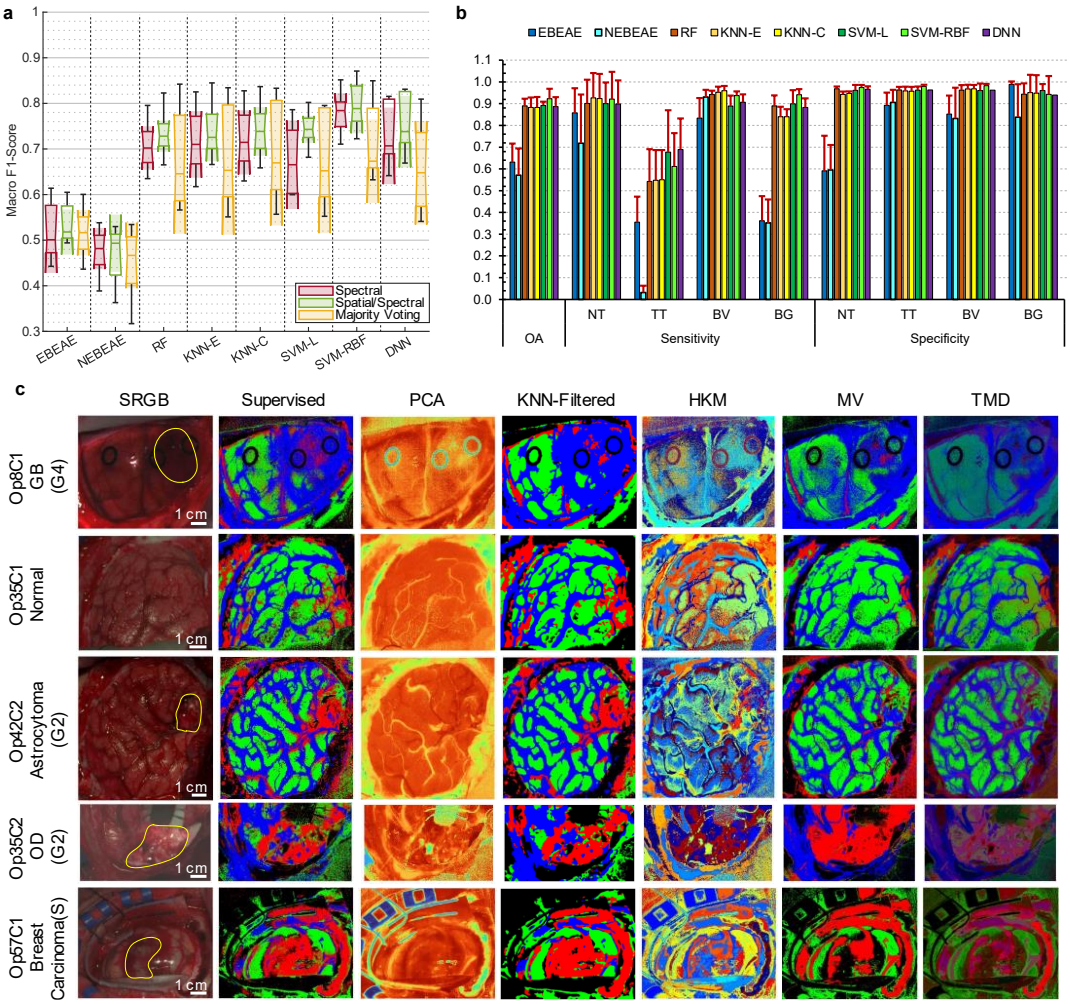

Figure 3-21: Quantitative and qualitative results at the different stages of the proposed framework in the validation set. a) Macro F1-Score of the validation set using the eight different classifiers at the three different stages. Two medians are significantly different at the 5% significance level if their intervals (shaded color areas) do not overlap. **b**) Average OA, sensitivity, and specificity results of the validation set from the 5 folds using the Spatial/Spectral approach. **c**) Example of SRGB images and output maps from different tumor types of the validation set at the different stages of the proposed framework (based on the DNN as supervised algorithm using the optimal hyperparameters).

After performing all the analysis and hyperparameter optimizations of the algorithms using the validation set, the test sets of the different k-folds were evaluated (Figure 3-22.a). Quantitative results of the macro F1-Score metric show, as expected, a performance reduction in the test set of 0.5-1% respect to the validation one, providing the best median score of 70.2±6.3% using the DNN algorithm in the *Spatial/Spectral* approach. Similar average OA results are obtained using SVM-L (86.6±5.5%) and DNN (86.8±3.4%) as supervised classifiers, while a slight increase of the SVM-L average TT sensitivity (57.8±23.7%) respect to the DNN (54.7±21.9%) is obtained (Figure 3-22.b).

Specificity average results are in general higher than 90% in all ML and DL-based approaches for all classes.

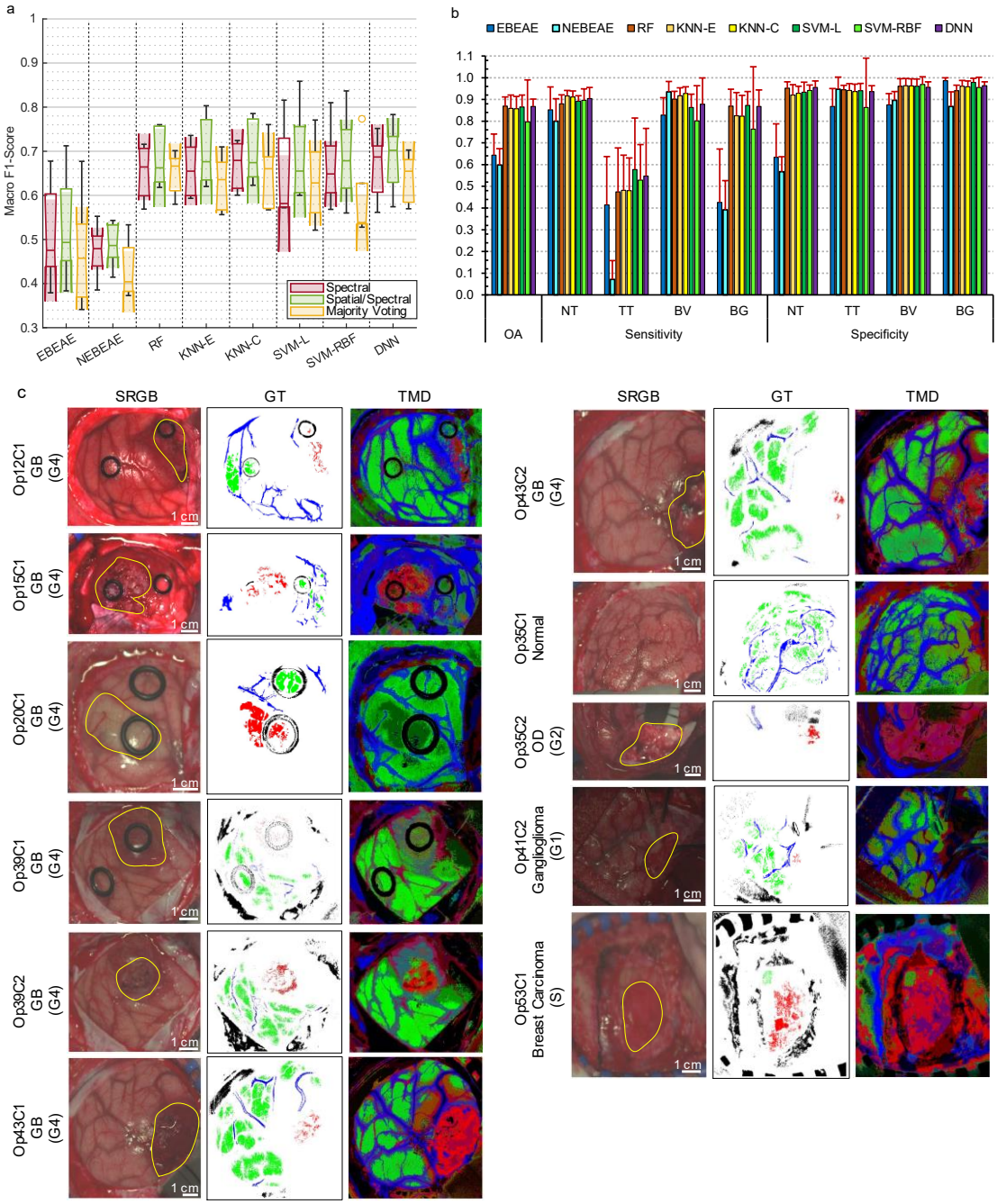

Figure 3-22: Quantitative results at the different stages of the proposed framework and qualitative TMD classification maps in the test set. a) Macro F1-Score of the test set using the eight different classifiers at the three different stages. Two medians are significantly different at the 5% significance level if their intervals (shaded color areas) do not overlap. **b**) Average OA, sensitivity, and specificity results of the test set from the 5 folds using the Spatial/Spectral approach. **c**) Examples of SRGB images, ground-truth maps and TMD maps from different tumor types (based on the DNN as supervised algorithm using the optimal hyperparameters).

Some examples of the TMD maps of the test set (Figure 3-22.c) show that the GB cases (Op12C1, Op15C1, Op39C2, Op43C1, and Op43C2) delineate in red the tumor areas, as expected by neurosurgeons (marked in yellow over the synthetic RGB images). Particularly, Op15C1 presents some decolored red/orange/purple areas that could represent the infiltrative nature of GBM tumors in the surrounding tissue. Moreover,

the surrounding blue areas could be related to the hypervascularized tissue that surrounds the tumor, also including the blood vessels in such regions (Op15C1 in Figure 3-22.c). The same fact can be visualized in Op12C1, Op43C1, and Op43C2. In the case of Op20C1 and Op39C1, the tumor is somehow revealed but not as a red area, since the tumors are located in a deep layer of the brain tissue. Op20C1 has not an additional image captured after the resection started, since the tumor resection in such location of the brain could cause serious damages and side effects to the patient, and, additionally, the tumor boundaries were not clear enough to perform a secure and effective resection. For such reason, the operating surgeon decided not to operate the patient, prevailing the quality of life of the patient over the tumor resection. On the contrary, after Op39C1 was captured, the operating surgeon continued the tumor resection, and a second image (Op39C2) was captured during resection, where it is possible to observe the correct delineation of the tumor area in a bright red color. This was also the case of Op43, but before starting the resection, the tumor was clearly visualized in the brain surface, showing a possible infiltration in the surrounding tissue (orange/purple color in the upper-left part of the tumor area).

Moreover, we qualitatively evaluated some examples of test cases not related to high-grade gliomas (Figure 3-22.c). Firstly, Op35C1 presents a healthy brain surface, since the tumor was in a deep layer, where there are no false positives in the parenchymal area, only those related to extravasated blood surrounding the parenchymal area. In Op35C2 and Op41C2, it is possible to observe that the proposed algorithm can identify not only high-grade tumors but also low-grade tumors, a G2 oligodendroglioma and a G1 ganglioglioma, respectively. Finally, secondary tumors are also detected by the proposed algorithm, as shown in Op35C1 where a metastatic breast carcinoma is identified, although some false positives surrounding the parenchymal area are also presented. These false positives could be produced because of the low quality of the image, where an optimal focus was not achieved.

3.5.7 Experimental Results Discussion

The work presented in this section demonstrates the high potential of HSI for in-vivo identification of brain tumor tissue and its boundaries during neurosurgical operations. Employing enhanced in-vivo HS human brain image database, which include three data acquisition campaigns, of exposed brain surface with respect to previous works [70], [77], [123], [125], [126], we have analyzed the spectral characteristics of the brain tissue (normal and tumor) and blood vessels, and the different tumor types according to their malignancy grades (G1 to G4) and origin (primary and secondary), performing a statistical analysis between all the medians of each spectral channel when comparing the different classes and tumor grades and origins. Moreover, a robust 5-fold cross-validation approach was used to evaluate eight different processing algorithms, first using only spectral information, and then using both spatial and spectral information following a processing framework that we previously developed [70].

The spectral-based classification results obtained using the validation set (Figure 3-19.a) showed that SVM-based and DNN methods provided the best macro F1-Score results, although no statistical differences were found among the other classifiers (except for the unmixing-based methods, which provided less accurate results). The qualitative results (Figure 3-19.c) demonstrate the ability of the proposed HSI-based

system to identify not only high-grade gliomas (Op8C1), but also other low-grade tumors (Op42C2 and Op35C2) and secondary tumors (Op57C1). Moreover, these results show the capability of HSI to accurately highlight the vascularization of the brain surface, being especially remarkable in Op35C1 and Op42C2.

It is worth noticing that HS images captured in suboptimal acquisition conditions, such as a lack of correct focus or illumination, can introduce inappropriate spectral signatures for training the algorithms and can produce inaccurate classification maps. This limitation is particularly evident in deep-layer tumors (Figure 3-23), where it was not possible to correctly focus the entire area of interest by using our pushbroom-based HSI system. In the case of Op37C2 (Figure 3-23.a), due to uncertainty at the time of labelling the tumor pixels in the center of the image, only NT, BV, and BG classes were labelled. The average spectral signatures (Figure 3-23.b) reveal an acquisition problem, possibly related to a lack of proper illumination, as the reflectance values in the three classes decrease dramatically in the infrared range (>700 nm). However, the DNN method seems to overcome this handicap and correctly identify the tumor area even using this non-optimal HS image.

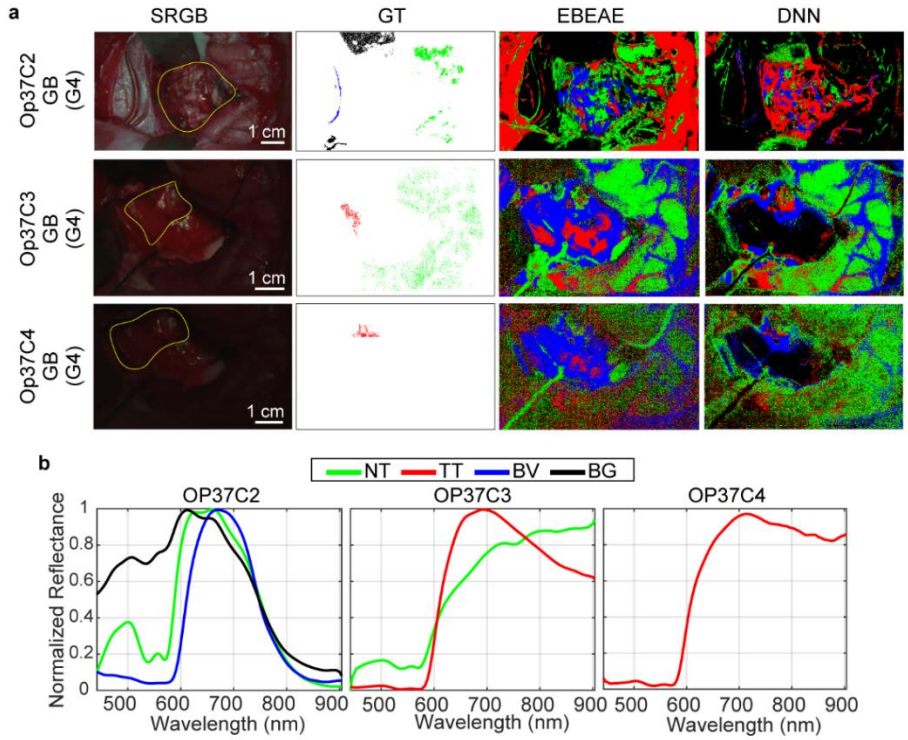

Figure 3-23: Examples of the limitations related to deep-layer tumors. a) Example of synthetic RGB images, ground-truth (GT) maps and supervised classification maps created using the EBEAE and DNN algorithms with the optimal hyperparameters from a deep-layer tumor captured in non-optimal conditions in the validation set. **b**) Average spectral signatures of the GT pixels from (a).

The inclusion of spatial information improved the macro F1-Score medians compared to using only spectral information, although no statistical differences were found between these results (Figure 3-21.a). After performing the hyperparameter optimization process using the validation set, the test data of each k-fold were processed providing both quantitative and qualitative results (Figure 3-22). The processing framework based on the DNN algorithm in the *Spatial/Spectral* approach provided a macro F1-Score of 70.2±7.9%, representing, as expected, a performance reduction of 3.6% respect to the validation results. Qualitative test results demonstrate the ability of the proposed framework to identify not only HG gliomas (e.g., GB), but

also LG and secondary tumors (e.g., G2 oligodendroglioma, G1 ganglioglioma, metastatic breast carcinoma in Figure 3-22.c) and also extra-axial tumors (e.g., G1 meningioma).

The processing of the test dataset allowed us to identify some HS image cases where the data acquisition conditions were not optimal, producing some errors in the classification results (Figure 3-24.a), which may degrade the quantitative results of the test sets. We found that in Op55C1 and Op55C2 the classification results identified most of the pixels as tumor, and only some parts related to background (Figure 3-24.a). After evaluating the spectral signatures of the labelled pixels in such HS images, we found some differences in the infrared region (from 700 to 900 nm) with respect to the other images. This unusual behavior was found also in Op56C2, where there is a decrease in the reflectance values of the labelled spectral signatures in the same infrared region (Figure 3-24.b), also producing wrong classification results where the parenchymal area is identified as background (Figure 3-24.b). The low sensitivity of the HS sensor in this spectral range, coupled with a possible misalignment of the light beam with the lens (due to an improper focusing), could lead to this decrease in reflectance.

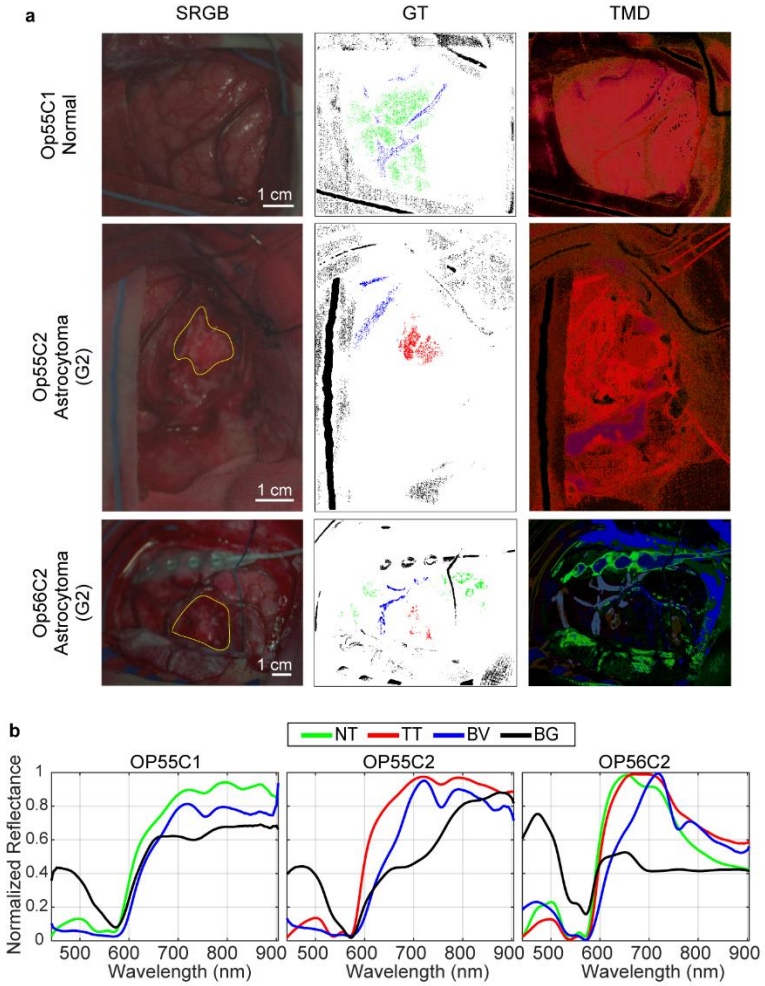

Figure 3-24: Examples of the limitations of the proposed framework after processing the test set. a) Example of SRGB images, ground-truth (GT) maps and TMD maps (based on the DNN algorithm) from HS images captured in non-optimal conditions in the test set. **b**) Average spectral signatures of the GT pixels from (a).

Despite these limitations, we have demonstrated with a robust classification validation approach, the potential benefits of HSI for brain tumor tissue identification, targeting a diagnostic support system for guiding neurosurgical interventions in real-time. In previous works, we demonstrated that it is possible to achieve near real-time HS data processing using graphical processing units, achieving processing times of ~6 s [202]. The proposed intraoperative HSI-based acquisition system must be optimized in further works by reducing the HS camera size, employing a snapshot-based HSI technology (which is able to capture the entire HS cube in a single shoot, providing also real-time performance) and integrating it into a surgical microscope. This new experimental setup will guarantee an improvement of the HS image quality to solve the focus problems, especially for deep-layer tumors. Additionally, an extensive clinical validation of the proposed framework must be carried out, employing a large number of patients and a multi-center trial. This clinical validation will perform a comprehensive pathological analysis of the entire tumor area outlined by the TMD map (especially in the boundaries between tumor and the surrounding normal tissue), as well as correlate the results with the MRI information to verify that the system can adequately identify tumor infiltration into normal brain tissue, especially in HG gliomas. Additionally, the relation between the improvement of the patient outcomes and the use of the proposed system during the surgery could be studied through the clinical validation.

3.5.7.1 Comparison with previous related works in HSI

Different previously published works used the first data campaign from the in-vivo HS brain database employed in this work. Different frameworks were employed using supervised and unsupervised machine learning methods to perform a classification and also different methodology were used as intra-patient or inter-patient. In [70] the spatial/spectral framework (Section 3.5.6) achieved an overall accuracy of 99.7% using 5 HS images from 5 patients an intra-patient methodology, which commonly provides unrealistic optimistic results. Later, the work was tested using the complete first data campaign (36 HS images from 22 patients), but only a qualitative analysis of the results was performed [123]. A DL approach was proposed to identify glioblastoma tumors obtaining an OA of 80% following an inter-patient approach using 26 HS images from 16 patients. In [203] was employed EBEAE with 26 HS images from 16 patients, where only 6 HS images contained tumor tissue pixels labelled, achieving an OA of 76.1% using a leave-one-patient-out cross-validation methodology. Later in [77], NEBEAE approach was tested performing an intra-patient validation process using 2 HS images from different patients. An OA of 97.9% was achieved, providing again unrealistic results that cannot be employed in a real-world scenario. Finally using the same database, in [127] it is proposed a method to use the spectral and spatial information to identify glioblastoma, achieving an OA of 96.6% for four-class classification and OA of 96.3% for glioblastoma identification adopting a leave-one-patient-out cross validation technique using 7 HS images from 5 patients.

Using the system presented in [129] and using 13 HS images from 12 patient, SVM model achieved a OA result of 60.0% using an intra-patient approach. Using the same HS database, a comparison between non-optimized models and optimized models was performed using an intra-patient approach with 10 HS images from 9 patients [130]. The study showed that the RF results did not provide significant improvement when the model was optimized with any of the three optimization methods. However, the optimized SVM model improved the tumor identification. In [131], the classification

results obtained from the HS images were overlapped with the RGB point cloud captured by the LiDAR camera and presented in an augmented reality visualization.

In the field of surgical microscopes combined with HS cameras, in [204] a proof of concept was performed with a single HS image using an RF classifier to discriminate different tissues using a 5-fold stratified cross-validation methodology and achieving an overall accuracy of 99.1%, again providing unrealistic results to be extrapolated in real-world scenarios. In [132], as a proof of concept, two HS images of in-vivo glioma tumors were labelled and used to train and test different ML algorithms, achieving the best OA of 98.3% and an accuracy to identify the glioma class of 97.7% using the light gradient boosting machine algorithm. Finally, in [134] different algorithms were used (RF, SVM, and DNN), obtaining an OA of 92.0% using an intra-patient methodology from 18 HS images from 5 patients.

Table 3-7 summarize and compare the current studies found in the literature which employs HSI for in-vivo brain tumor detection. In particular, a significant number of studies are based on small datasets and focus primarily on the identification of high-grade tumors. Moreover, these studies are developed to utilize an intra-patient framework. In contrast, our work uses an extensive and diverse database that includes the four tumor grades and different tumor types, both primary and secondary. The use of this database and the validation framework based on an inter-patient approach and a three-way data partition (*training*, *validation,* and *test*) combined with a 5-fold cross-validation approach, allow us to obtain robust results mitigating the risk of overfitting commonly caused by AI-based algorithms.

Table 3-7: Summary of the studies which employs HSI for in-vivo brain tumor detection.

Ref.	Yr.	HSI System	Wav. (nm)	#B	#P	#I	TG	PV	Validation Methodology	OA (%)	Tumor ACC (%)
[70]	2018	Pushbroom	400-1,000	826	5	5	4	Intra-patient	10-fold CV	99.7	99.5
[123]	2018	Pushbroom	400-1,000	826	26	43	1, 2, 3, & 4	Inter-patient	Training/test (85%/15%)	n/a	n/a
[125]	2019	Pushbroom	400-1,000	826	16	26	4	Inter-patient	LOPO-CV	80.0	42.0
[126]	2020	Pushbroom	400-1,000	826	16	26	4	Inter-patient	LOPO-CV	76.1	n/a
[127]	2021	Pushbroom	400-1,000	826	5	7	4	Inter-patient	LOPO-CV	96.6	96.3
[128]	2021	Pushbroom - Surgical Microscope	500-1,000	100	1	1	3	Intra-patient	Training/test (80%/20%) + 5-fold CV	99.1	n/a
[129]	2021	Snapshot	655-975	25	12	13	3 & 4	Intra-patient	Training/test (80%/20%) +5-fold CV	60.1	73.0
[77]	2022	Pushbroom	400-1,000	826	2	2	4	Intra-patient	n/a	97.7	n/a
[130]	2022	Snapshot	655-975	25	9	10	3 & 4	Intra-patient	Training/test (80%/20%)	n/a (AUC=98.6%)	n/a
[131]	2023	Snapshot	655-975	25	12	13	3 & 4	Intra-patient	Training/test (80%/20%)	n/a (AUC=95.2%)	n/a (AUC=95.1%)
[132]	2023	Snapshot - Surgical Microscope	500-900	n/a	1	2	1 & 3	Intra-patient	Training/test (75%/25%)	98.3	97.7
[134]	2023	Snapscan - Surgical Microscope	470-780	104	5	18	1 & 2	Intra-patient	Training/test (70%/30%)	92.0	n/a
This work	2023	Pushbroom	400-1,000	826	34	61	1, 2, 3, & 4	Inter-patient	3-way data partition (60%/20%/20%) + 5-fold CV	86.8±3.4	57.8±23.7

ACC: Accuracy; **AUC**: Area Under the Curve; **B**: Band; **CV**: Cross-validation; **I**: Image; **LOPO**: Leave-one-patient-out; **n/a**: Not Available; **OA**: Overall accuracy; **P**: Patient; **PV**: Patient Variability; **Ref.**: reference; **TG**: Tumor Grade; **Wav.**: Wavelength; **Yr.**: year.

3.6 VNIR-NIR Hyperspectral Imaging Fusion targeting Intraoperative Brain Cancer Detection

As stated in Section 2.3, HS cameras generally use CCD or CMOS sensors to cover the spectral range between 400 and 1000 nm (VNIR), while InGaAs and MCT sensors are used to cover the range from 900 to 1700 nm (NIR) and 900 to 2500 nm (SWIR), respectively [2]. Thus, to obtain a broadband spectral range image, more than one HS sensor is required, involving image registration and fusion algorithms to generate a combined HS image.

On the one hand, image fusion techniques are used in many applications to merge information from different sensors with the goal of improving the classification or segmentation results [205]. Usually this image fusion procedure is performed using MS images, which have high-spectral but low-spatial resolution, combined with panchromatic images, which have high-spatial but low-spectral resolution, to obtain a new fused image with high-spatial and high-spectral resolution [206]. Spectral fusion is applied to combine the spectral information from different sensors aiming to obtain an HS image with a broadband spectral range. This approach has been employed to identify geographical origins of herbal medicines [207] or to identify metallic alloys from the recycling industry [208].

On the other hand, image registration techniques have the goal to match two or more images of the same scene obtained by using different sensors or devices. The image registration is a necessary step to correctly perform the image fusion. Image registration methods can be classified into two groups: intensity-based and features-based techniques [209]. The former uses the intensity values of the image to find similarities between the images in the scene to perform the registration. This technique is widely used to register Computerized Tomography (CT), MRI with PET images, among other imaging modalities for computer-aided diagnosis, e.g. in brain tumor detection [210], [211]. The latter uses the morphological structures presented in the image to extract points, lines, curves, etc. to find similar features in the images and perform the image registration. There are different feature detectors and extractors, including Scale Invariant Feature Transform (SIFT) [212], Features From Accelerated Segment Test (FAST) [213] or Harris detector [214]. All these methods have been widely used in the literature due to they are robust and automatic feature extraction algorithms [215]. Features-based technique have been used in fusion information from different sensors or image mosaic technology [216], [217].

The proposed method is composed by two main stages: 1) VNIR-NIR spatial registration; 2) VNIR-NIR spectral fusion (Figure 3-25). In the first stage, the VNIR and NIR raw images are pre-processed applying image calibration to avoid the influence of environmental illumination, noise filtering and band removing to reduce the noise in the spectral signatures due to the camera sensor performance (especially in the extreme bands). After that, the NIR image is upsampled to reach the VNIR pixel size, allowing to perform the image registration using a transformation model previously generated. In this transformation the fixed image is the VNIR, and the moving image is the NIR. When both VNIR and NIR images are registered, both images are cropped to obtain the same coincident ROI. Finally, in the last stage, the spectra

from both VNIR and NIR images are combined, applying a reflectance offset to the NIR spectrum, to perform the spectral fusion and generate a single HS image.

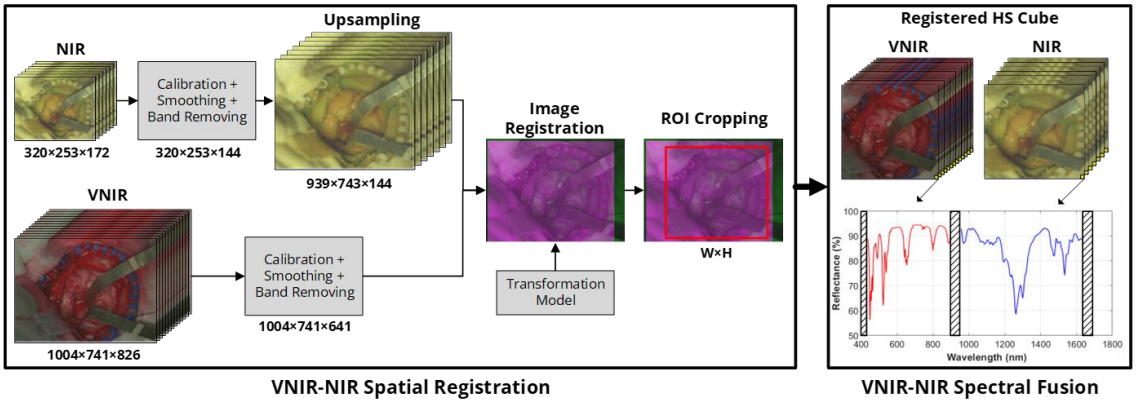

Figure 3-25: Block diagram of the proposed processing framework based on VNIR-NIR spatial registration combined with spectral fusion. NIR: Near-Infrared; VNIR: Visual and Near-Infrared; ROI: Region of Interest; W: Width; H: Height; HS: Hyperspectral.

3.6.1 VNIR-NIR fusion reference image database

Different HSI datasets were collected using the demonstrator described in Section 3.2 to develop and validate the proposed VNIR-NIR fusion method. Three different datasets were acquired (Figure 3-26).

- The HSI registration dataset was composed by seven HS images obtained from four different spatial patterns, i.e., a shooting target and patterns based on brain morphological structures (Figure 3-26.a).

- The HSI spectral reference dataset (Figure 3-26.b) was composed by six HS images obtained from three different Spectralon White Diffuse Reflectance Standards (Labsphere Inc., North Sutton, US) with a reflectance value of 99%, where two consecutive captures were obtained from each white reference. In addition, an HS image from a Zenith Polymer Reflectance Standard (SphereOptics GmbH, Germany), composed by rare earth oxides, was captured (SR4 in Figure 3-26.b).

- The HSI plastic dataset (Figure 3-26.c) was composed by different samples of 3D printing filament, as Polylactic Acid (PLA), Acrylonitrile Butadiene Styrene (ABS), and Polyethylene Terephthalate Glycol (PETG). Using the Ultimaker 3 Extended (Utrecht, Netherlands) 3D printer, several 32×32×4.8 mm square samples were printed to create the HSI plastic dataset. In addition to the three different materials, different colors were also printed. At the end, twenty HS images from sixteen different plastic samples were obtained.

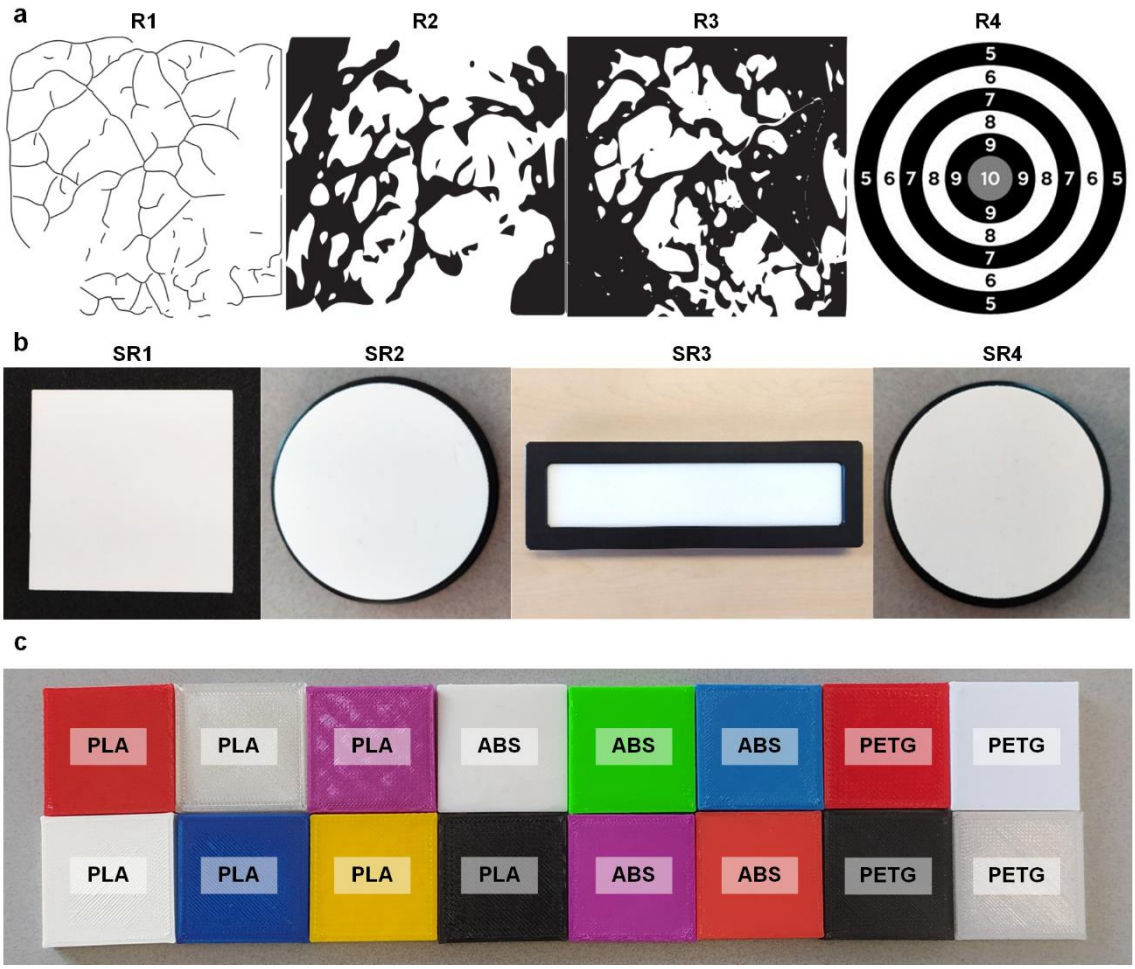

Figure 3-26: HS datasets used in this research. a) Patterns based on brain morphological structures and a shooting target employed to generate the HSI registration dataset (seven HS images) used to evaluate the image registration techniques. **b**) Three different 99% Spectralon White Diffuse Reflectance Standards and a Zenith Polymer Reflectance Standard used to obtain the HSI spectral reference dataset (seven HS images) employed to evaluate the proposed spectral fusion approach. **c**) Sixteen square plastic samples of different colors and three materials: polylactic acid (PLA), acrylonitrile butadiene styrene (ABS), and polyethylene terephthalate glycol (PETG). These samples were employed to generate the HSI plastic dataset (twenty HS images), which was used to evaluate the fusion performance qualitatively and quantitatively.

The HSI plastic dataset was partitioned into training (four HS images), validation (three HS images) and test (thirteen HS images) sets. Additionally, the dataset was organized into three groups for addressing different classification and segmentation problems: color, material, and material-color. Then, each sample was labelled in different classes corresponding to each problem type. The labelled pixels were divided into training, validation, and test set. The training set was reduced using a methodology based on K-Means explained in Section 3.5.4. The goal of this methodology is to reduce the number of pixels in each class, avoiding the inclusion of redundant information, and drastically reducing the training execution time. The K-means was applied to each class of the twenty-seven classes contained in the dataset, obtaining a total of 1,000 pixels per class, reducing the total number of pixels from 2,631,192 to 27,000 (Table 3-8).

Table 3-8: Number of pixels labeled from the HSI plastic dataset in training, validation, and test sets divided into color, material, and material-color. Original training sets contain all pixels labeled before applied data reduction. Reduced training sets contain the pixels used to train the supervised classifier.

Problem	Class Name	#Original Pixels Training	#Reduced Pixels Training	#Pixels Validation	#Pixels Test
Color	Red	163,510	1,000	159,608	480,283
	Yellow	53,782	1,000	51,544	52,172
	Black	113,084	1,000	109,323	280,492
	Magenta	108,124	1,000	106,648	216,632
	Blue	111,145	1,000	109,319	219,221
	Transparent	110,026	1,000	109,660	167,104
	White	164,366	1,000	161,605	486,471
	Green	53,027	1,000	52,404	52,497
Material	PLA	384,966	1,000	378,996	764,847
	ABS	271,182	1,000	266,150	644,241
	PETG	220,916	1,000	214,965	545,784
Material-Color	PLA Red	55,173	1,000	54,195	161,662
	PLA Yellow	53,782	1,000	51,544	52,172
	PLA Black	56,216	1,000	54,422	112,548
	PLA Magenta	54,555	1,000	53,859	108,786
	PLA Blue	56,858	1,000	55,757	111,534
	PLA Transparent	54,502	1,000	55,804	55,645
	PLA White	53,880	1,000	53,415	162,500
	ABS Red	54,801	1,000	52,926	159,378
	ABS Magenta	53,569	1,000	52,789	107,846
	ABS Blue	54,287	1,000	53,562	107,687
	ABS White	55,498	1,000	54,469	216,833
	ABS Green	53,027	1,000	52,404	52,497
	PETG Red	53,536	1,000	52,487	159,243
	PETG Black	56,868	1,000	54,901	167,944
	PETG Transparent	55,524	1,000	53,856	111,459
	PETG White	54,988	1,000	53,721	107,138

ABS: Acrylonitrile Butadiene Styrene; **PLA**: Polylactic Acid; **PETG**: Polyethylene Terephthalate Glycol.

3.6.1.1 VNIR-NIR Spatial Registration Approach

Before performing the VNIR-NIR spatial registration, the HS images were pre-processed to facilitate the registration procedure. After that, intensity-based and feature-based techniques were analyzed in order to obtain the best transformation model using the intraoperative HS acquisition system.

3.6.1.2 NIR pre-processing

Due to both HS cameras have different spatial resolutions, it was necessary to resample one of the two HS images to be able to register them. The VNIR camera covered the spectral range between 400 and 1000 nm and can capture 1,004 spatial pixels with a pixel pitch of 7.4 μm, while the NIR camera captured information within the 900-1700 nm spectral range, with 320 spatial pixels and a pixel pitch of 30 μm. The lens used in VNIR camera was a Xenoplan 1.4 (Schneider Optics, Hauppauge, NY,

USA) with a focal length of 23 mm and a working distance of ~42 cm. In the case of the NIR camera, the lens used was a Kowa LM25HC-SW 1.4 (Kowa Optimed Deutschland GmbH, Düsseldorf, Germany) with 25 mm of focal length and a working distance of ~33 cm.

Upsampling and downsampling methods were evaluated to achieve the same spatial resolutions in both HS images. To exploit the higher VNIR spatial resolution for a later visualization and manual labeling of the images with high detail in the targeting application (intraoperative HS brain cancer detection), the downsampling method, where the VNIR spatial resolution is reduced to reach the NIR resolution, was discarded. In this targeted application, to generate a labelled dataset, the brain images must be manually labeled, identifying the different classes (tumor, normal and hypervascularized tissue). The high VNIR spatial resolution and the possibility of generating a RGB image allows neurosurgeons to visualize the different brain regions and identify the relevant pixels to be labeled using a semi-automatic labeling tool developed to this end [124]. However, the low spatial resolution in the NIR camera was not enough for performing a reliable labeling of the brain surface. For this reason, the spatial resolution of the NIR image was upsampled until reaching the VNIR pixel size.

The scale factor to perform the spatial resampling is specified by the relation between the Instantaneous Field of View (IFOV) of both cameras. The IFOV is calculated employing the parameters of each camera following Eq. (27), achieving an IFOV value of 0.402 and 0.137 nm for the NIR and VNIR cameras, respectively. Hence, a scale factor of 2.93 was obtained following Eq. (28). This scale factor remains the same independently of the sample type, as long as the HS acquisition system does not suffer any modification. Hence, the HS images have a fixed width and height in both HS cameras with a fixed working distance of ~33 and ~42 cm in NIR and VNIR cameras, respectively. However, if there is any modification in the system, such as different HS cameras, lenses, distance between the HS cameras or the working distance, the scale factor must be recalculated with the new parameters.

$$IFOV\ (mm) = \frac{Pixel\ Pitch \cdot Working\ Distance}{Focal\ Length} \tag{27}$$

$$Scale\ Factor\ (\%) = \frac{IFOV_{NIR}}{IFOV_{VNIR}} \tag{28}$$

The upsampling algorithm used to increase the NIR spatial resolution (from 320×253 to 939×743 pixels using a scale factor of 2.93) and to estimate the upsampled spectral signatures is based on a bilinear interpolation, considering the nearest 2-by-2 neighborhood of a certain pixel. Nearest-neighbor, bilinear, and bicubic interpolation methods were evaluated in terms of execution time and spectral similarity. This evaluation was performed using the Zenith Polymer Reflectance Standard.

First, the execution time was evaluated performing the interpolation of the entire HS image. This measure was calculated by taking the average one thousand consecutive executions. Next, the quality of the interpolated spectral signatures was analyzed using the SAM algorithm. To conduct this evaluation, the mean spectral signature of a region of 15×15 pixels was selected from the reference image (original HS image without interpolation) and was compared to the corresponding region of the interpolated image, which consisted of 45×45 pixels.

Table 3-9 shows the SAM results obtained with each interpolation method and the corresponding execution times. It can be observed that the nearest-neighbor interpolation offered the lowest execution time, followed by the bilinear and bicubic methods. In addition, all methods obtain very low SAM values, suggesting that there are no relevant differences between the methods. This can be observed in Figure 3-27, where the three methods are compared respect to the original.

Table 3-9: Spectral Angle Mapper (SAM) and execution time results of different interpolation methods for the evaluation. The SAM algorithm was computed using the mean spectral signature of a region of 15×15 before and after the interpolation using Zenith Polymer Reflectance Standard. The execution time was computed by interpolating the original HS image (320×253).

	Nearest-neighbor		Bilinear		Bicubic	
	SAM	**Time (ms)**	**SAM**	**Time (ms)**	**SAM**	**Time (ms)**
Polymer	4.91E-04	330.97	2.87E-04	424.41	3.02E-04	425.82

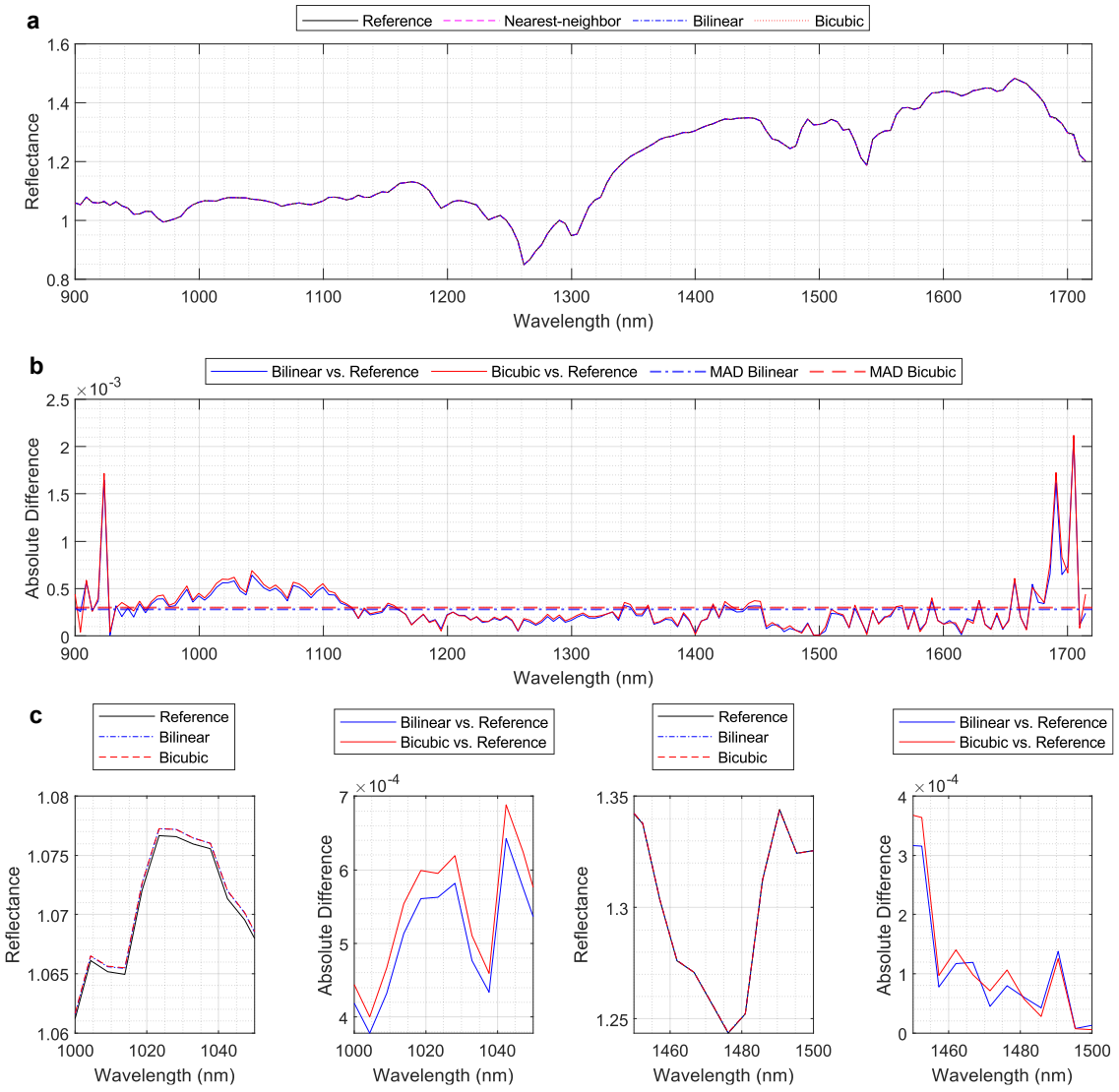

Figure 3-27: Comparison of interpolation methods. a) Mean spectral signature before (reference) and after interpolation using nearest-neighbor, bilinear, and bicubic methods. **b)** Absolute differences between the bilinear and bicubic interpolation methods and the reference, along with the mean absolute difference (MAD) for each comparison. **c)** Two different spectral regions, including reflectance values and absolute differences, to observe similarities.

Figure 3-27.a shows the mean spectral signature before and after the interpolation, where it is possible to observe that all spectral signatures are practically overlapped. However, to observe the small differences between the reference and the interpolated spectral signatures, the absolute difference was computed (excluding the nearest-neighbor interpolation due to its lower spectral similarity performance). Figure 3-27.b represents high differences in the extreme bands due to the low response of the sensor. Figure 3-27.c shows two different spectral regions in detail, including reflectance values and absolute differences, to observe in detail such similarities. It is possible to notice that the bilinear interpolation slightly improves the results compared to bicubic interpolation. This could be motivated due to the bicubic interpolation oversmoothes the spectral signatures in the HS image, while the bilinear interpolation better preserves the original shape. For these reasons, the subsequent experiments employed bilinear interpolation due to its spectral similarity and convenient execution time.

3.6.1.3 Spatial Registration

Intensity-based and feature-based techniques were employed for registering the VNIR and NIR images. MATLAB® Image Processing Toolbox and Computer Vision Toolbox (The MathWorks Inc., Natick, MA, USA) was employed to implement the registration algorithms.

On the one hand, intensity-based techniques find the maximum (or minimum) intensity value and correlate it with the intensity value of the reference image to transform the misaligned image. To obtain the maximum (or minimum) intensity value an iterative process is performed, where the parameters of the transformation model are modified in each iteration. An evolutionary optimizer was used to find the best geometric transformation model. The intensity value was measured applying Mattes Mutual Information (MMI) [218]. The geometric transform types evaluated in this technique were: 1) Translation transformations, where each pixel is displaced the same amount in the same direction, but the size and orientation are not modified; 2) Similarity transformations, which preserve shape, but not size, including isotropic scaling, rotation, and translation; and 3) Affine transformations, which include all similarity transformations and also preserve parallel lines.

On the other hand, feature-based techniques detect and extract interest points, curves, or surfaces present in both images without consider the image intensity. The number of common features detected in both images must be enough to perform the registration, determining the quality results [219]. The feature-based techniques are composed by several steps: 1) Feature detection and extraction, where regions, lines, and curves are detected using feature detectors and subsequently extracted using feature extractors; 2) Feature matching, where all possible matching points between both images are found using an exhaustive matching method computing the pair-wise distances between features; 3) Geometric transform estimation, where different transformation types can be used (similarity, affine or projective). The projective transformation includes all affine transformations and also supports tilting. The matching pair are used to estimate the transformation matrix and the M-estimator SAmple Consensus (MSAC) algorithm is used to exclude outlier points [220]. This algorithm has a randomized nature and can offers different results in consecutive executions. Two feature detectors and extractors were evaluated: Speeded Up Robust Features (SURF) [221] and Maximally Stable Extremal Regions (MSER) [222]. SURF is

a fast algorithm based on the Hessian-Matrix to find the keypoints. SURF has been used to detect skin features to track patient position in navigated spinal surgery [223]. On the contrary, MSER algorithm is a shape-based method that detects regions using image intensity. Regions where the intensity values do not change are considered maximally stable. MSER has been used in the literature as shape detector in medical applications to segment cells [224]. Also, SURF and MSER algorithms were selected as they are robust to changes in scale and rotation.

The VNIR-NIR spatial registration was evaluated computing the SSIM, the MI, and the PCC metrics (Section 2.4.4.2). To evaluate the performance of the different registration techniques and geometric transformations, a gray-scale image was generated from a pseudo-RGB image of both VNIR and NIR HS cubes for performing the registration. After selecting the registration techniques and geometric transformations, the transformation matrix was obtained comparing a pair of VNIR and NIR spectral bands. The pseudo-RGB images were generated selecting three bands which correspond with red, green, and blue colors in the VNIR range and other three bands for creating a false-color RGB in the NIR range. The wavelengths selected for VNIR pseudo-RGB image were 708.97 nm (red), 539.44 nm (green), and 479.06 nm (blue). The wavelengths selected for NIR pseudo-RGB image were 1094.89 nm (red), 1247.44 nm (green), and 1595.45 nm (blue). These wavelengths were selected to maintain the compatibility with the original software (Hyperspec III software, Headwall Photonics Inc., Fitchburg, MA, USA) provided by the camera manufacturer. Additionally, these wavelengths have been employed in previous works for generating the NIR pseudo-RGB image [123]).

First, a preliminary analysis using the *HSI registration dataset* was performed using the gray-scale images from the pseudo-RGB images. In the case of intensity-based techniques, translation, similarity, and affine transformations were applied. In the case of feature-based techniques using MSER and SURF detectors, the transformations employed were affine, similarity and projective. Due to the randomized nature of MSAC algorithm, in the feature-based technique, one thousand consecutive executions were performed to estimate the geometric transformation. Figure 3-28 shows the results applying the three registration metrics. Feature-based technique using SURF detector offered the best registration. The results obtained using affine and projective transformations were quite similar. This is produced due to the projective transformation performs the same geometric transform (scaling, shear, rotation, and translation) than the affine transformation, in addition to apply tilt to the transformation. These results outperform the feature-based technique using MSER and also the intensity-based technique.

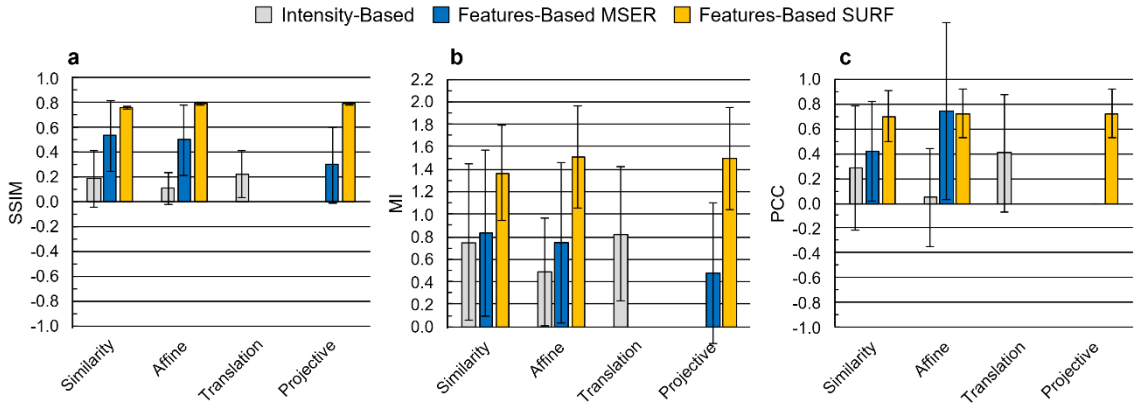

Figure 3-28: Average image registration results. Gray-scale representation of the pseudo-RGB images from HSI registration dataset were used applying intensity-based techniques with similarity, affine, and translation transformations and featured-based using Maximally Stable Extremal Regions (MSER) and Speeded Up Robust Features (SURF) detector and similarity, affine and projective transformation. **a**) Structural Similarity Index Measure (SSIM); **b**) Mutual Information (MI); **c**) Pearson's Correlation Coefficient (PCC) values.

Figure 3-29.a shows two example results of the *HSI registration dataset*, R2C2 and R4C1. The first column shows the registration result without applying any geometric transformation, while the remaining columns show the best results obtained with each registration technique and the best geometric transformation. These images present an overlay of the VNIR and NIR pseudo-RGB images using green-magenta false-color images. Magenta and green pixels indicate misregistration between the VNIR and NIR images, respectively. The areas with gray-scale pixels indicate areas where the two registered images have similar intensity values. Using the translation transformation in the intensity-based registration, R2C2 is incorrectly registered, while R4C1 improves the registration respect to the result without applying any transformation. These incorrect registrations can be produced due to the random noise that can be found in some spectral bands, affecting to the maximum intensity. The feature-based MSER technique using similarity transformation improves the intensity-based technique but some misregistered pixels can be observed in both images. Finally, the feature-based SURF technique with projective transformation offered the best results. For this reason, this method was selected to be applied in the subsequent experiments.

A coarse-to-fine search was performed using gray-scale images from a single spectral band extracted from both cameras to identify the VNIR and NIR bands, which offer the best registration performance. To reduce the high computational time, the coarse search was performed using steps of seven and three bands in the VNIR and NIR images, respectively, to diminish the number of combinations. Figure 3-29.b shows the R2C2 and R4C1 heatmaps resulting from the coarse search using SSIM, MI and PCC metrics. It can be observed that in all metrics the lower and higher bands for each camera do not offer a correct registration mainly due to the low performance of the sensor in such bands. The MI and PCC metrics indicate all band combinations in the central region offer similar results. In opposite, SSIM metric indicates that regions of 500-700 nm and 950-1500 nm in the VNIR and NIR ranges, respectively, achieve the highest results. This is caused because the SSIM metric takes into account the image structure while the other metrics only consider the image intensity. For this reason, to select the optimal spectral bands in the coarse-to-fine search only the SSIM metric was employed. The fine search was performed within the previously selected regions using steps of one band for both cameras.

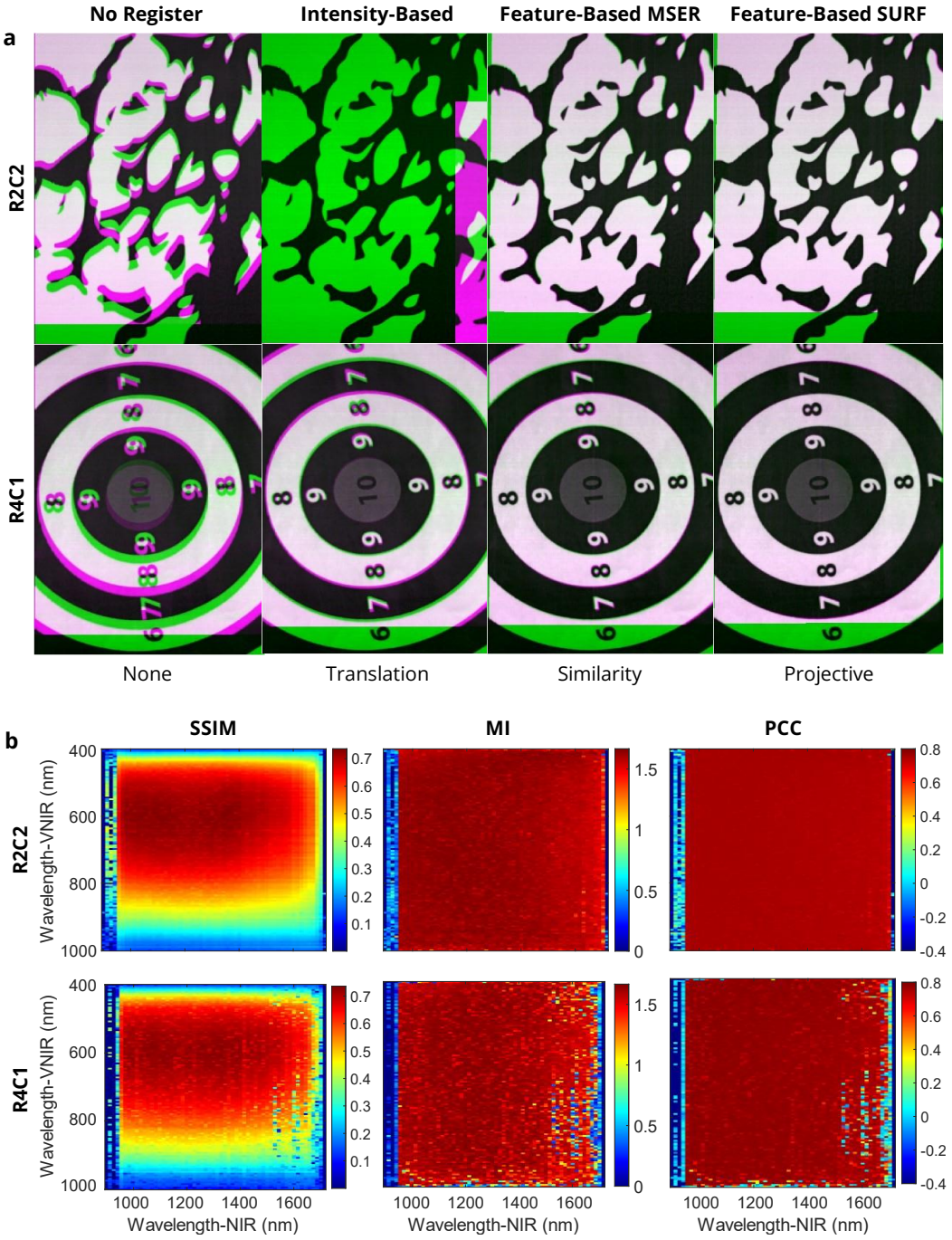

Figure 3-29: VNIR-NIR Spatial Registration using the HSI registration dataset. a) Two registration result examples applying different registration techniques. Both images are overlapped using green-magenta false-color, VNIR (green) and NIR (magenta). First column shows the default registration without applying any type of transformation to the data. Second, third and fourth columns show the results of the intensity-based, feature-based with MSER, and feature-based with SURF techniques, respectively, using the best transformation method. **b**) Coarse search results of the structural similarity index measure (SSIM), the mutual information (MI), and the Pearson's correlation coefficient (PCC) for identifying the suitable spectral bands for the registration using the feature-based SURF technique with projective transformation.

Figure 3-30.a shows the SSIM results using the optimal band combination and summarizes the bands/wavelengths employed. One thousand consecutive executions were performed using the best band combination of each VNIR-NIR HS image pair to obtain the transformation with the highest SSIM value. Finally, the best transformation model was selected after applying each projective transformation to all the images from

the *HSI registration dataset*. Figure 3-30.b shows the SSIM boxplot results for each transformation model, where an average SSIM value of ~0.78 was obtained for all models. The R2C1 model was selected as it presented the lowest IQR. No statistically significant differences were found across the mean SSIM values between R2C1 and R2C2 (which has the higher mean value), using a paired, two-tailed Student's T-test at the 5% significance level.

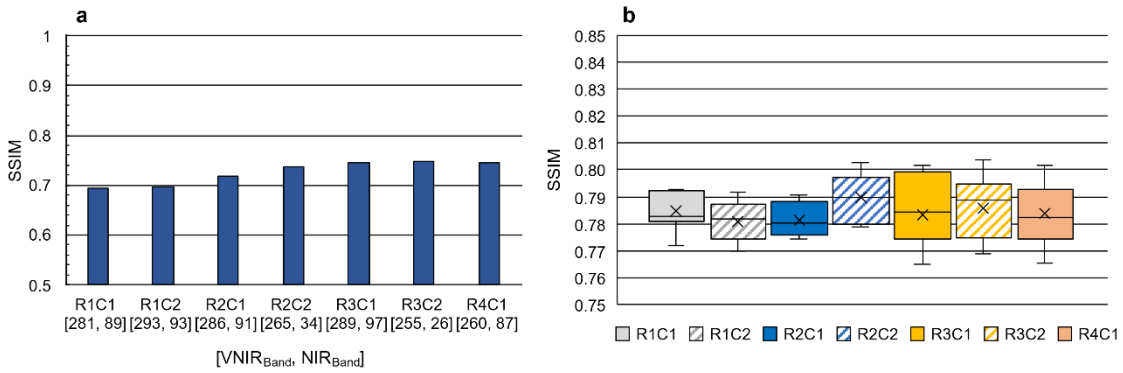

Figure 3-30: Structural Similarity Index Measure (SSIM) results. a) SSIM values using the best spectral band for each HS image from the HSI registration dataset. The relation between the band number and the wavelength in the VNIR is the following: 281=604.20 nm; 293=612.93 nm; 286=607.84 nm; 265=592.56 nm; 289=610.02 nm; 255=585.28 nm; 260=588.92 nm; and in the NIR is the following: 89=1318.95 nm; 93=1338.02 nm; 91=1328.48 nm; 34=1056.76 nm; 97=1357.09 nm; 26=1018.62 nm; 87=1309.42 nm. **b**) SSIM results using the seven different transformation models obtained using the optimal spectral bands for each image pair. The box boundaries represent the IQR (Interquartile Range) of the results. Central bars and error bars depict median and minimum/maximum values of SSIM, respectively.

3.6.2 VNIR-NIR Spectral Fusion Approach

The final step of the proposed framework (Figure 3-25) aims to combine the spectra from the registered NIR and VNIR HS images into a single HS image. First, a spectral analysis of the data generated in both HS images was performed to evaluate the optimal spectral cutoff points where the HS sensors present low performance (i.e., low signal-to-noise ratios). For this purpose, the *HSI spectral reference dataset* was employed to evaluate which bands should be removed before performing the spectral fusion.

Both HS cameras have a common spectral range between 900 and 1000 nm (Figure 3-31.a). However, performing a spectral fusion based on the use of this common spectral region is not suitable in this case due to the low performance of the VNIR sensor in those bands. As shown in Figure 3-31.b, this method causes the NIR region of the fused spectral signature to have a higher standard deviation than the VNIR region when capturing a calibration polymer. Hence, a spectral analysis was performed computing the absolute relative difference percentage (RD) metric using the image pairs of each image in the *HSI spectral reference dataset* for both VNIR and NIR cameras. Figure 3-31.c and d show the RD_{mean} values for each wavelength in the VNIR and NIR spectral signatures of a white reference (SR1), respectively. The RD_{mean} represents the average RD value of all pixels in the image at a certain wavelength. In the case of the VNIR data (Figure 3-31.c), the RD_{mean} is higher than the average from 400 to 435 nm and from 800 to 1000 nm. In the case of the NIR data (Figure 3-31.d), the RD_{mean} values obtained in the ranges 900-960 nm and 1619-1700 nm are higher than the average. These ranges are represented in the figures using the vertical red dashed lines. The $Average\ RD_{mean}$ value was used to establish the initial

and final cutoff point for the selection of the operating bandwidth in each image of the *HSI spectral reference dataset*.

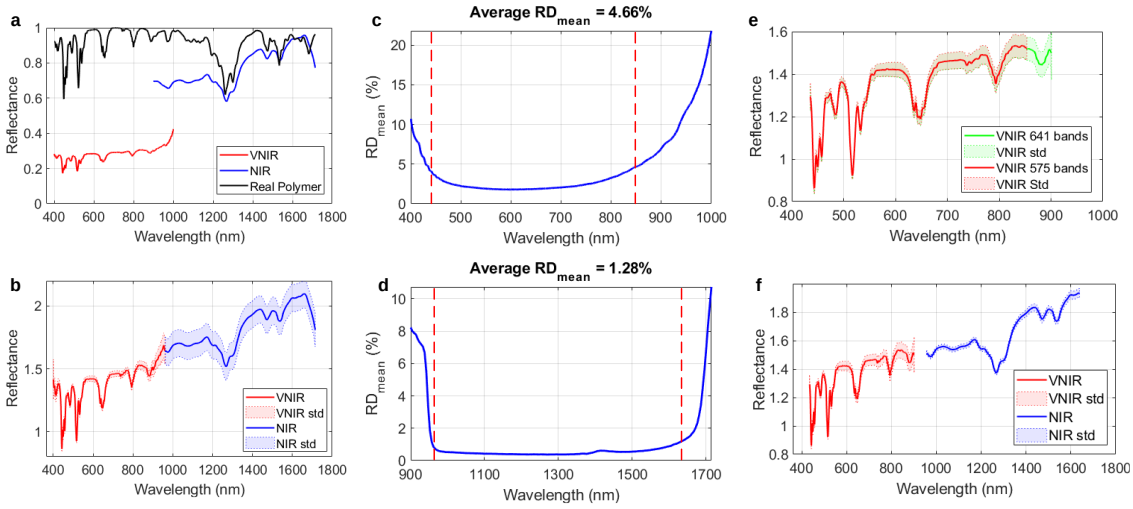

Figure 3-31: VNIR–NIR spectral fusion. a) Manufactured certified spectral signature of the Zenith Polymer® and spectral signatures captured by the VNIR and NIR cameras. **b**) Fused spectral signature using a common spectral band in the overlapped spectral region between VNIR and NIR data. **c**, **d**) Average absolute relative difference percentage (RD) results of SR1 using VNIR and NIR data. Red dashed lines represent the initial and final cutoff points for voiding the low performance of the HS sensors. **e**) Comparison between the mean and std of the Zenith Polymer® VNIR spectral signature with 641 spectral bands (green) and 575 spectral bands (red). **f**) Fused spectral signature of the Zenith Polymer® after applying the proposed VNIR-NIR spectral fusion method.

Employing the *HSI spectral reference dataset* the initial cutoff points in the NIR data are the same in the three cases ($\lambda = 956.6 \pm 0\ nm$), while in the VNIR data there are quite similar values around $\lambda = 435.2 \pm 0.4\ nm$. Considering the final cutoff point, the NIR data values are close to $\lambda = 1632.0 \pm 11.0\ nm$, while the VNIR data values are close to $\lambda = 849.6 \pm 3.3\ nm$. In the VNIR case, the final cut off point involves the removal of ~200 spectral bands. With the purpose of reducing the number of bands to be removed, an additional analysis was performed using three image pairs from the *HSI plastic dataset*.

In this case, the initial cutoff point does not coincide in two of three VNIR image pairs respect to the *HSI spectral reference dataset*, providing an average point of $\lambda = 496.5 \pm 70.1\ nm$. This is produced mainly due to the spectral contributions of the plastic color (red and magenta). Considering the final cutoff point in the VNIR data, the average value is higher with respect to the *HSI spectral reference dataset* ($\lambda = 896.0 \pm 14.7\ nm$). In the case of the NIR data, the initial and final cutoff points are similar to the previous ones, $\lambda = 959.8 \pm 2.8\ nm$ and $\lambda = 1{,}638.4 \pm 9.5\ nm$, respectively. At this point, a qualitative assessment of the VNIR cutoff points was performed by plotting the mean and standard deviation (std) of the spectral signatures of the Zenith Polymer® reflectance standard.

Figure 3-31.e shows that the std values between 849 and 900 nm (green) are quite similar to the previous spectral bands (red). For this reason, the selected cutoff points for the VNIR data were 435 and 901 nm, having 641 spectral bands, while the NIR data covered a spectral range between 956 and 1,638 nm formed by 144 spectral bands. Finally, the VNIR-NIR spectral fusion was performed applying a reflectance offset to the NIR spectrum in order to adjust the reflectance values of both spectral signatures.

The fused spectral signature has a gap between 901 and 956 nm (Figure 3-31.f), in order to preserve the original standard deviation of the NIR spectrum.

Then, a reflectance offset was applied to the NIR spectrum with the goal of adjusting the reflectance values of both spectral signatures with respect to a reference. This procedure requires the use of the NIR image ($N \in \mathbb{R}^P \times \mathbb{R}^B$) and the VNIR image ($V \in \mathbb{R}^P \times \mathbb{R}^B$) of the captured scene, as well as the certified spectral signature provided by the manufacturer of the Zenith Polymer Reflectance Standard ($P \in \mathbb{R}^B$). B represents the number of spectral bands in each HS image and P the number of pixels of the corresponding HS image. The procedure is as follows. First, the difference in the reflectance levels in the Zenith Polymer (P_{Offset}) is computed following Eq. (29), where the value corresponding with the first spectral band of the NIR image ($\lambda_{NIR} = 956\,nm$) is $P(\lambda_{NIR})$ and the value corresponding with the last spectral band of the VNIR image ($\lambda_{VNIR} = 901\,nm$) is $P(\lambda_{VNIR})$. The manufacturer provided the certified data in percentage format. Figure 3-32.a shows a graphical representation of this first step.

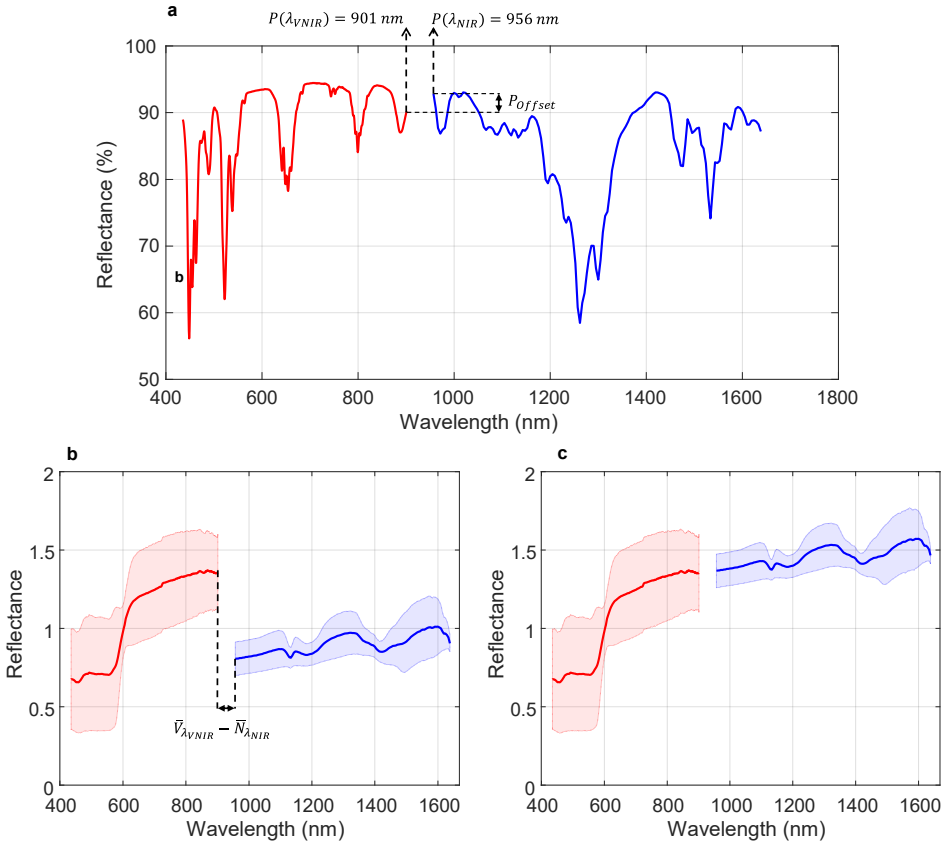

Figure 3-32: Proposed VNIR-NIR spectral fusion explanation using, as example, one sample of the *HSI plastic dataset*. **a**) Zenith Polymer Reflectance Standard spectrum provided by the manufacturer representing the P_{Offset} constant used to perform the spectral fusion. **b**) Average and standard deviation of the spectral signatures extracted from the plastic sample before applying the reflectance offset adjustment to the NIR data. **c**) Average and standard deviation of the spectral signatures extracted from the plastic sample after applying the reflectance offset adjustment to the NIR data.

Next, the average value of all pixels in the last band of the VNIR image ($\bar{V}_{\lambda_{VNIR}}$) and the first band of the NIR image ($\bar{N}_{\lambda_{NIR}}$) are computed as expressed in Eq. (30-31). The difference of these two values (Figure 3-32.b) is employed to obtain the reflectance offset value (F_{Offset}) for the captured scene following Eq. (32). Finally, this offset is

applied to each pixel of the NIR image from the captured scene independently, resulting in the fused spectra as show in Figure 3-32.c.

$$P_{Offset}(\%) = P(\lambda_{NIR}) - P(\lambda_{VNIR}) \quad (29)$$

$$\bar{V}_{\lambda_{VNIR}} = \sum_{i=1}^{P} \frac{V(i,\lambda_{VNIR})}{P} \quad (30)$$

$$\bar{N}_{\lambda_{NIR}} = \sum_{i=1}^{P} \frac{N(i,\lambda_{NIR})}{P} \quad (31)$$

$$F_{Offset} = \left(\bar{V}_{\lambda_{VNIR}} - \bar{N}_{\lambda_{NIR}}\right) \cdot (P_{Offset} + 1) \quad (32)$$

Finally, the spectral signatures are normalized using min-max normalization in the [0,1] range (Eq. (4) in Section 2.4.1) to homogenize reflectance levels in each pixel of the HS image for the subsequent segmentation and classification analyses. Figure 3-33 shows the average spectral signatures of the *HSI plastic dataset* after performing the VNIR-NIR spectral fusion.

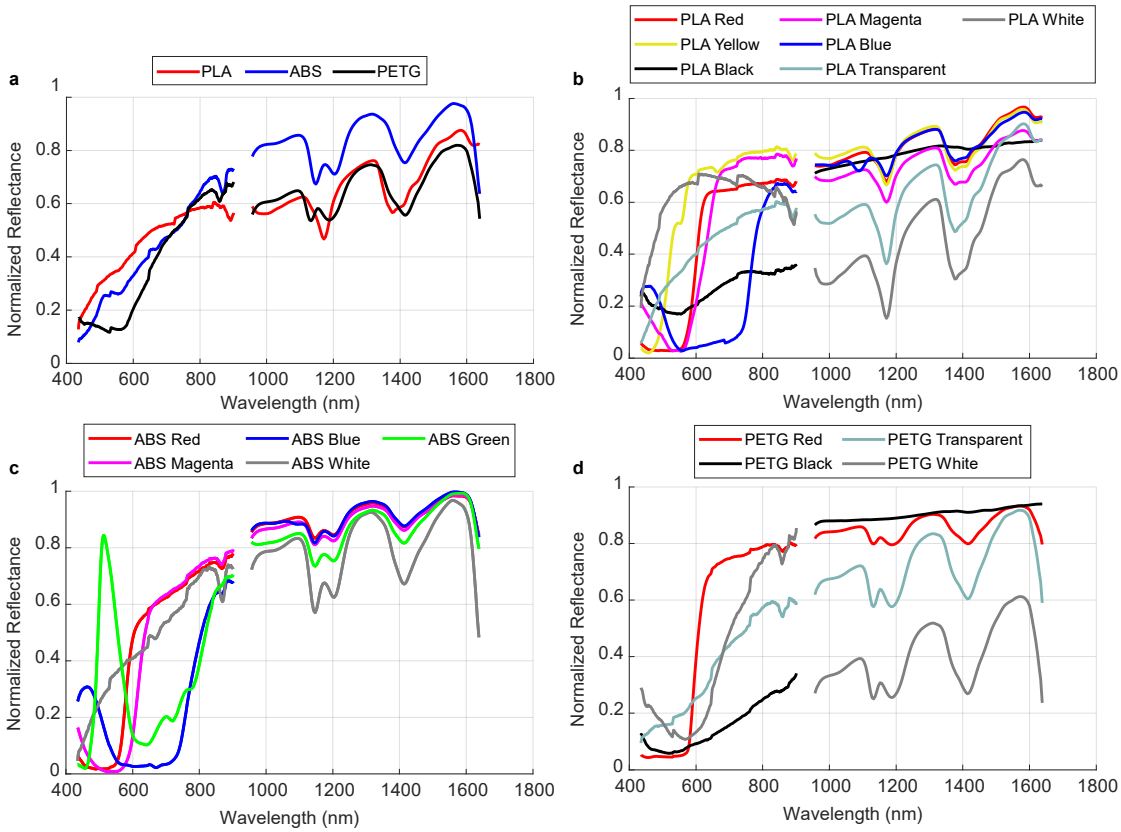

Figure 3-33: Average spectral signatures of the Fused data from the HSI plastic dataset. a) Material spectral signatures. **b**, **c**, **d**) Color spectral signatures from polylactic acid (PLA), acrylonitrile butadiene styrene (ABS), and polyethylene terephthalate glycol (PETG) materials.

3.6.3 Segmentation and classification of the fused data

The VNIR-NIR imaging fusion performance was evaluated in unsupervised segmentation and supervised classification problems. The goal was to quantitatively and qualitatively determine if the proposed fusion approach allows to improve the different segmentation/classification problems (*color*, *material*, and *material-color* identification) with respect to the exclusive use of either VNIR or NIR data separately.

3.6.3.1 Segmentation results

The segmentation methods employed were the K-means, K-medoids, and HKM algorithms to segment the HS images into *K* different clusters, since they are the most widely used segmentation algorithms in scientific literature. The number of clusters (*K*) was previously selected and, in the case of *HSI plastic dataset*, the selected K value corresponds to the number of classes present in the ground-truth of each HS image to be processed. Figure 3-34.a-c shows, as examples, the segmentation maps obtained with K-means algorithm from three of the thirteen test HS images, as well as the average Jaccard results obtained with the entire dataset for the three segmentation algorithms. As expected, the VNIR data achieved the highest results in the *color* segmentation using K-means algorithm, followed by the Fused data using K-medoids and HKM (Figure 3-34.a), while the *material* identification using the NIR data was superior in all three algorithms (Figure 3-34.b). However, the *material-color* segmentation of the NIR data using HKM improved the segmentation results followed by the Fused data using K-means (Figure 3-34.c). Statistical analysis was performed to the segmentation results using a paired, one-tailed Student's T-test at 5% significance level. No statistically differences were found between the results of the *material-color* segmentation problem.

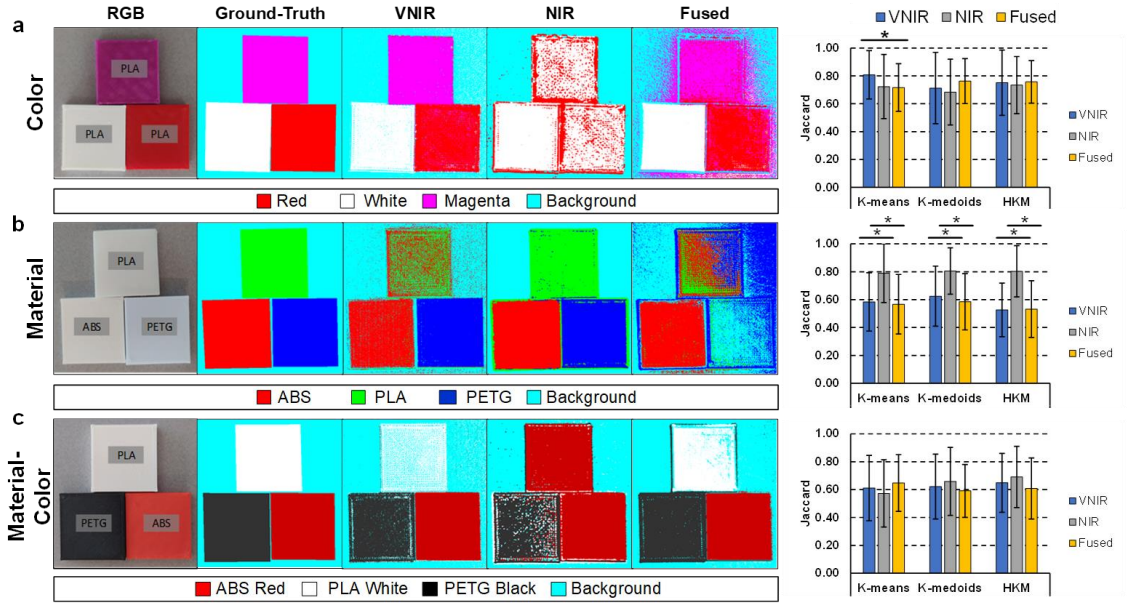

Figure 3-34: Segmentation maps of three examples of the test set from the *HSI plastic dataset* and average Jaccard results obtained from the thirteen images. Color, material, and material-color segmentation (**a, b, c**) problems using VNIR, NIR, and fused data. Each column (from left to right) represents the RGB images obtained with a digital camera, the ground-truth (GT) maps, the VNIR, NIR, and fused segmentation results, respectively, and the average Jaccard results obtained with the entire test set for the three different segmentation algorithms. Results were statistically analyzed using a paired, one-tailed Student's T-test at the 5% significance level. (*) Statistically significant difference *(p<0.05)*. (**) Highly statistically significant difference *(p<0.001)*. ABS: Acrylonitrile Butadiene Styrene; PLA: Polylactic Acid; PETG: Polyethylene Terephthalate Glycol. HKM: Hierarchical K-means.

3.6.3.2 Classification results

The pixel-wise supervised classification was based on the SVM, RF and KNN classifiers. In the classification problem, the *HSI plastic dataset* was partitioned into training, validation, and test sets. The training and validation sets were used to optimize, evaluate, and generate the classification model. A coarse-to-fine search (in

the case of SVM) and a coarse search (in the case of RF and KNN) were performed to optimize the hyperparameters of each classifier. After the hyperparameter optimization, the performance of the model was evaluated using the test set. Table 3-10 shows the optimal hyperparameter values found for each classifier, data type and classification problem, as well as the OA results obtained in the validation set.

Table 3-10: Coarse-to-fine search to optimize hyperparameters. The Cost (C), the number of trees (T) and number of nearest neighbors (K) hyperparameters of the SVM, RF, and KNN classifiers were optimized using the validation set of the HSI plastic dataset. Fine search was not performed in RF and KNN algorithm because the execution time in these classifiers is lower than SVM classifier.

Classifier	HP	Sensor	Method	Coarse Search		Fine Search		OA (%)
				I/S/F	Optimal	I/S/F	Optimal	
SVM-Linear	*C*	VNIR	Color	$2^{-20}/2^{2}/2^{60}$	2^{2}	$2^{0}/2^{0.5}/2^{4}$	2^{2}	82.93
			Material	$2^{-20}/2^{2}/2^{60}$	2^{0}	$2^{-2}/2^{0.5}/2^{2}$	$2^{0.5}$	72.83
			Material-Color	$2^{-20}/2^{2}/2^{60}$	2^{-4}	$2^{2}/2^{0.5}/2^{6}$	2^{2}	79.68
		NIR	Color	$2^{-20}/2^{2}/2^{60}$	2^{-2}	$2^{-4}/2^{0.5}/2^{0}$	$2^{-2.5}$	59.30
			Material	$2^{-20}/2^{2}/2^{60}$	2^{2}	$2^{-2}/2^{0.5}/2^{2}$	2^{1}	93.10
			Material-Color	$2^{-20}/2^{2}/2^{60}$	2^{-4}	$2^{-6}/2^{0.5}/2^{-2}$	2^{-3}	53.25
		Fusion	Color	$2^{-20}/2^{2}/2^{60}$	2^{8}	$2^{6}/2^{0.5}/2^{10}$	2^{7}	89.15
			Material	$2^{-20}/2^{2}/2^{60}$	2^{-2}	$2^{-4}/2^{0.5}/2^{0}$	2^{-3}	83.56
			Material-Color	$2^{-20}/2^{2}/2^{60}$	2^{4}	$2^{2}/2^{0.5}/2^{6}$	2^{5}	82.65
RF	*T*	VNIR	Color	1/2/300	261	-	-	87.33
			Material	1/2/300	183	-	-	79.17
			Material-Color	1/2/300	133	-	-	77.37
		NIR	Color	1/2/300	277	-	-	56.47
			Material	1/2/300	107	-	-	93.01
			Material-Color	1/2/300	271	-	-	52.98
		Fusion	Color	1/2/300	111	-	-	88.39
			Material	1/2/300	245	-	-	84.65
			Material-Color	1/2/300	257	-	-	77.43
KNN	*K*	VNIR	Color	1/2/300	5	-	-	85.47
			Material	1/2/300	1	-	-	81.03
			Material-Color	1/2/300	3	-	-	76.82
		NIR	Color	1/2/300	19	-	-	54.24
			Material	1/2/300	19	-	-	93.16
			Material-Color	1/2/300	19	-	-	50.86
		Fusion	Color	1/2/300	1	-	-	87.47
			Material	1/2/300	1	-	-	76.50
			Material-Color	1/2/300	1	-	-	77.38

HP: Hyperparameter; **I**: Initial value; **S**: Step value; **F**: Final value**.**

Once SVM, KNN, and RF models were trained and optimized for each case, the classifiers were evaluated using the test set to assess the results obtained in the validation set. Figure 3-35 shows, as examples, the classification maps obtained with the SVM classifier from three of the thirteen test HS images, as well as the average OA results obtained with the entire dataset for the three supervised algorithms. The OA was computed using the ground-truth image and the classification map of each HS image. In the *color* classification VNIR and Fused data, using SVM and RF classifiers, obtained quite similar performance, while NIR data decreases the accuracy in the three classifiers (Figure 3-35.a). As it can be observed in the SVM example, NIR data

misclassifies the three plastic samples, while the VNIR and Fused data identify correctly two out of three samples, misclassifying the white color, which is identified as transparent (orange color in Figure 3-35.a). On the contrary, in the *material* classification, the NIR data achieved the highest accuracy in all three classifiers, followed by the Fused data using SVM classifier (Figure 3-35.b). In the *material* example applying SVM classifier, VNIR data only classified two out of three samples correctly, while NIR and Fused data were able to successfully identify the three samples. Finally, in the *material-color* classification the Fused data outperformed the other two data types (Figure 3-35.c). Statistical analysis was performed to the classification results using a paired, one-tailed Student's T-test at 5% significance level. In the material-color classification problem, statistically significant differences were found between the VNIR and Fused data results.

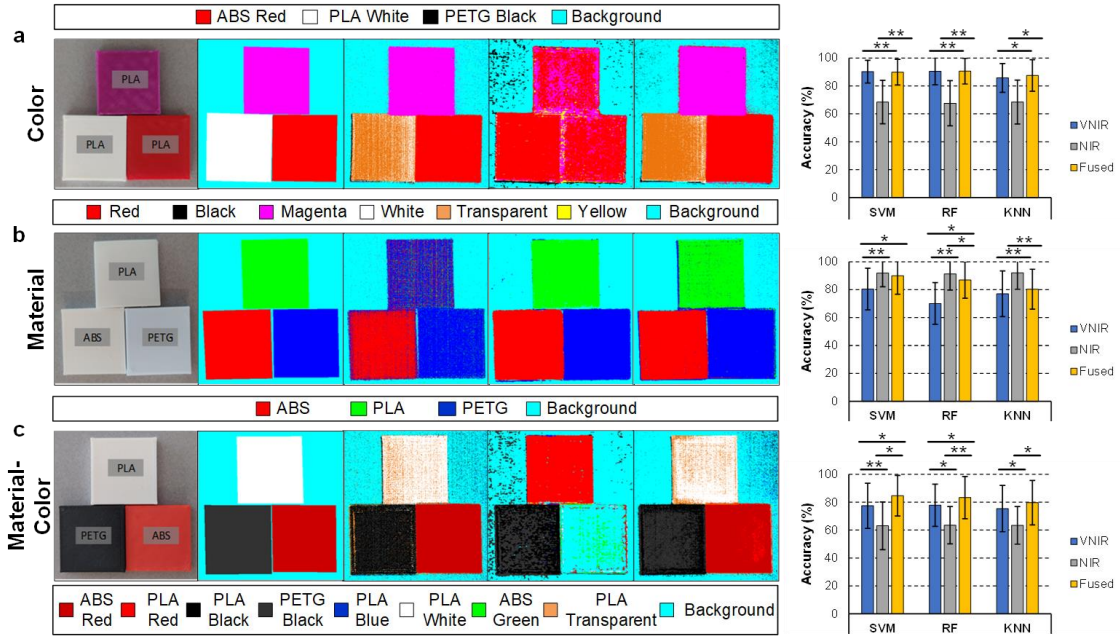

Figure 3-35: Classification maps of three examples of the test set from the *HSI plastic dataset* and average accuracy results obtained from the thirteen images. Color, material, and material-color classification (**a, b, c**) problems, using VNIR, NIR, and fused data. Each column (from left to right) represents the RGB images obtained with a digital camera, the ground-truth (GT) maps, the VNIR, NIR, and fused classification results, respectively, and the average accuracy results obtained with the entire test set for the three different classification algorithms. Results were statistically analyzed using a paired, one-tailed Student's T-test at the 5% significance level: (*) Statistically significant difference *(p<0.05)*. (**) Highly statistically significant difference *(p<0.001)*. ABS: Acrylonitrile Butadiene Styrene; PLA: Polylactic Acid; PETG: Polyethylene Terephthalate Glycol. SVM: Support Vector Machines; RF: Random Forest; KNN: K-Nearest Neighbors.

3.6.4 Experimental Results Discussion

Previous works of this research group employed an HS acquisition system composed by VNIR and NIR cameras to capture HS images of in-vivo human brain tissue during surgical procedures with the goal of identifying tumor boundaries in real-time [70], [123], [125]. However, in these works only VNIR information was processed due to the impossibility of performing a reliable labeling in the NIR HS images. In this research, this acquisition system has been modified to combine both sources of information (VNIR and NIR) and propose a VNIR-NIR imaging fusion approach to determine, as a proof-of-concept, if the fused data can improve the delineation of different brain tissue structures compared to using both sources of data independently. In the previous

configuration, the VNIR and NIR image registration was not possible to be performed due to the non-perpendicularity of the camera with respect to the scene, especially in non-flat surface situations (e.g., after tumor resection beginning). Hence, the VNIR labeling could not be used for the NIR images. Additionally, the labeling could not be directly performed over the NIR images due to their low spatial resolution and the false color representation of the pseudo-RGB. The proposed acquisition system configuration allows performing the VNIR-NIR spatial registration, being possible to extrapolate the VNIR labeling to the NIR images and perform a spectral fusion of both sources of data. Additionally, a speedup factor of 2× was achieved in the acquisition time since the capturing is performed in a single scanning.

To achieve an accurate VNIR-NIR spatial registration, several techniques and geometric transformations were analyzed and tested using different HS images. Additionally, a coarse-to-fine search was performed using all the combinations of gray-scale images (extracted from each spectral band) from both HS cameras to identify the most suitable bands for performing the spatial registration. The feature-based technique using SURF detector and projective transformation was selected for the VNIR-NIR spatial registration. Next, a detailed analysis of the VNIR and NIR spectral signatures was performed to determine the optimal operating bandwidth captured by each camera, being combined in the subsequent spectral fusion process. The resulting HS cube was formed by 641 spectral bands in the VNIR range (435–901 nm) and 144 spectral bands in the NIR range (956–1638 nm).

To determine the discrimination capability of the fused data compared with the use of the VNIR and NIR data independently, three segmentation and classification problems have been proposed using a controlled HSI dataset based on plastic samples of different materials and colors. The results show that VNIR data identified better the color of the samples than the NIR and fused data, while the material is more accurately identified using the NIR data. However, when the goal is to identify the material and color of the sample, the fused data offered better results than the VNIR and NIR data independently. Therefore, the selection of the data type to be employed in a certain classification/segmentation problem will be determined by the nature of the materials, substances or tissue to be analyzed. If the optical properties are more relevant in the VNIR region than in the NIR region (or vice versa), then, using the fused data could provide misclassifications in the results. On the contrary, if relevant optical properties can be found in the two spectral ranges (as in the *material-color* problem), the fused data could provide improved discrimination performance.

3.7 Evaluation of VNIR-NIR Hyperspectral Imaging Fusion Method for In-vivo Brain Tumor Identification and Delineation

The proposed VNIR-NIR spatial-spectral fusion method explained in Section 3.6 was applied to the third data campaign of the enhanced HS brain cancer database. This campaign was collected after performing the acquisition system modifications to allow the data fusion process. In total, due to the difficulties in obtaining intraoperative data of in-vivo human brain, the third campaign is formed only by 10 HS images captured from 8 different subjects (third data campaign in Table 3-1). After performing the

fusion process, the ground-truth generated using VNIR images can be reused in the NIR images. Thanks to this approach, the spectral characterization, segmentation, and classification of both spectral regions were performed.

3.7.1 Spectral Characterization of Brain Tumors in the VNIR-NIR Range

The VIS spectral range between 380-780 nm is the most used for medical HSI due to hemoglobin contribution in this part of the spectrum. Absorbance peaks related to deoxyhemoglobin are located at ~555 and ~760 nm [198], [199], while two oxyhemoglobin absorbance peaks are situated at ~540 and ~575 nm [197]. However, the NIR range between 700-1870 nm can additionally provide information related to the presence of fat, collagen, or water [225]. Water absorption determines the permeability of tissues and its peaks are located around 970, 1180, 1450, and 1775 nm [226]. The collagen peaks are present at 1050, 1190, 1500, 1690, 1730, and 1760 nm, being the most abundant protein in the human body [226]. Biological tissues contain lipids as essential constituents, with peaks in the NIR range at 920, 1040, 1210, 1430, 1730, 1760, and 1900 to 2600 nm [226]. Reflectance and absorbance analysis were performed in the VNIR and NIR spectral ranges in order to identify relevant features between spectral signatures.

Figure 3-36 show the mean reflectance and absorbance spectra of each tumor type of different grades (G1, G2 and G3), NT, and HT. In the VNIR range can be observed that the reflectance value of astrocytoma grade 2 is higher than other tumor type, having the HT the lowest reflectance values (Figure 3-36.a). In addition, reflectance values increase rapidly over 580 nm and therefore, decrease the absorbance values (Figure 3-36.b). Between 500 and 600 nm, the absorbance increases due to the absorption peak of the hemoglobin [227]. In HT and meningioma grade 2 is observed an absorbance peak at 760 nm due to the deoxy-hemoglobin [199].

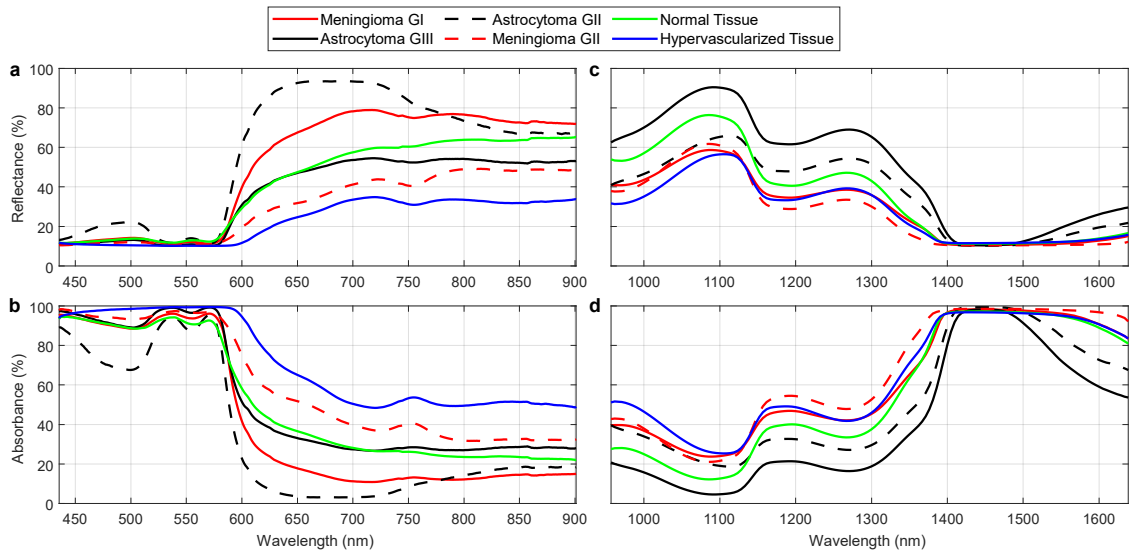

Figure 3-36: Spectral analysis of brain tumors and tissues in VNIR and NIR ranges. a, b) Mean reflectance and absorbance spectral signatures, respectively, of different brain tumors, normal, and hypervascularized tissue in the VNIR range. **c, d)** Mean reflectance and absorbance spectral signatures, respectively, of different brain tumors, normal, and hypervascularized tissue in the NIR range.

In the NIR range, it is possible to observe the reflectance values decrease as wavelengths increase and therefore (Figure 3-36.c), increasing the absorbance value as wavelength increases (Figure 3-36.d). Astrocytoma grade 3 achieves the highest reflectance in this spectral range, while NT and meningioma grades 1 and 2 have lower reflectance values. Water absorbance peaks are observed in this range at 970 and 1450 nm [228]. In addition, water molecules without a hydroxy group are absorbed at 1160 nm [229].

A statistical analysis was performed to evaluate each pair of class sets (TT vs. NT, TT vs. HT, and NT vs. HT). Figure 3-37 shows the mean and standard deviation of each class (from all the HS images in the dataset) of the VNIR and NIR data, respectively, employed to perform the statistical analysis. First, Lilliefors test was computed to identify if each group at each wavelength has normal or non-normal distribution. After performing the test, it was found that all three groups had a non-normal distribution. For this reason, the Wilcoxon Rank-Sum test was employed for the statistical evaluation.

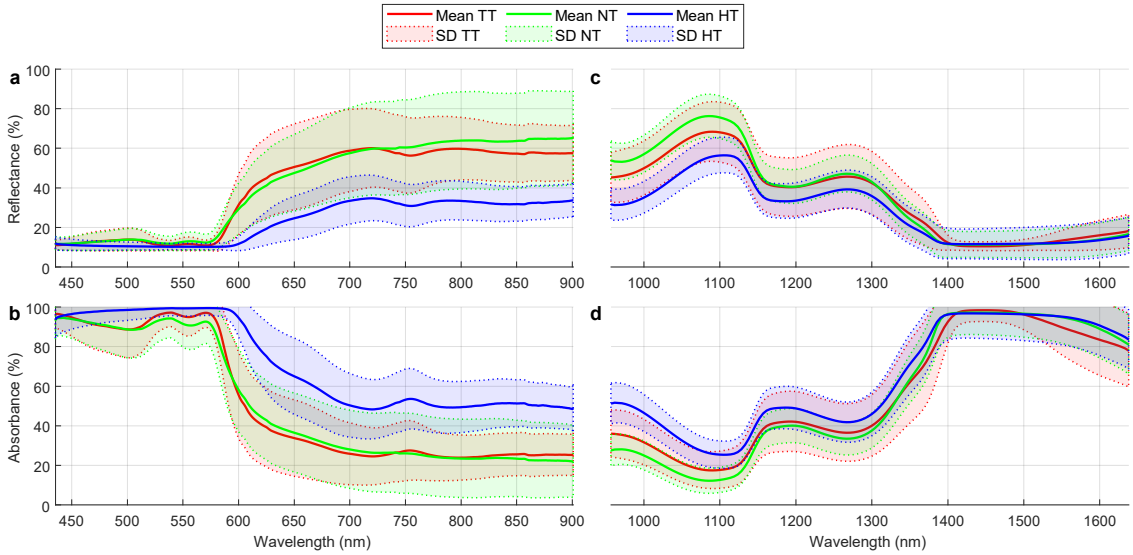

Figure 3-37: Spectral analysis of brain tissues in VNIR and NIR ranges. a, b) Mean and standard deviation reflectance and absorbance spectral signatures, respectively, of different brain tumors, normal, and hypervascularized tissue in the VNIR range. **c, d**) Mean and standard reflectance and absorbance spectral signatures, respectively, of different brain tumors, normal, and hypervascularized tissue in the NIR range. SD: Standard Deviation; TT: Tumor Tissue; NT: Normal Tissue; HT: Hypervascularized Tissue.

Figure 3-38 show the p-value obtained from the statistical analysis among the different classes from the VNIR and NIR data, respectively. In this figure, each graph represents a pair of classes comparison. In the case of the VNIR data, HT shows highly statistically significant difference with respect to TT (Figure 3-38.a) and NT (Figure 3-38.e) ($p < 0.01$) in reflectance and absorbance, except for the 444 nm where no statistically significant differences between HT and TT was found ($p > 0.05$). In Figure 3-38.c, it can be observed that the spectral ranges 460-510 nm, 590-600 nm, and 700-740 nm have no statistically significant differences between TT and NT ($p > 0.05$), while in the spectral range 481-484 nm statistically significant differences were found between TT and NT ($0.01 < p < 0.05$). In the case of NIR range, HT shows highly statistically significant differences respect to TT (Figure 3-38.b) and NT (Figure 3-38.f) ($p < 0.01$). However, in the spectral range between 1,340 and 1,376 nm, no statistically

significant differences were found between TT and NT ($p > 0.05$) (Figure 3-38.d). Finally, in 1,633 nm statistically significant difference between TT and NT was found ($0.01 < p < 0.05$).

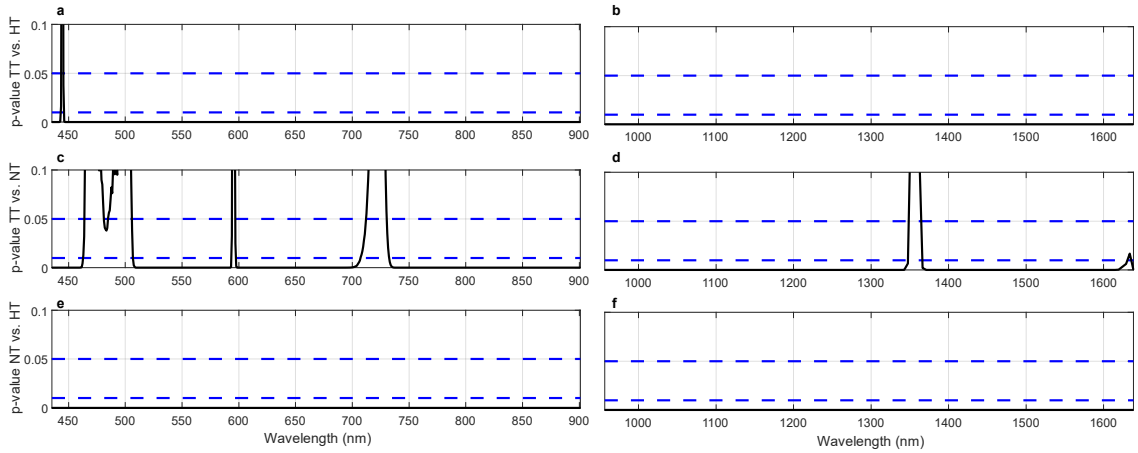

Figure 3-38: *p*-value of each pair of tissue groups. a, c, e) p-value of TT vs. HT, TT vs. NT, and NT vs. HT, respectively, in VNIR range. **b, d, f**) p-value of TT vs. HT, TT vs. NT, and NT vs. HT, respectively, in NIR range. TT: Tumor Tissue; NT: Normal Tissue; HT: Hypervascularized Tissue.

3.7.2 Brain Tissue Segmentation using the VNIR-NIR Range

The main goal of this experiment was to evaluate, as a proof-of-concept, if the proposed data fusion method could improve the morphological edge detection of different tissue structures (particularly normal tissue and blood vessels) that can be found in the exposed brain surface during surgery. Image segmentation based on the K-means algorithm was performed in each HS image independently for a qualitative evaluation of the results obtained using the three data types, VNIR, NIR, and Fused. The number of clusters used was twenty-four. This number was selected based on the results of a previous work [70]. Finally, to obtain the segmentation maps, the clusters more similar to the ground-truth were selected using the Jaccard metric. In these experiments, the clusters initialization was performed using the same seed. Quantitative evaluation was not performed due to the low number of pixels labeled in each image, which produced extremely low Jaccard values.

Figure 3-39 shows the pseudo-RGB images (generated from the VNIR data, where the approximate tumor area has been delineated with a yellow line by visual inspection of the operating surgeon according to the patient's MRI), the ground-truth maps (green and blue pixels represent normal and blood vessel classes, respectively, and white pixels are non-labelled pixels), and the segmentation maps for the VNIR, NIR, and Fused data overlapped with the pseudo-RGB images. Blue and green colors were selected to be consistent with previous works [70]. After a visual evaluation of the segmentation maps by the operating surgeons, it can be observed that in Op50C1, the VNIR map presents normal pixels in the tumor area and normal and blood vessel pixels out of the parenchymal area. In contrast, NIR and fused maps reduce the misclassifications in the tumor area. Moreover, the anatomical structures of the parenchymal area are better defined in the fusion map than in the VNIR and NIR maps, although some pixels are identified as normal within the tumor area. In Op51C1, the VNIR map defines well the anatomical structures of the vessels and normal tissues, while the NIR map avoids misclassifications within the tumor area, delimiting well the parenchyma. The fused map offers a tradeoff between the information shown in the

VNIR and NIR maps, but some false negatives are presented in the tumor area. In Op54C1, the tumor area was correctly defined in the VNIR map without false negatives, but the anatomical structures of vessels are not accurately identified. In opposite, the NIR map improve de delineation of blood vessels, but the anatomical structure of normal tissue is poorly defined, including also false negatives in the tumor area. Finally, the fused map offers the best anatomical structures and delineation of tumor area. These results were assessed by the operating surgeons analyzing the MRI of the patient and the pathological diagnosis of the tissue.

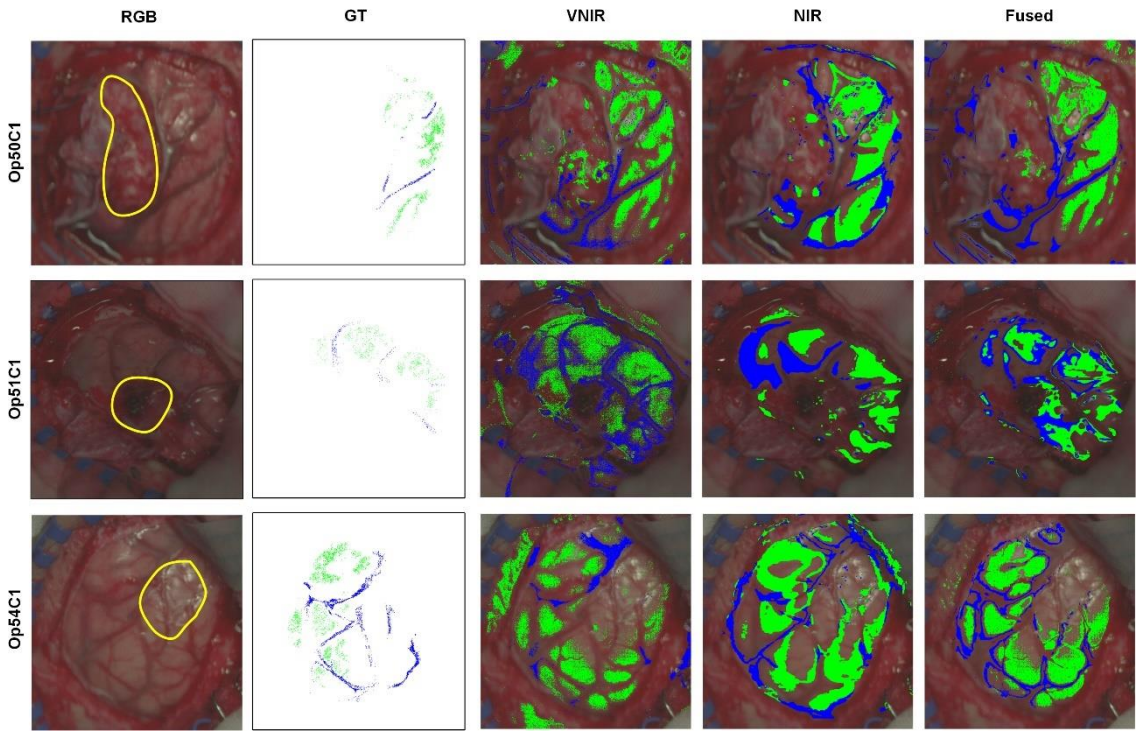

Figure 3-39: Results of the image segmentation of the HSI brain dataset. Each column (from left to right) represents the pseudo-RGB image generated form the VNIR data, the ground-truth (GT) map, the VNIR, NIR, and fused segmentation maps overlapped with the pseudo-RGB image, respectively. Green color represents normal tissue and blue color represents blood vessels. Op50C1: Meningioma Grade 1; Op51C1: Glioblastoma Grade 4; Op54C1: Glioblastoma Grade 4.

3.7.3 Brain Tissue Classification using the VNIR-NIR Range

Due to the limited number of patients in this dataset, a leave-one-patient-out cross-validation approach was employed in this study. Each HS image was used as test and the training set contains all HS images except those of the corresponding patient. Three algorithms were evaluated to perform the classification: SVM, KNN, and RF. In addition, this approach was applied using NIR, VNIR, and fused images, independently, in order to evaluate the contribution of the fusion process in the classification performance.

Figure 3-40.a shows the boxplots of the OA results obtained from each classifier. The highest median (horizontal bar within the box) and average (cross mark) OA were obtained with the SVM-L model using fused data (94.1% and 93.0%, respectively). Fusion and NIR results using KNN-C and KNN-E obtain similar OA results, while VNIR results improve ~5% the average OA value. A similar trend occurs in SVM-RBF, where VNIR achieves better results, but in all three cases (fusion, NIR, and VNIR) the

IQR dispersion decreases with respect to the other algorithms. The RF algorithm obtains similar average OA results using fusion, NIR, and VNIR images.

To avoid the high contribution of the background in the OA results due to the large number of labeled pixels in such class, the macro F1-Score metric was computed. Figure 3-40.b shows such results, where it can be observed that the values decrease with respect to the OA. The highest median and average results were obtained using the KNN-C model with VNIR data (69.4% and 65.9%, respectively). In general, the VNIR classification achieves the best results in all classifiers but shows a large IQR compared to the NIR and fusion results. Fusion results obtain similar results than NIR results, and the results are comparable to the VNIR ones when using the SVM-L model.

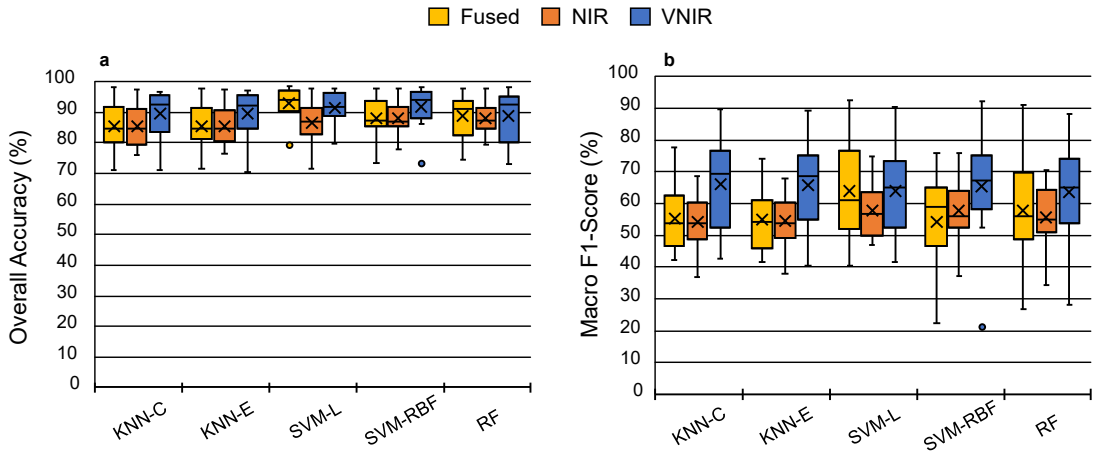

Figure 3-40: Fusion, NIR, and VNIR classification results using five classifiers. a) Overall accuracy. **b**) Macro F1-Score.

Figure 3-41 shows the sensitivity results obtained for each class. The sensitivity of the NT class can be observed in Figure 3-41.a, where in general the NIR data obtain less data dispersion in all classifiers with respect to the VNIR data. KNN-C and KNN-E obtain the best average sensitivity results employing fusion data (81.6% and 79.5%, respectively). The highest median sensitivity of the NT class was obtained using the KNN-C model and VNIR data (94.5%). NIR data improve the performance using SVM-L, SVM-RBF, and RF algorithms. Figure 3-41.b shows the sensitivity of the TT class where the NIR data obtain less IQR except in the SVM-L algorithm and low average results. VNIR obtains the best average values in all classifiers, where the highest median result was obtained using the RF model (69.4%). For VNIR, a similar trend occurs in the HT class (Figure 3-41.c), which may be caused by the presence of hemoglobin in the visible range. The highest median value was obtained using the SVM-L algorithm and fused data (96.4%), while the highest average result was obtained using KNN-C model and VNIR data (80.9%). The specificity results were calculated obtaining an average result of up to 90% in all classifiers and data.

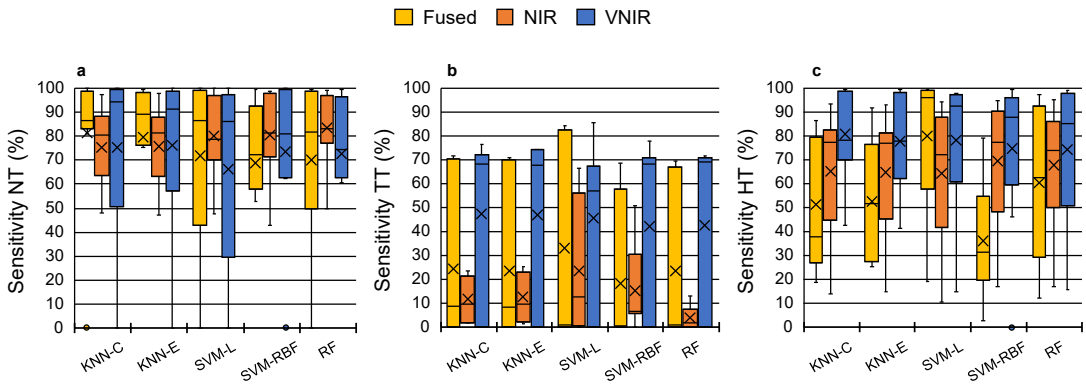

Figure 3-41: Fusion, NIR, and VNIR sensitivity results using five classifiers. a) Sensitivity of normal tissue. **b**) Sensitivity of tumor tissue. **c**) Sensitivity of hypervascularized tissue.

In addition, some outliers can be observed in Figure 3-41.a and Figure 3-41.b with a value of zero in the fusion and VNIR data. This is caused by a non-optimal image acquisition process of the image Op56C2, where the cold light emitter was not aligned with the captured line, affecting the spectral range from 750 to 900 nm of the VNIR sensor. This can be observed in Figure 3-42, where the normalized mean reflectance of NT and TT classes from the Op56C1 and Op56C2 images are shown to compare both consecutive captures.

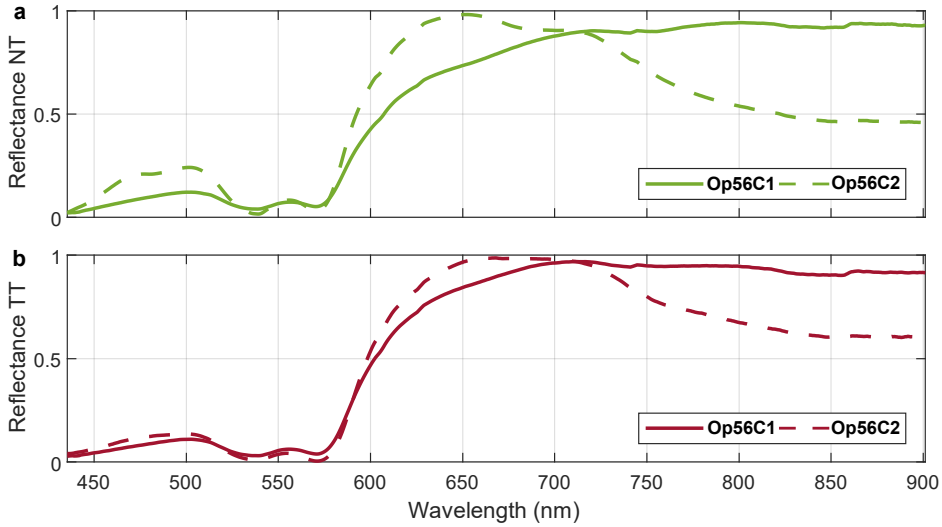

Figure 3-42: Mean reflectance spectral signature of normal (a) and tumor (b) tissue from the VNIR image Op56C1 and Op56C2.

After applying the five supervised classification models to the entire VNIR, NIR, and fusion HS images, four-class classification maps were generated. These maps were used to analyze the results quantitatively. The synthetic RGB images and ground-truth maps are also displayed.

Regarding the Op50C1 image (Figure 3-43), it can be observed that the VNIR maps have more details about the hypervascularized class than the NIR maps due to the hemoglobin contribution in the VIS region, as expected from HT sensitivity results. The tumor is identified in the five classifiers using the VNIR image, however using NIR data the SVM-L offers the high performance to identify TT. In addition, NIR provides better delineation of background area. Employing both KNN algorithms, the resulting maps

are noisy in the NIR case. The SVM-L model using fused data provides maps with fewer artifacts.

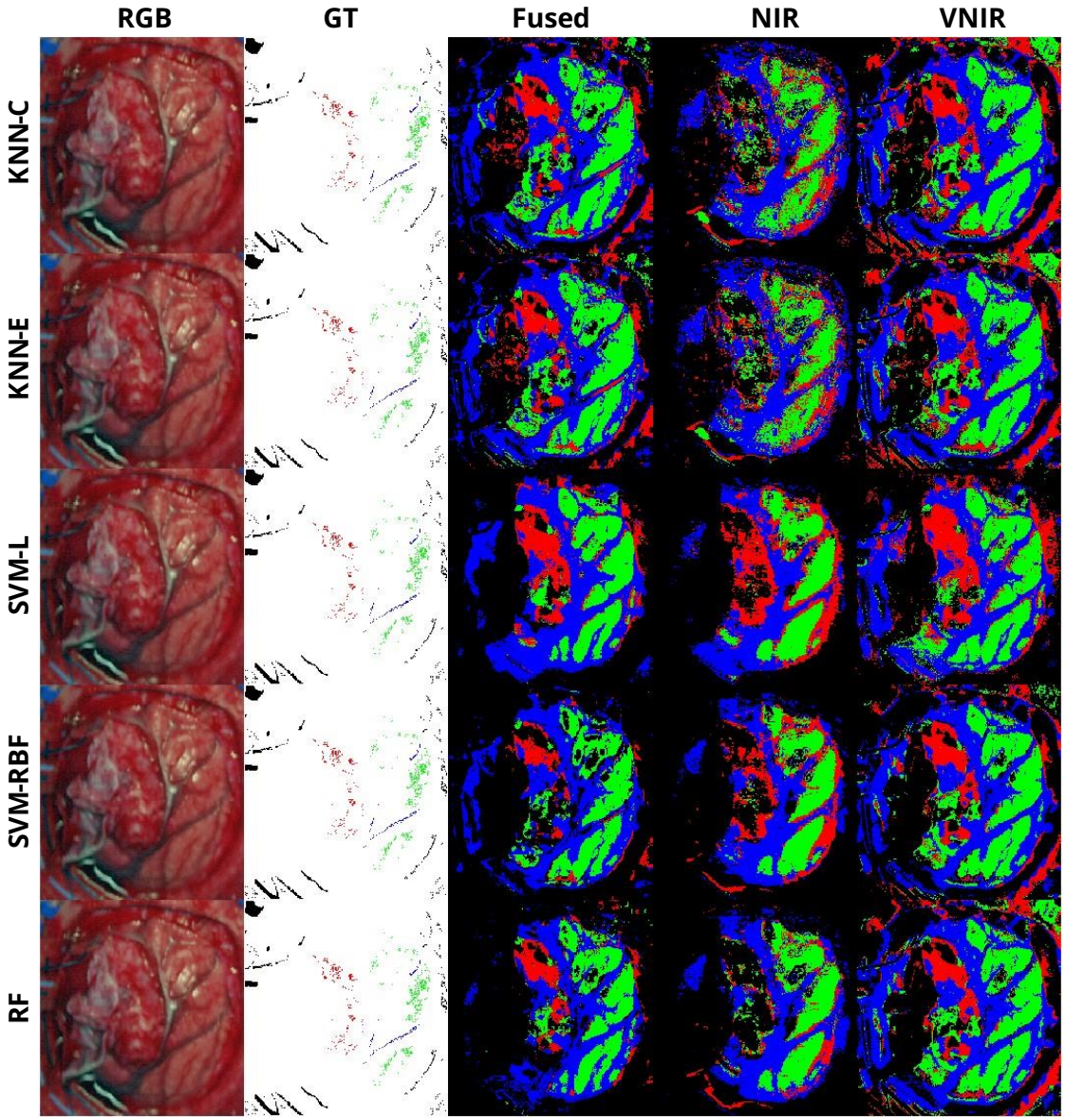

Figure 3-43: Spectral classification results of Op50C1. Synthetic RGB images, ground-truth (GT) maps, and classification maps generated using, KNN-C, KNN-E, SVM-L, SVM-RBF, and RF algorithms for fusion, NIR, and VNIR data.

Image Op51C1 (Figure 3-44) shows a high number of pixels misclassified as HT class using NIR and VNIR. The background delineation is improved using NIR and fusion data. The classification map using the fusion data improves the identification of NT, reducing the false positives presented using NIR and VNIR, and obtaining better performance using KNN-C and KNN-E models. False positives regarding TT class are presented in NIR and VNIR images, while using fusion data these misclassified TT pixels are located in the background area.

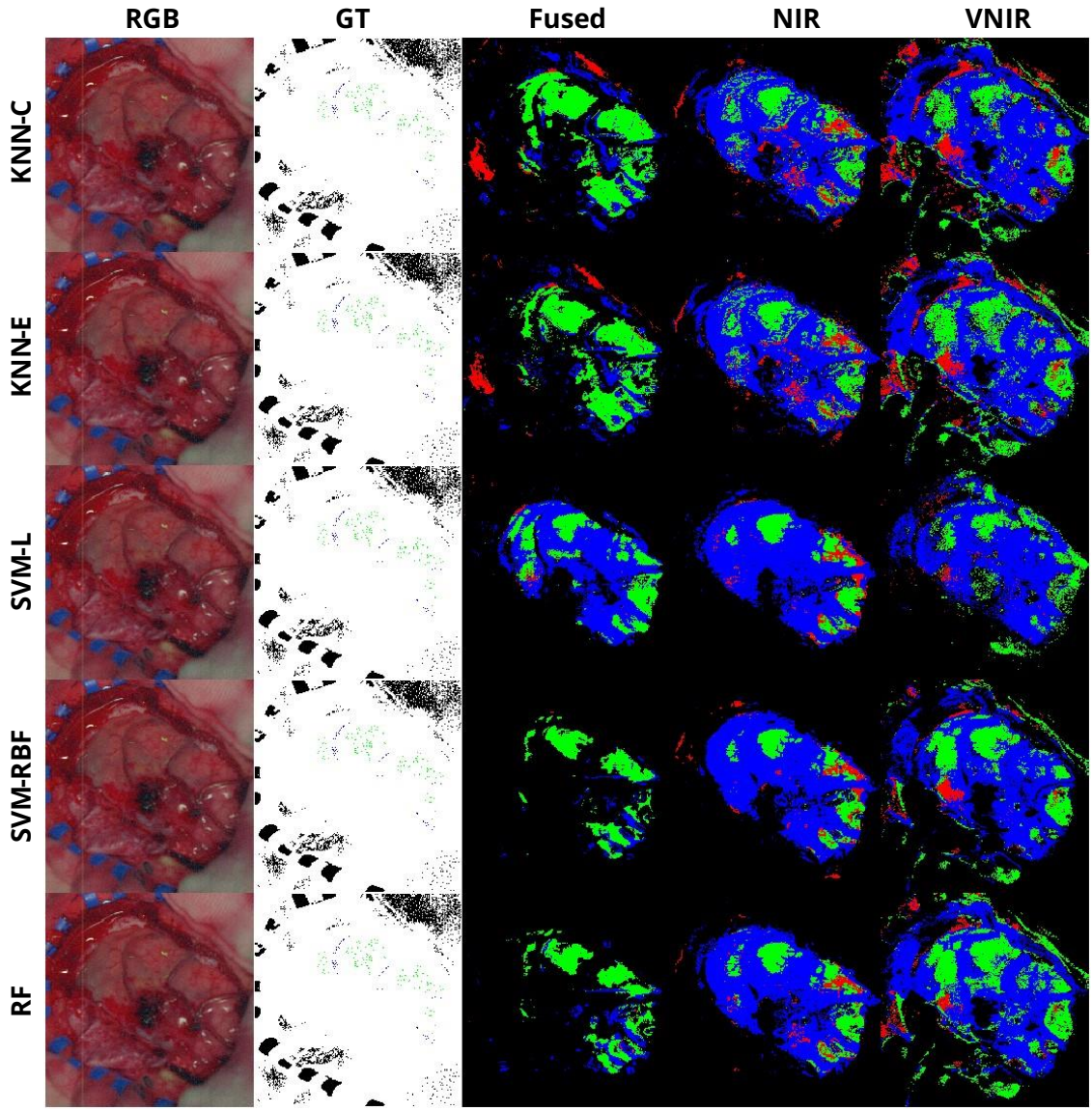

Figure 3-44: Spectral classification results Op51C1. Synthetic RGB images, ground-truth (GT) maps, and classification maps generated using, KNN-C, KNN-E, SVM-L, SVM-RBF, and RF algorithms for fusion, NIR, and VNIR data.

In the case of Op56C1 (Figure 3-45), the TT was correctly identified in the VNIR image by all classifiers, except the SVM-L model, where some TT pixels are identified as NT. The HT class is identified with more detail using the fusion image. However, SVM-L correctly identify the tumor area, but some NT pixels were identified as HT.

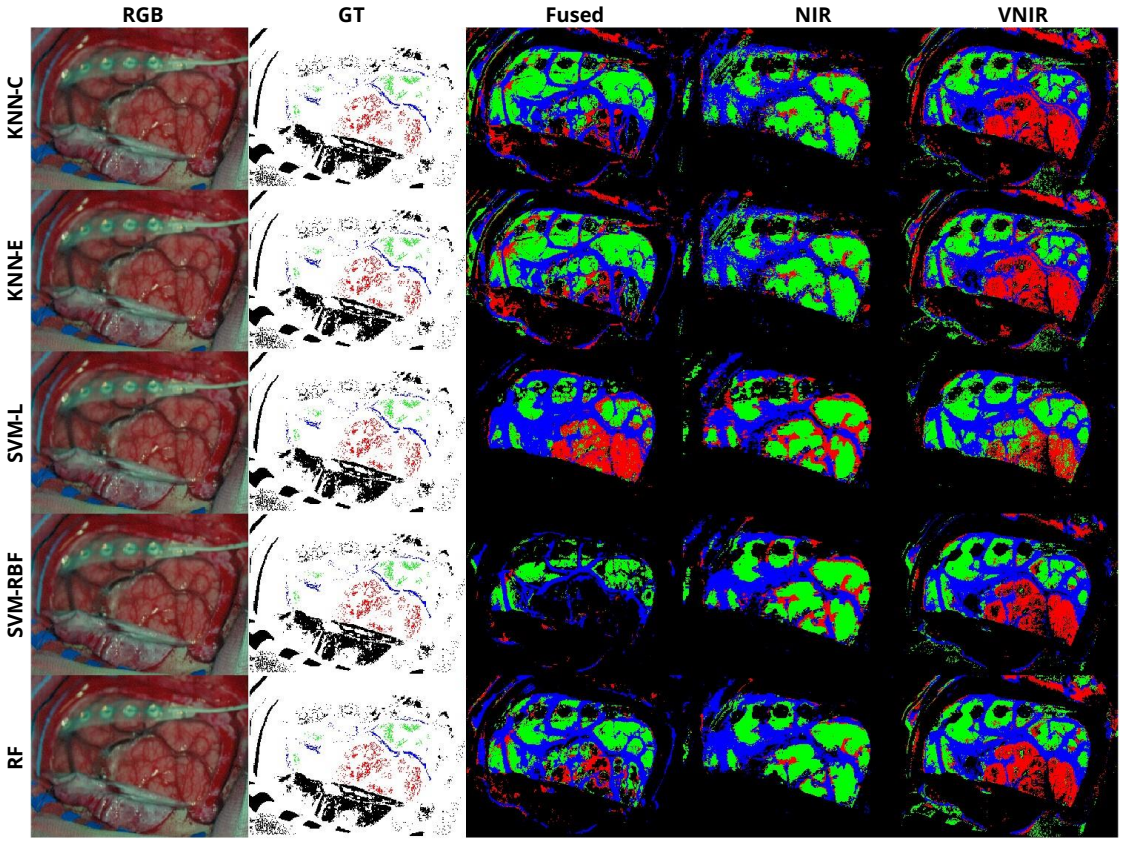

Figure 3-45: Spectral classification results Op56C1. Synthetic RGB images, ground-truth (GT) maps, and classification maps generated using, KNN-C, KNN-E, SVM-L, SVM-RBF, and RF algorithms for fusion, NIR, and VNIR data.

3.7.4 Experimental Results Discussion

In this section, an in-vivo HS brain cancer dataset was analyzed using supervised classification algorithms. This dataset was composed of VNIR, NIR and VNIR-NIR fused images covering the spectral range between 400 and 1700 nm. SVM, KNN, and RF algorithms were employed using a leave-patient-one-out data partition strategy. In addition, the K-means algorithm was employed to perform image segmentation. NIR and VNIR images were classified and segmented to determine if the fusion improved the classification.

First, a preliminary analysis of three HS images of in-vivo human brain tissue obtained during surgical procedures was performed to evaluate, as a proof-of-concept, the segmentation results generated after processing the three data types. In this preliminary analysis, only two classes (normal and blood vessel) were labeled in the ground-truth maps and employed to reveal the two best clusters associated to such labeled pixels. Analyzing these segmentation results, specialists determined that the Fused maps provided a good tradeoff between the information presented in the VNIR and NIR maps, offering improved anatomical structures delineation. In this experiment, no tumor pixels were labeled or taken into account for the clustering analysis. For such reason, further experiments must be conducted including an increased dataset of HS images from in-vivo brain (where tumor pixels will be also labeled) with the goal of performing both segmentation and classification problems, aiming to identify tumor boundaries and compare the results obtained with the three data types. Moreover, a clinical study, including large number of patients, different

tumor types, and performing histological verification of several biopsies (within the tumor area and margins), should be performed to validate the classification results provided by the proposed method.

The classification results show that the presence of hemoglobin in the VIS region improves the tumor and hypervascularized tissue using only VNIR images, while the NIR images correctly delineate the parenchymal area. Classification maps obtained using the VNIR-NIR fused images present more detailed maps, removing false positives present in the VNIR and NIR images. The main characteristics observed in the VNIR and NIR classification maps are reflected in the fused images.

This work represents an initial exploration into using VNIR-NIR analysis for detecting and identifying brain cancer. While the results are promising, the dataset size is the main limitation of this study. While the current dataset was sufficient to demonstrate the potential of the approach, increasing the size of the dataset would improve the robustness of the results. For future research, the size of the dataset will be increased to employ other partition sets, avoiding the leave-one-patient-out approach. In addition, hyperparameter optimization is an important step in the training process to find the optimal configuration that leads to the best performance on a given dataset. The results obtained in this work can be pessimistic and can be improved after hyperparameter optimization.

Another important future work is to perform an analysis to determine the most significant spectral bands within each range (VNIR and NIR). By identifying the most significant spectral bands within each range, the total number of bands used in the analysis and the computation time can be reduced. In addition, this band reduction can lead to the use of HS sensors that employ only these specific bands.

3.8 Conclusions

Current guidance tools employed to assist brain tumor resection during surgery have several limitations [230]–[233]. The IGS neuronavigation provide an accurate identification of tumor boundaries in low-grade gliomas, but not in high-grade ones, being affected also by the brain shift phenomenon. To accurately identify high-grade gliomas, it is necessary the use of contrast agents with complex and expensive systems, such as 5-ALA, or employing intraoperative MRI devices that requires especial operating rooms and significatively extends the duration of the surgery. Moreover, the treatment and decision made during surgery normally is determined by the intraoperative pathological result, which may take up to 45 minutes. Reducing the surgery time implies decreasing the risk of complications during the operation, such as infection, ischemia, respiratory problems, etc., thus improving cost-efficiency. Furthermore, an accurate delimitation between tumor and normal tissue improves the average survival of the patient [17]. For these reasons, it is desirable to develop minimally invasive, label-free, and flexible guidance tools that allow identifying brain tumor boundaries in real-time during surgery. The use of HSI in medical applications has been proved to be a valuable resource to identify tumor tissue [3].

Additionally, an analysis of the most relevant spectral bands of the fused HS images for an accurate delineation of the tumor boundaries will be explored in future works with the goal of determining the minimum number of wavelengths required to develop

customized HS cameras. This will allow a reduction of the acquisition system size and also a time reduction of the data acquisition and processing, targeting real-time performance during surgery. This identification of the most relevant spectral bands in the NIR range will also allow to increase the spatial resolution of this HS images, possibly avoiding the resampling process employed in this work. These advances could allow the development of a novel guidance tool based on HSI technology for the accurate identification of brain tumors, regardless of tumor grade, avoiding the use of several independent devices during surgery and, hence, reducing the operation time.

Chapter 4: Dermatoscopic HS system for Skin Cancer Detection

4.1 Introduction

This chapter explores the potential of HS images in non-surgical medical diagnostics, specifically in dermatology, with a focus on the identification of PSLs. In this sense, the main goal of this research is the design and development of a HS-based instrumentation and a data processing framework based on HS image segmentation and supervised classification, following a similar methodology as the one presented in the previous chapter. A customized dermatologic HSI system was developed and employed to capture real-time HS data of in-vivo PSLs composed by 125 bands in the 450–950 nm spectral range. This study aims to demonstrate, as a proof-of-concept, the potential use of HSI technology to assist dermatologists in their clinical routine practice for discriminating between benign and malignant PSLs (including both NMSC and melanoma lesions) using a real-time, non-invasive, label-free and non-ionizing hand-held device. To the best of our knowledge, this is the first work focused in using snapshot HS cameras within the VNIR range to segment and classify among benign and malignant PSLs using only spectral information.

This work was performed in collaboration with the research group of Prof. Francesco Leporati at University of Pavia during a research stay. The work related with the data collection has been carried out in a very close collaboration with the research group of Dr. Gregorio Carretero and Dr. Irene Castaño from the Department of Dermatology at the University Hospital of Gran Canaria Doctor Negrín (Spain), and Dr. Javier A Hernandez and Dr. Pablo Almeida from the Department of Dermatology at the Complejo Hospitalario Universitario Insular-Materno Infantil of Las Palmas de Gran Canaria (Spain), and also with Dr. Bernardino Clavo from the Research Unit of the University Hospital of Gran Canaria Doctor Negrín.

4.2 Dermatoscopic HS system

The HS dermatoscopic acquisition system used in this study for the assistance in the diagnosis of PSLs is a custom development described in detail in [234]. The system is composed by a snapshot HS camera (Cubert UHD 185, Cubert GmbH, Ulm, Germany) capable of capturing HS data in the VNIR spectral range from 450 to 950 nm, having a

spectral resolution of 8 nm (125 spectral bands) and a spatial resolution of 50×50 pixels (i.e. a pixel size of 240×240 μm) (1 in Figure 4-1). This camera has coupled a Cinegon 1.9/10 (Schneider Optics Inc., Hauppauge, NY, USA) lens with a F-number of 1.9 and a focal length of 10.4 nm. The acquisition system employs a 150 W QTH-based illumination system (Dolan-Jenner, Boxborough, MA, USA) (2 in Figure 4-1) coupled to a fiber optic ring light guide to obtain cold light emission in the skin surface, avoiding the high temperatures produced by the halogen lamp (3 in Figure 4-1). The illumination system is attached to the HS camera through a 3D printed customized dermatoscopic contact structure where the skin contact part is a dermatoscopic lens with the same refraction index as the human skin (4 in Figure 4-1). The HS dermatologic system can capture HS images, with an effective area of 12×12 mm, with an acquisition time of ~250 ms. This system is connected to a laptop where the acquisition software is executed (5 in Figure 4-1). Figure 1.6 shows an example of the use of the developed HS dermatologic acquisition system during a clinical data acquisition campaign at the University Hospital of Gran Canaria Doctor Negrin, Spain.

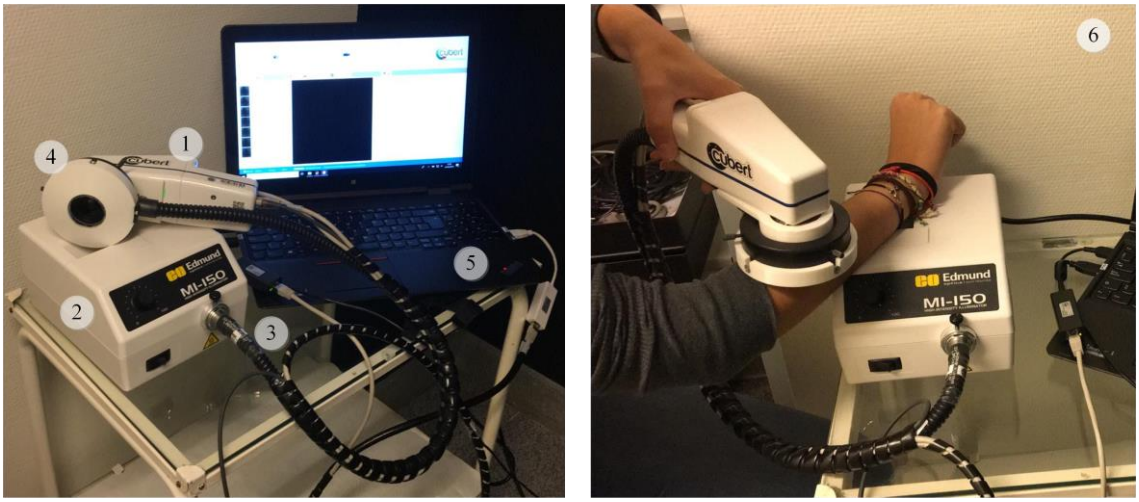

Figure 4-1: HS dermatologic acquisition system. (1) HS snapshot camera; (2) QTH (Quartz-Tungsten Halogen) source light; (3) Fiber optic ring light guide; (4) 3D printed customized dermoscopic contact structure attached to the ring light; (5) Acquisition software installed onto a laptop; (6) System employed during a data acquisition campaign.

4.3 HS dermatoscopic database for skin cancer detection

The HS dermatologic acquisition system was employed to obtain an HS in-vivo human PSL database to evaluate the efficiency of HS images to discriminate between benign and malignant lesions. The data acquisition campaign was performed from March 2018 to June 2019. Several types of PSLs from different parts of the body were captured from 116 subjects in two different hospitals, the University Hospital of Gran Canaria Doctor Negrín and Complejo Hospitalario Universitario Insular - Materno Infantil (Spain). The study protocol and consent procedures were approved by the *Comité Ético de Investigación Clínica-Comité de Ética en la Investigación (CEIC/CEI)* from both hospitals. Written informed consent was obtained from all subjects.

After a preliminary analysis of the captured data, 55 subjects/images were removed from the database due to the PSLs were located in areas that were extremely difficult to be captured (e.g., shoulders, nose, chin, and some difficult to access parts of the face)

and, hence, the HS images were not captured in optimal conditions. The dermatoscopic lens had no complete contact with the skin surface, producing shadows or glares in the images and, consequently, it was impossible to perform reliable image calibration or PSL labeling on captured HS images. The final database was composed by 76 images from 61 subjects as shown in Figure 4-2.a.

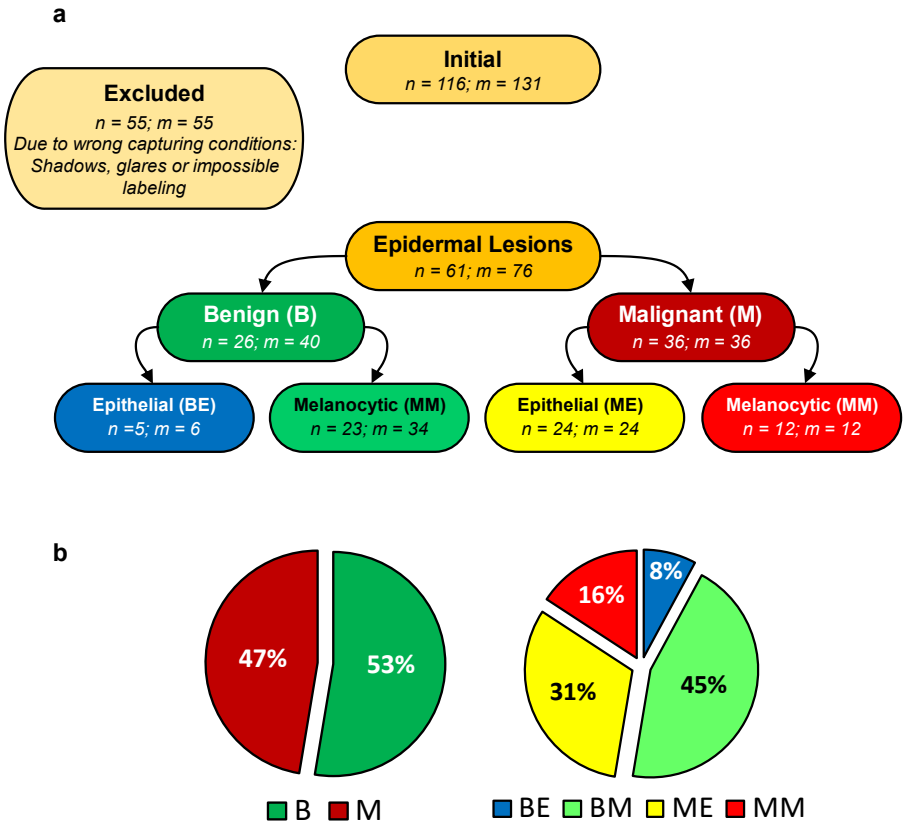

Figure 4-2: Patient/image flow scheme in this study. n: number of patients; m: number of HS images. There are several subjects with different lesions captured.

In addition to the HS image, a standard digital dermatoscopic camera (3Gen Dermlite Dermatoscope, 3Gen Inc., San Juan Capistrano, CA, USA) was employed to capture conventional RGB images of 3,000×4,000 pixels (i.e. a pixel size of 6.6×6.6 μm) of the same PSL for dermatologist evaluation. Suspected malignant lesions were diagnosed through histological assessment. Figure 4-3 shows some RGB dermatoscopic images obtained by using the digital dermatoscopic camera. The HS images corresponding to these image IDs were employed as validation and test sets in the experimental setup.

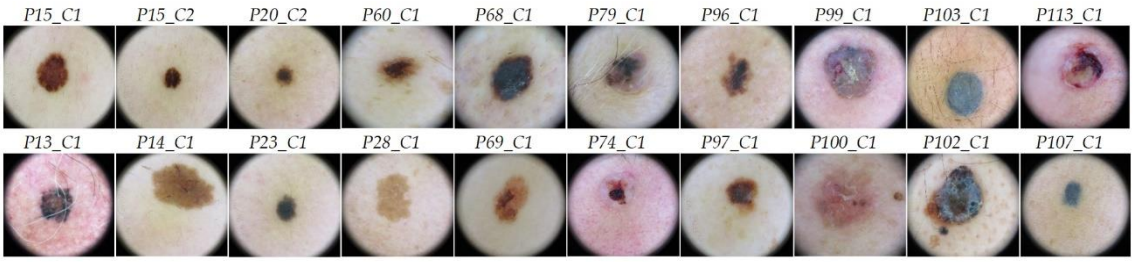

Figure 4-3: RGB images obtained with the digital dermatoscopic camera with their correspondent image ID above. The first row shows the validation set images and the second row the test set images.

A labeled dataset was created employing the HS images by assigning to certain pixels the diagnostic class of the PSL obtained from the dermatologist/pathologist assessment. This assignation was performed by using a semi-automatic labeling tool based on the SAM algorithm. This algorithm determines the spectral similarity between two spectral signatures, where lower spectral angle values indicate higher similarity among both spectral signatures [235]. The semi-automatic labeling tool allows labeling the most similar pixels in the image with respect to a reference pixel, which is manually selected and identify to belong to a certain class. Only pixels with high confidence to belong to a class were labeled. This tool has been already employed to label HS images in-vivo brain surface for brain tumor classification [124]. After performing the labeling of the entire database, a total of 15,961 pixels were used for the classification experiments employing ML algorithms. The data were labeled in two different classes: *Benign* and *Malignant*. In addition, each class was split into melanocytic and epidermal [236] (Table 4-1). Concretely, the labeled dataset was composed by 61 patients, but two of them have different lesions captured where one lesion belongs to the benign class and the other lesion belongs to the malignant class. Table 4-2 shows the number of patients, images and labeled pixels per class, while the Figure 4-4 shows the training, validation, and test set distribution of this preliminary study.

Table 4-1: HS epidermal dataset description.

Capture Date	Subject ID	Capture ID	Binary ID	Multilabel ID	Lesion Location	Diagnosis
20/03/2018	13	C1	M	ME	Chest	Basal cell carcinoma
		C2	B	BM	Stomach	Blue nevus
		C3	B	BM	Stomach	Blue nevus
	14	C1	B	BM	Right Arm	Congenital nevus
	15	C1	B	BM	Back Centre	Nevus
		C2	B	BM	Back Top	Nevus
	16	C1	B	BM	Right Forearm	Nevus
22/03/2018	17	C1	B	BM	Back	Nevus
		C2	B	BM	Back	Nevus
	18	C1	B	BM	Centre Back	Nevus
	20	C2	B	BM	Back	Melanocytic nevus
	21	C1	M	ME	Jaw	Basal cell carcinoma
05/04/2018	23	C1	B	BM	Left Arm	Nevus
	24	C1	B	BM	Left Cheekbone	Solar lentigo
	25	C2	B	BM	Stomach	Nevus
		C3	B	BM	Back	Nevus
	26	C1	B	BM	Right Forearm	Nevus
10/04/2018	27	C1	B	BM	Top Right Back	Nevus
		C2	B	BM	Centre Back	Nevus
		C3	B	BM	Top Left Back	Nevus
		C4	B	BM	Top Left Back	Nevus
	28	C1	B	BM	Neck	Solar lentigo
	29	C1	B	BM	Left Arm	Nevus spilus
		C2	B	BM	Left Arm	Nevus spilus
		C3	B	BM	Left Back	Nevus
	30	C1	B	BM	Right Chest	Nevus
	32	C1	B	BE	Nose	Atypical keratosis
08/08/2018	56	C1	M	ME	Left cheek	Infiltrative basal cell carcinoma
15/02/2019	60	C1	B	BE	Back	Atypical nevus
		C2	B	BM	Left side	Atypical nevus
		C3	B	BE	Left side	Angioma
	61	C1	B	BE	Left leg	Seborrheic keratosis
	62	C1	M	MM	Left eyebrow	Melanoma
22/02/2019	63	C1	B	BM	Stomach	Atypical nevus
	66	C1	M	ME	Left nose	Basal cell carcinoma
	67	C1	M	ME	nose	Carcinoma with Merkel cells

Capture Date	Subject ID	Capture ID	Binary ID	Multilabel ID	Lesion Location	Diagnosis
28/02/2019	68	C1	M	MM	Left leg	Melanoma
04/03/2019	69	C1	B	BM	Back	Melanocytic nevus
08/03/2019	71	C1	B	BM	Stomach	Atypical nevus
18/03/2019	74	C1	M	ME	Eye	Basal cell carcinoma
	75	C1	M	ME	Nose/Eye	Basal cell carcinoma
	77	C1	M	ME	Nose	Basal cell carcinoma
25/03/2019	78	C3	B	BE	Ear	Seborrheic keratosis
	79	C1	M	ME	Brow	Basal cell carcinoma
	80	C1	M	ME	Head	Epidermoid carcinoma
	81	C1	M	MM	Abdomen	Melanoma
28/03/2019	82	C1	M	MM	Right arm	Melanoma
01/04/2019	83	C1	B	BE	Nose	Seborrheic keratosis
05/04/2019	86	C1	B	BM	Chest	Atypical nevus
		C2	B	BM	Stomach	Atypical nevus
		C3	B	BM	Back	Atypical nevus
		C4	B	BM	Back	Atypical nevus
	87	C1	M	MM	Left cheek	Malignant lentigo
08/04/2019	88	C1	M	ME	Right shoulder	Basal cell carcinoma
	89	C1	M	ME	Left ear	Basal cell carcinoma
	90	C1	M	ME	Head	Basal cell carcinoma
22/04/2019	91	C1	M	ME	Face	Basal cell carcinoma with infiltration
	92	C1	M	ME	Neck	Epidermoid carcinoma
23/04/2019	94	C1	M	MM	Back	Melanoma Clark level III-IV
26/04/2019	95	C1	M	MM	Buttock	Melanoma
06/04/2019	96	C1	M	MM	Right leg	Melanoma
29/04/2019	97	C1	M	MM	Chest	Melanoma Clark level II
	98	C1	M	MM	Back	Dysplastic Nevus
	99	C1	M	ME	Face	Basal cell carcinoma
06/05/2019	100	C1	M	ME	Neck	Basal cell carcinoma
	101	C1	M	ME	Right hand	Basal cell carcinoma
07/05/2019	102	C1	M	MM	Back	Melanoma Clark level IV
17/05/2019	103	C1	B	BM	Right forearm	Blue nevus
20/05/2019	104	C1	M	ME	Nasal wing	Basal cell carcinoma
24/05/2019	106	C1	M	MM	Nose	Malignant lentigo
27/05/2019	107	C1	B	BM	Left arm	Blue nevus
	109	C1	M	ME	Back left hand	Epidermoid carcinoma
03/06/2019	110	C1	M	ME	Head	Basal cell carcinoma
	112	C1	M	ME	Helix	Basal cell carcinoma
	113	C1	M	ME	Nose	Epidermoid carcinoma
10/06/2019	116	C1	M	ME	Face	Basal cell carcinoma

B: Benign; **M**: Malignant; **MM**: Malignant Melanocytic; **ME**: Malignant Epithelial; **BM**: Benign Melanocytic; **BE**: Benign Epithelial.

Table 4-2: HS Dermatological Labeled Dataset.

Type	#Patients	#Images	#Labeled Pixels
Benign	27	40	7471
Malignant	36	36	8490
Total	618 *	76	15,961

* The total number of patients is not the sum of Benign and Malignant patients as two patients had several lesion types captured.

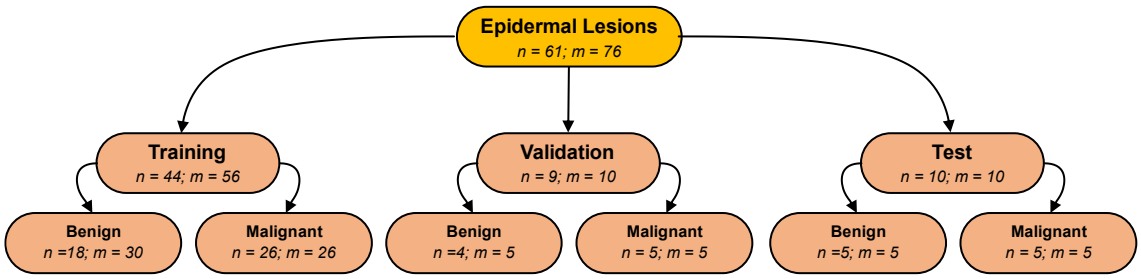

Figure 4-4: Proposed data partition employing the HS dermatoscopic database for skin cancer detection. The database was split in training, validation, and test sets.

4.4 Two-class Dermatology HS Processing Framework

The HS dermatologic classification framework is composed of three main steps: HS data pre-processing, automatic PSL segmentation, and supervised classification. Figure 4-5 shows a block diagram of this framework. The first step consists in performing the pre-processing chain to homogenize the incoming raw HS image captured by the HS dermatologic acquisition system. After performing the pre-processing, the resulting image is automatically segmented, where the normal skin and PSL pixels are discriminated. This discrimination is performed using a spectral signature reference library, composed of three spectral signatures of benign, malignant and atypical PSL (in blue, red and black colors respectively in Figure 4-5) and three normal skin spectral signatures (in green color in Figure 4-5). Finally, the pixels previously identified as lesion are classified by a supervised classifier, providing the class results, benign or malignant.

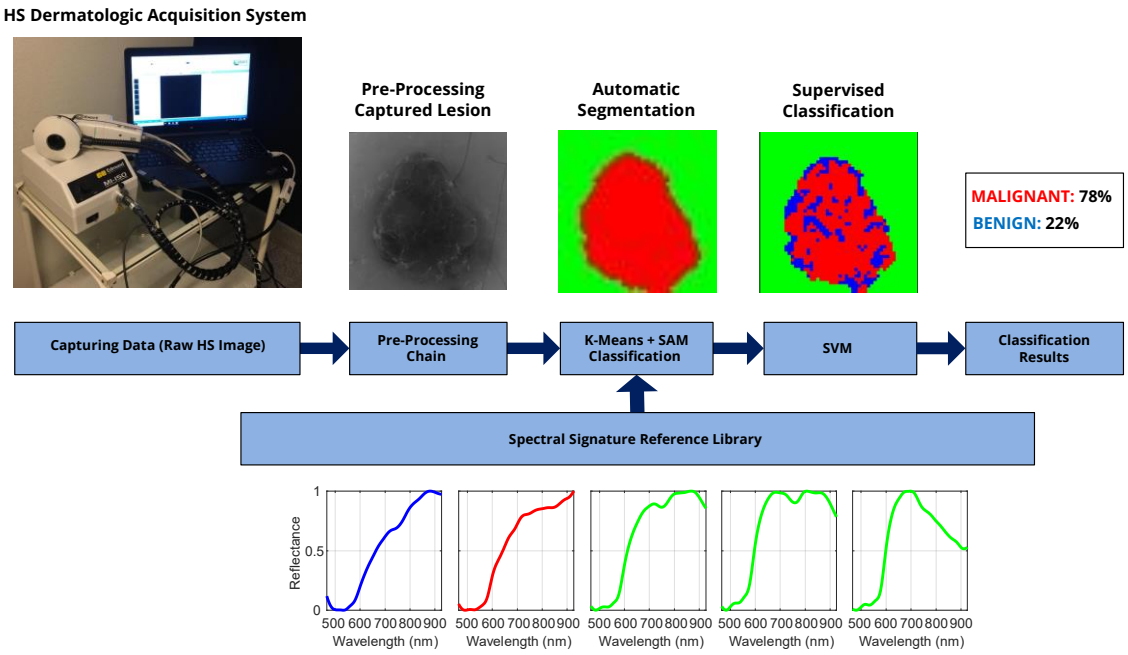

Figure 4-5: Block diagram of the HS dermatologic classification framework (pre-processing, automatic segmentation, and supervised classification) and HS dermatologic acquisition system. Spectral signature reference library is composed of six spectral signatures: benign, malignant, and atypical PSL spectral signatures in blue, red, and black colors respectively, and three different normal skin spectral signatures in green color.

4.4.1 HS Dermatologic Data Pre-Processing

The HS data were pre-processed to homogenize the spectral signatures among the different patients and data campaigns. First, data calibration was performed employing a white and dark reference acquired under the same conditions. In order to reduce the spectral noise found in the spectral signatures, the first 4 bands and the last 5 bands were removed due to the HS sensor low response in such bands. Moreover, a smooth filter was applied with a windows size of 5. The final spectral signature was formed by 116 bands. In the final step, a normalization was applied to each spectral signature to make the data range between 0 and 1 with the goal of homogenizing its amplitude, thus avoiding the subsequent processing methods to be affected by the amplitude differences caused by non-uniform illumination conditions.

4.4.2 HS Dermatologic Segmentation Framework

A processing framework to automatically segment the captured HS image into normal skin and PSL pixels based on an unsupervised segmentation algorithm is proposed (Figure 4-6). The proposed segmentation framework aims to select only PSL pixels in a HS image to reduce the data that will be sent to the classification stage and, consequently, decrease the computational cost of the classifiers, performing a two-class classification. The K-means clustering algorithm was selected to perform the segmentation as it is a well-established algorithm that provides a good delimitation of the different areas presented in an HS image scene [70]. This algorithm divides an input HS image into *K* different clusters for a previously selected *K* value. However, the identification of each cluster is not associated to any pre-established class, so the segmentation maps only represent relevant spectral differences. In this framework, first, the evaluation of the optimal *K* value for this application is performed. Different clustering evaluation methods were employed to determine the optimal *K* value, such as Silhouette, Calinski Harabasz and Davies Bouldin methods. The training dataset was used to find the optimal *K* value. Table 4-3 shows the minimum and maximum *K* values obtained from the different methods, where the most frequent value to segment the image is two. Considering this result, the range between two and seven clusters will be evaluated to compare the results and select the *K* value that provides the best result.

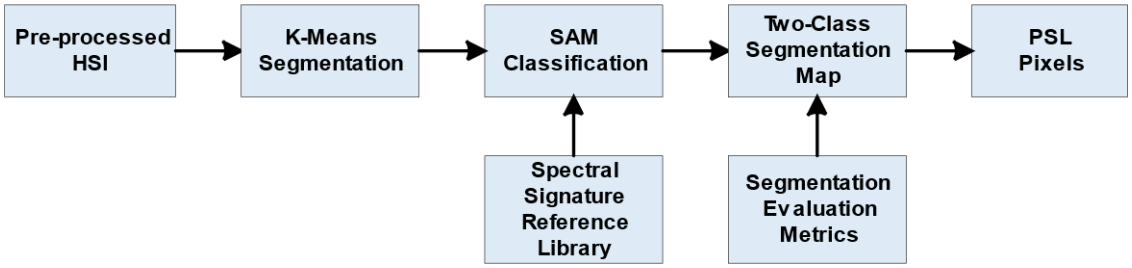

Figure 4-6: Block diagram of the HS dermatologic segmentation framework.

Table 4-3 *K* value using Silhouette, Calinski Harabasz and Davies Bouldin clustering evaluation methods.

K Value	Silhouette	Calinski Harabasz	Davies Bouldin
Minimum	2	2	2
Maximum	6	6	7
Most Frequent	2	2	2

After the *K* value evaluation, a two-class segmentation map is generated, where the PSL and the normal skin pixels are identified considering the information of each cluster of the segmentation map, using the SAM algorithm. In order to perform the SAM comparison, a spectral signature reference library of normal skin and PSL data was created, employing only the spectral signatures of the labeled training set in order to avoid the inclusion of validation or test HS images in the reference library. This library contains five different spectral signatures: three from normal skin, and two from malignant and benign PSLs (see Figure 4-7). These reference spectral signatures were obtained computing the average of the labeled data per class. The normal skin data were divided into three groups using the K-means clustering algorithm, where the number of clusters employed was selected after evaluating the results using the Silhouette, Calinski Harabasz and Davies Bouldin methods. The Silhouette and Davies Bouldin methods indicate that the optimal number of clusters to segment the normal skin data was three; taking into account the smallest index value achieved in Figure 4-8.a,b. Instead, for Calinski Harabasz method the optimal *K* value was two, considering the highest index value reached in Figure 4-8.c. Taking into account these results, the selected number of clusters to segment the training set was established in three. These reference spectral signatures were employed to automatically identify the PSL pixels through the SAM algorithm, which will be next considered as input for the supervised classification.

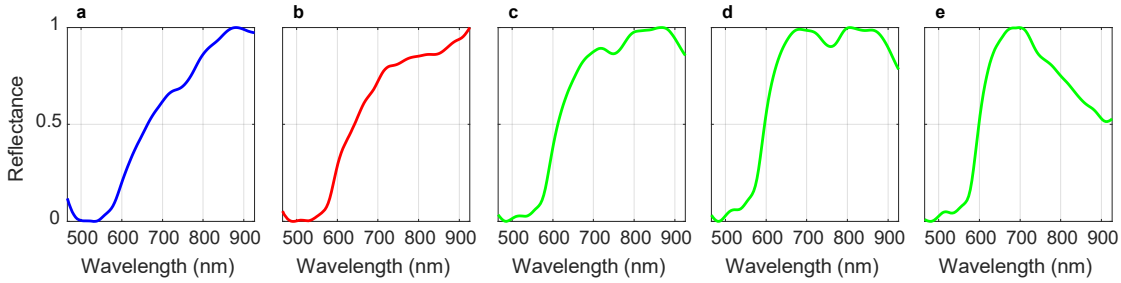

Figure 4-7: Reference spectral signatures included in the skin/PSL library. a) Benign spectral signature. **b**) Malignant spectral signature. **c, d, e**) PSL spectral signatures. Three different normal skin spectral signatures of the training dataset.

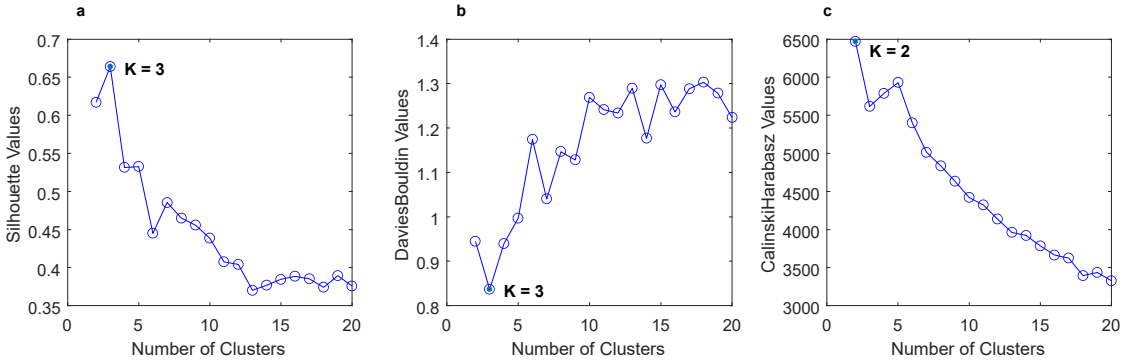

Figure 4-8: Clustering evaluation to segment the normal skin training dataset. Results of the optimal cluster number evaluation using the following methods: **a**) Silhouette (maximum K indicates optimal value). **b**) Davies Bouldin (minimum K indicates optimal value). **c**) Calinski Harabasz (maximum K indicates optimal value).

For the computation of the SAM algorithm, two different methods were employed to generate the two-class segmentation maps. The first method (called *per centroid*) compared the centroid from each cluster of the segmentation map with the spectral signatures of the reference library. In this method, the most similar spectral signature

to each centroid was assigned to a certain class (PSL or normal skin). The second method (called *per pixel*) compared each pixel in a certain cluster with the spectral signatures of the reference library and computed the sum of the resulting SAM values. Then, the smallest sum in each centroid is assigned to a certain class (PSL or normal skin). Finally, a morphological closing operation based on dilatation followed by erosion was applied to the two-class segmentation map in order to remove small and isolated regions and to obtain a better representation of the lesion. Figure 4-9 shows an example of a segmentation, where Figure 4-9.a shows the gray-scale image and Figure 8.b shows the segmentation map of an HS image using seven clusters, where the colors are randomly assigned. Figure 4-9.c shows the classification map obtained after applying the SAM methodology, while Figure 4-9.d shows the same two-class segmentation map after the morphological post-processing. In these maps, normal skin and PSL pixels are represented in green and red colors, respectively. Finally, these results were compared with the ground-truth maps of the validation dataset using segmentation evaluation metrics to select the most appropriate K value and SAM comparison method. The PSL pixels were used as input for the supervised classification in the complete processing framework.

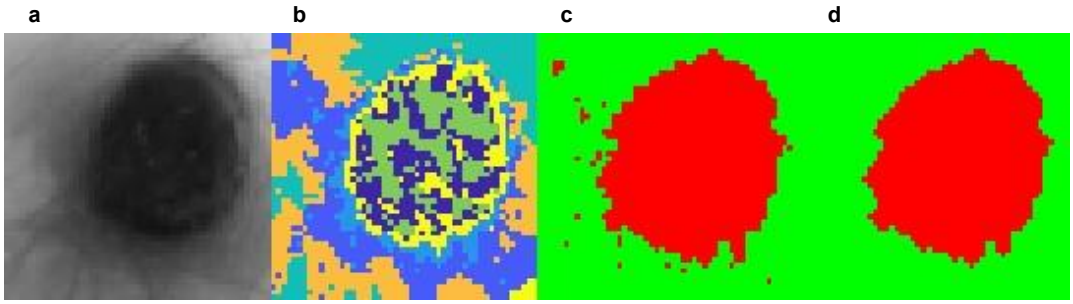

Figure 4-9: HS dermatologic segmentation example. a) Gray-scale image. **b**) Segmentation map using seven clusters (colors are randomly assigned). **c**) Two-class segmentation map obtained after comparing the five centroids with the reference library using the SAM algorithm (red indicates PSL and green normal skin). **d**) Two-class segmentation map after applying morphological closing operation.

Ten HS validation images from 8 different patients were evaluated with two methods (*per centroid* and *per pixel*) based on the K-means and the SAM algorithms, using different K values to find out which combination of method and number of clusters offers the best results.

Figure 4-10 shows the boxplot results of the Jaccard coefficient metric using the 10 HS validation images for each method (per centroid and per pixel) using different number of clusters in the range $2 \leq K \leq 7$. In the figure, the boxes boundaries represent the IQR, which refers to the results of the validation set comprised between the first quartile (Q1, 25th percentile) and the third quartile (Q3, 75th percentile). The central bars represent the median result values (Q2, 50th percentile), while the error bars depict minimum and maximum values of the Jaccard coefficient for such method excluding any outliers. The outlier values are represented in the plot with the small dots. Attending to the boxplots, $K = 2$ with the per centroid method offers the best IQR value with a median of 0.81, while $K = 3$ and $K = 7$ provide the best median results in both methods higher than 0.82, also representing a reduced IQR for $K = 3$. However, it should be noted that most of the results in the boxplot present one or two outliers (represented with small dots), where their vertical positions show the Jaccard value for a specific HS image of the validation set in such method. This abnormal distance from

the other values is produced due to the fact that images *P20_C2* and *P113_C1* were not taken in optimal conditions, producing shadows or glares in the HS images (see gray-scale images in Figure 4-11). Considering these outliers and analyzing the two-class segmentation maps when $K = 2$ and $K = 3$, no PSL pixels are detected in *P113_C1* image. On the contrary, it is observed that the results using $K = 7$ provide a better segmentation of the PSLs. For example, *P113_C1* is better segmented than the $K = 2$ and $K = 3$ results (as it is shown in Figure 4-11), allowing PSL classification to be performed by the supervised classifier. In addition, using $K = 7$, the per pixel method provides a better median value (0.82) than the per centroid method (0.71), representing an improvement of 11%. For this reason, we selected $K = 7$ with the per pixel method as the most suitable configuration for the overall framework.

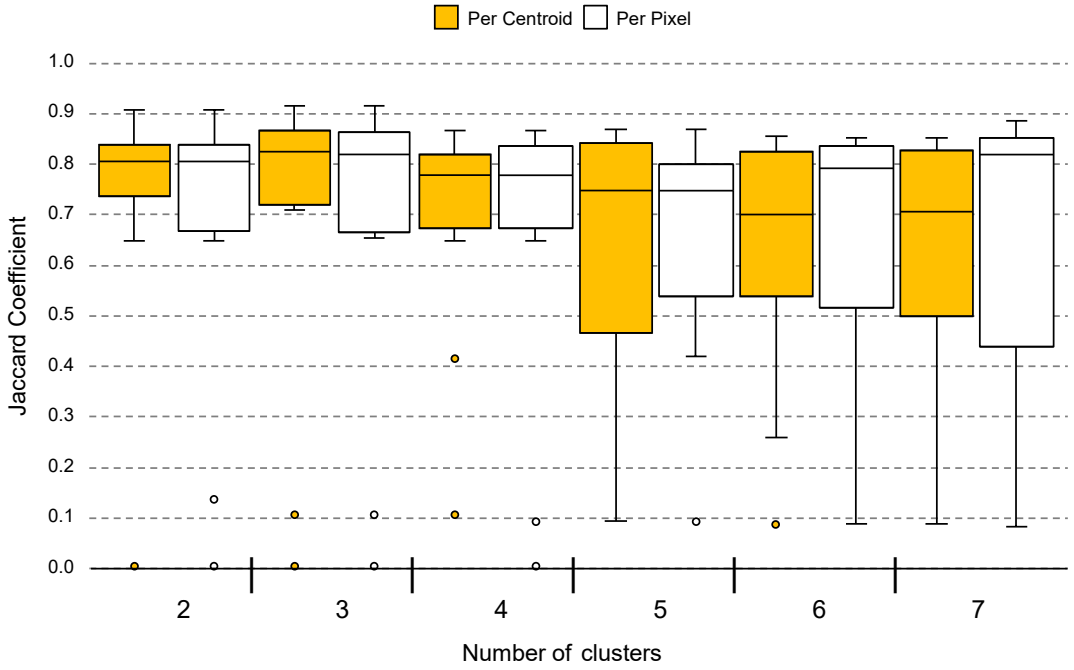

Figure 4-10: Comparison between *per centroid* and *per pixel* methods using different number of clusters for the validation data using the Jaccard coefficient. The box boundaries represent the IQR of the results. Central bars and error bars depict median and minimum/maximum values of Jaccard coefficient, respectively. The small dots outside the minimum/maximum values represent the outliers of the Jaccard coefficient found in each method.

Figure 4-11 shows the qualitative results obtained in the segmentation framework using the per pixel method. Figure 4-11.a shows the gray-scale images for each HS validation cube, while Figure 4-11.b shows the ground-truth, where the PSL has been manually segmented by an expert. Figure 4-11.c-d show the two-class segmentation maps obtained with $K = 3$ and $K = 7$, respectively. It is observed that the results in both cases are very similar. Nonetheless, in the case of *P113_C1* using $K = 7$, the qualitative results are better than in the other cases. Finally, Figure 4-11.e shows the two-class segmentation maps after performing a morphological closing operation to remove small-isolated regions of PSL pixels, ensuring that in the next classification stage, only PSL pixels will be employed. The PSL area is clearly identified in almost all images, except in images *P20_C2, P60_C1*, and *P113_C1*, achieving an average Jaccard value of 0.82.

Taking into account the results obtained, it has been concluded that the per pixel method with $K = 7$ and morphological post-processing provides the best results with

the validation database. Next, the evaluation of the test database, composed by 10 HS images from 10 different patients, using the selected method was performed to validate the algorithm for the automatic identification of the PSL pixels. Figure 4-12 shows the qualitative and quantitative results for each HS test image. The resulting two-class segmentation maps after applying the morphological post-processing are shown in Figure 4-12.c, and below, their respective Jaccard coefficients. It is worth noticing that the results obtained in images *P13_C1, P14_C1, P23_C1, P74_C1, P97_C1, P102_C1*, and *P107_C1*, the PSL areas are clearly identified, achieving an average Jaccard value of 0.81.

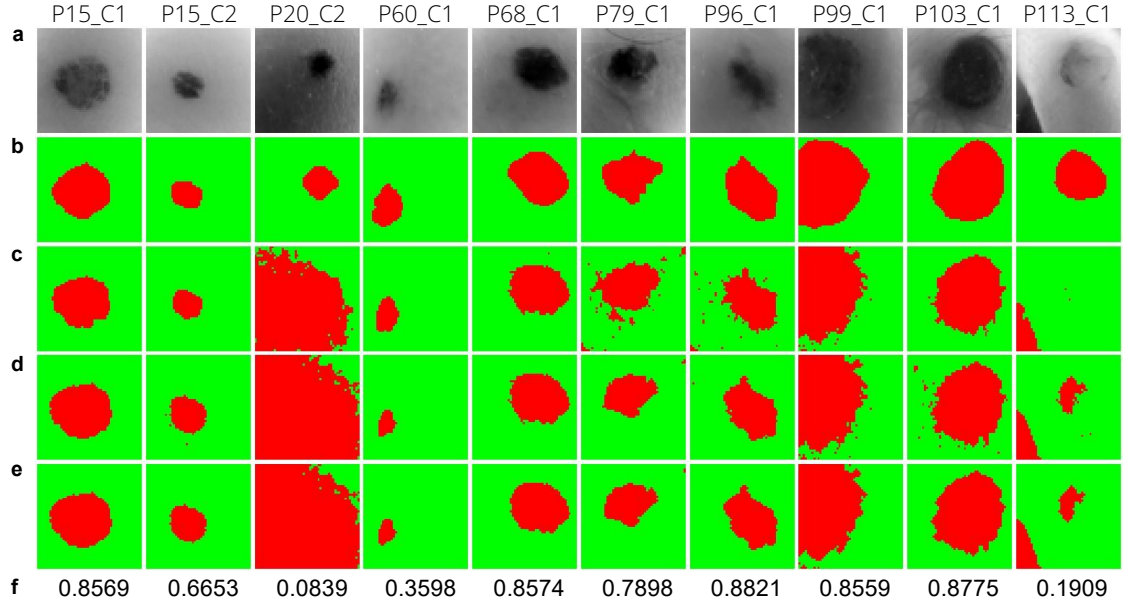

Figure 4-11: Two-class segmentation maps of the validation database using the per pixel method. a) Gray-scale images. b) Ground-truth maps. c) Results with K = 3. d) Results with K = 7. e) Results with K = 7 and morphological post-processing. f) Jaccard coefficient values of the results with K = 7 and morphological post-processing.

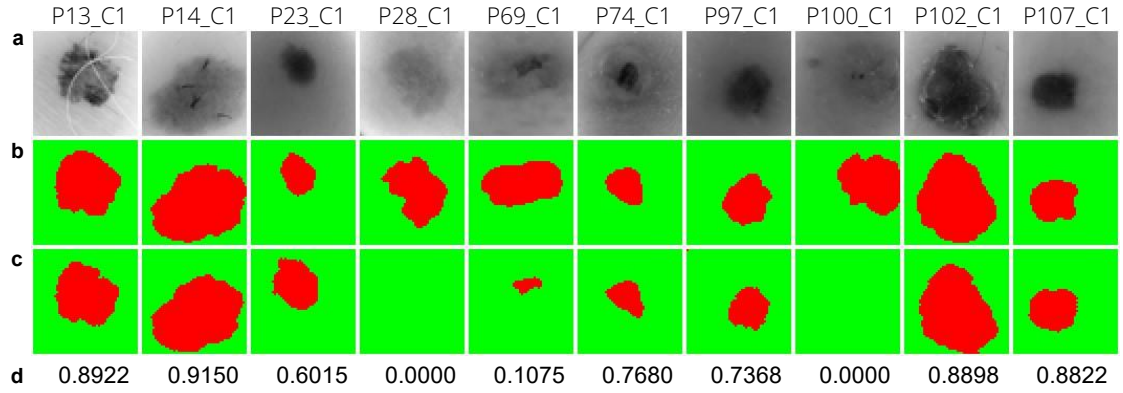

Figure 4-12: Two-class segmentation maps of the test database using *per pixel* method with *K* = 7. a) Gray-scale images. b) Ground-truth maps. c) Results with morphological post-processing. d) Jaccard coefficient values of the results with morphological post-processing.

Nonetheless, in image *P69_C1*, a small area of the PSL pixels was identified with a Jaccard value of 0.10. However, this area corresponds with the center of the lesion, enabling the more relevant pixels of the PSL to be processed by the next classification stage. On the other hand, in images *P28_C1*, and *P100_C1* the segmentation process did not detect any PSL pixel. After analyzing the spectral signatures of these images and comparing them with the spectral signatures of the reference library, it was observed

that the PSL spectral signatures of both images were very similar to the normal skin references. This phenomenon can be observed in Figure 4-13, where a comparison between the reference spectral signatures and the average of the PSL and normal skin pixels was performed. In the case of image *P28_C1* (Figure 4-13.a), the PSL was diagnosed as a benign lesion; however, the average spectral signature of the PSL is more similar to the normal skin references than to the benign reference. In the case of *P100_C1* (Figure 4-13.b), the PSL was diagnosed as a malignant lesion, but the average spectral signature of the PSL is more similar to the normal skin references than to the malignant reference. These results suggest the necessity of increasing the HS database to improve the spectral signature reference library with a wider variability of PSLs and normal skin types.

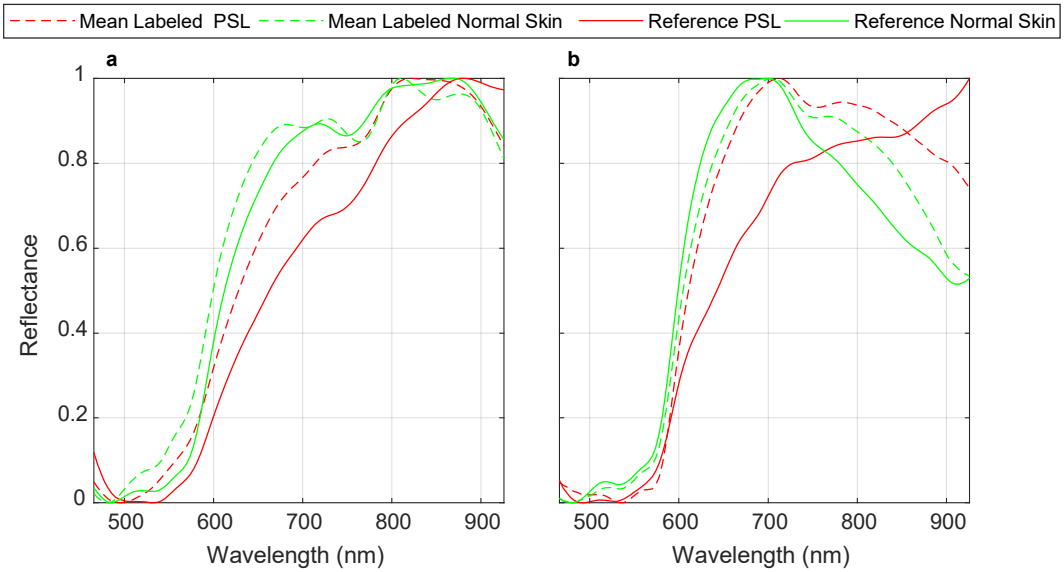

Figure 4-13: Average spectral signatures of the test set. Labeled PSL (dashed red line) and normal skin (dashed green line) pixels, and reference spectral signatures of PSLs (red line) and normal skin (green line)**. a**) P28_C1 (benign PSL). **b**) P100_C1 (malignant PSL).

4.4.3 HS Dermatologic Classification Framework

The HS dermatologic classification framework developed in this section is based on a supervised classification with an automatic fine tuning of the classifier hyperparameters employing an optimization algorithm. The pre-processed HS labeled dataset was employed to find the most suitable classification model using the data presented in Section 4.3. The HS labeled dataset of PSL spectral signatures was employed to train, validate, and test the developed classification algorithms. The validation process was performed using a stratified patient assignment where the labeled data were divided into three independent sets: test, validation, and training. The test set was composed by labeled data from 10 HS images from 10 patients with 2,472 pixels. The validation set was formed by labeled data from 10 HS images from 9 patients, having 1,931 pixels and, the training set was composed by the remaining labeled data of 56 HS images from 44 patients, formed by 11,558 pixels. Figure 4-14 shows the block diagram of this processing framework, where a Genetic Algorithm (GA) was employed to optimize the hyperparameter values of the supervised classifier using the training and validation sets. The AUC was used for the evaluation of the validation results. After finding the optimal hyperparameters, the classifier is trained with the training set and evaluated with the test set, obtaining the final evaluation metrics. The

supervised classification algorithms evaluated in this section are SVM, RF and ANNs. The experimental results obtained in the classification of the labeled samples are presented. Table 4-4 shows the AUC results obtained with each supervised classifier using the default and the optimal hyperparameters to classify the validation dataset.

Table 4-4: Area under the ROC Curve (AUC) results obtained with default and optimized hyperparameters.

Classifier	Default Hyperparameters	AUC	Optimized Hyperparameters	AUC
SVM Linear	$C = 1$	0.70	$C = 94.07$	0.89
SVM RBF	$C = 1; \gamma = 1/116$	0.66	$C = 13.41; \gamma = 8.43$	0.77
SVM Sigmoid	$C = 1; s = 1/116; cf = 0$	0.50	$C = 45.75;\ s = -9.53; cf = -14.22$	0.83
RF	$nTrees = 500$	0.61	$nTrees = 3$	0.61
ANN	$neurons_{per\ layer} = [1]$	0.59	$neurons_{per\ layer} = [1; 3; 443; 2]$	0.61

$\boldsymbol{C}$: Cost; $\boldsymbol{\gamma}$: Gamma; $\boldsymbol{cf}$: Intercept Constant; $\boldsymbol{s}$: Slope.

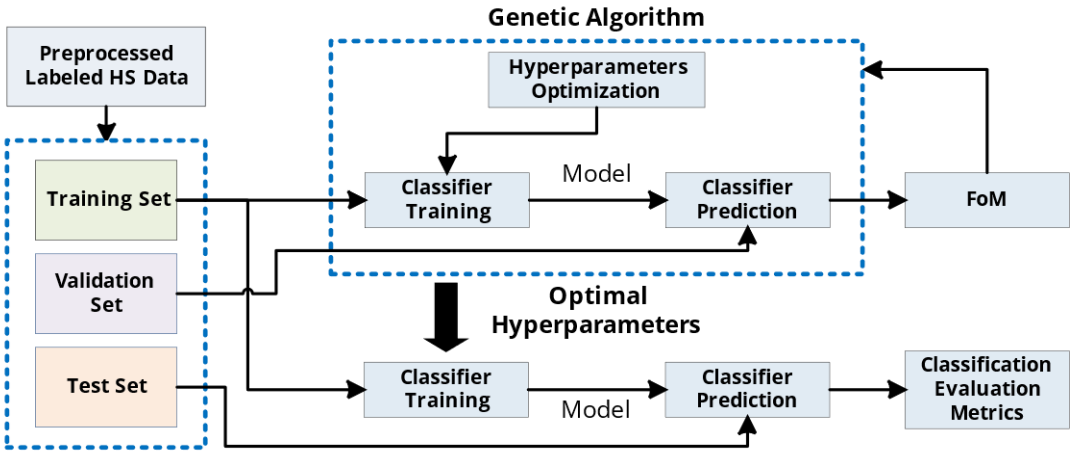

Figure 4-14: Proposed block diagram of the HS dermatologic classification processing framework.

As can be seen from the results, the optimized SVM Linear algorithm achieved the best AUC (0.89), followed by the SVM Sigmoid and SVM RBF algorithms (0.83 and 0.77, respectively). In addition to these results, Figure 4-15 shows the ROC curves obtained with each classifier with and without hyperparameters optimization. In this figure it is possible to observe the differences between the curves, where SVM Linear, Sigmoid and RBF classifiers improve the results after the optimization. Nevertheless, RF and ANN classifiers show no relevant improvement in the results. Taking into account these results, the SVM Linear was selected for the classification of the PSLs to complete the processing framework, achieving a sensitivity of 96.7%.

In order to assess the results obtained with the SVM Linear classifier optimized with the validation set, the classifier was evaluated on the test set. Figure 4-16 shows the ACC results of each HS test image, where it is possible to observe that 8 images were classified with an ACC higher than 80%, one image (*P102_C1*) was identified with a 53% of ACC, and only one HS image (*P13_C1*) was not correctly classified. As it can be seen in Figure 4-17, the average spectral signatures of the malignant lesions *P13_C1* and *P102_C1* are quite different from the reference spectral signatures of such classes (Figure 4-17.a,b). On the contrary, *P14_C1* offers an excellent classification accuracy value as its average spectral signature is very similar to the benign reference spectrum (Figure 4-17.c). In this sense, it is possible that the skin cancer database requires more data and patients' variability to generalize a classification model able to achieve higher

accuracy. Summarizing, on the test set, the classifier provided an average ACC of 78%, correctly identifying 9 PSLs and incorrectly identifying 1 PSL.

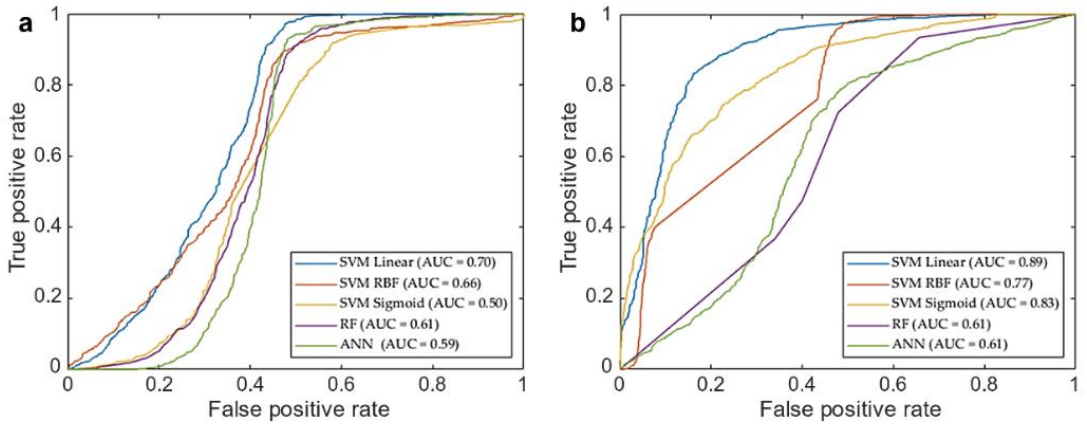

Figure 4-15: ROC curves for validation classification results obtained with the five classifiers. a) Classification results with default parameters. **b**) Classification results with optimized hyperparameters.

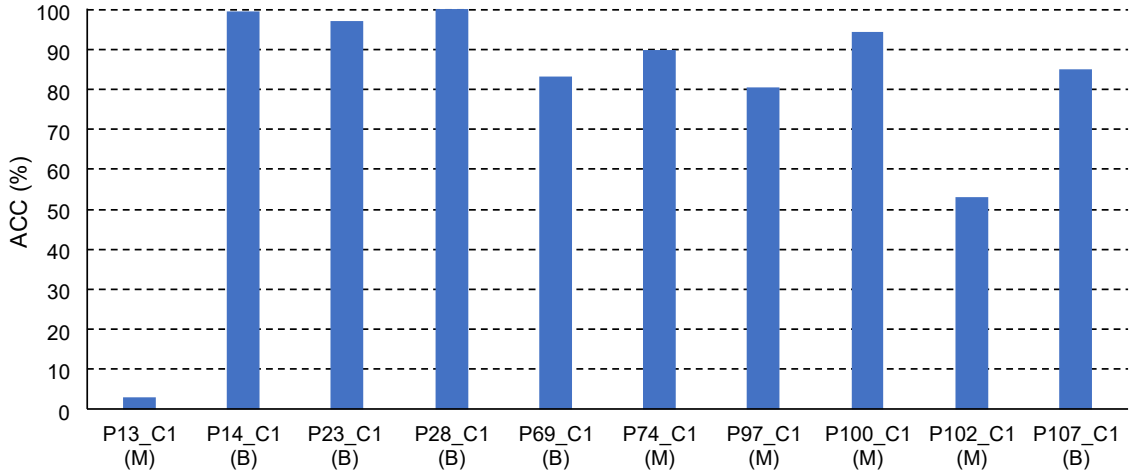

Figure 4-16: Test classification accuracy results obtained with the SVM Linear classifier. Below each patient ID, the correct diagnosis of the PSL is presented. B: Benign; M: Malignant.

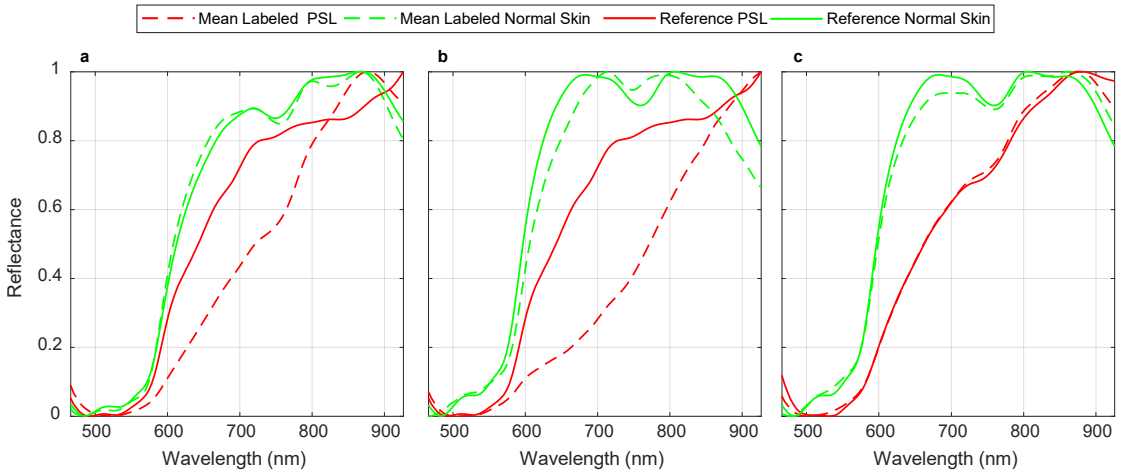

Figure 4-17: Average spectral signatures of the labeled PSL (dashed red line) and normal skin (dashed green line) pixels, and reference spectral signatures of PSLs (red line) and normal skin (green line). a) P13_C1 (malignant PSL). **b**) P102_C1 (malignant PSL). c) P14_C1 (benign PSL), correctly classified.

4.4.4 Experimental Results Discussion

The results obtained with the fully HS dermatologic processing framework has been presented. This framework is composed by the selected segmentation and classification algorithms which provided the best results in the previous analysis.

Figure 4-18 shows the ACC results for each HS test image after applying the segmentation and classification of the PSL pixels. On the one hand, in the images *P28_C1*, and *P100_C1*, no pixels were identified as PSL by the segmentation stage. Thus, the classification stage could not provide the identification of the pixels. In this case, the system will require asking the user a new acquisition of the PSL due to the non-optimal conditions of the captured HS image. On the other hand, the PSL image *P13_C1* achieved a very low accuracy in the identification of the lesion (10%), while image *P102_C1* obtained an accuracy of 45%. As explained in the previous section, the spectral signatures of these lesions are quite different from the reference spectra, indicating the need for an expanded database where the inter-patient and inter-lesion variability were taken into account. The remaining HS test images (*P14_C1, P23_C1, P69_C1, P74_C1, P97_C1*, and *P107_C1)* provided competitive results in the identification of the PSL type with an average ACC of 85%.

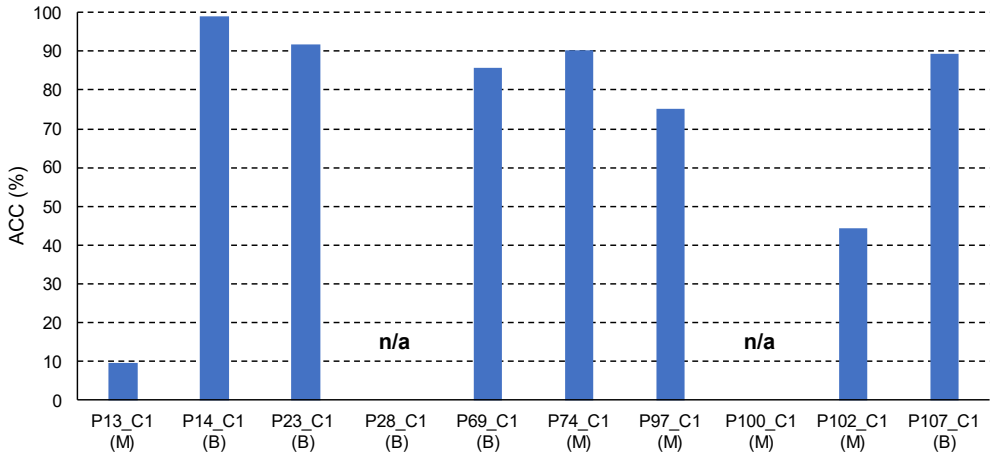

Figure 4-18: Test classification ACC results obtained with the SVM Linear classifier and with the pixel segmentation dataset. n/a: HS images without PSL pixels identified in the segmentation stage.

Summarizing, using the proposed processing framework in this preliminary study, two of the HS test images were not evaluated due to non-optimal conditions of the acquisition procedure. In addition, another HS test image was not correctly identified due to the necessity of increasing the HS PSL database in order to better generalize the segmentation and classification models for the large diversity of PSLs and skin types. However, using a risk threshold of 40% for the discrimination of the malignant lesions, 7 of 8 evaluable HS test images (87.5%) were accurately classified according to the PSL pathological diagnosis. In this sense, the malignant PSLs with an accuracy higher than 40% will be considered to have clear evidence of malignant behavior.

These preliminary results are very promising due to the rigorous validation methodology employed, which is based on dividing the database into training, validation, and test sets. In this sense, the test set consists of data from patients who were not involved in the generation of the processing models. This guarantees the reliability of the achieved results without producing overfitting, which can provide

optimistic accuracy results. In addition, the average execution time for the proposed HS dermatologic framework is ~500 ms, requiring ~220 ms to perform the pre-processing stage, ~135 ms for the segmentation stage and ~145 ms to execute the supervised classification. The implementation was performed using MATLAB® in an Intel i7-4790K with a working frequency of 4,00 GHz and a RAM memory of 8 GB. Therefore, this preliminary study reveals the potential use of HSI as a non-invasive imaging modality for in-situ clinical support during the routine clinical practice.

In order to compare the results obtained in this preliminary study with the state-of-the-art, a summary table is shown in Table 4-5. It is worth noting that our work cannot be directly compared with most of the studies already published since our focus is on distinguishing between benign and malignant PSLs, whereas the other research works are based on distinguishing between melanoma and non-melanoma lesions. In consequence, since the dataset used in each research is different, the comparative between different approaches is not fair. Nevertheless, we would like to present the most relevant results of the current state of the art.

Table 4-5: Comparison of the obtained results with the state-of-the-art.

Reference	Patients	Images	Bands	Spectral Range (nm)	Sensitivity (%)	Specificity (%)
[152]	1278	1391	15	483–950	80.4 *	75.6
[147]	311	348	8	400–1000	100.0 *,¥	5.5
[145]	111	360	10	430–950	100.0 *,¥	5.5
[237]	55	36	10	430–950	71.4 *,α	25.0
[144]	1257	1612	10	430–950	98.2 *	9.5
[162]	97	134	124	380–780	96.0 *	87.0
[156]	-	157	10	365–1000	97.0	97.0
[156]	-	712	10	365–1000	99.0	93.0
This work	61	76	116	450–950	87.5/100.0 *	100.0

* Sensitivity for melanoma detection. ¥ Only reported sensitivity for 3 melanoma lesions. α Only reported sensitivity for 4 melanoma lesions.

In [152], the research of Tomatis *et al.* used a dataset of 1,278 patients with 1,391 images, where 184 lesions were melanomas. The dataset was divided into three sets, where the test set was composed by 347 images, including 41 melanomas. The sensitivity obtained was 80.4% with a specificity of 75.6%. Moncrieff *et al.* performed a discrimination between melanoma and non-melanoma lesions by using the MS SIAscope/SIAscopy system to generate a database composed by 52 melanomas and 296 non-melanomas, achieving a sensitivity and specificity of 82.7% and 80.1%, respectively [147]. The studies performed by Fink *et al.* [145] and Song *et al.* [237] were based on MelaFind system, achieving a 100% and 71.4% of sensitivity, respectively, but having a very low number of melanomas in the database (3 and 4 melanomas, respectively). However, the multicenter study of Monheit *et al.* [144] evaluated the MelaFind tool with a dataset of 1,612 images (including 114 melanomas) and achieved a sensitivity of 98.2% but with a very low specificity (9.5%). In another study performed by Nagaoka *et al.* authors generated a database composed by 24 melanomas and 110 non-melanoma lesions using a HS system capable of obtaining 124 bands, achieving a sensitivity and specificity of 96% and 87%, respectively [162].

To the best of our knowledge, the only work found in the literature which deals with the discrimination between malignant and benign PSL was performed by Stamnes *et al.* [156]. In this work, two datasets were evaluated: a small dataset with 157 images (35 malignant and 39 benign); and a large dataset, which included lesions employed to train the system, composed by 712 images (80 malignant and 217 benign). The results

were promising achieving sensitivity and specificity of 97% and 99%; and 97% and 93% for the small and large datasets, respectively. Compared to our proposed system, MelaFind performs similar in the identification of melanoma, but fails in the identification of non-melanoma lesions. The fairest comparison is regarding the results obtained by Stammes *et al.* that employed a similar annotation scheme to our work, i.e., malignant vs. benign. Our system provided the best specificity results that can be found in the literature, but the sensitivity result for the malignant lesions is lower than other works. We have computed the sensitivity of our approach in classifying melanoma lesions. In the test set, 2 melanoma lesions (P102_C1 and P97_C1) were included in the malignant class. Using the risk threshold of 40%, these two lesions were correctly identified as melanoma; hence, the sensitivity of our proposed approach for melanoma detection would be 100%. In any case, the reduced number of HS images in the test set (10 images, 5 benign and 5 malignant) in our study, highly penalizes the results when an HS image is misclassified, especially for the less common class (i.e., melanoma).

4.5 Three-class Dermatology HS Processing Framework

A variation of the segmentation and classification framework was developed with the goal of differentiating between malignant, benign, and atypical PSLs. An Atypical mole, or *dysplastic nevus*, is a transition between benign moles and melanoma. A significant number of atypical moles evolve into melanoma and, for this reason, they should be promptly noticed and diagnosed [238]. The HS dermatoscopic database presented in Section 4.3 included nine HS images from atypical moles that were labeled as benign. In this section we present the experimentation after dividing the dataset as shown in Table 4-6, where the dataset is labelled into three classes: *Benign*, *Atypical* and *Malignant*.

Table 4-6: Three-class HS Dermatological dataset. Including number of patients, number of HS images and number of labeled pixels.

Type	#Patients	#Images	#Labeled Pixels
Benign	22	31	6,003
Atypical	5	9	1,468
Malignant	39	39	8,734
Total	**66**	**79**	**16,205**

In previous experiments, it was deduced that the most effective number of clusters for the segmentation of the PSL and healthy skin was seven ($K = 7$) using clustering evaluation methods. After that, a two-class segmentation map was generated using the spectral signature reference library. The PSL and the normal skin pixels were identified considering the information of each cluster of the segmentation map and the spectral library, using the SAM algorithm. However, the two best number of clusters in the experiments presented in Section 4.4.2 (Figure 4-10) were $K = 3$ and $K = 7$. Therefore, a pragmatic decision was made for this three-class dermatology HS processing framework, selecting the optimal k value in three clusters ($K = 3$). This choice was motivated by the good trade-off between the computational requirements and the PSL segmentation accuracy, especially since this approach was orientated to achieve a hardware implementation on low-power platforms, targeting its future use as a hand-held device. After that, the spectral signature reference library used to generate the

two-class segmentation map was modified. A new spectral signature reference was added, atypical lesion. In the previous section, this type of lesion had been added as benign lesion. In this sense, the benign spectral signature reference was modified. Finally, the library contains six different spectral signatures: three from PSL (*malignant*, *benign*, and *atypical* lesions, in Figure 4-19, represented in red, blue, and black colors, respectively) and three from normal skin (in green color in Figure 4-19).

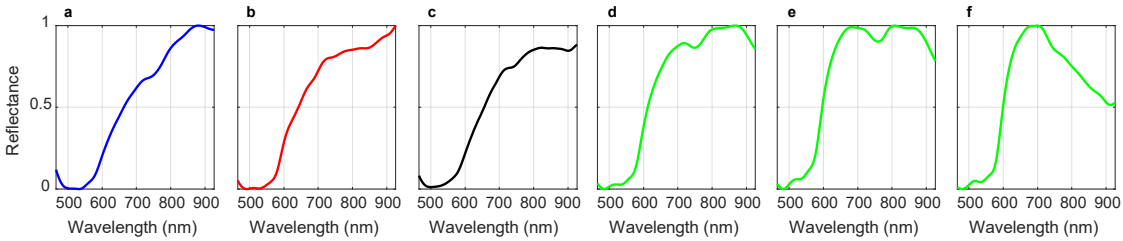

Figure 4-19: Reference spectral signatures included in the skin for the three-class PSL library. a) Benign spectral signatures **b**) Malignant spectral signature. **c**) Atypical spectral signature. **d,e,f**) Three different normal skin spectral signatures of the training dataset.

Finally, the SVM model was generated again to perform a three-class classification: malignant, benign, and atypical lesions. In order to find the optimal configuration of the SVM, the hyperparameters for each type of kernel were adjusted using a GA and a custom Figure of Merit (FoM) conceived to obtain the most balanced accuracy results among the three classes. The FoM is shown in Eq. (33), where the similarity measure is calculated as the sum of the accuracy per class (ACC) divided by the absolute difference of the accuracies plus a regularization term (1). In addition, the FoM applied a normalization term that depends on the total number of classes, which is intended to adjust the FoM to be independent of the number of classes and to ensure that the FoM is comparable in different contexts. In this FoM, i and j are the indices of the classes that are being computed and n is the number of classes. Higher FoM values imply simultaneously increasing the ACC and reducing the differences between classes. Finally, to evaluate the results obtained for the optimized classifier, the false negative rate per class (FNR_c) was computed. FNR_c reveals the misclassifications produced by the classifier and discovers which classes were misclassified. Eq. (34) shows the mathematical expression of the FNR_c, where FN_i is the number of false negatives in the *i-th* class and P is the total number of positive samples.

$$FoM = \frac{1}{2} \cdot \left(\sum_{\substack{i,j \\ i<j}}^{n} \frac{ACC_i + ACC_j}{|ACC_i - ACC_j| + 1} \right) \cdot \binom{n}{2}^{-1} \tag{33}$$

$$FNRc = \frac{FN_i}{P} \tag{34}$$

Following the same procedure as in Section 4.4, the segmentation framework was validated, achieving similar results. Figure 4-20 shows the qualitative and quantitative results of each HS test image. The resulting two-class segmentation maps after applying the morphological post-processing are shown in Figure 4-20.c, and below (Figure 4-20.d), their respective Jaccard coefficient using the ground-truth (Figure 4-20.b) to compute this metric. The segmentation process does not detect PSL pixels in *P28_C1*, *P71_C1*, and *P100_C1* images. After analyzing the spectral signatures of these images and comparing them with the spectral signatures of the reference library, it is observed

that the PSL spectral signatures of each image are very similar to the normal skin references. This phenomenon can be observed in Figure 4-21, where a comparison between the reference spectral signatures and the average of the PSL and normal skin pixels was performed. In the case of *P28_C1* (Figure 4-21.a), the PSL was diagnosed as a benign lesion; however, the average spectral signature of the PSL is more similar to one of the normal skin references than to the benign reference. In the case of *P71_C1* (Figure 4-21.b), the PSL was diagnosed as an unknown lesion, but the average spectral signature of the PSL is more comparable to one of the normal skin references than to the unknown reference. The same behavior is found in *P100_C1* (Figure 4-21.c) where the PSL was diagnosed as a malignant lesion.

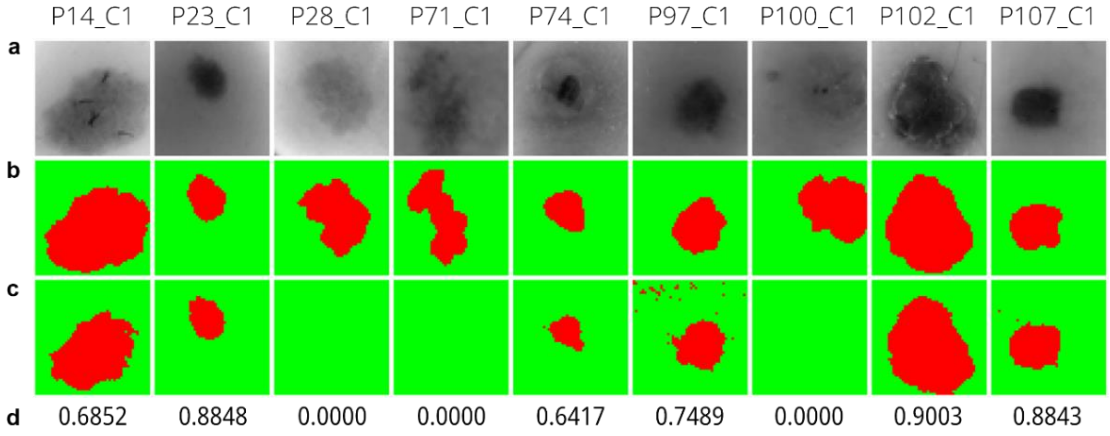

Figure 4-20: Two-class segmentation maps of the test database using *per pixel* method with $K = 3$. a) Gray-scale images. b) Ground-truth maps. c) Results with morphological post-processing. d) Jaccard coefficient values of the results with morphological post-processing.

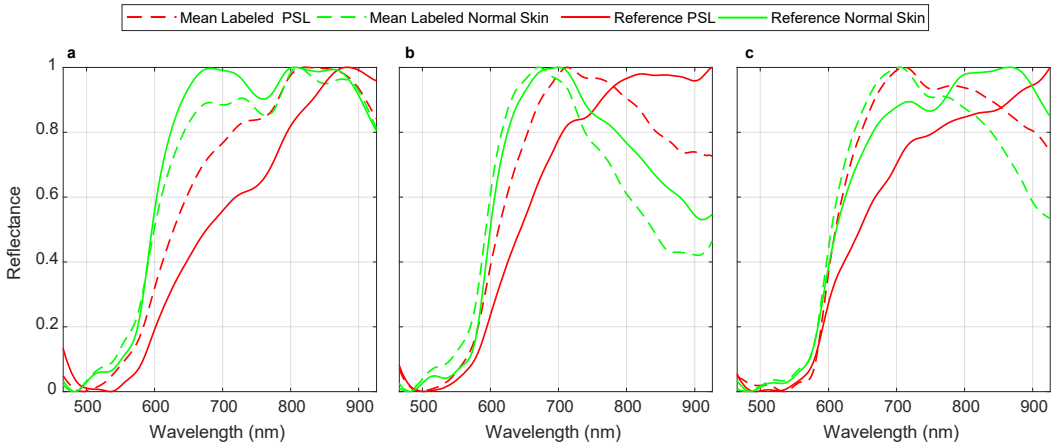

Figure 4-21: Average spectral signatures of the labeled PSL (dashed red line) and normal skin (dashed green line) pixels and reference spectral signatures of PSLs (red line) and normal skin (green line). a) P28_C1 (benign PSL). **b**) P71_C1 (atypical PSL). **c**) P100_C1 (malignant PSL).

Using the SVM algorithm and the labeled samples of the PSL from the HS dataset, three different models were obtained. Table 4-7 shows the *FoM* results and the values of the optimized hyperparameters obtained with the GA algorithm for each kernel classifier. The obtained results show that the SVM Sigmoid model achieved the best *FoM* (60.67%), followed by the SVM Linear and the RBF (38.82% and 29.98%, respectively). Considering these results, the SVM with Sigmoid kernel was selected for the HS dermatologic classification framework.

Table 4-7: Figure of Merit (FoM) results obtained with the optimized hyperparameters.

Classifier	Hyperparameters	*FoM* (%)
SVM Linear	$C = -21.56$	38.82
SVM RBF	$C = 9.85; \gamma = 4.83$	29.98
SVM Sigmoid	$C = 1.54; s = -20.79; cf = -1.97$	60.67

C: Cost; γ: Gamma; cf: Intercept Constant; s: Slope.

Figure 4-22.a illustrates the *FNRc* results for each validation HS image, where it is possible to observe that images *P15_C1*, *P15_C2*, *P20_C2* and *P113_C1* present an accurate identification of the diagnosed PSL, while images *P96_C1* and *P99_C1* have some pixels that were misclassified but clearly reveal the correct diagnosis. On the contrary, images *P60_C1, P60_C2* and *P68_C1* misclassified more than 50% of the labeled pixels. Image *P68_C1* classified 58.2% and 9.9% of the pixels as benign and atypical classes, respectively, being a malignant PSL. In summary, six out of nine images of the validation set were correctly diagnosed with the proposed classification framework based on the optimized SVM Sigmoid classifier. Figure 4-22.c shows the qualitative classification maps obtained for the validation set where green color indicates the skin pixels, while red, orange, and blue colors represent the pixels classified as malignant, atypical, and benign PSLs, respectively. These results also include the detailed percentage of pixels classified as each PSL in each HS cube (Figure 4-22.d).

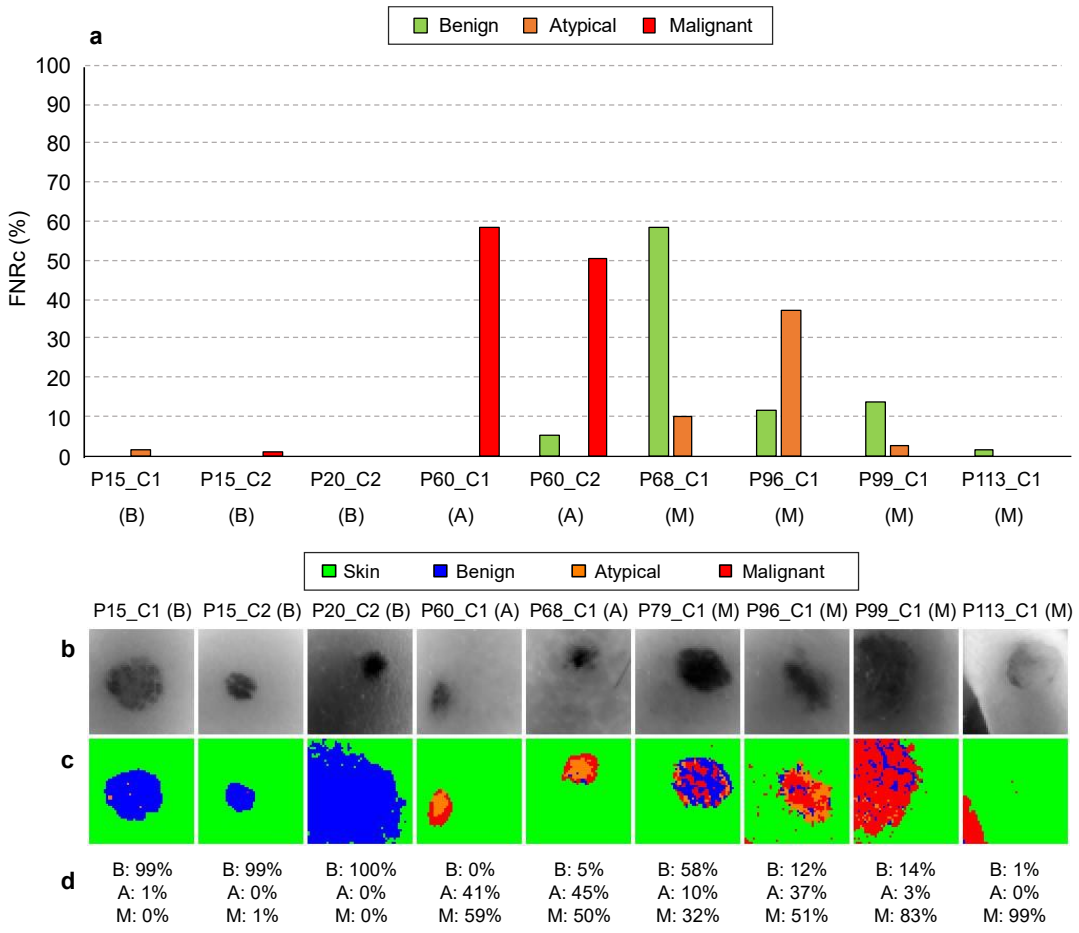

Figure 4-22: Quantitative and qualitative classification results using validation set. **a**) FNRc results per each HS image obtained with the SVM Sigmoid classifier. **b**) Grayscale image. **c**) classification map, where skin, malignant, benign, and atypical pixels are represented in green, red, blue, and orange colors, respectively. **d**) Percentages of PSL pixels classified to each class. On the right side of each patient ID, the correct diagnosis of the PSL is presented between brackets. B: Benign; A: Atypical; M: Malignant.

In order to assess the results obtained with the SVM Sigmoid classifier optimized with the validation set, the classifier was evaluated on the test set. Figure 4-23.a shows the *FNRc* results of each HS test image. On the one hand, in the images *P28_C1, P71_C1,* and *P100_C1*, no pixels were identified as PSL by the segmentation stage and the classification stage could not provide the results. The lack of identification of PSL pixels in such cases occurs because the PSL spectral signatures of these HS images were highly similar to the normal skin references employed in the K-means segmentation. This can be appreciated in the gray scale images of the PSLs presented in Figure 4-23.b, where the PSL pixels of such images are quite similar to the skin pixels. These results could indicate the necessity of increasing the HS skin database for including high inter-patient variability of data. On the other hand, the PSL images *P14*_C1, *P23_C1*, and *P97_C1* were correctly identified, having in the latter one only 22.3% of pixels misclassified as atypical class. In the case of image *P74_C1*, 48.7% of the pixels were misclassified as atypical class, but the remaining 51.3% were correctly identified as malignant PSL. In the remaining images (*P102_C1*, and *P107_C1)* the misclassifications values were above 50%. *P102_C1* misclassified 51% and 12.5% of pixels as benign and atypical classes, respectively, being a malignant PSL. Finally, in *P107_C1,* 59.6% of pixels were classified as malignant class, being a benign PSL.

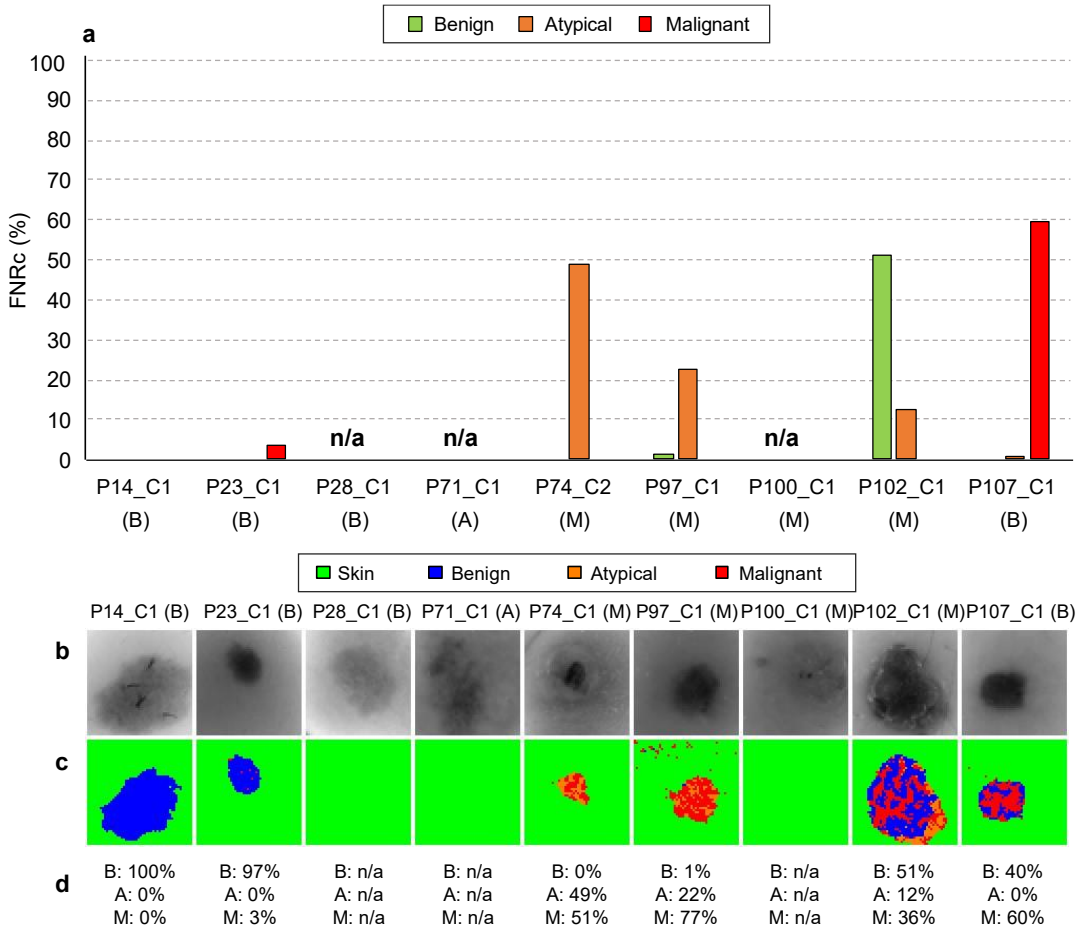

Figure 4-23: Quantitative and qualitative classification results using test set. a) FNRc results per each HS image obtained with the SVM Sigmoid classifier. **b**) Grayscale image. **c**) classification map, where skin, malignant, benign, and atypical pixels are represented in green, red, blue, and orange colors, respectively. **d**) Percentages of PSL pixels classified to each class. On the right side of each patient ID, the correct diagnosis of the PSL is presented between brackets. B: Benign; A: Atypical; M: Malignant.

Figure 4-24 shows the processing time of each HS image of the test set when applying the complete HS dermatologic classification framework implemented in MATLAB®. These results were obtained using an Intel i7-4790K with a working frequency of 4.00 GHz and a RAM of 8 GB.

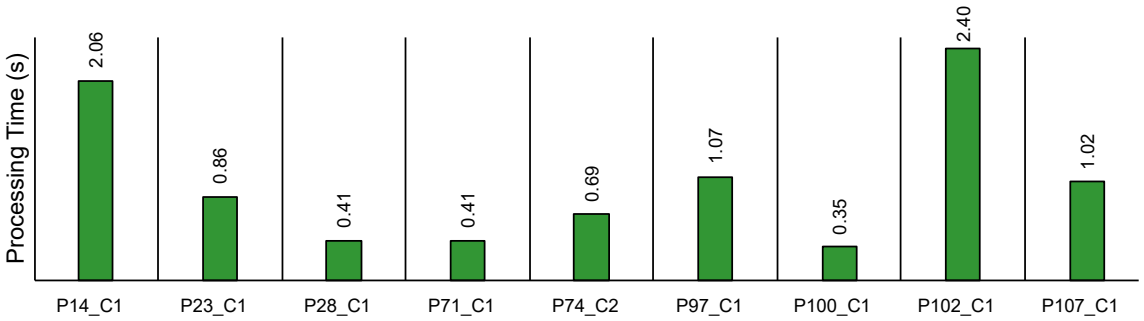

Figure 4-24: Processing time (in seconds) of the MATLAB® execution for each HS image of the test set.

4.5.1 Experimental Results Discussion

Additional research must be carried out to validate and improve the obtained results taking into account the current limitations of this study. One of these limitations is related with the low number of samples in each class (benign: 31; malignant: 39; atypical: 9). Although this number of samples is enough for a preliminary study, our future investigations will aim to increase the number of samples for each class with different types of skins and PSLs to improve the segmentation and classification results. Moreover, other processing approaches should be investigated, such as developing specific mathematical models for processing the data or the employment of DL techniques. Other limitation is related with the low spatial resolution of the HS camera employed in this study. The use of a higher spatial resolution HS camera could improve the results by including spatial features of the PSLs. Another future challenge for this application is the generation of the classification results in real-time while the HS image is captured, providing in-situ diagnosis support. For this task, future research to accelerate the processing framework in specific hardware platforms, such as GPUs (Graphics Processing Unit) or FPGAs (Field-Programmable Gate Array), will be explored. In the future, this system could reduce the number of biopsies of non-malignant PSLs, making the dermatologist's diagnosis more confident, as well as making it easier for non-experimented medical doctors (or even patients themselves) to diagnosis potentially malignant lesions.

4.6 Conclusions

The work presented in this chapter had the goal of using HSI technology as a non-invasive clinical support system for diagnosing PSLs during dermatological routine practice. A customized HS dermatologic acquisition system for capturing HS data of PSLs was developed, obtaining an HS database composed by 76 images from 61 subjects. Using this HS database, a processing framework to classify the PSLs was proposed and validated using a methodology based on a three data partition fashion (train, validation, and test sets), which provides an unbiased evaluation of the final processing model. The proposed framework isolates the PSL pixels in the HS image

using a segmentation methodology, and classifies such pixels using a supervised classifier, with the main goal of achieving real-time processing for in-situ diagnosis support.

Two different image segmentation methods were proposed. Both methods combined the K-means and SAM algorithms to identify the PSL pixels using a reference spectral signature library of PSL and normal skin. The first one compared each cluster obtained by the K-means with the library, while the second one compared each pixel from each cluster from the K-means with the library. In addition, different classifiers were employed to obtain the most accurate results in the discrimination of the different types of PSL. The GA algorithm was used to find the optimal hyperparameters for each classifier. This preliminary study provides evidence that the combination of HSI and machine learning algorithms allows achieving promising differentiation of PSL types.

Chapter 5: SWIR-based acquisition system targeting early detection of Major Neurocognitive disorders.

5.1 Introduction

Previous chapters have explored the use of different spectral ranges (VNIR and NIR) for cancer identification in *in-vivo* tissue samples through the use of a data processing framework based on supervised and unsupervised machine learning methods. In this chapter, a similar methodology is applied to explore its potential use for the early detection of MNCD using blood plasma samples (a distinct sample type). Additionally, in this work a new spectral range, covering between 900 and 2500 nm, is explored by using a SWIR-based acquisition system capable of capturing blood plasma samples in a transmittance illumination mode. The goal of this study is to explore, as a proof-of-concept, the potential use of HSI and the proposed methodology based on segmentation and pixel-wise supervised classification to discriminate between subjects affected by MNCD and healthy controls via blood plasma sample analysis. The main contribution of this research is the development of a methodology for the analysis of blood plasma samples, including the selection of subjects, the preparation of blood plasma samples, and their subsequent capture and analysis using the HSI system. Additionally, the proposed processing framework evaluates and compares three different data normalizations approaches with the goal of homogenizing the distribution of features in the spectral dimension to highlight as much as possible the differences between the two target groups. Finally, the data processing framework has primarily relied on supervised classifiers, where two approaches have been evaluated: a ML approach using SVM, KNN and RF classifiers; and a DL approach with a DNN classifier.

The work related with the data collection was carried out in a very close collaboration with Dr. Francisco J. Balea-Fernandez from the Department of Psychology, Sociology and Social Work at the University of Las Palmas de Gran Canaria.

5.2 SWIR-based acquisition system

The HS acquisition system employed to capture the blood plasma samples was based on a halogen-based illumination system and a pushbroom HS camera recording data in transmittance mode (Figure 5-1.a). The HS camera used in this study was a Hyperspec® SWIR pushbroom camera (Headwall Photonics, Inc., Bolton, Massachusetts, United States), covering the spectral range of 900-2500 nm and capturing 273 spectral channels, also called spectral bands, with a spectral resolution of 12 nm. To provide the necessary movement for capturing the whole scene by moving the pushbroom camera in one spatial dimension, the HS camera was coupled to a scanning platform, generating a complete HS cube. The halogen-based illumination system consisted of a power supply and a QTH lamp able to emit in the spectral range from 400 to 2200 nm (MI-150 Fiber-Lite®, Dolan-Jenner, Boxborough, Massachusetts, United States), coupled to a fiber-optic backlight illuminator (QVABL 4×3, Dolan-Jenner, Boxborough, Massachusetts, United States), able to emit in the spectral range from 400-2000 nm. The glass slide (Figure 5-1.b) with the plasma sample was placed over the backlight illuminator (Figure 5-1.c) and the HS camera captured the sample with a spatial resolution of 384×162 pixels.

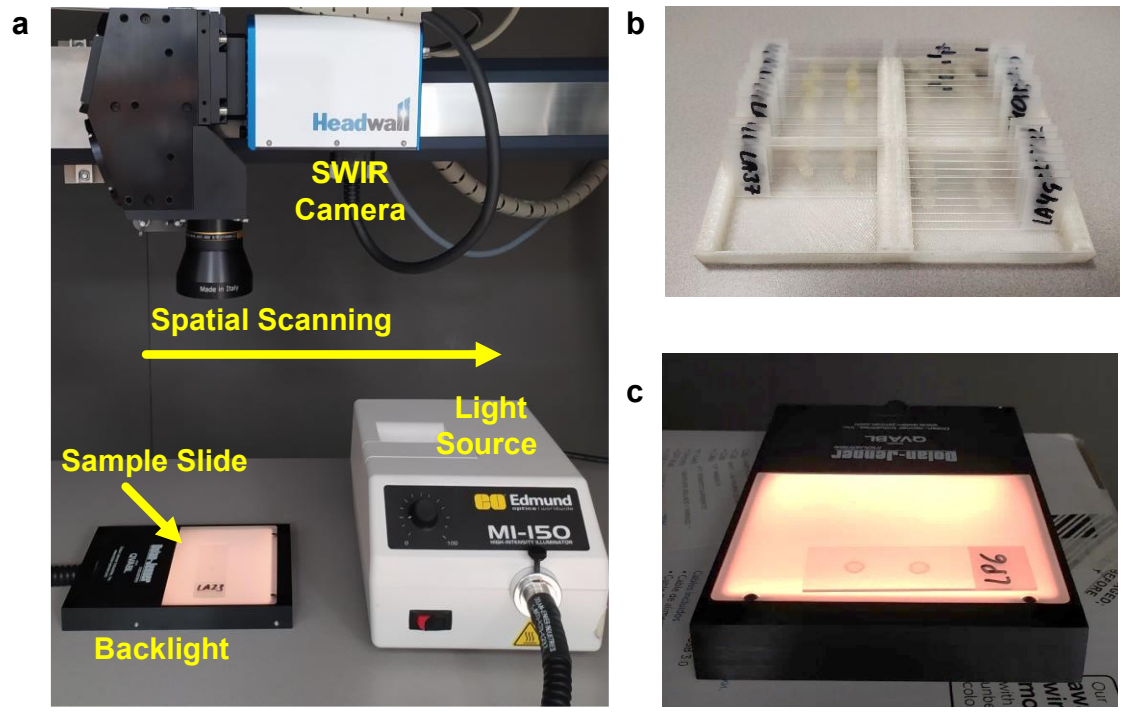

Figure 5-1: SWIR-based acquisition system. a) HS SWIR camera, scanning platform, light source, and backlight illuminator. **b**) Blood plasma slides. **c**) Glass slide over the backlight illuminator.

5.3 HS plasma database

The blood plasma samples used to create the HS SWIR blood plasma database were obtained from participants who were divided into two groups: control (healthy subjects) and case (subjects affected by MNCD with Alzheimer's disease). The case participants were recruited at the *Hospital Insular de Lanzarote* (Canary Islands, Spain) and the *Asociación de Alzheimer Gran Canaria* (Canary Islands, Spain). The

control participants were recruited at the *Hospital Insular de Lanzarote* and *Peritia et Doctrina* program (university program for students over 55 years) of the University of Las Palmas de Gran Canaria (ULPGC, Canary Islands, Spain). The study protocol and consent procedures were approved by the *Comité de Bioética* of *the Hospital Universitario de Gran Canaria Doctor Negrin* (2019-054-1).

The subject selection criteria are as follows. The control group was formed by subjects over 65 years old, with no previous diagnosis of NCD (neither MNCD nor mNCD), a Pfeiffer test result less than or equal to 2, and a blood test performed no more than 6 months prior to taking the sample in a baseline situation. The case group was formed by subjects over 65 years old, with a previous diagnosis of MNCD (not produced due to a cerebrovascular disease), a blood test performed no more than 6 months prior to taking the sample in a baseline situation, and an interview with a first-degree relative or guardian who was the primary caregiver.

The data acquisition campaign was performed from March 2019 to October 2019. The protocol followed to recruit the subjects in both groups was the same: to provide information about the research project, to request the participation, and to sign a written informed consent. For the subjects from the case group, a written informed consent was signed by the primary caregiver. Then, an interview was conducted with the subject (for the case group, in the presence of the primary caregiver). Finally, the blood collection was performed in a tube with anticoagulant, and an identification code was assigned. The tube with the blood sample was transported to the ULPGC pharmacology department within a maximum time of 2 hours after the blood draw. Then, the sample was centrifuged at 3,000 rpm for 10 minutes at room temperature. Afterwards, the plasma serum was extracted by using a Pasteur pipette and deposited in a storage tube (Figure 5-2.a). Centrifugation and subsequent extraction of the plasma prevent interferences produced by the red and white blood cells, and other elements contained in the blood sample. Then, the plasma samples were frozen at a temperature of -25ºC after collection. The plasma samples obtained at the *Hospital Insular de Lanzarote* were sent in a portable aseptic refrigerator by air transportation from Lanzarote to the Research Institute for Applied Microelectronics (IUMA) of the ULPGC, in Gran Canaria. Prior to the capture of the samples with the HS acquisition system, the samples were defrosted at room temperature (~23ºC) for one hour. Two drops of plasma were placed in different locations of a blank glass slide with a syringe, 0.05 mL for each drop, and dried at room temperature (~23ºC) over the course of ~24 hours (Figure 5-2.b). Only one drop of the sample was then captured with the HS acquisition system, choosing the most homogeneous drop. Finally, this study included 83 subjects, of which 45 were cases and 38 were controls, as shown in Figure 5-3. One case subject was excluded due to nonoptimal acquisition conditions.

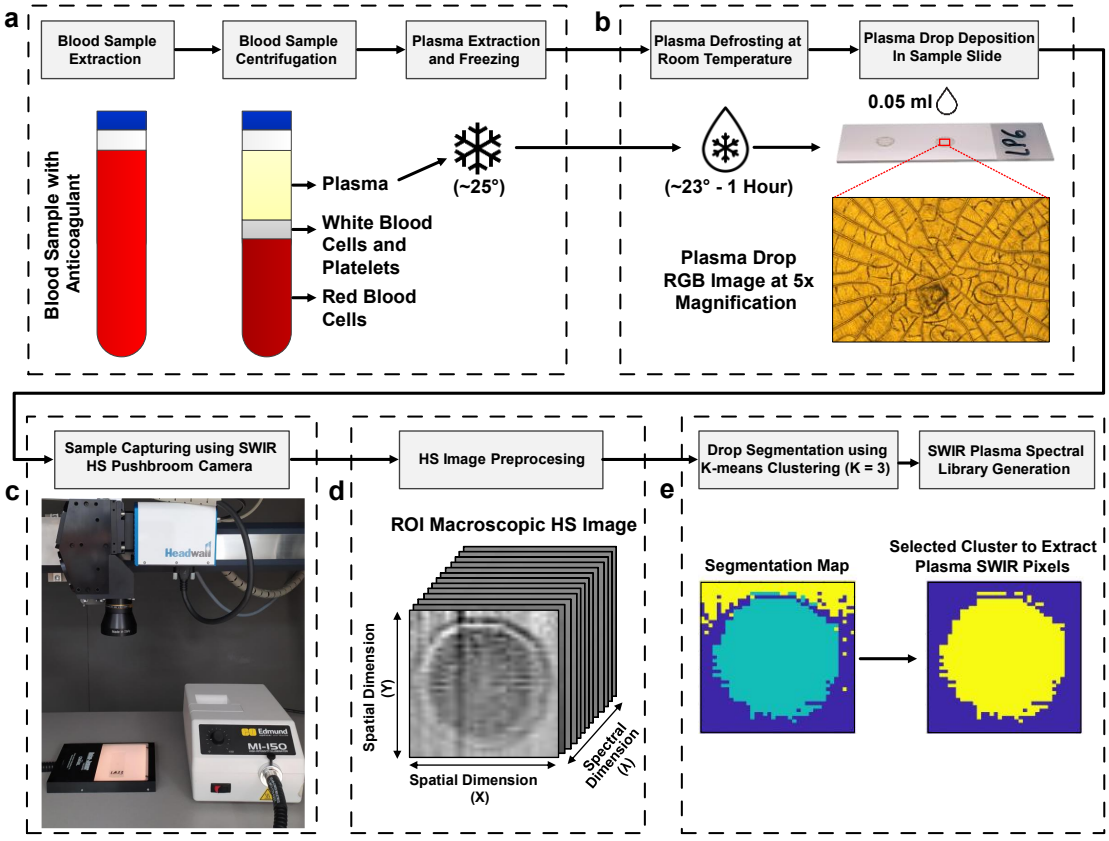

Figure 5-2: Methodology scheme of blood plasma samples acquisition. a) Blood plasma sample extraction. **b**) Plasma sample slide and red-blue-green (RGB) image of the plasma drop captured with a microscope at 5× magnification. **c**) HS acquisition system based on a SWIR camera. **d**) Example of a region of interest (ROI) of the HS cube captured macroscopically with the SWIR camera. **e**) Segmentation map obtained using a K-means algorithm with K = 3 to identify the pixels that belong to the plasma sample (colors are assigned randomly) and selected cluster (yellow pixels) to extract the spectral signatures of the plasma.

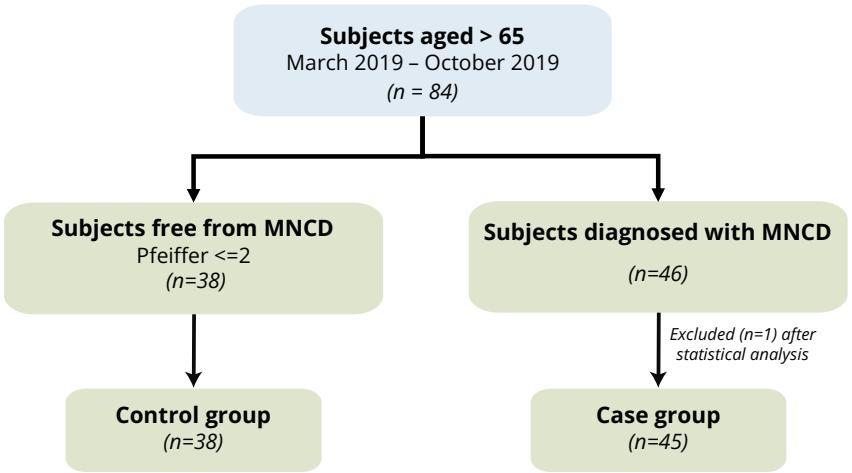

Figure 5-3: Subject dataset summary scheme of this study. n: number of subjects.

5.3.1 HS Data Pre-processing

The HS image obtained with the acquisition system previously described was pre-processed according to the following steps. First, ROI, where the plasma drop was located, was identified and cropped (Figure 5-2.d). The acquisition system was able to capture the complete slide and the ROI identification was performed manually.

The second step consisted on the calibration of the HS image using both the white and dark reference images (Eq. (1), Section 2.4.1). In this case, the white reference was obtained by capturing a blank area of the sample glass slide under the same illumination conditions as the image was taken. In this way, the white reference used for calibration contains both the spectral response of the backlight illuminator and the sample slide.

Next, the last 139 spectral channels were removed due to the low response of the backlight illuminator from 1700 to 2500 nm (Figure 5-4.a). The spectral channels in this range did not contain any relevant information, as can be observed in Figure 5-4.b. Hence, the final spectral signature was formed by 134 spectral channels. After calibration, a data-smoothing approach based on a moving average filter was employed to reduce the high-frequency noise. Each smoothed value was averaged using a window of five data points. Finally, a segmentation algorithm based on the K-Means algorithm was applied in order to automatically isolate the plasma sample from the background. This algorithm divides an input HS image into K different clusters for a previously selected K value. The number of clusters used in this approach was $K = 3$, and the cluster that contained the plasma sample was manually identified and selected (Figure 5-2.e). Then, the plasma pixels were extracted from the segmented area, generating the SWIR plasma spectral library employed in the subsequent analyses.

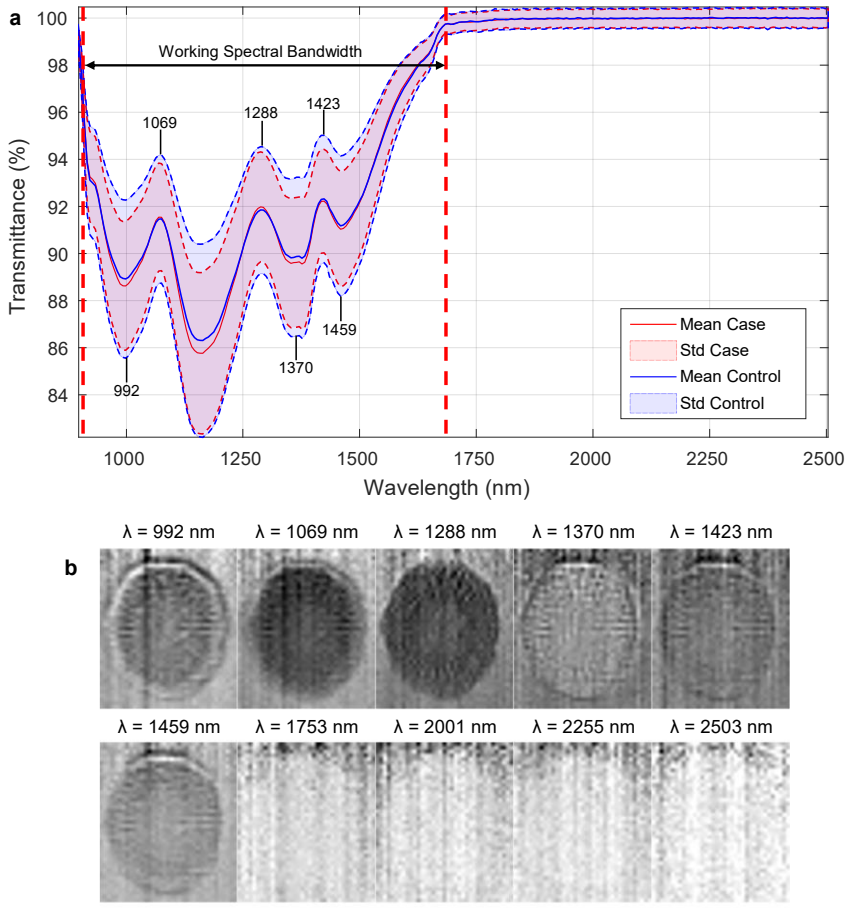

Figure 5-4: Case and control SWIR plasma sample spectral signatures. a) Mean and standard deviation (std) of the training dataset of plasma pixels from control and case subjects. The most relevant wavelengths are identified, where the differences among the means of the control and case classes are visually identified. **b**) Gray-scale images of an example HS image at each highlighted wavelength and some examples out of the selected working spectral bandwidth.

5.3.2 HS Data Partition

The SWIR plasma spectral library was created using the subjects selected during the acquisition campaign, including 84 subjects, of which 46 were cases and 38 were controls. The dataset was divided into three independent sets following a distribution of 60% for training, 20% for validation, and 20% for test. In the proposed data partition, every subject is assigned to a unique dataset. The training set was used to generate a pixel-wise classification model based on supervised classifiers. The validation set was employed to optimize the hyperparameters of the classification models in the ML approaches and to identify the best model in the DL approach. After finding the optimal models, the classifiers were evaluated over the test set.

A preliminary analysis of the spectral data included in the training set was performed, representing case and control samples independently using the mean and standard deviation (Figure 5-4.b). Figure 5-5 shows the case and control boxplots of each spectral channel in the training set, where it is possible to observe that samples belonging to the case class present several outliers (Figure 5-5.a), especially in the range between 900 and 1300 nm, in contrast to control case samples (Figure 5-5.b). After analyzing the pixels with such outliers, it was determined that all of these pixels belong to the same HS image. Hence, it was concluded that this sample was not acquired under the appropriate conditions. For this reason, the sample was excluded from the dataset, being it finally composed by 83 subjects (45 cases and 38 controls). Table 5-1 shows the data partition and the number of images/subjects and pixels that comprise the HS database.

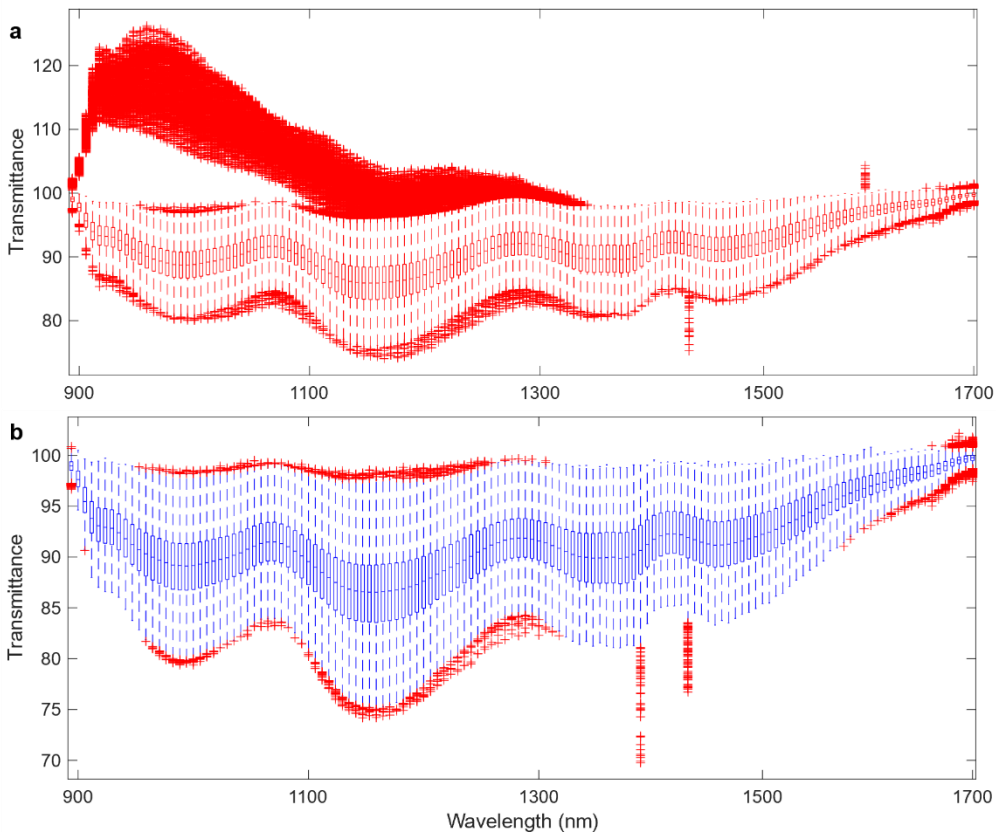

Figure 5-5: Spectral data exploration of the training set using boxplot. a) Case boxplot. **b**) Control boxplots. The small dots outside the minimum/maximum values represent the outliers. The box boundaries represent the interquartile range (IQR) of the results.

Table 5-1: HS data partition between the training, validation, and test sets.

	Number of images/subjects			Number of Pixels		
	Training	**Validation**	**Test**	**Training**	**Validation**	**Test**
Case	27	9	9	24,107	7,022	7,389
Control	22	8	8	20,315	6,955	8,362
Total	49	17	17	44,422	13,977	15,751

5.3.3 Statistical pre-processing approach

The HSI modality is characterized by high dimensionality defined by $\mathbb{X} \in \mathbb{R}^W \times \mathbb{R}^H \times \mathbb{R}^B$, where B represents the spectral resolution, and W and H correspond to the spatial resolution of the image. However, in this work, the spatial resolution is not taken into account based on the hypothesis that HS information should contain enough information to discriminate between case and control samples employing pixel-wise supervised classifiers.

Considering the aforementioned hypothesis, the spatial resolution is dismissed, and only the spectral information is used, so the HS data is reduced to $\mathbb{X} \in \mathbb{R}^B$. In this way, the dataset X comprises a number of N samples, which corresponds to the total number of pixels extracted after the segmentation performed on all of the HS images.

In this work, data standardization (or z-score normalization) was employed to homogenize the distribution of features in the spectral dimension, resulting in a zero mean and unit variance. Let $x_i \in X, i = 1, 2, \ldots, N$ denote data points. The standardization function is defined as:

$$x'_i = \frac{x_i - \mu}{\sigma}, \tag{35}$$

where $\mu \in \mathbb{R}^B$ represents the mean value in each spectral channel, and $\sigma \in \mathbb{R}^B$ represents the standard deviation.

As can be seen in Eq. (35), the standardization depends on μ and σ, and these statistics were computed using the *training dataset* to apply them to the validation and test sets. For this purpose, three different approaches were proposed to compute these parameters. Two of these approaches were based on the detection of outliers employing the well-known IQR methodology. The first approach employed the full dataset without removing outliers (called NOR – No Outlier Removal) for calculating μ and σ. In the second approach, outliers were detected and the spectral signatures that contained such outliers were removed (called SOR –Signature Outlier Removal) to compute μ and σ. Finally, the third approach computed the μ and σ values after removing only the outliers located at specific wavelengths, and hence not discarding the complete spectral signature from the dataset. In the latter approach, only the conflictive spectral bands were removed for the calculation of μ and σ (called BOR – Band Outlier Removal).

Figure 5-6 shows the mean and the standard deviation of each proposed normalization approach for each wavelength. As a result, Figure 5-7 illustrates, as an example, some spectral signatures extracted from the training dataset X and the normalized dataset X' using the NOR approach.

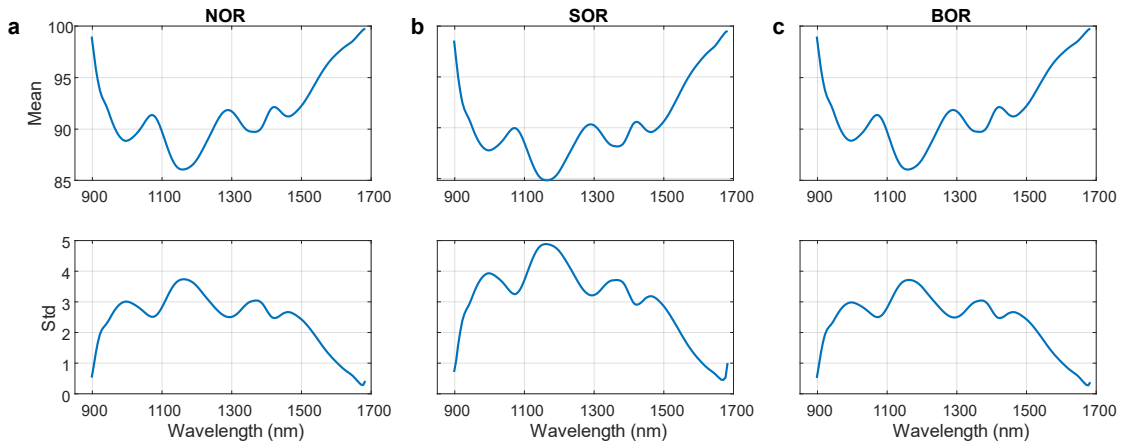

Figure 5-6: Mean and standard deviation (std) statistic values of the training set for the z-score normalization obtained from the full dataset. a) Without removing outliers (NOR). **b**) Removing the samples with outliers (SOR). **c**) Removing only the values of the spectral bands with outliers (BOR).

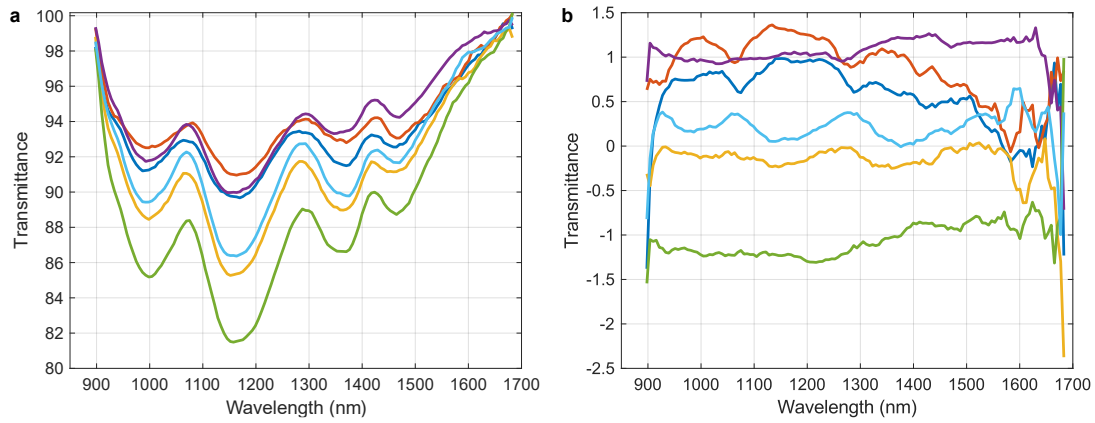

Figure 5-7: Spectral signature comparison using blood plasma samples. a) Examples of spectral signatures of the training set. **b**) Examples of spectral signatures of the training set after z-score normalization using the NOR (No Outlier Removal) approach.

5.4 HS Processing Framework for Major Neurocognitive Disorders Detection through Plasma Analysis

The processing framework proposed in this section is based on a pixel-wise supervised classification. Two approaches were evaluated based on ML and DL algorithms. Figure 5-8 shows the block diagram of the processing framework where the ML approach performs an hyperparameter optimization to find the best AUC on the validation set. In the DL approach, the model was also optimized attending to the best AUC to select the best epoch. After generating the optimal models of each classifier, an optimal *decision threshold* (th_{AUC}) was selected using the ROC curve. The heat maps in Figure 5-8 show two examples of HS images from the validation set, where the scores obtained in the pixel-wise classification of the drop sample are represented in different colors (red to blue gradient indicates the maximum to minimum probability for a certain pixel to belong to the case class). Once this threshold was identified for each classifier, the validation set was classified to obtain the evaluation metrics. At this point, the classification results are provided in a pixel-wise fashion (pixel-based

classification). The classification maps in Figure 5-8 show the pixel-wise classification, using each sample independently (each HS image for each subject) of the two HS image examples, where blue, red, and black colors represent control, case, and background classes, respectively. Based on the pixel-wise classification and considering the proportion of positive pixels (case pixels) that are correctly identified by the classifier, a classification result per sample (HS image) is provided by a thresholding method. This threshold, called *sample threshold* (th_{HSI}), provides information on the number of pixels needed in a HS image to determine whether this image should be classified as a case or control. Finally, using the optimal th_{AUC} and th_{HSI} selected, the test set was classified to assess the results.

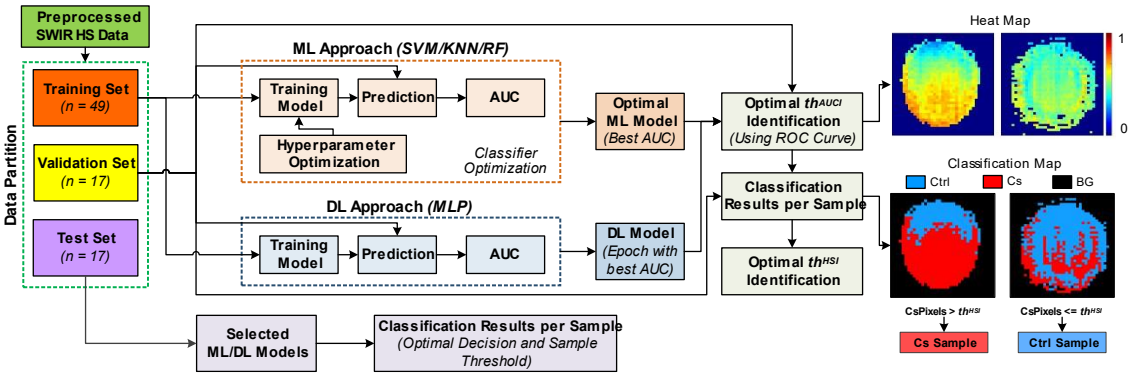

Figure 5-8: Block diagram of the proposed processing framework for the HS SWIR blood plasma samples analysis. AUC: Area Under the Curve; BG: Background; Cs: Case; Ctrl: Control; KNN: K-Nearest Neighbors; DNN: Deep Neural Networks; RF: Random Forest; ROC: Receiver Operating Characteristic; SVM: Support Vector Machine; th_{AUC}: decision threshold; th_{HSI}: sample threshold.

5.4.1 Machine Learning approach

The ML approach was based on three different supervised classifiers: SVM, KNN, and RF. Different SVM kernel were evaluated such as RBF or Sigmoid, however only the linear kernel was reported. The SVM linear hyperparameter to be optimized was the cost (C) parameter, which controls the decision limit that separates the positive and negative classes. In the case of KNN, several distance metrics were evaluated, such as, Chebyshev, Cosine, Euclidian, Hamming, Jaccard, and Spearman metrics. However, since the results obtained using all of them were quite similar, only the Euclidian distance metric is reported in this work because it provided the best results, being also one of the most commonly used metrics in the literature. The number of nearest neighbors (K_{NN}) hyperparameter was optimized to obtain the best model. The optimization of the RF model was performed by searching for the most appropriate number of trees (N_T) in the model.

Hyperparameter optimization of the SVM, KNN, and RF classifiers was performed by modifying each hyperparameter within a range of values and performing a grid search to find the higher AUC value. After identifying the best AUC result using the validation set, the best classification model was obtained.

5.4.2 Deep Learning approach

Several tests were conducted to determine the DNN architecture used in the DL approach. Finally, the DNN architecture was composed of 6 layers: an input layer of size B (which corresponds to the number of spectral channels, 134); 4 hidden layers of size 512, 256, 64 and 32; and an output layer of size NC (which corresponds to the

number of classes in our classification problem, 2). As Φ function, a Rectified Linear Unit (ReLU) function is applied to each neuron output.

For training process, the Stochastic Gradient Descent (SGD) method was selected as optimization algorithm, applying an initial learning rate of 0.001 that decreases every 75 epochs, a momentum of 0.9, and a batch size of 128. During training, dropout layers were used, which randomly apply zeros to their inputs with probability $p = 0.5$ using samples from a Bernoulli distribution, being those commonly used as technique for regularization [239], [240].

5.4.3 Validation Classification Results

The validation set was employed to optimize the hyperparameters of the ML algorithms. The results obtained after performing the grid search using the ML approach are presented in Table 5-2, where the selected hyperparameters were those that achieved the higher AUC values. Furthermore, in this table, it can be observed the AUC values that were obtained applying different data normalizations, where the SVM classifier with the linear kernel (SVM-L) achieved the higher AUC value for each data normalization type. The data normalization has no effect on the AUC results obtained using the RF classifier. In the case of the SVM-L and KNN classifiers, the data normalization worsens the AUC results respect to the use of the data without normalization. These results suggest that the data normalization does not suppose an improvement in the classification performance. Hence, the best classification model is obtained with the SVM-L without applying data normalization, achieving an AUC of 0.72.

Table 5-2: Grid search results using different ML classifiers with and without applying the different data normalizations.

Normalization Type	Classifier	HP	Grid Search		
			Initial/Step/Final	Optimal HP	AUC
None	SVM-L	C	$2^{-20}/2^{2}/2^{20}$	2^{-14}	0.720
	KNN	N_T	1/2/600	17	0.612
	RF	K_{NN}	1/2/600	197	0.625
NOR	SVM-L	C	$2^{-20}/2^{2}/2^{20}$	2^{-8}	0.707
	KNN	N_T	1/2/600	11	0.573
	RF	K_{NN}	1/2/600	197	0.625
SOR	SVM-L	C	$2^{-20}/2^{2}/2^{20}$	2^{-8}	0.706
	KNN	N_T	1/2/600	7	0.573
	RF	K_{NN}	1/2/600	197	0.625
BOR	SVM-L	C	$2^{-20}/2^{2}/2^{20}$	2^{-8}	0.707
	KNN	N_T	1/2/600	7	0.572
	RF	K_{NN}	1/2/600	55	0.625

AUC: Area Under the Curve; BOR: Band Outlier Removal; *C*: Cost; HP: Hyperparameters; K_{NN}: Number of Nearest Neighbors; N_T: Number of Trees; NOR: No Outlier Removal; SOR: Signature Outlier Removal.

Considering the DL approach based on the DNN classifier, the results obtained are presented in Table 5-3 with and without applying the different data normalizations. Unlike the previous results using the ML approach, in this case, the higher AUC values are obtained by employing data normalization. The BOR normalization achieved the highest AUC result (~0.78), followed by the SOR normalization (~0.77). Table 5-3 also shows the number of epochs required to achieve the best result. These DL results

represent an AUC improvement of 0.06 with respect to the results obtained with the ML approach.

Table 5-3: Best AUC results obtained using the proposed DL approach with and without applying the different data normalizations.

Normalization Type	Best AUC	Number Epoch
None	0.768	15
NOR	0.765	25
SOR	0.775	53
BOR	0.786	21

AUC: Area Under the Curve; BOR: Band Outlier Removal; NOR: No Outlier Removal; SOR: Signature Outlier Removal.

After finding the optimal models in both approaches, the ROC curve was generated, plotting all possible cut-off values of the true positive rate (TPR), also called *sensitivity*, versus the false positive rate (FPR), which corresponds to *1 - specificity*. Figure 5-9.a shows the ROC curves corresponding to the best classifier per each normalization type in the ML approach, i.e. SVM-L. As previously stated, here it is also possible to observe that the SVM-L classifier without data normalization offers a higher AUC with respect to the different normalization types. However, the DL approach based on the MLP classifier achieves higher AUC values with and without normalization than the ML approach, achieving the best AUC value with the DNN classifier using BOR normalization (Figure 5-9.b). The optimal th_{AUC} can be obtained for each classifier by analyzing the ROC curves. Normally, the class assignment of the results is performed using a default th_{AUC} with a value of 0.5. If a classification result has a probability value below or equal to 0.5, it is predicted as the control class, meanwhile a sample with a probability value above 0.5 is assigned to the case class. Hence, the optimal operating point is used to find the th_{AUC} located in the upper-left part of the ROC curve, where subtraction between TPR and FPR achieves its maximum [241]. Table 5-4 shows the optimal th_{AUC} found for the best classifiers of each approach with and without applying data normalization, indicating the TPR and FPR values corresponding to the optimal operating point.

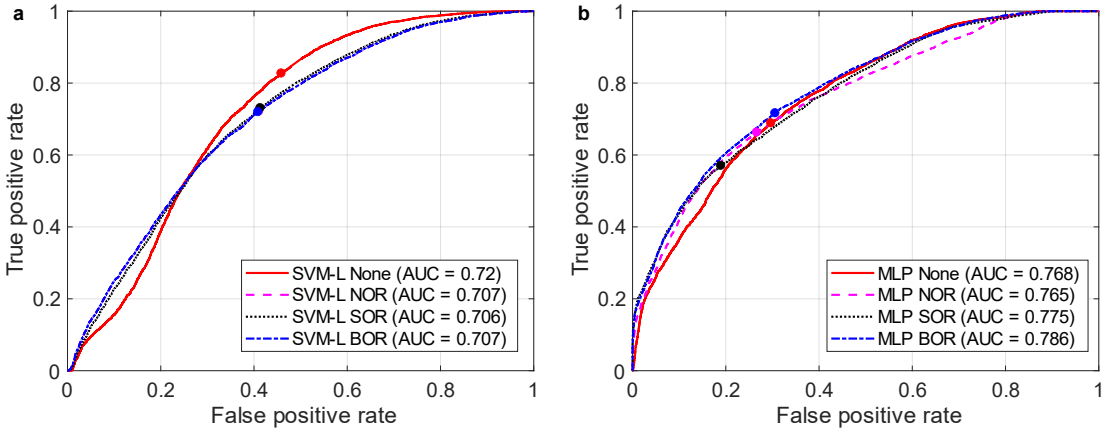

Figure 5-9: ROC curves of the validation results using the different normalizations. a) ROC curves for the SVM-L classifiers. **b**) ROC curves for the DNN classifiers. Dots show the optimal operating point. AUC: Area Under the Curve; BOR: Band Outlier Removal; NOR: No Outlier Removal; SOR: Signature Outlier Removal.

Table 5-4: Optimal decision threshold (th_{AUC}) for each classifier and normalization type presented in the ROC curves.

Normalization Type	Classifier	TPR	FPR	Optimal th_{AUC}
None	SVM-L	0.828	0.458	0.513
	MLP	0.690	0.296	0.717
NOR	SVM-L	0.723	0.410	0.536
	MLP	0.664	0.266	0.667
SOR	SVM-L	0.732	0.413	0.532
	MLP	0.571	0.189	0.898
BOR	SVM-L	0.721	0.408	0.537
	MLP	0.717	0.305	0.708

AUC: Area Under the Curve; **BOR**: Band Outlier Removal; **FPR**: False Positive Rate; **NOR**: No Outlier Removal; **SOR**: Signature Outlier Removal; th_{AUC}: decision threshold; **TPR**: True Positive Rate.

Once the optimal th_{AUC} was found, the ACC, sensitivity, specificity, and F1-score metrics were computed to determine which method offered the best tradeoff between these metrics. Table 5-5 shows the classification results obtained by classifying the entire validation set after applying the th_{AUC}. SVM-L without data normalization offered the highest sensitivity and F1-score results of 82.8% and 72.6%, respectively, but with a reduced specificity of 54.2% and an ACC of 68.6%. However, the MLP classifier using BOR normalization achieved the best ACC (70.6%), with balanced results of sensitivity and specificity, 71.7% and 69.5%, respectively. Regarding the F1-score value, it decreased 1.6 with respect to the SVM-L without data normalization. Considering these results, the following experiments were carried out using only these two classifiers that obtained the highest F1-score values.

Table 5-5: Validation results of pixel-based classification

Normalization Type	Classifier	ACC (%)	Sensitivity (%)	Specificity (%)	F1 (%)
None	SVM-L	68.6	82.8	54.2	72.6
	MLP	69.7	69.0	70.4	69.6
NOR	SVM-L	65.7	72.3	59.0	67.9
	MLP	69.9	66.4	73.4	68.9
SOR	SVM-L	66.0	73.2	58.7	68.4
	MLP	69.1	57.1	81.1	65.0
BOR	SVM-L	65.7	72.1	59.2	67.8
	MLP	70.6	71.7	69.5	71.0

ACC: Accuracy; **BOR**: Band Outlier Removal; **NOR**: No Outlier Removal; **SOR**: Signature Outlier Removal.

Figure 5-10 shows the percentage of pixels classified as the case class in each validation image independently. In this sense, images from control subjects should have a low sensitivity percentage value (low number of pixels classified as case), while case images should have a high sensitivity percentage value (high number of pixels classified as case). Both classifiers misclassified several control pixels as the case class. However, SVM-L better identified the case pixels than the DNN classifier.

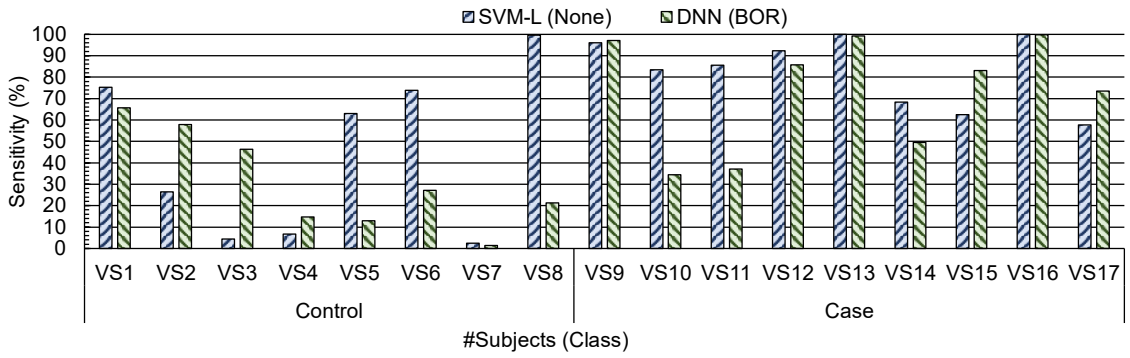

Figure 5-10: Validation results of the pixel-based classification for each independent sample using the selected two best classifiers. VS: Validation Subject.

In the final step of the processing framework, a sample-based classification was performed using the two previously selected classifiers (SVM-L without normalization and MLP using BOR normalization). This step implied the determination of a th_{HSI} to obtain the classification results in a sample-based fashion. For this purpose, the sensitivity metric from the pixel-based classification results (Figure 5-10) was employed to determine the th_{HSI} for a potential improvement in the discrimination between case and control samples. For example, in a most-voted approach, if 50% or more pixels of the plasma sample of a subject are classified as case, then the sample is classified as case. In contrast, if 50% or more pixels of a certain plasma sample of a subject are classified as control, then the sample is classified as control. To select an appropriate th_{HSI} for this application, an analysis of the evaluation metrics was performed by sweeping the th_{HSI} value and computing the evaluation metrics for each threshold.

Figure 5-11 shows the ACC, sensitivity, specificity, and F1-score results for each th_{HSI} value in both selected ML and DL approaches. It can be observed that in both approaches the sensitivity metric achieved high values when using low th_{HSI} and the specificity improves when the th_{HSI} is increased. At this point, the goal is to select the optimal th_{HSI} that provides the best classification results in the validation set. For this application, we tried to select a th_{HSI} that provided the best trade-off between sensitivity and specificity, but always attempted to have high sensitivity values.

In the ML approach (Figure 5-11.a), the best trade-off between sensitivity (77.7%) and specificity (62.5%) is obtained using a th_{HSI} of 0.65, with an ACC of 70.5% and an F1-score of 73.6%. In the DL approach (Figure 5-11.b), the th_{HSI} value selected was 0.3, obtaining the best ACC (82.3%) and sensitivity (100%), with a specificity of 62.5% and an F1-score of 85.7%. As it can be seen in these results, although the pixel-based classification revealed that the selected SVM-L classifier seemed to perform better than the selected DNN classifier, when employing this sample-based classification methodology, the results of the DNN classifier were improved.

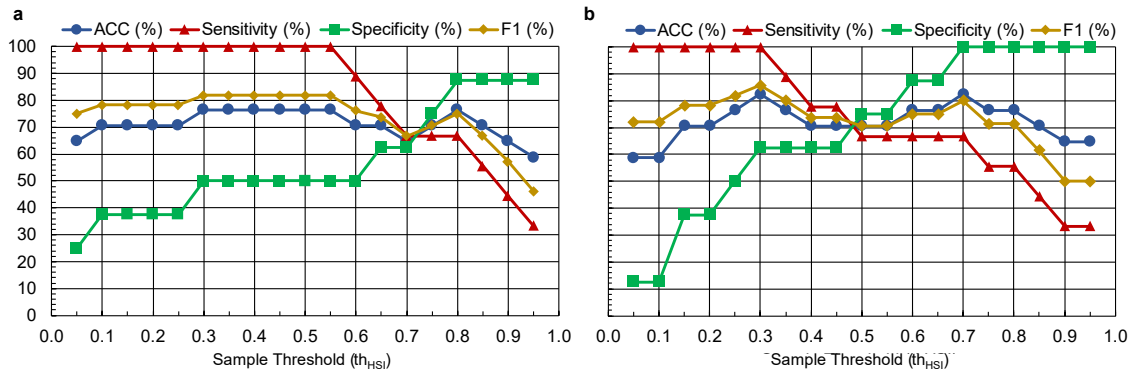

Figure 5-11: Sample threshold (th_{HSI}) analysis of the validation results for an optimal sample-based classification. a) SVM-L classifier without data normalization. b) DNN classifier with BOR normalization.

5.4.4 Test Classification Results

At this point in the experimentation, the best classifiers, th_{AUC} and th_{HSI} have been selected. In this section, the proposed approaches will be evaluated in the test set to indicate if the developed models are able to accurately predict the diagnosis in new samples. The SVM-L classifier without data normalization (configured with $th_{AUC} = 0.513$ and $th_{HSI} = 0.65$) and the DNN classifier using BOR normalization (configured with $th_{AUC} = 0.708$ and $th_{HSI} = 0.3$) were evaluated employing the test set. First, Table 5-6 shows the pixel-based classification results for each classifier using the optimal th_{AUC}, where SVM-L offers better results than DNN. However, the results in both cases are quite low with respect to the results achieved using the validation set. Additionally, Figure 5-12 shows the sensitivity results obtained in each test sample independently. Here, it can be also observed that the SVM-L classifier correctly identified more case samples than the DNN classifier.

Finally, the ACC, sensitivity, and specificity metrics were computed using the test samples, applying the selected th_{HSI} for each classifier in the validation phase. Figure 5-13 shows these results where, on the one hand, it can be observed that the SVM-L classifier offers high specificity (88%), correctly classifying 7 out of 8 control samples, but with a sensitivity value of 44%, which correctly identifies 4 out of 9 case samples. On the other hand, the MLP classifier correctly identified only 1 out of 8 control samples but with high sensitivity, correctly classifying 7 out of 9 samples.

Table 5-6: Test classification results of the pixel-based classification using the optimal decision threshold (th_{AUC}).

Normalization Type	Classifier	ACC (%)	Sensitivity (%)	Specificity (%)	F1 (%)
None	SVM-L	62.4	56.2	67.9	58.4
BOR	DNN	51.1	44.3	57.0	45.9

ACC: Accuracy; BOR: Band Outlier Removal.

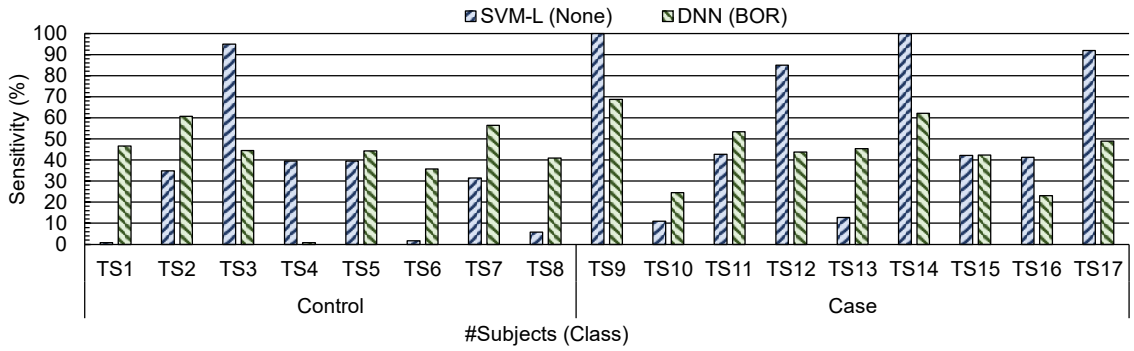

Figure 5-12: Test classification results of pixel-based classification for each independent sample using the optimal decision threshold (th_{AUC}). TS: Test Subject.

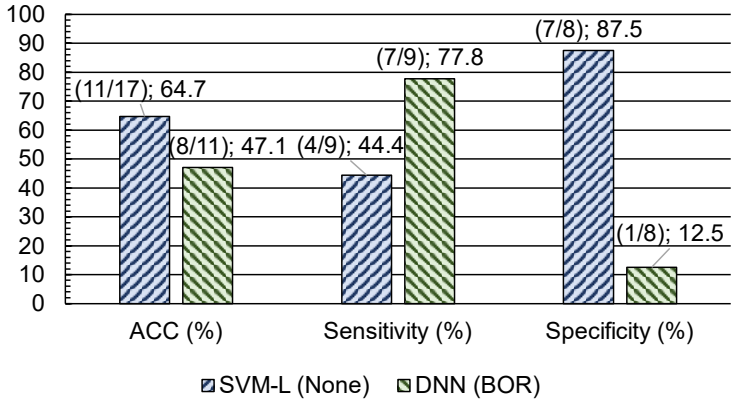

Figure 5-13: Test results of sample-based classification. Numbers between parenthesis represent the subjects correctly identified over the total number of subjects for the ACC metric, and the total number of subjects in the case and control class for the sensitivity and specificity metrics, respectively.

5.4.5 Limitations of the study

After analyzing the results obtained in the validation and test sets, additional research must be carried out to validate and improve the obtained results considering the current limitations of this work. One of these limitations is related to the low number of samples available in this study. It is necessary to increase the dataset to improve the results obtained with different algorithms and better generalize a solution that could enhance the test results. In addition, other processing approaches must be considered in future research, such as employing other DL algorithms, using spatial information, or exploring the use of other spectral ranges, such as the VNIR or the SWIR range between 1700 and 2500 nm. Inclusion of spatial information could improve the discrimination between subjects affected by MNCD and healthy control subjects using the morphology of drying blood plasma [242], [243]. In this sense, the use of a higher spatial resolution HS camera will be necessary to better analyze the drop morphology and possibly locate the protein deposition associated with MNCD. The use of other spectral ranges, or a combination of several ranges should be investigated to determine if spectral biomarkers can be identified to improve the discrimination. To perform such experiments, the development of a new HS acquisition system is necessary to associate both spectral ranges. Other preliminary research of our group is based on use of HSI microscopy for potential identification of spectral biomarkers using VNIR information for eventual classification using macroscopic image samples [191].

5.5 Conclusions

The work presented in this chapter shows a methodology that utilizes HSI in the SWIR spectral range combined with pixel-wise supervised classifiers to discriminate between subjects affected by MNCD and healthy control subjects through blood plasma samples analysis. This study shows, as a proof-of-concept, the limitations, and the potential of HSI technology to assist in the diagnosis of MNCD as an alternative to other highly invasive or more expensive methods. We proposed a methodology for the analysis of blood plasma samples, including subject selection, blood plasma sample preparation and their subsequent capture and analysis using HSI. By means of this methodology, a database composed of 83 images (45 cases and 38 controls) was generated using an HSI system able to capture blood plasma drop samples deposited on a glass slide, capturing information between 900 and 1700 nm. In addition, in this methodology, three different data normalizations were proposed with the goal of homogenizing the distribution of features in the spectral dimension. The dataset was partitioned into training, validation, and test set. The classification results were evaluated using the different data normalizations, and two classification approaches: an ML approach applying SVM, KNN and RF classifiers; and a DL approach with an DNN classifier.

To the best of our knowledge, this is the first work focused on using HSI to analyze blood plasma samples and discriminate between healthy subjects and subjects affected by MNCD. Considering the obtained results, it seems that the spectral information in the SWIR range could contain relevant information for the potential identification of spectral biomarkers in blood plasma samples, which might be useful for diagnostic purposes. Additionally, further experiments might involve the use of other processing strategies to improve the performance of the classification results, as well as increase the HS dataset for a better generalization.

Chapter 6: Conclusions & Future Lines

6.1 Introduction

This chapter summarizes the main contributions of this dissertation and outlines the main conclusions drawn from this research. In addition, the future lines of research that have emerged from the development of this dissertation are presented. Finally, the scientific and academic production developed in the context of this dissertation is presented.

6.2 Conclusions

The aim of this PhD Thesis was the use of HSI for the identification of different diseases in three medical applications: neurosurgery, dermatology, and neurogeriatrics. Many studies in the literature have demonstrated the high potential of the HSI technology for improving remote and non-destructive detection of chemical compositions in different applications, with promising results. In medical applications, HSI technology has been extensively researched analyzing the spectral properties of tissue and other types of biological samples due to its non-contact, non-ionizing, and label-free nature. One of the major advantages of this technology is that it can be used for real-time in-situ diagnosis and guidance in clinical routine practice in different medical scenarios.

6.2.1 Neurosurgery

In the field of brain cancer, this technology is arising as a novel imaging technique that can offer new capabilities to assist neurosurgeons to identify and delineate brain tumor tissue in surgical-time. The accurate identification of the boundaries between tumor and normal tissue during surgery improves the resection and a successful resection of the tumor is associated with prolonged survival. Nonetheless, due to the nature and location of the tumor, the complete resection is not always possible or can produce neurological damages to the patient. Hence, surgeons must strike a balance between removing the tumor and preserving neurological functions. Currently, neurosurgeons use several intraoperative guidance tools for tumor resection assistance, such as IGS neuronavigation, intraoperative MRI, or fluorescent tumor markers (e.g., 5-ALA). However, these tools present several limitations. For example, intraoperative MRI is a costly procedure as it requires specific operating rooms without ferromagnetic

elements and significatively increases surgical time. The changes in tumor volume that occurs during craniotomy and the problem of brain shift are not covered by IGS neuronavigation. 5-ALA is only able to identify high-grade gliomas by administering orally a contrast agent to the patient, being an invasive methodology that can cause side effects in the patient. Therefore, there is a current need to explore new imaging modalities that could overcome such limitations.

In this PhD Thesis, an intraoperative HS acquisition system for brain cancer was optimized with the goal of delineating brain tumors during surgical operations. This demonstrator was composed by two pushbroom HS cameras: a VNIR and NIR cameras covering the spectral ranges 400-1000 nm and 900-1700 nm, respectively. Using this optimized HS system, an HS human brain image database was collected, consisting of 10 HS images from 8 different patients. Employing this database and another two data acquisition campaigns obtained by the original system, a total of 61 HS images of exposed brain surface from 34 different patients have been analyzed in this dissertation.

Vascular enhanced maps using diffuse absorbance hemoglobin spectral ratios were studied, allowing the discrimination of different in-vivo human brain tissue structures. This ratio reflects a maximized difference between deoxyhemoglobin and oxyhemoglobin. The identification of the blood vessels in the enhanced vascular maps could help to improve the identification of tumor areas during surgical procedures, by reducing the number of classes to be differentiated by a ML classifier. In addition, a robust 5-fold cross-validation approach was used to evaluate eight different processing algorithms, first using only spectral information, and then using both spatial and spectral information. ML algorithms were trained by employing the three data acquisition campaigns only using the VNIR HS images. The spectral-based classification results obtained showed that SVM-based and DNN methods provided the best results. The qualitative results demonstrate the ability of the proposed HSI-based system to identify not only high-grade gliomas, but also other low-grade tumors and secondary tumors. Moreover, these results show the capability of HSI to accurately highlight the vascularization of the brain surface.

Finally, an exploration of the use of VNIR-NIR fused data for brain cancer tumor detection and identification was performed using the in-vivo HS brain cancer dataset acquired in this PhD Thesis. Due to the challenges of obtaining in-vivo HS images during human neurosurgical procedures, creating a comprehensive database that encompasses the full diversity of different patients and brain tumor types, has supposed a challenging task. For this reason, the fusion experiments were performed using a dataset composed by 10 HS images acquired from 8 different subjects, using a leave-patient-one-out data partition strategy. The results of the classification indicate that the presence of hemoglobin in the VIS region enhances the identification of tumors and hypervascularized tissue when using only VNIR images, while NIR images accurately outline the parenchymal area. The classification maps generated from the VNIR-NIR fused images provide more detailed maps, eliminating false positives present in the independent VNIR and NIR results.

6.2.2 Dermatology

Skin cancer is one of the most common forms of cancer worldwide and its early detection its key to achieve an effective treatment of the lesion. Commonly, skin cancer

diagnosis is based on dermatologist expertise and pathological assessment of biopsies. To avoid unnecessary surgical procedures, because of the uncertainty in the current diagnoses, and to achieve cost-effective early diagnosis, new methods to improve skin cancer diagnosis should be investigated. Despite that the state-of-the-art works and commercial systems available for assisting in skin cancer diagnosis mainly use MS imaging for melanoma and non-melanoma discrimination, there is still room for improvement and investigation using HSI for malignant and benign PSL discrimination, providing higher number of spectral bands in larger spectral ranges.

In this sense, one of the goals of this PhD Thesis was the development of a data processing framework based on HS image segmentation and supervised classification. To do this, a customized dermatologic HSI system able to capture real-time HS data of in-vivo PSLs was developed, providing HS images composed by 125 bands in the 450–950 nm spectral range. This preliminary study aimed to demonstrate, as a proof-of-concept, the potential use of HSI technology to assist dermatologists in the discrimination of benign and malignant PSLs (including both NMSC and melanoma lesions) during clinical routine practice. A skin cancer database composed by 76 HS images from 61 subjects was collected using this system. The framework was able to segment and classify among benign and malignant PSLs using only spectral information. Two-class segmentation maps were generated where the PSL and the normal skin pixels were identified. A spectral signature reference library of normal skin and PSL data was created, employing only the spectral signatures of the labeled training set in order to avoid the inclusion of validation or test HS images in the reference library. Although the number of samples was low, this reference library was enough for a preliminary study. However, increasing the number of samples for each class with different types of skins and PSLs could improve the segmentation and classification results. In the classification step, high sensitivity was obtained when discriminating between benign and malignant lesions. In the case of atypical PSLs, misclassifications may occur due to the low number of samples in this class, indicating the need of an increased database where the inter-patient and inter-lesion variability are taken into account. Evaluating the entire framework, a risk threshold was applied to discriminate malignant PSLs, i.e., PSLs with an accuracy higher than 40% in the malignant class were considered to have clear evidence of malignant behavior.

6.2.3 Neurogeriatrics

In this PhD Thesis, the VNIR spectral range has been investigated in two medical fields, while the NIR spectral range has been analyzed only in the brain tumor application due to the possibility of capturing data in such spectral range during surgical operations. However, the use of the SWIR range was motivated to be studied in a different medical context, where the HS images of the samples could be acquired in a laboratory. The purpose of this investigation is to uncover new insights and potential applications of using SWIR for disease diagnosis through blood plasma samples. As stated in Chapter 2, NCDs are a rapidly growing public health issue and a major cause of disability and dependency among older people, being a not natural or inevitable consequence of ageing. Alzheimer's disease is the most common form of NCD. The common clinical tests to diagnose a possible MNCD are based on in-vivo neuroimaging biomarkers using PET or MRI, and CSF biomarkers. These biomarker identification methods are widely used to detect Alzheimer's disease in the absence of symptoms, or in cases showing neuropathologic changes independently of clinical symptoms.

However, these procedures are expensive, invasive and with restricted availability for verifying the diagnosis. For these reasons, alternative methods are necessary to identify MNCD biomarkers, such as blood-based biomarkers, which are a less-invasive and cost-effective alternative for early detection. Plasma is used to identify proteins related with the disease, such as albumin, fibrinogen, and immunoglobulins. Plasma is composed of mostly water (90%), various proteins (6%), inorganic electrolytes (1%), glucose, and other minor components.

In this area, the last goal of this PhD Thesis was the analysis of blood plasma samples using HSI technology and supervised ML and DL classifiers to discriminate between subjects affected by MNCD and healthy control subjects, evaluating the potential use of this technology in this field. A methodology for the analysis of blood plasma samples, including subject selection, blood plasma sample preparation and their subsequent capture and analysis using HSI was proposed. By means of this methodology, a database composed of 83 images (45 *cases* and 38 *controls*) was generated using an HSI system able to capture blood plasma drop samples deposited on a glass slide, capturing information between 900 and 1700 nm in transmittance mode. In addition, three different data normalizations were proposed, evaluated and compared with the goal of homogenizing the distribution of features in the spectral dimension. The dataset was partitioned into training, validation, and test set. The classification results were evaluated using the different data normalizations, and two classification approaches: a ML approach applying SVM, KNN and RF classifiers; and a DL approach with a DNN classifier. Using a coarse-to-fine search, the hyperparameters of the classifiers were optimized to provide the optimal results. After that, using the ROC curves, the optimal threshold of each classifier was identified for a pixel-based classification. At this point, HS images from control subjects should have a low sensitivity percentage value (low number of pixels classified as *case*), while case subjects should have a high sensitivity percentage value (high number of pixels classified as *case*). On the one hand, SVM-L and DNN classifiers misclassified several *control* pixels as *case* class. On the other hand, SVM-L better identified *case* pixels than the DNN classifier. Finally, the plasma samples were classified via an image-based methodology. This step implied the determination of a threshold to obtain the classification results in a sample-based manner. This threshold was selected by performing an analysis of the evaluation metrics. For this application, we selected a threshold that provided the best trade-off between sensitivity and specificity, but always attempting to have high sensitivity values. Considering the obtained results, it seems that the spectral information in the SWIR range could contain relevant information for the potential identification of spectral biomarkers in blood plasma samples, which might be useful for diagnostic purposes.

In summary, this PhD Thesis demonstrates the potential use of HSI as an innovative, non-invasive, and non-ionizing aid system for real-time visualization, delineation, and identification of different lesions or diseases. This technology has the potential to enhance patient outcomes across various medical applications.

6.3 Future lines

As stated before, the research presented in this PhD Thesis demonstrates the high potential of the HSI as a supportive imaging modality to aid in different applications in

the medical field. Upon completion of this dissertation, several lines of research are available for future investigation to improve and progress beyond the state-of-the-art.

In the field of neurosurgery, we have demonstrated with a robust classification validation approach, the potential benefits of HSI for brain tumor tissue identification, targeting a diagnostic support system for guiding neurosurgical interventions in real-time. After performing the optimization of the intraoperative HS acquisition system, it is possible to achieve near real-time HS data processing using graphical processing units, achieving processing times of ~6 s. The proposed intraoperative HSI-based acquisition system must be optimized in further works by reducing the number of HS cameras, and the HS camera size, possibly employing a snapshot-based HSI technology (which is able to capture the entire HS cube in a single shoot, providing also real-time performance) and integrating it into a surgical microscope.

In this sense, an analysis of the most relevant spectral bands of the fused HS images for an accurate delineation of the tumor boundaries will be explored in future works with the goal of determining the minimum number of wavelengths required to develop customized HS cameras while maintaining accurate identification of the tumor. This will allow a reduction of the acquisition system size and also a time reduction of the data acquisition and processing, achieving, hence, real-time performance during surgery. This identification of the most relevant spectral bands in the NIR range will also allow to increase the spatial resolution of this type of HS images by developing specific HS sensors able to capture these bands. The use of this customized sensors could avoid the resampling process employed in this dissertation. These advances could help in the development of a novel guidance tool based on HSI technology for the accurate identification of brain tumors, regardless of tumor grade, avoiding the use of several independent devices during surgery and, hence, reducing the operation time.

This new experimental setup will guarantee an improvement of the HS image quality to solve the focus problems, especially for deep-layer tumors. Additionally, an extensive clinical validation of the proposed framework must be carried out, employing a large number of patients and a multi-center trial. This clinical validation will perform a comprehensive pathological analysis of the entire tumor area outlined by the TMD map (especially in the boundaries between tumor and the surrounding normal tissue), as well as correlate the results with the MRI information to verify that the system can adequately identify tumor infiltration into normal brain tissue, especially in HG gliomas. Additionally, the relation between the improvement of the patient outcomes and the use of the proposed system during the surgery could be studied through the clinical validation. Currently it is not possible to make a fair comparison between the results obtained from HSI systems and intraoperative fluorescence imaging systems, due to the lack of rigorous clinical studies to evaluate the actual accuracy of HSI systems. However, it could be very useful to carry out this comparison in future clinical studies by using HSI systems in real environments during brain surgical procedures to test their usability, safety, efficacy, and efficiency respect to the tools currently employed.

In the dermatology application, this study demonstrated the potential use of HSI technology to assist dermatologists in the discrimination of different types of PSLs. However, additional research must be carried out to validate and improve the results obtained in this work, targeting its use during clinical routine practice using a real-time and non-invasive handheld device. One of these limitations is related with the low

number of samples in each class. Although the number of samples is enough for a preliminary study, our future investigations will aim to increase the number of samples for each class, including different types of skins and PSLs to improve the segmentation and classification results. Particularly, a multicenter clinical trial whereby more patients and samples are included in the database will be necessary to further validate the proposed approach.

The proposed dermatoscopic HS system based on a 50 x 50 pixels HS camera based on halogen illumination faces limitations in ergonomic design and real-time HS image processing capabilities. For this reason, some optimizations must be performed in order to improve such limitations. In terms of design, the ergonomic design needs to be refined to allow for single-handed operation to enhance user comfort during examinations. Regarding the instrumentation, a HS camera with a resolution higher than the current 50×50 HS pixels could improve the results by including spatial features of the PSLs. In addition, transitioning from halogen to LED-based illumination will reduce the system size and power consumption by eliminating the need for an external illumination system. A critical consideration in this transition is the cost reduction. Halogen systems requires an external illumination system that uses specific halogen bulbs, and fiber optics to emit cold light. However, the LED illumination must cover adequately the operating spectral range.

Another future challenge for this application is the generation of the classification results in real-time while the HS image is captured, providing in-situ diagnosis support. For this task, future research to accelerate the processing framework in specific hardware platforms, such as low-power GPUs or FPGAs, will be explored. In the future, this system could allow reducing the number of biopsies of non-malignant PSLs, giving more confidence to the dermatologist's diagnosis as well as to facilitate to non-specialist medical doctors (general physicians, nurses or even patients themselves) the diagnosis of potential malignant lesions.

In the field of neurogeriatrics, further research is necessary to validate and improve the obtained results for diagnosing MNCDs through blood plasma samples, considering the current limitations of this work. This study was performed using a SWIR camera capable of capturing wavelengths between 900 to 2,500 nm. However, due to limitations in the illumination system, the spectral range between 1,700 and 2,500 nm was not captured. To capture the entire spectral range between 1,700 and 2,500 nm, it is crucial to address the limitations of the illumination system. Improving the illumination setup could overcome these limitations and enable a more comprehensive investigation of the spectral characteristics within this range. In this sense, analyzing additional spectral ranges, such as VNIR, could be essential to identify potential biomarkers.

Furthermore, the incorporation of spatial information to examine the morphology of drying blood plasma shows potential to determine whether a subject is affected by MNCD or is a healthy control subject. In this sense, it is crucial to improve the spatial resolution of the HS camera to capture these details and enable a more accurate morphological analysis. This could provide valuable information on the structural alterations that occur in blood plasma due to MNCD, assisting in distinguishing affected individuals from healthy controls. Related to the morphology, further studies should be performed using microscopy to analyze structural patterns. In addition, potential identification of spectral biomarkers can be performed using microscopy.

6.4 Impact of the PhD Thesis

This section contains all scientific communications published during the development of the work described in this dissertation. The communications are divided into journal publications, book chapters, and conference presentations, organized chronologically. During the course of this dissertation, 11 Journal Citation Reports (JCR) papers, 2 book chapters, and 15 peer-reviewed conference papers directly related to this research have been achieved, including 1 Best Paper Award in the SPIE Medical Imaging 2022 Conference. In total, 28 scientific contributions have been accomplished.

6.4.1 Publications and dissemination

In this subsection, we provide a list of publications and dissemination, which may include international collaborations or publications in open access journals. This list uses the following acronyms to highlight the special characteristics of each one of the publications: ***OA**: Open Access; **OC**: Open Code; **OD**: Open Data; **IC**: International collaboration; **CA**: Corresponding author; **IF**: Impact Factor.*

6.4.1.1 Journal publications

[1] Alejandro Cruz-Guerrero; Daniel Campos-Delgado; Aldo R. Mejía-Rodríguez; **Raquel Leon**; Samuel Ortega; Himar Fabelo; Gustavo M. Callico. “Hybrid Brain Tumor Classification of Histopathology Hyperspectral Images by Linear Unmixing and an Ensemble of Deep Neural Networks”, *Healthcare Technology Letters,* **2024. [IF: 2.1 (2022)- Q3] [Related with Chapter 3] [OA, IC]**

[2] **Raquel Leon**; Himar Fabelo; Samuel Ortega; Ines A. Cruz-Guerrero; Daniel Ulises Campos-Delgado; Adam Szolna; Juan F. Piñeiro; Carlos Espino; Aruma J. O’Shanahan; Maria Hernandez; David Carrera; Sara Bisshopp; Coralia Sosa; Francisco J. Balea-Fernandez; Jesus Morera; Bernardino Clavo; Gustavo M. Callico. “Hyperspectral Imaging Benchmark based on Machine Learning for Intraoperative Brain Tumour Detection,” *npj Precision Oncology*, **2023,** 7, pp. 119. doi:10.1038/s41698-023-00475-9 **[IF: 7.9 (2022)- Q1] [Related with Chapter 3] [OA, OC, OD, IC, CA]**

[3] Marco La Salvia; Emanuele Torti; **Raquel Leon**; Himar Fabelo; Samuel Ortega; Francisco Balea-Fernandez; Beatriz Martinez-Vega; Irene Castaño; Pablo Almeida; Gregorio Carretero; Javier A. Hernandez; Gustavo M. Callico; Francesco Leporati. “Neural Networks-Based On-Site Dermatologic Diagnosis through Hyperspectral Epidermal Images”. *Sensors*. **2022**, vol. 22, p. 7139. doi:10.3390/s22197139 **[IF: 3.9 - Q2] [Related with Chapter 4] [OA, OC, OD, IC]**

[4] Marco La Salvia; Emanuele Torti; **Raquel Leon**; Himar Fabelo; Samuel Ortega; Beatriz Martinez-Vega; Gustavo M. Callico; Francesco Leporati. “Deep Convolutional Generative Adversarial Networks to Enhance Artificial Intelligence in Healthcare: A Skin Cancer Application”. *Sensors*. **2022,** vol. 22, p. 6145. doi:10.3390/s22166145 **[IF: 3.9 - Q2] [Related with Chapter 4] [OA, IC]**

[5] Alejandro Morales; Pablo Horstrand; Raúl Guerra; **Raquel Leon**; Samuel Ortega; María Díaz; José M Melián; Sebastián López; José F. López; Gustavo M. Callico;

Ernestina Martel; Roberto Sarmiento. "Laboratory Hyperspectral Image Acquisition System Setup and Validation". Sensors. **2022**, vol. 22, p. 2159. doi: 10.3390/s22062159 **[IF: 3.9 - Q2] [Related with Chapter 2] [OA]**

[6] **Raquel Leon**; Himar Fabelo; Samuel Ortega; Juan F. Pineiro; Adam Szolna; Maria Hernandez; Carlos Espino; Aruma J. O'Shanahan; David Carrera; Sara Bisshopp; Coralia Sosa; Mariano Marquez; Jesus Morera; Bernardino Clavo; Gustavo M. Callico. "VNIR–NIR hyperspectral imaging fusion targeting intraoperative brain cancer detection," *Scientific Reports*, **2021**, 11, pp. 19696. doi:10.1038/s41598-021-99220-0 **[IF: 4.997 - Q2] [Related with Chapter 3] [OA, OD, CA]**

[7] Francisco Javier Balea-Fernandez; Beatriz Martinez-Vega; Samuel Ortega; Himar Fabelo; **Raquel Leon**; Gustavo M. Callico; Cristina Bibao-Sieyro. "Analysis of Risk Factors in Dementia Through Machine Learning". *Journal of Alzheimer's Disease*. **2021,** vol. 79, no. 2, pp. 845-861. doi: 10.3233/JAD-200955 **[IF: 4.160 – Q2] [Related with Chapter 5]**

[8] **Raquel Leon;** Beatriz Martinez-Vega; Himar Fabelo; Samuel Ortega; Veronica Melian; Irene Castaño; Gregorio Carretero; Pablo Almeida; Aday Garcia; Eduardo Quevedo; Javier A. Hernandez; Bernardino Clavo; Gustavo M. Callico. "Non-Invasive Skin Cancer Diagnosis Using Hyperspectral Imaging for In-Situ Clinical Support," *Journal of Clinical Medicine*, **2020**, 9, pp. 1662. doi:10.3390/jcm9061662 **[IF: 4.242 – Q1] [Related with Chapter 4] [OA, CA]**

[9] Emanuele Torti; **Raquel Leon**; Marco La Salvia; Giordana Florimbi; Beatriz Martinez-Vega; Himar Fabelo; Samuel Ortega; Gustavo Marrero Callico; Francesco Leporati. "Parallel Classification Pipelines for Skin Cancer Detection Exploiting Hyperspectral Imaging on Hybrid Systems," *Electronics*, **2020**, 9, 1503. doi:10.3390/electronics9091503 **[IF: 2.397 – Q3] [Related with Chapter 4] [OA, IC]**

[10] Alejandro Cruz-Guerrero; **Raquel Leon**; Daniel Campos-Delgado; Samuel Ortega; Himar Fabelo; Gustavo M. Callico. "Classification of Hyperspectral in-vivo Brain Tissue Based on Linear Unmixing". *Applied Sciences*. **2020**, 10 - 16, pp. 5686. doi:10.3390/app10165686 **[IF: 2.679 – Q2] [Related with Chapter 3] [OA, IC]**

[11] Beatriz Martinez; **Raquel Leon**; Himar Fabelo; Samuel Ortega; Juan F. Piñeiro; Adam Szolna; Maria Hernandez; Carlos Espino; Aruma J. O'Shanahan; David Carrera; Sara Bisshopp; Coralia Sosa; Mariano Marquez; Rafael Camacho; Maria de la Luz Plaza; Jesus Morera; Gustavo M. Callico. "Most Relevant Spectral Bands Identification for Brain Cancer Detection Using Hyperspectral Imaging". *Sensors*. **2019**, 19 - 24. doi:10.3390/s19245481 **[IF: 3.275 – Q1] [Related with Chapter 3] [OA]**

[12] Raquel Lazcano; Daniel Madroñal; Giordana Florimbi; Jaime Sancho; Sergio Sanchez; **Raquel Leon**; Himar Fabelo; Samuel Ortega; Emanuele Torti; Rubén Salvador; Margarita Marrero-Martin; Francesco Leporati; Eduardo Juárez;

Gustavo M. Callico; César Sanz. "Parallel Implementations Assessment of a Spatial-Spectral Classifier for Hyperspectral Clinical Applications". *IEEE Access*. **2019**, 7, pp. 152316 - 152333. doi:10.1109/access.2019.2938708 **[IF: 3.745 – Q1] [Related with Chapter 3] [OA, OD, IC]**

6.4.1.2 Book chapters

[1] Ines A. Cruz-Guerrero; **Raquel Leon**; Aldo Rodrigo Mejía-Rodríguez; Daniel Ulises Campos-Delgado; Himar Fabelo; Samuel Ortega; Gustavo M. Callico. "Hyperspectral Imaging for Cancer Applications", in *Diagnosis and Treatment of Cancer using Thermal Therapies,* CRC Press, **2023**, pp. 81-101. doi:10.1201/9781003342663 **[Related with Chapter 2] [IC]**

[2] **Raquel Leon**; Abian Hernandez; Himar Fabelo; Samuel Ortega; Francisco Balea-Fernandez; Gustavo M. Callico. "SWIR Hyperspectral Imaging to Assess Neurocognitive Disorders Using Blood Plasma Samples", in *Short-Wavelength Infrared Windows for Biomedical Applications*, SPIE, **2021,** pp. 407-437. doi:10.1117/3.2604326.ch13 **[Related with Chapter 5] [IC, CA]**

6.4.1.3 International conferences

[1] **Raquel Leon**; Himar Fabelo; Samuel Ortega; Juan F. Piñeiro; Adam Szolna; Jesus Morera; Bernardino Clavo; Gustavo M. Callico "Evaluation of Hyperspectral Imaging Fusion for in-vivo Brain Tumor Identification and Delineation," in *26th Euromicro Conference on Digital System Design (DSD)*, Dürres, Albania, **2023**. **[Related with Chapter 3] [IC, CA]**

[2] Beatriz Martinez-Vega; **Raquel Leon**; Himar Fabelo; Samuel Ortega; Eduardo Quevedo; Angeles Canovas-Molina; Francisco Rodriguez-Esparagon; Bernardino Clavo; Gustavo M. Callico. "Analysis of the Behavior of Ozone Therapy in Chemotherapy-Induced Neuropathy Using Hyperspectral Imaging Technology", in *26th Euromicro Conference on Digital System Design (DSD)*, Dürres, Albania, **2023**. **[Related with Chapter 3]**

[3] Emanuele Torti; Marco Gazzoni; Elisa Marenzi; **Raquel Leon**; Gustavo M. Callico; Giovanni Danese; Francesco Leporati. "An Attention-Based Parallel Algorithm for Hyperspectral Skin Cancer Classification on Low-Power GPUs", in *26th Euromicro Conference on Digital System Design (DSD)*, Dürres, Albania, **2023**. **[Related with Chapter 4] [IC]**

[4] Mario Guanche-Hernández, **Raquel Leon**, Pedro P. Carballo. "MPSoC FPGA Implementation of Algorithms of Machine Learning for Clinical Applications Using High-Level Design Methodology", in *26th Euromicro Conference on Digital System Design (DSD)*, Dürres, Albania, **2023**. **[Related with Chapter 4]**

[5] **Raquel Leon**; Sofia H. Gelado; Himar Fabelo; Samuel Ortega; Laura Quintana; Adam Szolna; Juan F. Piñeiro; Francisco Balea-Fernandez; Jesus Morera; Bernardino Clavo; Gustavo M. Callico. "Hyperspectral imaging for in-vivo/ex-vivo

tissue analysis of human brain cancer," in *Medical Imaging 2022: Image-Guided Procedures, Robotic Interventions, and Modeling*, San Diego, United States, **2022**, p. 78. **[Related with Chapter 3] [Best Paper Award] [IC, CA]**

[6] Marco La Salvia; Emanuele Torti; Marco Gazzoni; Elisa Marenzi; **Raquel Leon**; Samuel Ortega; Himar Fabelo; Gustavo M. Callico; Francesco Leporati. "Hyperspectral Imaging and Applications II", in *SPIE Photonex: Hyperspectral Imaging and Applications II*, Birmingham, United Kingdom, **2022.** doi:10.1117/12.2646782 **[Related with Chapter 4] [IC]**

[7] Marco La Salvia; Emanuele Torti; Marco Gazzoni; Elisa Marenzi; **Raquel Leon**; Samuel Ortega; Himar Fabelo; Gustavo M. Callico; Francesco Leporati. "Attention-based Skin Cancer Classification Through Hyperspectral Imaging", in *25th Euromicro Conference on Digital System Design (DSD)*, Maspalomas, Spain, **2022.** doi:10.1109/DSD57027.2022.00122 **[Related with Chapter 4] [IC]**

[8] Carlos Vega; **Raquel Leon**; Norberto Medina; Himar Fabelo; Samuel Ortega; Francisco J. Balea-Fernández; Aday García; Margarita Medina; Silvia De León; Alicia Martín; Gustavo M. Callico. "Development of a Hyperspectral Colposcope for Early Detection and Assessment of Cervical Dysplasia", in *25th Euromicro Conference on Digital System Design (DSD)*, Maspalomas, Spain, **2022.** doi:10.1109/DSD57027.2022.00121 **[Related with Chapter 3]**

[9] Ines A. Cruz-Guerrero; **Raquel Leon**; Liliana Granados-Castro; Himar Fabelo; Samuel Ortega; Daniel U. Campos-Delgado; Gustavo M. Callico. "Reflectance Calibration with Normalization Correction in Hyperspectral Imaging", in *25th Euromicro Conference on Digital System Design (DSD)*, Maspalomas, Spain, **2022.** doi:10.1109/DSD57027.2022.00120 **[Related with Chapter 3] [IC]**

[10] Laura Quintana; Samuel Ortega; **Raquel Leon**; Himar Fabelo; Francisco J Balea-Fernández; Esther Sauras; Marylene Lejeune; Ramon Bosch; Carlos Lopez; Gustavo M Callico. "In the use of artificial intelligence and hyperspectral imaging in digital pathology for breast cancer cell identification", *Medical Imaging 2022: Digital and Computational Pathology*, San Diego, United States, **2022**, doi:10.1117/12.2611419 **[Related with Chapter 3]**

[11] **Raquel Leon**; Himar Fabelo; Samuel Ortega; Gustavo. M. Callico, "Hyperspectral VNIR and NIR Sensors for the Analysis of Human Normal Brain and Tumor Tissue," in *XXXVI Conference on Design of Circuits and Integrated Systems (DCIS)*, Vila do Conde, Portugal, **2021**. doi:10.1109/DCIS53048.2021.9666168 **[Related with Chapter 3] [CA]**

[12] Laura Quintana; Samuel Ortega; **Raquel Leon**; Himar Fabelo; Gustavo M Callico; Carlos Lopez; Marylene Lejeune; Ramon Bosch. "Instrumentation Evaluation for Hyperspectral Microscopy Targeting Enhanced Medical Histology", in *XXXVI Conference on Design of Circuits and Integrated Systems (DCIS)*, Vila do Conde, Portugal, **2021**. doi:10.1109/DCIS53048.2021.9666188 **[Related with Chapter 3]**

[13] Himar Fabelo; **Raquel Leon**; Samuel Ortega; Francisco Balea-Fernandez; Bernardino Clavo; Gustavo M. Callico; Ana Wagner. "Evaluating the use of

Hyperspectral Imaging as Complementary Blood Sample Tests", in *XXXVI Conference on Design of Circuits and Integrated Systems (DCIS)*, Vila do Conde, Portugal, **2021**. doi:10.1109/DCIS53048.2021.9666164 **[Related with Chapter 5]**

[14] Beatriz Martinez-Vega; **Raquel Leon**; Himar Fabelo; Samuel Ortega; Gustavo M. Callico; David Suarez-Vega; Bernardino Clavo. "Oxygen saturation measurement using hyperspectral imaging targeting real-time monitoring", in *24th Euromicro Conference on Digital System Design (DSD)*, Palermo, Italy, **2021**. doi:10.1109/DSD53832.2021.00078 **[Related with Chapter 3]**

[15] **Raquel Leon**; Beatriz Martinez-Vega; Himar Fabelo; Samuel Ortega; Gustavo M. Callicó; Francisco Balea-Fernández; Cristina Bilbao Sieyro. "Hyperspectral Imaging for Major Neurocognitive Disorder Detection in Plasma Samples," in *XXXV Conference on Design of Circuits and Integrated Systems (DCIS)*, Segovia, Spain **2020**. doi:10.1109/DCIS51330.2020.9268625 **[Related with Chapter 5] [CA]**

[16] Himar Fabelo; **Raquel Leon**; Samuel Ortega; Francisco Javier Balea-Fernandez; Cristina Bibao-Sieyro; Gustavo M. Callico; Ana Wagner. "Novel Methodology for Alzheimer's Disease Biomarker Identification in Plasma using Hyperspectral Microscopy", in *XXXV Conference on Design of Circuits and Integrated Systems (DCIS)*, Segovia, Spain, **2020**. doi:10.1109/DCIS51330.2020.9268654 **[Related with Chapter 5]**

[17] Beatriz Martinez-Vega; Eduardo Quevedo; **Raquel Leon**; Himar Fabelo; Samuel Ortega; Gustavo M. Callico; Irene Castaño; Gregorio Carretero; Pablo Almeida; Aday Garcia; Javier A. Hernandez; Stig Uteng; Fred Godtliebsen. "Statistics-based Classification Approach for Hyperspectral Dermatologic Data Processing", in *XXXV Conference on Design of Circuits and Integrated Systems (DCIS)*, Segovia, Spain, **2020**. doi:10.1109/DCIS51330.2020.9268646 **[Related with Chapter 4] [IC]**

[18] Jose Cabrera; Noemi Falcon; Aythami Yanez; Samuel Ortega; **Raquel Leon**; Himar Fabelo; Gustavo M. Callico. "Regulated Power Supply with High Power Factor for Hyperspectral Imaging Applications", in *XIV Technologies Applied to Electronics Teaching Conference (TAEE),* Porto, Portugal, **2020**. doi:10.1109/TAEE46915.2020.9163660 **[Related with Chapter 2]**

6.4.2 Participation in research projects

6.4.2.1 European projects

[1] **Ref. 101137416**: *STRATUM (3D Decision Support Tool for Brain Tumor Surgery – GA:* 101137416*)*. European Union's Horizon Europe Programme HORIZON-IA action. PI: Gustavo M. Callico. ULPGC. 01/12/2023 - 30/11/2028. 9,990,566.25 €. **Task**: *Project manager, coordinator assistant and researcher*.

[2] **Ref. 101017385**: *WARIFA (Artificial intelligence and the prevention of chronic conditions – GA:* 101017385*)*. European Union's Horizon 2020 research and innovation programme. PI: Gustavo M. Callico and Ana Wägner. ULPGC. 01/01/2021 – 31/12/2024. 6,726,468.75 €. **Task**: *HS acquisition system development and multimodal data collection*.

6.4.2.2 National projects

[1] **Ref. PID2020-116417RB-C42**: *TALENT (HypErsPEctRal Imaging for Artificial intelligence applications)*. Spanish Government and European Union (FEDER funds). PI: Gustavo M. Callico and Sebastian Lopez. ULPGC. 01/09/2021 - 01/09/2024 175,813.00 €. **Task**: *Project manager and scientific coordinator*.

[2] **Ref. TEC2017-86722-C4-1-R**: *PLATINO (Plataforma HW/SW Distribuida para el Procesamiento Inteligente de Información Sensorial Heterogénea en Aplicaciones de Supervisión de Grandes Espacios Naturales)*. MINECO (Spain) Proyectos I+D+i – Retos Investigación. PIs: Sebastian Lopez and Gustavo M. Callico. ULPGC. 01/01/2018 - 31/12/2020. 228,690.00 €. **Task**: *HS data acquisition and processing*.

6.4.2.3 Regional projects

[1] **Ref. ProID2017010164**: *ITHACA (IdenTificacion Hiperespectral de tumores CerebrAles)*. Gobierno de Canarias (Canary Islands) Programa de Apoyo a la Investigación María del Carmen Betancourt y Molina. PI: Gustavo M. Callico. ULPGC. 01/01/2018-30/09/2019. 69,914.45 €. **Task**: *Project manager and main researcher in the project*.

[2] **Ref. FFPI21/BE01**: *Use of hyperspectral imaging as a prognostic factor for relapse due to distant metastasis in breast cancer*. Fundació Doctor Ferran. PI: Esther Sauras. Hospital Verge de La Cinta. 01/01/2022-31/12/2022. 3,000 €. **Task**: *Development of an HS image processing algorithms*.

[3] **Ref. PIFIISC23/13**: *Valor diagnóstico y predictivo de la imagen hiperespectral en la neuropatíaperiférica inducida por quimioterapia*. Fundación Canaria Instituto de Investigación Sanitaria de Canarias (FIISC). PI: Bernardino Clavo Varas. Hospital Univ. de Gran Canaria Dr. Negrín. 01/12/2023 - 30/12/2025. 25.000 €. **Task**: *Development of an HS acquisition system*.

[4] **Ref. PIFIISC23/44**: *Evaluación con imagen hiperespectral del estrés oxidativo en pacientes con toxicidad por radioterapia o quimioterapia*. Fundación Canaria Instituto de Investigación Sanitaria de Canarias (FIISC). PI: Francisco Rodriguez Esparragon; Francisco Balea Fernandez. Hospital Univ. de Gran Canaria Dr. Negrín. 01/12/2023 - 30/12/2025. 12.000 €. **Task**: *Development of HS acquisition system and HS image processing algorithms*.

[5] **Ref. 016/2019**: *Dolor por neuropatía periférica inducida por quimioterapia: Valor diagnóstico y predictivo de la imagen hiperespectral en pacientes del ensayo clínico "O3NPIQ" [(Clinical Trial: EudraCT 2019-000821-37) - (BF1-19-03) - (PI 19/00458) - (016/2019)].* Fundación DISA (Canary Islands) Premios Fundación DISA 2019 a la Investigación Biomédica. PI: Bernardino Clavo Varas. Hospital Univ. de Gran Canaria Dr. Negrín. 01/01/2020-01/01/2022. 15,600.00 €. **Task**: *Development of an HS and thermal infrared acquisition system.*

[6] **Ref. PIFUN44/17**: *O3Cardio (Effectiveness and cost-effectiveness of Ozone therapy in patients with ischemic heart disease refractory to medical and surgical treatment: Randomized, triple-blind clinical trial [EudraCT 2018-000201-24]).* FUNCANIS (Canary Islands) Ayudas para la financiación de proyectos de investigación, desarrollo einnovación en Biomedicina y Ciencias de la Salud. PI: Bernardino Clavo. Hospital Univ. de Gran Canaria Dr. Negrín. 01/01/2018-31/12/2019. 21,804.00 €. **Task**: *Development of an HS and thermal infrared acquisition system.*

6.4.3 Grants obtained

[1] **Pre-doctoral grant** given by the “Agencia Canaria de Investigacion, Innovacion y Sociedad de la Información (ACIISI)” of the “Consejería de Economía, Conocimiento y Empleo” of the “Gobierno de Canarias”, which is part-financed by the European Social Fund (FSE) (POC 2014-2020, Eje 3 Tema Prioritario 74 (85%)).

[2] **Research intership movility grant** given by the “Agencia Canaria de Investigacion, Innovacion y Sociedad de la Información (ACIISI)” of the “Consejería de Economía, Conocimiento y Empleo” of the “Gobierno de Canarias”, which is part-financed by the European Social Fund (FSE) (POC 2014-2020, Eje 3 Tema Prioritario 74 (85%)).

6.4.4 Research contracts

[1] **Project Manager and Researcher** in the ITHaCA project. 01/11/2018 - 14/07/2020.

Annex A: Resumen en español

A1.1. Introducción y motivación

La imagen hiperespectral es una técnica emergente capaz de proporcionar una guía intraoperatoria sin etiquetas, sin contacto, casi en tiempo real y mínimamente invasiva mediante el uso de iluminación no ionizante y sin emplear ningún agente de contraste, por lo que es totalmente inocuas para el paciente. Las imágenes hiperespectrales están formadas por cientos de bandas espectrales dentro y fuera del rango espectral visual humano. Esta técnica proporciona, para cada píxel, un espectro continuo que permite identificar el tejido, material o sustancia presente en la escena capturada basándose en su composición química.

En los últimos años, la imagen hiperespectral médica ha empezado a lograr resultados prometedores en muchas especialidades diferentes (como por ejemplo en la oncología, patología digital, oftalmología, dermatología o gastroenterología) mediante la utilización de algoritmos de inteligencia artificial de vanguardia y gracias al aumento de la potencia computacional. Actualmente, se están consiguiendo resultados prometedores en diferentes tipos de cáncer utilizando la imagen hiperespectral. En particular, la imagen hiperespectral ha sido ampliamente estudiada en la literatura para el cáncer gastrointestinal tanto en muestras de tejido in-vivo como ex-vivo, incluyendo estómago, hígado, esófago, páncreas y cáncer colorrectal. Además, la imagen hiperespectral se está convirtiendo en una herramienta no sólo para la detección del cáncer, sino también para el diagnóstico de otras enfermedades, como el descubrimiento y la validación de biomarcadores o la medición de la perfusión tisular.

En este sentido, esta tesis doctoral evalúa el potencial de la imagen hiperespectral como herramienta de diagnóstico para tres aplicaciones médicas diferentes: *neurocirugía*, *dermatología* y *neurogeriatría*.

Esta Tesis presenta los resultados alcanzados gracias a la colaboración entre el Instituto de Microelectrónica Aplicada (IUMA) de la Universidad de Las Palmas de Gran Canaria (ULPGC) y varias instituciones de investigación:

- Universidad de Pavía (Italia).
- Universidad Autónoma de San Luis Potosí (México).
- Departamento de Neurocirugía del Hospital Universitario de Gran Canaria Doctor Negrín de Las Palmas de Gran Canaria (España).
- Departamento de Dermatología del Hospital Universitario de Gran Canaria Doctor Negrín de Las Palmas de Gran Canaria (España).

- Departamento de Dermatología del Complejo Hospitalario Universitario Insular-Materno Infantil de Las Palmas de Gran Canaria (España).
- Unidad de Investigación del Hospital Universitario de Gran Canaria Doctor Negrín de Las Palmas de Gran Canaria (España).

Además, esta investigación se ha realizado en el marco del proyecto ITHaCA (Identificación Hiperespectral de Tumores Cerebrales), financiado por el Gobierno de Canarias mediante Convenio de Subvención ProID2017010164.

Por último, esta tesis se desarrolló mientras Raquel León era beneficiaria de una beca predoctoral concedida por la "Agencia Canaria de Investigación, Innovación y Sociedad de la Información (ACIISI)" de la "Consejería de Economía, Conocimiento y Empleo" del "Gobierno de Canarias", cofinanciada por el Fondo Social Europeo (FSE) (POC 2014-2020, Eje 3 Tema Prioritario 74 (85%)).

A1.2. Sistema de adquisición intraoperatoria hiperespectral para el diagnóstico y guiado en neurocirugía

En el campo del cáncer cerebral, esta tecnología está surgiendo como una novedosa técnica de imagen que podría ofrecer nuevas capacidades para delimitar el tejido tumoral cerebral en tiempo quirúrgico. La identificación precisa de los límites entre el tumor y el tejido normal durante la cirugía mejora la resección. Una resección exitosa del tumor se asocia a una supervivencia prolongada. No obstante, debido a la naturaleza y localización del tumor, la resección completa no siempre es posible o puede producir daños neurológicos al paciente. Por lo tanto, los cirujanos tienen que encontrar un equilibrio entre la extirpación del tumor y el compromiso neurológico. Actualmente, los neurocirujanos utilizan varias herramientas de guía intraoperatoria para ayudar a la resección tumoral, como la neuronavegación, la imagen por resonancia magnética o marcadores tumorales fluorescentes como el 5-ALA. Sin embargo, estas herramientas presentan varias limitaciones, por ejemplo, la imagen por resonancia magnética es un procedimiento caro debido a que requiere quirófanos específicos sin elementos ferromagnéticos, lo que aumenta el tiempo quirúrgico. Los cambios en el volumen del tumor que se producen durante la craneotomía y el desplazamiento del cerebro no se contemplan en la neuronavegación. El 5-ALA sólo es capaz de identificar gliomas de alto grado administrando por vía oral un agente de contraste al paciente, siendo una metodología invasiva que puede provocar efectos secundarios en el paciente. Por tanto, existe una necesidad actual de explorar nuevas modalidades de imagen que puedan superar dichas limitaciones.

En esta Tesis se optimizó un sistema de adquisición de imagen hiperespectral intraoperatorio para cáncer cerebral con el objetivo de delinear tumores cerebrales durante operaciones quirúrgicas. Este demostrador estaba compuesto por dos cámaras hiperespectrales de tipo *pushbroom*: la cámara que cubre el rango visible e infrarrojo cercano (VNIR) cubría el rango espectral entre 400 y 1000 nm y la del rango infrarrojo cercano (NIR) entre 900-1700 nm. Utilizando este sistema hiperespectral optimizado, se recopiló una base de datos de hiperespectral de cerebro humano compuesta por 10 imágenes de 8 pacientes diferentes. Utilizando esta base de datos y otras dos campañas

de adquisición de datos obtenidas por el sistema original, se analizaron un total de 61 imágenes hiperespectrales de cerebro humano de 34 pacientes diferentes.

Se crearon y evaluaron una serie de mapas vasculares que utilizan ratios espectrales de hemoglobina de absorbancia difusa, permitiendo así la discriminación de diferentes estructuras de tejido cerebral humano in-vivo. Esta relación refleja una diferencia maximizada entre hemoglobina desoxigenada y oxigenada. La identificación de los vasos sanguíneos en los mapas vasculares podría ayudar a mejorar la identificación de áreas tumorales durante procedimientos quirúrgicos, al reducir el número de clases que debe diferenciar un clasificador. Además, se utilizó un método robusto de validación cruzada para evaluar ocho algoritmos de procesamiento diferentes (Figure A 1), primero utilizando sólo información espectral y después utilizando información espacial y espectral. Los algoritmos de *machine learning* se entrenaron empleando las tres campañas de adquisición de datos, utilizando únicamente las imágenes VNIR. Los resultados de clasificación espectral obtenidos mostraron que los métodos basados en SVM (*Support Vector Machine*) y DNN (*Deep Neural Network*) proporcionaron los mejores resultados. Los resultados cualitativos demuestran la capacidad del sistema propuesto basado en imagen hiperespectral para identificar no sólo gliomas de alto grado, sino también otros tumores de bajo grado y tumores secundarios. Además, estos resultados muestran la capacidad de la imagen hiperespectral para resaltar con precisión la vascularización de la superficie cerebral.

Por último, se realizó una exploración del uso del análisis de los datos fusionados VNIR-NIR para la detección e identificación de tumores de cáncer cerebral utilizando la base de datos capturada en esta Tesis. Debido a las dificultades que plantea la obtención de imágenes hiperespectrales in vivo durante procedimientos neuroquirúrgicos en humanos, la creación de una base de datos exhaustiva que abarque toda la diversidad de diferentes pacientes y tipos de tumores cerebrales es una tarea ardua. Por esta razón, los experimentos de fusión se realizaron utilizando un conjunto de datos compuesto por 10 imágenes de HS adquiridas de 8 sujetos diferentes, utilizando una estrategia de partición *leave-patient-one-out*. Los resultados de la clasificación indican que la presencia de hemoglobina en la región visible mejora la identificación de tumores y tejido hipervascularizado cuando se utilizan únicamente imágenes VNIR, mientras que las imágenes NIR delimitan con precisión la zona parenquimatosa. Los mapas de clasificación generados a partir de las imágenes VNIR-NIR fusionadas proporcionan mapas más detallados, eliminando los falsos positivos presentes en los resultados VNIR y NIR de manera independiente.

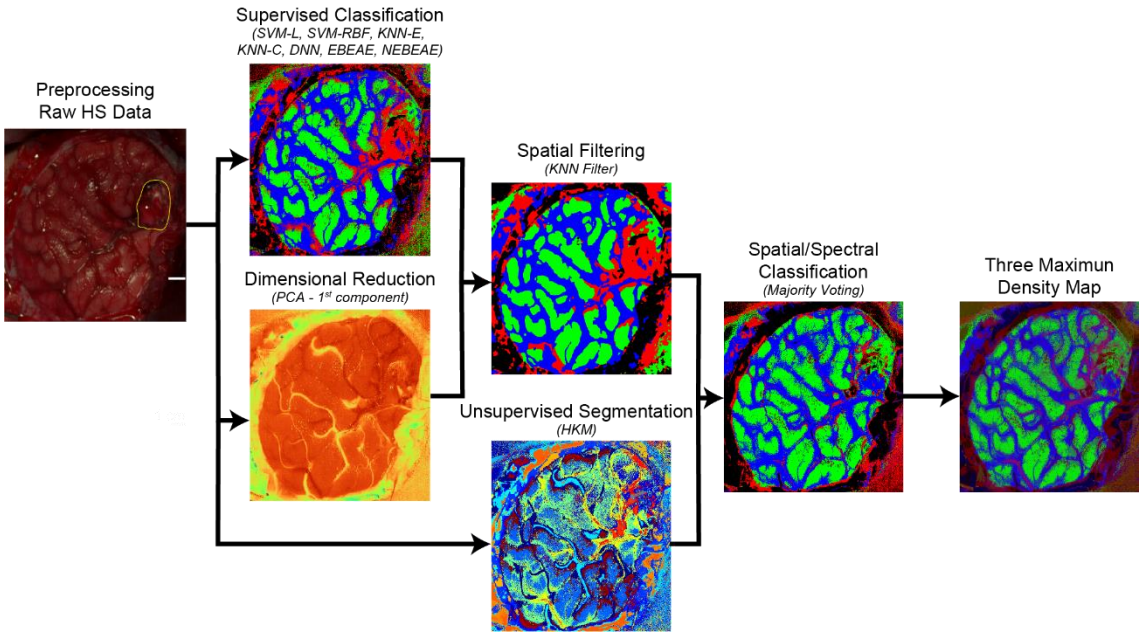

Figure A 1: Propuesta de marco de procesamiento para generar los mapas de densidad para la cirugía intraoperatoria asistida por patología.

A1.3. Sistema dermatoscópico hiperespectral para la detección del cáncer de piel

El cáncer de piel es una de las formas de cáncer más comunes en todo el mundo y su detección precoz es clave para lograr un tratamiento eficaz de la lesión. Habitualmente, el diagnóstico del cáncer de piel se basa en la experiencia del dermatólogo y en la evaluación patológica de las biopsias. Para evitar procedimientos quirúrgicos innecesarios, debido a la incertidumbre en los diagnósticos actuales, se deben investigar nuevos métodos para mejorar el diagnóstico del cáncer de piel. A pesar de los trabajos de vanguardia y los sistemas comerciales disponibles para ayudar en el diagnóstico del cáncer de piel utilizando principalmente imágenes multiespectrales para la discriminación de melanoma y no melanoma, existe margen para realizar mejoras e investigaciones utilizando la imagen hiperespectral para la discriminación de lesiones pigmentadas malignas y benignas, proporcionando un mayor número de bandas espectrales en rangos espectrales más amplios.

En este sentido, el objetivo principal de esta Tesis es el desarrollo de un marco de clasificación (Figure A 2) basado en la segmentación de imágenes hiperespectrales y la clasificación supervisada mediante el empleo de un sistema dermatológico hiperespectral personalizado. El sistema es capaz de capturar datos hiperespectral en tiempo real de lesiones pigmentadas in vivo compuestos por 125 bandas en el rango espectral de 450-950 nm. Este estudio preliminar pretende demostrar, como prueba de concepto, el uso potencial de la tecnología hiperespectral para ayudar a los dermatólogos en la discriminación de lesiones benignas y malignas (incluyendo tanto lesiones de no melanoma como de melanoma) durante la práctica clínica rutinaria. Se recopiló una base de datos de cáncer de piel compuesta por 76 imágenes hiperespectrales de 61 sujetos utilizando este sistema para la asistencia en el diagnóstico de lesiones pigmentadas.

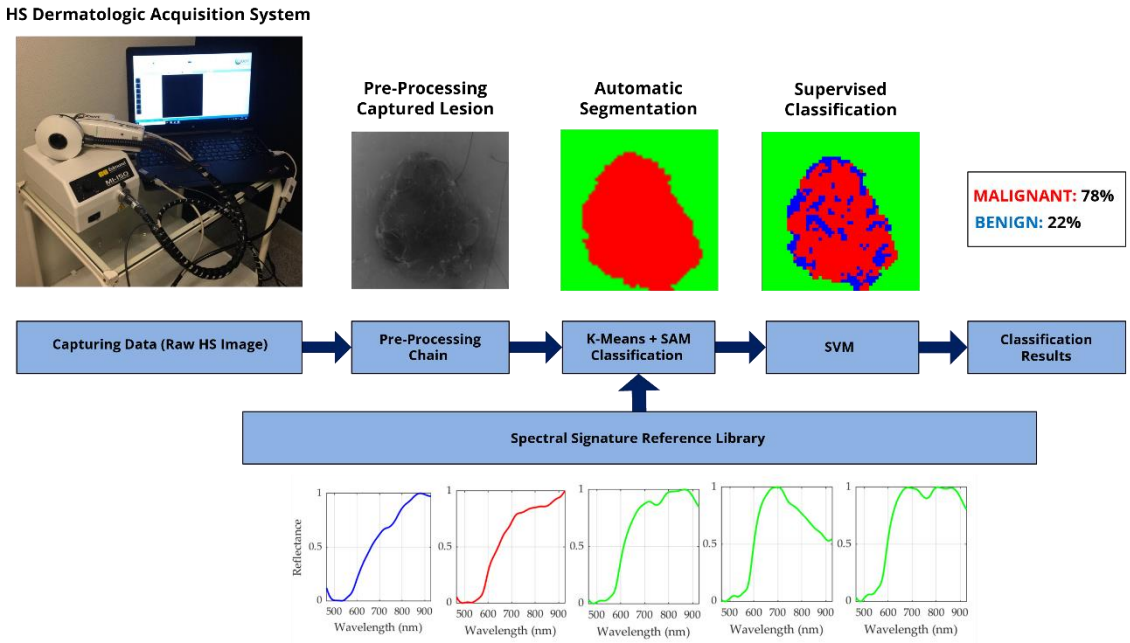

Figure A 2: Diagrama de bloques del marco de clasificación dermatológica hiperespectral (preprocesamiento, segmentación automática y clasificación supervisada) y del sistema de adquisición.

El método propuesto fue capaz de segmentar y clasificar entre lesiones benignas y malignas utilizando únicamente información espectral. Se generó un mapa de segmentación de dos clases en el que se identificaron las lesiones pigmentadas y los píxeles de piel normal. Además, se creó una biblioteca de referencia de firmas espectrales de datos de piel normal y lesiones pigmentadas, empleando únicamente las firmas espectrales del conjunto de entrenamiento etiquetado para evitar la inclusión de imágenes hiperespectrales de validación o prueba en la biblioteca de referencia. Aunque el número de muestras es bajo, esta biblioteca de referencia fue suficiente para un estudio preliminar. Sin embargo, aumentar el número de muestras para cada clase con diferentes tipos de pieles y lesiones pigmentadas podría mejorar los resultados de la segmentación. En los casos en los que la segmentación de la lesión era incorrecta, normalmente esto se producía por una adquisición no óptima de las imágenes hiperespectrales. En el paso de clasificación, se obtuvo una alta sensibilidad para discriminar entre lesión benigna y maligna. En el caso de lesiones atípicas, el bajo número de muestras de esta clase puede producir una clasificación errónea, lo que indica la necesidad de una base de datos mayor en la que se tenga en cuenta la variabilidad entre pacientes y entre lesiones. Evaluando el marco completo, se aplicó un umbral de riesgo para discriminar las lesiones malignas. Las lesiones malignas con una precisión superior al 40% se considerarán que tienen claras evidencias de comportamiento maligno.

A1.4. Sistema de adquisición basado en SWIR para la detección precoz de trastorno neurocognitivo mayor

En esta Tesis, el rango espectral VNIR se ha investigado en dos campos médicos, mientras que el rango espectral NIR se ha analizado únicamente en la aplicación de neurocirugía debido a la posibilidad de capturar datos en dicho rango espectral durante

operaciones quirúrgicas. Sin embargo, el uso del rango SWIR estuvo motivado en ser estudiado en un contexto médico diferente donde las imágenes hiperespectrales de las muestras pueden ser adquiridas en un laboratorio. El propósito de esta investigación es descubrir nuevas perspectivas y aplicaciones potenciales del uso de SWIR para el diagnóstico de enfermedades a través de muestras de plasma sanguíneo. El trastorno neurocognitivo constituye un problema de salud pública en rápido crecimiento y es una de las principales causas de discapacidad y dependencia entre las personas mayores, ya que no son una consecuencia natural o inevitable del envejecimiento. La enfermedad de Alzheimer es la forma más común de trastorno neurocognitivo. Las pruebas clínicas habituales para diagnosticar un posible trastorno neurocognitivo mayor se basan en biomarcadores de neuroimagen in vivo mediante tomografía de emisión de positrones o resonancia magnética, y en biomarcadores en el líquido cefalorraquídeo. Estos métodos de identificación de biomarcadores se utilizan ampliamente para detectar la enfermedad de Alzheimer en ausencia de síntomas, o en casos que muestran cambios neuropatológicos independientemente de los síntomas clínicos. Sin embargo, estos procedimientos son caros, invasivos y con una disponibilidad restringida para verificar el diagnóstico. Por estos motivos, se necesitan métodos alternativos para identificar biomarcadores de trastorno neurocognitivo mayor, como los biomarcadores sanguíneos, que son una alternativa menos invasiva y rentable para la detección precoz. El plasma se utiliza para identificar proteínas relacionadas con la enfermedad, como la albúmina, el fibrinógeno y las inmunoglobulinas. El plasma se compone principalmente de agua (90%), diversas proteínas (6%), electrolitos inorgánicos (1%), glucosa y otros componentes menores.

El objetivo de esta Tesis fue el análisis de muestras de plasma utilizando la tecnología hiperespectral y clasificadores supervisados para discriminar entre sujetos afectados por trastorno neurocognitivo mayor y sujetos de control sanos, evaluando el potencial uso de esta tecnología en este campo. Se propuso una metodología para el análisis de muestras de plasma sanguíneo, incluyendo la selección de sujetos, la preparación de muestras de plasma sanguíneo y su posterior captura y análisis mediante imagen hiperespectral. Mediante esta metodología se generó una base de datos compuesta por 83 imágenes (45 casos y 38 controles) utilizando un sistema hiperespectral capaz de capturar muestras de gotas de plasma sanguíneo depositadas sobre un portaobjetos de vidrio, captando información entre 900 y 1700 nm. Además, en esta metodología se propusieron, evaluaron y compararon tres normalizaciones diferentes de los datos con el objetivo de homogeneizar la distribución de las características en la dimensión espectral. El conjunto de datos se dividió en conjunto de entrenamiento, validación y prueba. Los resultados de la clasificación se evaluaron utilizando las diferentes normalizaciones de datos, y dos enfoques de clasificación: un enfoque usando *machine learning* aplicando clasificadores SVM, KNN (*K-Nearest Neighbors*) y RF (*Random Forest*); y un enfoque usando *Deep learning* con un clasificador DNN.

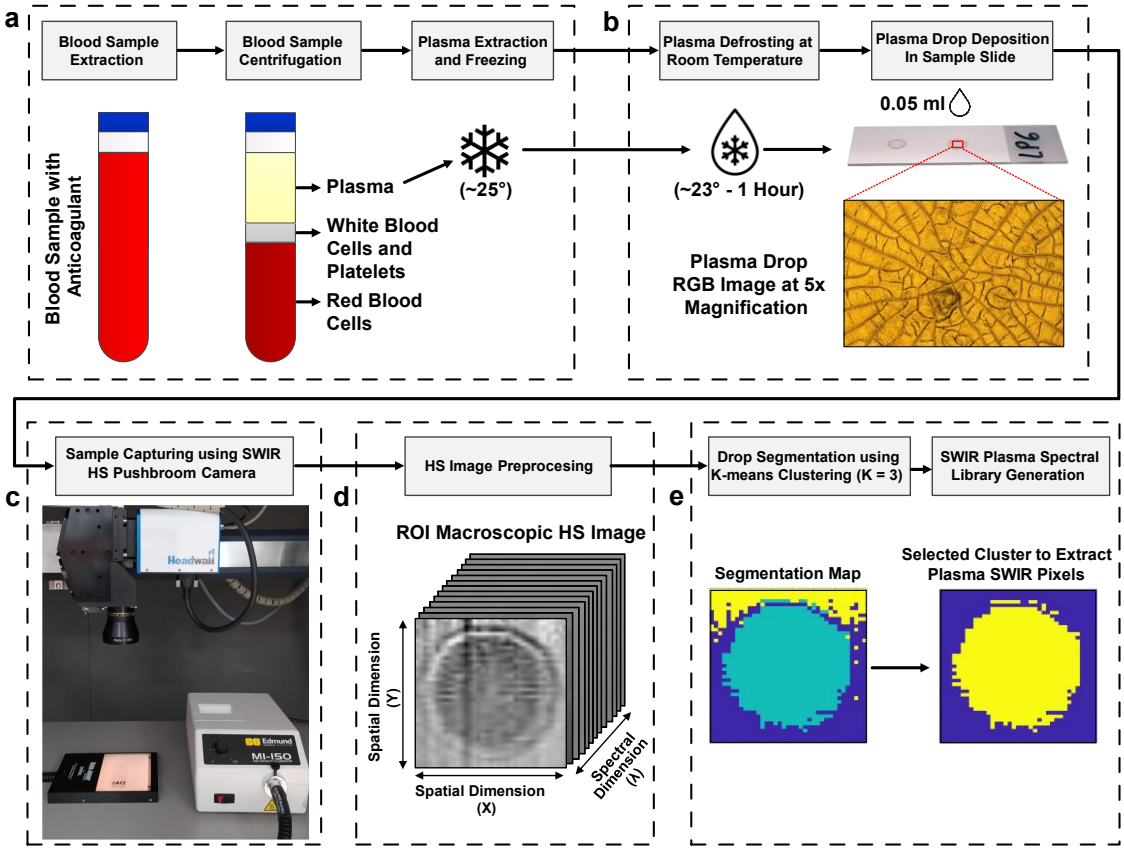

Figure A 3: Esquema metodológico de la adquisición de muestras de plasma sanguíneo. a) Extracción de la muestra de plasma sanguíneo. **b**) Portaobjetos de la muestra de plasma e imagen RGB de la gota de plasma capturada con un microscopio a 5×. **c**) Sistema de adquisición hiperespectral basado en una cámara SWIR. **d**) Ejemplo de una región de interés del cubo hiperespectral capturado macroscópicamente con la cámara SWIR. **e**) Mapa de segmentación obtenido mediante un algoritmo K-means con K = 3 para identificar los píxeles que pertenecen a la muestra de plasma (los colores se asignan aleatoriamente) y clúster seleccionado (píxeles amarillos) para extraer las firmas espectrales del plasma.

Mediante una metodología de búsqueda *coarse-to-fine*, se optimizaron los hiperparámetros de los clasificadores para obtener resultados óptimos. Después, utilizando las curvas ROC, se identificó el umbral óptimo de cada clasificador para la clasificación basada en píxeles. En este punto, las imágenes hiperespectrales de sujetos de control deberían tener un valor de porcentaje de sensibilidad bajo (bajo número de píxeles clasificados como caso), mientras que las imágenes de caso deberían tener un valor de porcentaje de sensibilidad alto (alto número de píxeles clasificados como caso). Sin embargo, los clasificadores SVM-L y DNN clasificaron erróneamente varios píxeles de control como clase de caso. A pesar de esto, SVM-L identificó mejor los píxeles de caso que el clasificador DNN. Por último, las muestras de plasma se clasificaron mediante una metodología basada en la imagen. Este paso implicó la determinación de un umbral para obtener los resultados de la clasificación de forma basada en la muestra. Este umbral se seleccionó realizando un análisis de las métricas de evaluación. Para esta aplicación, se intentó seleccionar un umbral que proporcionara el mejor compromiso entre sensibilidad y especificidad, pero siempre intentando tener valores de sensibilidad altos. En el enfoque de *machine learning*, el mejor compromiso entre sensibilidad (77,7%) y especificidad (62,5%) se obtiene utilizando un umbral de 0,65, con un ACC del 70,5% y una puntuación F1 del 73,6%. En el enfoque *Deep learning*, el valor umbral seleccionado fue 0,3, obteniéndose el mejor ACC (82,3%) y sensibilidad (100%), con una especificidad del 62,5% y una puntuación F1 del 85,7%.

Este umbral se validó utilizando las muestras de prueba. El clasificador SVM-L ofrece una especificidad elevada (88%), clasificando correctamente 7 de 8 muestras de control, pero con un valor de sensibilidad del 44%, que identifica correctamente 4 de 9 muestras de caso. Por otro lado, el clasificador DNN sólo identificó correctamente 1 de cada 8 muestras de control, pero con una alta sensibilidad, clasificando correctamente 7 de cada 9 muestras.

A1.5. Conclusiones

En resumen, esta tesis destaca el potencial de la imagen hiperespectral como ayuda innovadora, no invasiva y no ionizante para la visualización, delineación e identificación de lesiones o enfermedades en tiempo real, mejorando los resultados de los pacientes en diversas aplicaciones médicas. La investigación muestra su utilidad para ayudar a los neurocirujanos durante la resección de tumores cerebrales. Además, la tesis presenta un prototipo que utiliza la imagen hiperespectral para identificar y clasificar lesiones pigmentadas de piel, diferenciando entre lesiones benignas, malignas y atípicas. Por último, esta tesis explora el uso de la imagen hiperespectral en muestras de plasma sanguíneo para la identificación temprana de trastornos neurocognitivos.

Aunque queda aún mucho recorrido y mucha experimentación por realizar en este campo y solventar las limitaciones existentes, el enfoque innovador presentado en esta Tesis es prometedor para el futuro desarrollo de herramientas de diagnóstico no invasivas y eficientes para su aplicación dentro del campo médico en diferentes modalidades.

Bibliography

[1] M. Barberio *et al.*, "Intraoperative Guidance Using Hyperspectral Imaging: A Review for Surgeons," *Diagnostics 2021, Vol. 11, Page 2066*, vol. 11, no. 11, p. 2066, Nov. 2021, doi: 10.3390/DIAGNOSTICS11112066.

[2] M. Kamruzzaman and D.-W. Sun, "Introduction to Hyperspectral Imaging Technology," *Comput. Vis. Technol. Food Qual. Eval.*, pp. 111–139, Jan. 2016, doi: 10.1016/B978-0-12-802232-0.00005-0.

[3] M. Halicek, H. Fabelo, S. Ortega, G. M. Callico, and B. Fei, "In-Vivo and Ex-Vivo Tissue Analysis through Hyperspectral Imaging Techniques: Revealing the Invisible Features of Cancer," *Cancers (Basel).*, vol. 11, no. 6, p. 756, May 2019, doi: 10.3390/cancers11060756.

[4] N. Thekkek and R. Richards-Kortum, "Optical imaging for cervical cancer detection: Solutions for a continuing global problem," *Nature Reviews Cancer*, vol. 8, no. 9. Nature Publishing Group, pp. 725–731, Sep. 2008. doi: 10.1038/nrc2462.

[5] S. Ortega, M. Halicek, H. Fabelo, G. M. Callico, and B. Fei, "Hyperspectral and multispectral imaging in digital and computational pathology: a systematic review [Invited]," *Biomed. Opt. Express*, vol. 11, no. 6, p. 3195, Jun. 2020, doi: 10.1364/BOE.386338.

[6] E. R. Reshef, J. B. Miller, and D. G. Vavvas, "Hyperspectral Imaging of the Retina: A Review," *Int. Ophthalmol. Clin.*, vol. 60, no. 1, pp. 85–96, Dec. 2020, doi: 10.1097/IIO.0000000000000293.

[7] T. H. Johansen *et al.*, "Recent advances in hyperspectral imaging for melanoma detection," *Wiley Interdiscip. Rev. Comput. Stat.*, p. e1465, Apr. 2019, doi: 10.1002/wics.1465.

[8] G. Saiko, P. Lombardi, Y. Au, D. Queen, D. Armstrong, and K. Harding, "Hyperspectral imaging in wound care: A systematic review," *Int. Wound J.*, vol. 17, no. 6, pp. 1840–1856, Dec. 2020, doi: 10.1111/iwj.13474.

[9] A. Grigoroiu, J. Yoon, and S. E. Bohndiek, "Deep learning applied to hyperspectral endoscopy for online spectral classification," *Sci. Rep.*, vol. 10, no. 1, pp. 1–10, Dec. 2020, doi: 10.1038/s41598-020-60574-6.

[10] S. Ortega *et al.*, "Use of Hyperspectral/Multispectral Imaging in Gastroenterology. Shedding Some–Different–Light into the Dark," *J. Clin. Med.*, vol. 8, no. 1, p. 36, Jan. 2019, doi: 10.3390/jcm8010036.

[11] B. Fei, "Hyperspectral imaging in medical applications," *Data Handl. Sci. Technol.*, vol. 32, pp. 523–565, Jan. 2019, doi: 10.1016/B978-0-444-63977-6.00021-3.

[12] S. Ortega, M. Halicek, H. Fabelo, E. Quevedo, B. Fei, and G. Marrero Callico, "Information Extraction Techniques in Hyperspectral Imaging Biomedical Applications," in *Multimedia Information Retrieval*, IntechOpen, 2021. doi: 10.5772/intechopen.93960.

[13] K. D. Davis *et al.*, "Discovery and validation of biomarkers to aid the development of safe

and effective pain therapeutics: challenges and opportunities," *Nat. Rev. Neurol.*, vol. 16, no. 7, pp. 381–400, Jul. 2020, doi: 10.1038/s41582-020-0362-2.

[14] S. F. Kleiss *et al.*, "Hyperspectral imaging for noninvasive tissue perfusion measurements of the lower leg: review of literature and introduction of a standardized measurement protocol with a portable system," *J. Cardiovasc. Surg. (Torino).*, vol. 60, no. 6, pp. 652–661, Jan. 2020, doi: 10.23736/S0021-9509.19.11101-9.

[15] S. Lapointe, A. Perry, and N. A. Butowski, "Primary brain tumours in adults," *The Lancet*, vol. 392, no. 10145. Lancet Publishing Group, pp. 432–446, Aug. 04, 2018. doi: 10.1016/S0140-6736(18)30990-5.

[16] N. Verburg and P. C. de Witt Hamer, "State-of-the-art imaging for glioma surgery," *Neurosurg. Rev.*, vol. 44, no. 3, pp. 1331–1343, Jun. 2021, doi: 10.1007/s10143-020-01337-9.

[17] R. S. D'Amico, Z. K. Englander, P. Canoll, and J. N. Bruce, "Extent of Resection in Glioma–A Review of the Cutting Edge," *World Neurosurgery*, vol. 103. Elsevier Inc., pp. 538–549, Jul. 2017. doi: 10.1016/j.wneu.2017.04.041.

[18] H. Tsao *et al.*, "Early detection of melanoma: Reviewing the ABCDEs American Academy of Dermatology Ad Hoc Task Force for the ABCDEs of Melanoma," *J. Am. Acad. Dermatol.*, vol. 72, no. 4, pp. 717–723, 2015, doi: 10.1016/j.jaad.2015.01.025.

[19] S. Jain, V. Jagtap, and N. Pise, "Computer aided melanoma skin cancer detection using image processing," *Procedia Comput. Sci.*, vol. 48, no. C, pp. 736–741, 2015, doi: 10.1016/j.procs.2015.04.209.

[20] K. Mokrani, "Classification of malignant melanoma and benign skin lesions: implementation of automatic ABCD rule," *IET Image Process.*, vol. 10, no. 6, pp. 448-455(7), Jun. 2016.

[21] J. R. Simpson, "DSM-5 and neurocognitive disorders," *J. Am. Acad. Psychiatry Law*, vol. 42, no. 2, pp. 159–164, Jun. 2014.

[22] T. T. Nguyen, Q. T. H. Ta, T. K. O. Nguyen, T. T. D. Nguyen, and V. G. Vo, "Role of body-fluid biomarkers in Alzheimer's disease diagnosis," *Diagnostics*, vol. 10, no. 5. MDPI AG, May 01, 2020. doi: 10.3390/diagnostics10050326.

[23] L. Mosconi, V. Berti, L. Glodzik, A. Pupi, S. De Santi, and M. J. De Leon, "Pre-clinical detection of Alzheimer's disease using FDG-PET, with or without amyloid imaging," *Journal of Alzheimer's Disease*, vol. 20, no. 3. IOS Press, pp. 843–854, 2010. doi: 10.3233/JAD-2010-091504.

[24] S. Y. Lin *et al.*, "Plasma amyloid assay as a pre-screening tool for amyloid positron emission tomography imaging in early stage Alzheimer's disease," *Alzheimer's Res. Ther.*, vol. 11, no. 1, p. 111, Dec. 2019, doi: 10.1186/s13195-019-0566-0.

[25] S. Li, W. Song, L. Fang, Y. Chen, P. Ghamisi, and J. A. Benediktsson, "Deep learning for hyperspectral image classification: An overview," *IEEE Trans. Geosci. Remote Sens.*, vol. 57, no. 9, pp. 6690–6709, Sep. 2019, doi: 10.1109/TGRS.2019.2907932.

[26] Y. Gu *et al.*, "Multimodal hyperspectral remote sensing: an overview and perspective," *Sci. China Inf. Sci. 2021 642*, vol. 64, no. 2, pp. 1–24, Jan. 2021, doi: 10.1007/S11432-020-3084-1.

[27] R. Vejarano, R. Siche, and W. Tesfaye, "Evaluation of biological contaminants in foods by hyperspectral imaging: A review," *Int. J. Food Prop.*, vol. 20, pp. 1–34, Jun. 2017, doi: 10.1080/10942912.2017.1338729.

[28] X. Su *et al.*, "A Review of Pharmaceutical Robot based on Hyperspectral Technology," *J. Intell. Robot. Syst.*, vol. 105, no. 4, p. 75, Aug. 2022, doi: 10.1007/s10846-022-01602-7.

[29] J. C. Montes-Herrera, E. Cimoli, V. Cummings, N. Hill, A. Lucieer, and V. Lucieer, "Underwater Hyperspectral Imaging (UHI): A Review of Systems and Applications for Proximal Seafloor Ecosystem Studies," *Remote Sens.*, vol. 13, no. 17, p. 3451, Aug. 2021, doi: 10.3390/rs13173451.

[30] G. Lassalle, S. Fabre, A. Credoz, R. Hédacq, D. Dubucq, and A. Elger, "Mapping leaf

metal content over industrial brownfields using airborne hyperspectral imaging and optimized vegetation indices," *Sci. Rep.*, vol. 11, no. 1, p. 2, Dec. 2021, doi: 10.1038/s41598-020-79439-z.

[31] T. Arnold, M. De Biasio, T. Bereczki, M. Baumgart, and A. Horn, "Development of inspection system for the detection and analysis of solid particles and oil droplets in process water of the petrochemical industry using hyperspectral imaging and fluorescence imaging," in *Algorithms, Technologies, and Applications for Multispectral and Hyperspectral Imaging XXVIII*, May 2022, p. 37. doi: 10.1117/12.2618760.

[32] M. Shimoni, R. Haelterman, and C. Perneel, "Hypersectral imaging for military and security applications: Combining Myriad processing and sensing techniques," *IEEE Geosci. Remote Sens. Mag.*, vol. 7, no. 2, pp. 101–117, Jun. 2019, doi: 10.1109/MGRS.2019.2902525.

[33] B. Lu, Y. He, and P. D. Dao, "Comparing the Performance of Multispectral and Hyperspectral Images for Estimating Vegetation Properties," *IEEE J. Sel. Top. Appl. Earth Obs. Remote Sens.*, vol. 12, no. 6, pp. 1784–1797, Jun. 2019, doi: 10.1109/JSTARS.2019.2910558.

[34] M. Govender, K. Chetty, and H. Bulcock, "A review of hyperspectral remote sensing and its application in vegetation and water resource studies," *Water {SA}*, vol. 33, no. 2, 2009, doi: 10.4314/wsa.v33i2.49049.

[35] M. Kamruzzaman and D.-W. Sun, "Introduction to Hyperspectral Imaging Technology," in *Computer Vision Technology for Food Quality Evaluation*, Elsevier, 2016, pp. 111–139. doi: 10.1016/B978-0-12-802232-0.00005-0.

[36] G. Sun, Z. Jiao, A. Zhang, F. Li, H. Fu, and Z. Li, "Hyperspectral image-based vegetation index (HSVI): A new vegetation index for urban ecological research," *Int. J. Appl. Earth Obs. Geoinf.*, vol. 103, p. 102529, Dec. 2021, doi: 10.1016/J.JAG.2021.102529.

[37] N. Sulaiman, N. N. Che'ya, M. H. Mohd Roslim, A. S. Juraimi, N. Mohd Noor, and W. F. Fazlil Ilahi, "The Application of Hyperspectral Remote Sensing Imagery (HRSI) for Weed Detection Analysis in Rice Fields: A Review," *Appl. Sci. 2022, Vol. 12, Page 2570*, vol. 12, no. 5, p. 2570, Mar. 2022, doi: 10.3390/APP12052570.

[38] M. J. Khan, H. S. Khan, A. Yousaf, K. Khurshid, and A. Abbas, "Modern Trends in Hyperspectral Image Analysis: A Review," *IEEE Access*, vol. 6. Institute of Electrical and Electronics Engineers Inc., pp. 14118–14129, Mar. 2018. doi: 10.1109/ACCESS.2018.2812999.

[39] K. Heia, A. H. Sivertsen, S. K. Stormo, E. Elvevoll, J. P. Wold, and H. Nilsen, "Detection of Nematodes in Cod (Gadus morhua) Fillets by Imaging Spectroscopy," *J. Food Sci.*, vol. 72, no. 1, pp. E011–E015, Jan. 2007, doi: 10.1111/J.1750-3841.2006.00212.X.

[40] G. Özdoğan, X. Lin, and D. W. Sun, "Rapid and noninvasive sensory analyses of food products by hyperspectral imaging: Recent application developments," *Trends Food Sci. Technol.*, vol. 111, pp. 151–165, May 2021, doi: 10.1016/J.TIFS.2021.02.044.

[41] M. Kamruzzaman, "Fraud Detection in Meat Using Hyperspectral Imaging," *Meat Muscle Biol.*, vol. 5, no. 3, Oct. 2021, doi: 10.22175/mmb.12946.

[42] A. Laborde, F. Puig-Castellví, D. Jouan-Rimbaud Bouveresse, L. Eveleigh, C. Cordella, and B. Jaillais, "Detection of chocolate powder adulteration with peanut using near-infrared hyperspectral imaging and Multivariate Curve Resolution," *Food Control*, vol. 119, p. 107454, Jan. 2021, doi: 10.1016/j.foodcont.2020.107454.

[43] M. Al Ktash, M. Stefanakis, B. Boldrini, E. Ostertag, and M. Brecht, "Characterization of Pharmaceutical Tablets Using UV Hyperspectral Imaging as a Rapid In-Line Analysis Tool," *Sensors*, vol. 21, no. 13, p. 4436, Jun. 2021, doi: 10.3390/s21134436.

[44] A. Holmer *et al.*, "Oxygenation and perfusion monitoring with a hyperspectral camera system for chemical based tissue analysis of skin and organs," *Physiol. Meas.*, vol. 37, no. 11, p. 2064, Oct. 2016, doi: 10.1088/0967-3334/37/11/2064.

[45] M. H. Fouad Aref, A. A. R. Sharawi, and Y. H. El-Sharkawy, "Delineation of the Arm Blood Vessels Utilizing Hyperspectral Imaging to Assist with Phlebotomy for Exploiting

the Cutaneous Tissue Oxygen Concentration," *Photodiagnosis Photodyn. Ther.*, vol. 33, p. 102190, Mar. 2021, doi: 10.1016/j.pdpdt.2021.102190.

[46] S.-H. Tseng, P. Bargo, A. Durkin, and N. Kollias, "Chromophore concentrations, absorption and scattering properties of human skin in-vivo," *Opt. Express*, vol. 17, no. 17, p. 14599, Aug. 2009, doi: 10.1364/OE.17.014599.

[47] L. Rey-Barroso, S. Peña-Gutiérrez, C. Yáñez, F. J. Burgos-Fernández, M. Vilaseca, and S. Royo, "Optical Technologies for the Improvement of Skin Cancer Diagnosis: A Review," *Sensors*, vol. 21, no. 1, p. 252, Jan. 2021, doi: 10.3390/s21010252.

[48] L. Gevaux *et al.*, "Real-time skin chromophore estimation from hyperspectral images using a neural network," *Ski. Res. Technol.*, vol. 27, no. 2, pp. 163–177, Mar. 2021, doi: 10.1111/SRT.12927.

[49] W. Markgraf, J. Lilienthal, P. Feistel, C. Thiele, and H. Malberg, "Algorithm for Mapping Kidney Tissue Water Content during Normothermic Machine Perfusion Using Hyperspectral Imaging," *Algorithms*, vol. 13, no. 11, p. 289, Nov. 2020, doi: 10.3390/a13110289.

[50] J. K. H. Lim *et al.*, "Retinal hyperspectral imaging in the 5xFAD mouse model of Alzheimer's disease," *Sci. Rep.*, vol. 11, no. 1, p. 6387, Dec. 2021, doi: 10.1038/s41598-021-85554-2.

[51] X. Fu and J. Chen, "A Review of Hyperspectral Imaging for Chicken Meat Safety and Quality Evaluation: Application, Hardware, and Software," *Compr. Rev. Food Sci. Food Saf.*, vol. 18, no. 2, pp. 535–547, Mar. 2019, doi: 10.1111/1541-4337.12428.

[52] M. W. Kudenov, C. G. Scarboro, A. Altaqui, M. Boyette, G. C. Yencho, and C. M. Williams, "Internal defect scanning of sweetpotatoes using interactance spectroscopy," *PLoS One*, vol. 16, no. 2, p. e0246872, Feb. 2021, doi: 10.1371/journal.pone.0246872.

[53] X. Fu and J. Chen, "A Review of Hyperspectral Imaging for Chicken Meat Safety and Quality Evaluation: Application, Hardware, and Software," *Compr. Rev. Food Sci. Food Saf.*, vol. 18, no. 2, pp. 535–547, Mar. 2019, doi: 10.1111/1541-4337.12428.

[54] J. Ma, D.-W. Sun, H. Pu, J.-H. Cheng, and Q. Wei, "Advanced Techniques for Hyperspectral Imaging in the Food Industry: Principles and Recent Applications," *Annu. Rev. Food Sci. Technol.*, vol. 10, no. 1, pp. 197–220, Mar. 2019, doi: 10.1146/annurev-food-032818-121155.

[55] T. Adão *et al.*, "Hyperspectral Imaging: A Review on UAV-Based Sensors, Data Processing and Applications for Agriculture and Forestry," *Remote Sens.*, vol. 9, no. 11, p. 1110, Oct. 2017, doi: 10.3390/rs9111110.

[56] A. Ciocia, A. Carullo, P. Di Leo, G. Malgaroli, and F. Spertino, "Realization and Use of an IR Camera for Laboratory and On-field Electroluminescence Inspections of Silicon Photovoltaic Modules," in *2019 IEEE 46th Photovoltaic Specialists Conference (PVSC)*, Jun. 2019, pp. 2734–2739. doi: 10.1109/PVSC40753.2019.8980711.

[57] J. M. Amigo and S. Grassi, "Configuration of hyperspectral and multispectral imaging systems," 2019, pp. 17–34. doi: 10.1016/B978-0-444-63977-6.00002-X.

[58] O. Gutierrez-Navarro, D. U. Campos-Delgado, E. R. Arce-Santana, M. O. Mendez, and J. A. Jo, "Blind end-member and abundance extraction for multispectral fluorescence lifetime imaging microscopy data," *IEEE J. Biomed. Heal. informatics*, vol. 18, no. 2, pp. 606–617, 2013.

[59] Y. Li *et al.*, "Research and Application of Several Key Techniques in Hyperspectral Image Preprocessing," *Front. Plant Sci.*, vol. 12, Feb. 2021, doi: 10.3389/fpls.2021.627865.

[60] B. Jia *et al.*, "Essential processing methods of hyperspectral images of agricultural and food products," *Chemom. Intell. Lab. Syst.*, vol. 198, p. 103936, Mar. 2020, doi: 10.1016/j.chemolab.2020.103936.

[61] P. Geladi, J. Burger, and T. Lestander, "Hyperspectral imaging: calibration problems and solutions," *Chemom. Intell. Lab. Syst.*, vol. 72, no. 2, pp. 209–217, Jul. 2004, doi: 10.1016/j.chemolab.2004.01.023.

[62] J. C. Keresztes, M. Goodarzi, and W. Saeys, “Real-time pixel based early apple bruise detection using short wave infrared hyperspectral imaging in combination with calibration and glare correction techniques,” *Food Control*, vol. 66, pp. 215–226, Aug. 2016, doi: 10.1016/j.foodcont.2016.02.007.

[63] G. ElMasry and D.-W. Sun, “Principles of Hyperspectral Imaging Technology,” in *Hyperspectral Imaging for Food Quality Analysis and Control*, Elsevier, 2010, pp. 3–43. doi: 10.1016/B978-0-12-374753-2.10001-2.

[64] I. T. Jolliffe, *Principal Component Analysis*. New York: Springer-Verlag, 2002. doi: 10.1007/b98835.

[65] G. Camps-Valls and L. Bruzzone, “Kernel-based methods for hyperspectral image classification,” *IEEE Trans. Geosci. Remote Sens.*, vol. 43, no. 6, pp. 1351–1362, Jun. 2005, doi: 10.1109/TGRS.2005.846154.

[66] C. Chang and C. Lin, “LIBSVM : A Library for Support Vector Machines,” *ACM Trans. Intell. Syst. Technol.*, vol. 2, pp. 1–39, 2013, doi: 10.1145/1961189.1961199.

[67] K. Huang, S. Li, X. Kang, and L. Fang, “Spectral–Spatial Hyperspectral Image Classification Based on KNN,” *Sens. Imaging*, vol. 17, no. 1, pp. 1–13, 2016, doi: 10.1007/s11220-015-0126-z.

[68] L. Breiman, “Random Forests,” *Mach. Learn.*, vol. 45, pp. 5–32, 2001.

[69] T. G. Dietterich, “Ensemble Methods in Machine Learning,” in *Multiple Classifier Systems*, Springer Nature, 2000, pp. 1–15. doi: 10.1007/3-540-45014-9_1.

[70] H. Fabelo *et al.*, “Spatio-spectral classification of hyperspectral images for brain cancer detection during surgical operations,” *PLoS One*, vol. 13, no. 3, pp. 1–27, 2018, doi: 10.1371/journal.pone.0193721.

[71] M. A. Massoud and M. M. Kaldas, “Comparative Study of Hyperspectral Partitioning Clustering Algorithms for Mineral Exploration,” *Minia J. Eng. Technol.*, vol. 38, no. 1, 2019.

[72] N. Gillis, D. Kuang, and H. Park, “Hierarchical Clustering of Hyperspectral Images using Rank-Two Nonnegative Matrix Factorization”.

[73] P. J. Rousseeuw, “Silhouettes: A graphical aid to the interpretation and validation of cluster analysis,” *J. Comput. Appl. Math.*, vol. 20, no. C, pp. 53–65, 1987, doi: 10.1016/0377-0427(87)90125-7.

[74] T. Calinski and J. Harabasz, “A dendrite method for cluster analysis,” *Commun. Stat. - Theory Methods*, vol. 3, no. 1, pp. 1–27, 1974, doi: 10.1080/03610927408827101.

[75] D. L. Davies and D. W. Bouldin, “A Cluster Separation Measure,” *IEEE Trans. Pattern Anal. Mach. Intell.*, vol. PAMI-1, no. 2, pp. 224–227, 1979, doi: 10.1109/TPAMI.1979.4766909.

[76] J. J. Rico-Jimenez, D. U. Campos-Delgado, M. Villiger, K. Otsuka, B. E. Bouma, and J. A. Jo, “Automatic classification of atherosclerotic plaques imaged with intravascular OCT,” *Biomed. Opt. Express*, vol. 7, no. 10, pp. 4069–4085, 2016.

[77] D. U. Campos-Delgado *et al.*, “Nonlinear extended blind end-member and abundance extraction for hyperspectral images,” *Signal Processing*, vol. 201, p. 108718, Dec. 2022, doi: 10.1016/j.sigpro.2022.108718.

[78] L. Gao, Z. Wang, L. Zhuang, H. Yu, B. Zhang, and J. Chanussot, “Using low-rank representation of abundance maps and nonnegative tensor factorization for hyperspectral nonlinear unmixing,” *IEEE Trans. Geosci. Remote Sens.*, vol. 60, pp. 1–17, 2021.

[79] R. Heylen, M. Parente, and P. Gader, “A review of nonlinear hyperspectral unmixing methods,” *IEEE J. Sel. Top. Appl. Earth Obs. Remote Sens.*, vol. 7, no. 6, pp. 1844–1868, 2014, doi: 10.1109/JSTARS.2014.2320576.

[80] N. Dobigeon, J.-Y. Tourneret, C. Richard, J. C. M. Bermudez, S. McLaughlin, and A. O. Hero, “Nonlinear unmixing of hyperspectral images: Models and algorithms,” *IEEE Signal Process. Mag.*, vol. 31, no. 1, pp. 82–94, 2013.

[81] D. U. Campos-Delgado *et al.*, "Extended Blind End-Member and Abundance Extraction for Biomedical Imaging Applications," *IEEE Access*, vol. 7, 2019, doi: 10.1109/ACCESS.2019.2958985.

[82] W. M. Wells, P. Viola, H. Atsumi, S. Nakajima, and R. Kikinis, "Multi-modal volume registration by maximization of mutual information," *Med. Image Anal.*, vol. 1, no. 1, pp. 35–51, Mar. 1996, doi: 10.1016/S1361-8415(01)80004-9.

[83] K. Pearson, "Mathematical Contributions to the Theory of Evolution. III. Regression, Heredity, and Panmixia," *Philos. Trans. R. Soc. A Math. Phys. Eng. Sci.*, vol. 187, no. 0, pp. 253–318, Jan. 1896, doi: 10.1098/rsta.1896.0007.

[84] Z. Wang, A. C. Bovik, H. R. Sheikh, and E. P. Simoncelli, "Image quality assessment: From error visibility to structural similarity," *IEEE Trans. Image Process.*, vol. 13, no. 4, pp. 600–612, Apr. 2004, doi: 10.1109/TIP.2003.819861.

[85] J. Muschelli, "ROC and AUC with a Binary Predictor: a Potentially Misleading Metric," *J. Classif.*, 2019, doi: 10.1007/s00357-019-09345-1.

[86] L. R. Dice, "Measures of the Amount of Ecologic Association Between Species," *Ecology*, vol. 26, no. 3, pp. 297–302, Jul. 1945, doi: 10.2307/1932409.

[87] P. Jaccard, "Étude comparative de la distribution florale dans une portion des Alpes et des Jura," *Bull. del la Société Vaudoise des Sci. Nat.*, vol. 37, pp. 547–579, 1901.

[88] H. W. Lilliefors, "On the Kolmogorov-Smirnov Test for Normality with Mean and Variance Unknown," *J. Am. Stat. Assoc.*, vol. 62, no. 318, p. 399, Jun. 1967, doi: 10.2307/2283970.

[89] D. Rey and M. Neuhäuser, "Wilcoxon-Signed-Rank Test," in *International Encyclopedia of Statistical Science*, Berlin, Heidelberg: Springer Berlin Heidelberg, 2011, pp. 1658–1659. doi: 10.1007/978-3-642-04898-2_616.

[90] D. Kalpić, N. Hlupić, and M. Lovrić, "Student's t-Tests," in *International Encyclopedia of Statistical Science*, Berlin, Heidelberg: Springer Berlin Heidelberg, 2011, pp. 1559–1563. doi: 10.1007/978-3-642-04898-2_641.

[91] G. Lu and B. Fei, "Medical hyperspectral imaging: a review.," *J. Biomed. Opt.*, vol. 19, no. 1, p. 10901, 2014, doi: 10.1117/1.JBO.19.1.010901.

[92] C. Caredda, L. Mahieu-Williame, R. Sablong, M. Sdika, J. Guyotat, and B. Montcel, "Optimal Spectral Combination of a Hyperspectral Camera for Intraoperative Hemodynamic and Metabolic Brain Mapping," *Appl. Sci. 2020, Vol. 10, Page 5158*, vol. 10, no. 15, p. 5158, Jul. 2020, doi: 10.3390/APP10155158.

[93] K. Iwaki *et al.*, "A Novel Hyperspectral Imaging System for Intraoperative Prediction of Cerebral Hyperperfusion Syndrome after Superficial Temporal Artery-Middle Cerebral Artery Anastomosis in Patients with Moyamoya Disease," *Cerebrovasc. Dis.*, vol. 50, no. 2, pp. 208–215, Apr. 2021, doi: 10.1159/000513289.

[94] M. Arnold *et al.*, "Global Burden of 5 Major Types of Gastrointestinal Cancer," *Gastroenterology*, vol. 159, no. 1, pp. 335-349.e15, Jul. 2020, doi: 10.1053/J.GASTRO.2020.02.068.

[95] W. Du *et al.*, "Review on the Applications of Deep Learning in the Analysis of Gastrointestinal Endoscopy Images," *IEEE Access*, vol. 7, pp. 142053–142069, 2019, doi: 10.1109/ACCESS.2019.2944676.

[96] J. Lin *et al.*, "Dual-modality endoscopic probe for tissue surface shape reconstruction and hyperspectral imaging enabled by deep neural networks," *Med. Image Anal.*, vol. 48, pp. 162–176, Aug. 2018, doi: 10.1016/J.MEDIA.2018.06.004.

[97] I. C. Wu *et al.*, "Early identification of esophageal squamous neoplasm by hyperspectral endoscopic imaging," *Sci. Reports 2018 81*, vol. 8, no. 1, pp. 1–10, Sep. 2018, doi: 10.1038/s41598-018-32139-1.

[98] J. Yoon *et al.*, "A clinically translatable hyperspectral endoscopy (HySE) system for imaging the gastrointestinal tract," *Nat. Commun. 2019 101*, vol. 10, no. 1, pp. 1–13, Apr. 2019, doi: 10.1038/s41467-019-09484-4.

[99] J. Yoon *et al.*, "First experience in clinical application of hyperspectral endoscopy for evaluation of colonic polyps," *J. Biophotonics*, vol. 14, no. 9, p. e202100078, Sep. 2021, doi: 10.1002/JBIO.202100078.

[100] H. Köhler *et al.*, "Laparoscopic system for simultaneous high-resolution video and rapid hyperspectral imaging in the visible and near-infrared spectral range," *J. Biomed. Opt.*, vol. 25, no. 08, p. 086004, Aug. 2020, doi: 10.1117/1.JBO.25.8.086004.

[101] D. Sato *et al.*, "Distinction of surgically resected gastrointestinal stromal tumor by near-infrared hyperspectral imaging," *Sci. Reports 2020 101*, vol. 10, no. 1, pp. 1–9, Dec. 2020, doi: 10.1038/s41598-020-79021-7.

[102] B. Jansen-Winkeln *et al.*, "Determination of the transection margin during colorectal resection with hyperspectral imaging (HSI)," *Int. J. Colorectal Dis.*, vol. 34, no. 4, pp. 731–739, Apr. 2019, doi: 10.1007/S00384-019-03250-0/FIGURES/6.

[103] B. Jansen-winkeln *et al.*, "Feedforward Artificial Neural Network-Based Colorectal Cancer Detection Using Hyperspectral Imaging: A Step towards Automatic Optical Biopsy," *Cancers 2021, Vol. 13, Page 967*, vol. 13, no. 5, p. 967, Feb. 2021, doi: 10.3390/CANCERS13050967.

[104] D. E. Johnson, B. Burtness, C. R. Leemans, V. W. Y. Lui, J. E. Bauman, and J. R. Grandis, "Head and neck squamous cell carcinoma," *Nat. Rev. Dis. Prim. 2020 61*, vol. 6, no. 1, pp. 1–22, Nov. 2020, doi: 10.1038/s41572-020-00224-3.

[105] M. Halicek, J. V. Little, X. Wang, A. Y. Chen, and B. Fei, "Optical biopsy of head and neck cancer using hyperspectral imaging and convolutional neural networks," *J. Biomed. Opt.*, vol. 24, no. 03, p. 1, Mar. 2019, doi: 10.1117/1.JBO.24.3.036007.

[106] S. G. Brouwer de Koning *et al.*, "Toward assessment of resection margins using hyperspectral diffuse reflection imaging (400–1,700 nm) during tongue cancer surgery," *Lasers Surg. Med.*, vol. 52, no. 6, pp. 496–502, Jul. 2020, doi: 10.1002/lsm.23161.

[107] D. Eggert *et al.*, "In vivo detection of head and neck tumors by hyperspectral imaging combined with deep learning methods," *J. Biophotonics*, vol. 15, no. 3, p. e202100167, Mar. 2022, doi: 10.1002/JBIO.202100167.

[108] C. Klein *et al.*, "Artificial intelligence for solid tumour diagnosis in digital pathology," *Br. J. Pharmacol.*, vol. 178, no. 21, pp. 4291–4315, Nov. 2021, doi: 10.1111/BPH.15633.

[109] S. Ortega *et al.*, "Hyperspectral Push-Broom Microscope Development and Characterization," *IEEE Access*, vol. 7, pp. 122473–122491, 2019, doi: 10.1109/ACCESS.2019.2937729.

[110] S. Ortega, G. M. Callico, M. L. Plaza, R. Camacho, H. Fabelo, and R. Sarmiento, "Hyperspectral database of pathological in-vitro human brain samples to detect carcinogenic tissues," in *Proceedings - International Symposium on Biomedical Imaging*, 2016, vol. 2016-June. doi: 10.1109/ISBI.2016.7493285.

[111] S. Ortega, H. Fabelo, R. Camacho, M. de la Luz Plaza, G. M. Callicó, and R. Sarmiento, "Detecting brain tumor in pathological slides using hyperspectral imaging," *Biomed. Opt. Express*, vol. 9, no. 2, p. 818, Feb. 2018, doi: 10.1364/BOE.9.000818.

[112] S. Ortega *et al.*, "Hyperspectral Imaging for the Detection of Glioblastoma Tumor Cells in H&E Slides Using Convolutional Neural Networks," *Sensors*, vol. 20, no. 7, p. 1911, Mar. 2020, doi: 10.3390/s20071911.

[113] S. Ortega *et al.*, "Hyperspectral imaging and deep learning for the detection of breast cancer cells in digitized histological images," in *Proceedings of SPIE--the International Society for Optical Engineering*, Mar. 2020, vol. 11320, p. 30. doi: 10.1117/12.2548609.

[114] L. Ma, M. Halicek, X. Zhou, J. D. Dormer, and B. Fei, "Hyperspectral Microscopic Imaging for Automatic Detection of Head and Neck Squamous Cell Carcinoma Using Histologic Image and Machine Learning," *Proc. SPIE--the Int. Soc. Opt. Eng.*, vol. 11320, p. 31, Mar. 2020, doi: 10.1117/12.2549369.

[115] M. M. Souza, F. A. Carvalho, E. F. V. Sverzut, M. B. Requena, M. R. Garcia, and S. Pratavieira, "Hyperspectral Imaging System for Tissue Classification in H&E Stained Histological Slides," in *2021 SBFoton International Optics and Photonics Conference*

(SBFoton IOPC), May 2021, pp. 1–4. doi: 10.1109/SBFotonIOPC50774.2021.9461972.

[116] International Association of Cancer Registries (IACR), "Cancer Today," *GLOBOCAN 2020*, 2021.

[117] International Association of Cancer Registries (IACR), "Cancer Tomorrow," *GLOBOCAN 2020*, 2021.

[118] A. P. Patel *et al.*, "Global, regional, and national burden of brain and other CNS cancer, 1990–2016: a systematic analysis for the Global Burden of Disease Study 2016," *Lancet Neurol.*, vol. 18, no. 4, pp. 376–393, Apr. 2019, doi: 10.1016/S1474-4422(18)30468-X.

[119] R. L. Siegel, K. D. Miller, H. E. Fuchs, and A. Jemal, "Cancer Statistics, 2021," *CA. Cancer J. Clin.*, vol. 71, no. 1, pp. 7–33, Jan. 2021, doi: 10.3322/caac.21654.

[120] E. Belykh *et al.*, "Intraoperative Fluorescence Imaging for Personalized Brain Tumor Resection: Current State and Future Directions," *Front. Surg.*, vol. 3, p. 55, Oct. 2016, doi: 10.3389/fsurg.2016.00055.

[121] M. Mori *et al.*, "Intraoperative visualization of cerebral oxygenation using hyperspectral image data: a two-dimensional mapping method," *Int. J. Comput. Assist. Radiol. Surg.*, vol. 9, no. 6, pp. 1059–1072, Nov. 2014, doi: 10.1007/s11548-014-0989-9.

[122] L. Giannoni and F. Lange, "Investigation of the quantification of hemoglobin and cytochrome-c-oxidase in the exposed cortex with near-infrared hyperspectral imaging: a simulation study," *J. Biomed. Opt.*, vol. 25, no. 04, p. 1, Apr. 2020, doi: 10.1117/1.JBO.25.4.046001.

[123] H. Fabelo *et al.*, "An Intraoperative Visualization System Using Hyperspectral Imaging to Aid in Brain Tumor Delineation," *Sensors*, vol. 18, no. 2, p. 430, Feb. 2018, doi: 10.3390/s18020430.

[124] H. Fabelo *et al.*, "In-Vivo Hyperspectral Human Brain Image Database for Brain Cancer Detection," *IEEE Access*, vol. 7, pp. 39098–39116, 2019, doi: 10.1109/ACCESS.2019.2904788.

[125] H. Fabelo *et al.*, "Deep Learning-Based Framework for In Vivo Identification of Glioblastoma Tumor using Hyperspectral Images of Human Brain," *Sensors*, vol. 19, no. 4, p. 920, Feb. 2019, doi: 10.3390/s19040920.

[126] I. A. Cruz-Guerrero, R. Leon, D. U. Campos-Delgado, S. Ortega, H. Fabelo, and G. M. Callico, "Classification of Hyperspectral In Vivo Brain Tissue Based on Linear Unmixing," *Appl. Sci.*, vol. 10, no. 16, p. 5686, Aug. 2020, doi: 10.3390/app10165686.

[127] Q. Hao *et al.*, "Fusing Multiple Deep Models for in Vivo Human Brain Hyperspectral Image Classification to Identify Glioblastoma Tumor," *IEEE Trans. Instrum. Meas.*, vol. 70, 2021, doi: 10.1109/TIM.2021.3117634.

[128] R. Mühle, H. Ernst, S. B. Sobottka, and U. Morgenstern, "Workflow and hardware for intraoperative hyperspectral data acquisition in neurosurgery," *Biomed. Eng. / Biomed. Tech.*, vol. 66, no. 1, pp. 31–42, Feb. 2021, doi: 10.1515/bmt-2019-0333.

[129] G. Urbanos *et al.*, "Supervised Machine Learning Methods and Hyperspectral Imaging Techniques Jointly Applied for Brain Cancer Classification," *Sensors 2021, Vol. 21, Page 3827*, vol. 21, no. 11, p. 3827, May 2021, doi: 10.3390/S21113827.

[130] A. Martin-Perez *et al.*, "Hyperparameter Optimization for Brain Tumor Classification with Hyperspectral Images," in *2022 25th Euromicro Conference on Digital System Design (DSD)*, Aug. 2022, pp. 835–842. doi: 10.1109/DSD57027.2022.00117.

[131] J. Sancho, M. Villa, M. Chavarrías, E. Juarez, A. Lagares, and C. Sanz, "SLIMBRAIN: Augmented reality real-time acquisition and processing system for hyperspectral classification mapping with depth information for in-vivo surgical procedures," *J. Syst. Archit.*, vol. 140, p. 102893, Jul. 2023, doi: 10.1016/j.sysarc.2023.102893.

[132] S. Puustinen *et al.*, "Hyperspectral Imaging in Brain Tumor Surgery—Evidence of Machine Learning-Based Performance," *World Neurosurg.*, vol. 175, pp. e614–e635, Jul. 2023, doi: 10.1016/j.wneu.2023.03.149.

[133] S. Puustinen *et al.*, "Towards Clinical Hyperspectral Imaging (HSI) Standards: Initial

Design for a Microneurosurgical HSI Database," in *2022 IEEE 35th International Symposium on Computer-Based Medical Systems (CBMS)*, Jul. 2022, pp. 394–399. doi: 10.1109/CBMS55023.2022.00077.

[134] T. Giannantonio *et al.*, "Intra-operative brain tumor detection with deep learning-optimized hyperspectral imaging," in *Optical Biopsy XXI: Toward Real-Time Spectroscopic Imaging and Diagnosis*, Mar. 2023, p. 5. doi: 10.1117/12.2646999.

[135] H. Sung *et al.*, "Global Cancer Statistics 2020: GLOBOCAN Estimates of Incidence and Mortality Worldwide for 36 Cancers in 185 Countries," *CA. Cancer J. Clin.*, vol. 71, no. 3, pp. 209–249, May 2021, doi: 10.3322/caac.21660.

[136] M. Zambrano-Román, J. R. Padilla-Gutiérrez, Y. Valle, J. F. Muñoz-Valle, and E. Valdés-Alvarado, "Non-Melanoma Skin Cancer: A Genetic Update and Future Perspectives," *Cancers (Basel).*, vol. 14, no. 10, p. 2371, May 2022, doi: 10.3390/cancers14102371.

[137] D. J. Kadouch *et al.*, "Diagnostic accuracy of confocal microscopy imaging vs. punch biopsy for diagnosing and subtyping basal cell carcinoma," *J. Eur. Acad. Dermatology Venereol.*, vol. 31, no. 10, pp. 1641–1648, Oct. 2017, doi: 10.1111/jdv.14253.

[138] J. Kato, K. Horimoto, S. Sato, T. Minowa, and H. Uhara, "Dermoscopy of Melanoma and Non-melanoma Skin Cancers," *Front. Med.*, vol. 6, p. 180, Aug. 2019, doi: 10.3389/FMED.2019.00180/BIBTEX.

[139] L. P. Aggarwal and F. A. Papay, "Applications of Multispectral and Hyperspectral Imaging in Dermatology," *Exp. Dermatol.*, Jun. 2022, doi: 10.1111/exd.14624.

[140] E. Aloupogianni, M. Ishikawa, N. Kobayashi, and T. Obi, "Hyperspectral and multispectral image processing for gross-level tumor detection in skin lesions: a systematic review," *J. Biomed. Opt.*, vol. 27, no. 06, Jun. 2022, doi: 10.1117/1.JBO.27.6.060901.

[141] R. Jolivot, Y. Benezeth, and F. Marzani, "Skin parameter map retrieval from a dedicated multispectral imaging system applied to dermatology/cosmetology," *Int. J. Biomed. Imaging*, vol. 2013, 2013, doi: 10.1155/2013/978289.

[142] D. Gutkowicz-Krusin, M. Elbaum, M. Greenebau, and A. Jacobs, "US6208749B1 - Systems and methods for the multispectral imaging and characterization of skin tissue - Google Patents," 2001 [Online]. Available: https://patents.google.com/patent/US6208749B1/en

[143] M. Elbaum *et al.*, "Automatic differentiation of melanoma from melanocytic nevi with multispectral digital dermoscopy: A feasibility study," *J. Am. Acad. Dermatol.*, vol. 44, no. 2, pp. 207–218, 2001, doi: 10.1067/mjd.2001.110395.

[144] G. Monheit *et al.*, "The performance of MelaFind: A prospective multicenter study," *Arch. Dermatol.*, vol. 147, no. 2, pp. 188–194, 2011, doi: 10.1001/archdermatol.2010.302.

[145] C. Fink, C. Jaeger, K. Jaeger, and H. A. Haenssle, "Diagnostic performance of the MelaFind device in a real-life clinical setting," *JDDG J. der Dtsch. Dermatologischen Gesellschaft*, vol. 15, no. 4, pp. 414–419, Apr. 2017, doi: 10.1111/ddg.13220.

[146] A. N. MacLellan *et al.*, "The use of noninvasive imaging techniques in the diagnosis of melanoma: a prospective diagnostic accuracy study," *J. Am. Acad. Dermatol.*, vol. 85, no. 2, pp. 353–359, Aug. 2021, doi: 10.1016/j.jaad.2020.04.019.

[147] M. Moncrieff, S. Cotton, E. Claridge, and P. Hall, "Spectrophotometric intracutaneous analysis: a new technique for imaging pigmented skin lesions," *Br. J. Dermatol.*, vol. 146, no. 3, pp. 448–457, Mar. 2002, doi: 10.1046/j.1365-2133.2002.04569.x.

[148] K. Govindan, J. Smith, L. Knowles, A. Harvey, P. Townsend, and J. Kenealy, "Assessment of nurse-led screening of pigmented lesions using SIAscope," *J. Plast. Reconstr. Aesthetic Surg.*, vol. 60, no. 6, pp. 639–645, Jun. 2007, doi: 10.1016/J.BJPS.2006.10.003.

[149] J. D. Emery, J. Hunter, P. N. Hall, A. J. Watson, M. Moncrieff, and F. M. Walter, "Accuracy of SIAscopy for pigmented skin lesions encountered in primary care: Development and validation of a new diagnostic algorithm," *BMC Dermatol.*, vol. 10, no.

1, pp. 1–9, Sep. 2010, doi: 10.1186/1471-5945-10-9/FIGURES/4.

[150] E. C. F. Wilson *et al.*, "The Cost-Effectiveness of a Novel SIAscopic Diagnostic Aid for the Management of Pigmented Skin Lesions in Primary Care: A Decision-Analytic Model," *Value Heal.*, vol. 16, no. 2, pp. 356–366, Mar. 2013, doi: 10.1016/J.JVAL.2012.12.008.

[151] D. Sgouros *et al.*, "Assessment of SIAscopy in the triage of suspicious skin tumours," *Ski. Res. Technol.*, vol. 20, no. 4, pp. 440–444, Nov. 2014, doi: 10.1111/srt.12138.

[152] S. Tomatis *et al.*, "Automated melanoma detection with a novel multispectral imaging system: results of a prospective study," *Phys. Med. Biol.*, vol. 50, no. 8, pp. 1675–1687, Apr. 2005, doi: 10.1088/0031-9155/50/8/004.

[153] M. Carrara *et al.*, "Multispectral imaging and artificial neural network: mimicking the management decision of the clinician facing pigmented skin lesions," *Phys. Med. Biol.*, vol. 52, no. 9, p. 2599, Apr. 2007, doi: 10.1088/0031-9155/52/9/018.

[154] P. A. Ascierto *et al.*, "The role of spectrophotometry in the diagnosis of melanoma," *BMC Dermatol.*, vol. 10, no. 1, p. 5, Dec. 2010, doi: 10.1186/1471-5945-10-5.

[155] I. Diebele *et al.*, "Clinical evaluation of melanomas and common nevi by spectral imaging," *Biomed. Opt. Express*, vol. 3, no. 3, p. 467, Mar. 2012, doi: 10.1364/BOE.3.000467.

[156] J. J. Stamnes, G. Ryzhikov, M. Biryulina, B. Hamre, L. Zhao, and K. Stamnes, "Optical detection and monitoring of pigmented skin lesions," *Biomed. Opt. Express*, vol. 8, no. 6, p. 2946, Jun. 2017, doi: 10.1364/boe.8.002946.

[157] X. Delpueyo *et al.*, "Multispectral imaging system based on light-emitting diodes for the detection of melanomas and basal cell carcinomas: a pilot study," *J. Biomed. Opt.*, vol. 22, no. 6, p. 065006, Jun. 2017, doi: 10.1117/1.JBO.22.6.065006.

[158] L. Rey-Barroso *et al.*, "Visible and Extended Near-Infrared Multispectral Imaging for Skin Cancer Diagnosis," *Sensors 2018, Vol. 18, Page 1441*, vol. 18, no. 5, p. 1441, May 2018, doi: 10.3390/S18051441.

[159] H. Ding, C. Chen, H. Zhao, Y. Yue, and C. Han, "Smartphone based multispectral imager and its potential for point-of-care testing," *Analyst*, vol. 144, no. 14, pp. 4380–4385, Jul. 2019, doi: 10.1039/C9AN00853E.

[160] R. D. Uthoff, B. Song, M. Maarouf, V. Shi, and R. Liang, "Point-of-care, multispectral, smartphone-based dermascopes for dermal lesion screening and erythema monitoring," *J. Biomed. Opt.*, vol. 25, no. 06, p. 1, Jun. 2020, doi: 10.1117/1.JBO.25.6.066004.

[161] D. T. Dicker *et al.*, "Differentiation of normal skin and melanoma using high resolution hyperspectral imaging," *Cancer Biol. Ther.*, vol. 5, no. 8, pp. 1033–1038, 2006, doi: 10.4161/CBT.5.8.3261.

[162] T. Nagaoka, Y. Kiyohara, H. Koga, A. Nakamura, T. Saida, and T. Sota, "Modification of a melanoma discrimination index derived from hyperspectral data: A clinical trial conducted in 2 centers between March 2011 and December 2013," *Ski. Res. Technol.*, vol. 21, no. 3, pp. 278–283, Aug. 2014, doi: 10.1111/srt.12188.

[163] T. Nagaoka, A. Nakamura, H. Okutani, Y. Kiyohara, and T. Sota, "A possible melanoma discrimination index based on hyperspectral data: A pilot study," *Ski. Res. Technol.*, vol. 18, no. 3, pp. 301–310, 2011, doi: 10.1111/j.1600-0846.2011.00571.x.

[164] T. Nagaoka *et al.*, "Hyperspectroscopic screening of melanoma on acral volar skin," *Ski. Res. Technol.*, vol. 19, no. 1, pp. e290–e296, Feb. 2012, doi: 10.1111/j.1600-0846.2012.00642.x.

[165] G. B. Christensen *et al.*, "Clinical performance of a novel hyperspectral imaging device for cutaneous melanoma and pigmented skin lesions in Caucasian skin," *Ski. Res. Technol.*, vol. 27, no. 5, pp. 803–809, Sep. 2021, doi: 10.1111/SRT.13023.

[166] N. Neittaanmäki-Perttu *et al.*, "Delineating margins of lentigo maligna using a hyperspectral imaging system," *Acta Derm. Venereol.*, vol. 95, no. 5, pp. 549–552, 2015, doi: 10.2340/00015555-2010/.

[167] M. Salmivuori, N. Neittaanmäki, I. Pölönen, L. Jeskanen, E. Snellman, and M. Grönroos,

"Hyperspectral imaging system in the delineation of Ill-defined basal cell carcinomas: a pilot study," *J. Eur. Acad. Dermatology Venereol.*, vol. 33, no. 1, pp. 71–78, Jan. 2019, doi: 10.1111/JDV.15102.

[168] J. Räsänen, M. Salmivuori, I. Pölönen, M. Grönroos, and N. Neittaanmäki, "Hyperspectral Imaging Reveals Spectral Differences and Can Distinguish Malignant Melanoma from Pigmented Basal Cell Carcinomas: A Pilot Study," *Acta Derm. Venereol.*, vol. 101, no. 2, pp. adv00405–adv00405, Feb. 2021, doi: 10.2340/00015555-3755.

[169] L. A. Zherdeva, I. A. Bratchenko, O. O. Myakinin, A. A. Moryatov, S. V. Kozlov, and V. P. Zakharov, "In vivo hyperspectral imaging and differentiation of skin cancer," in *Optics in Health Care and Biomedical Optics VII*, Nov. 2016, vol. 10024, no. November, p. 100244G. doi: 10.1117/12.2246433.

[170] A. M. Hosking *et al.*, "Hyperspectral imaging in automated digital dermoscopy screening for melanoma," *Lasers Surg. Med.*, vol. 51, no. 3, pp. 214–222, Mar. 2019, doi: 10.1002/LSM.23055.

[171] L. A. Courtenay *et al.*, "Hyperspectral imaging and robust statistics in non-melanoma skin cancer analysis," *Biomed. Opt. Express, Vol. 12, Issue 8, pp. 5107-5127*, vol. 12, no. 8, pp. 5107–5127, Aug. 2021, doi: 10.1364/BOE.428143.

[172] L. A. Courtenay *et al.*, "Deep Convolutional Neural Support Vector Machines for the Classification of Basal Cell Carcinoma Hyperspectral Signatures," *J. Clin. Med. 2022, Vol. 11, Page 2315*, vol. 11, no. 9, p. 2315, Apr. 2022, doi: 10.3390/JCM11092315.

[173] V. Lindholm *et al.*, "Differentiating Malignant from Benign Pigmented or Non-Pigmented Skin Tumours - A Pilot Study on 3D Hyperspectral Imaging of Complex Skin Surfaces and Convolutional Neural Networks," *J. Clin. Med. 2022, Vol. 11, Page 1914*, vol. 11, no. 7, p. 1914, Mar. 2022, doi: 10.3390/JCM11071914.

[174] F. Vasefi *et al.*, "Polarization-Sensitive Hyperspectral Imaging in vivo: A Multimode Dermoscope for Skin Analysis," *Sci. Reports 2014 41*, vol. 4, no. 1, pp. 1–10, May 2014, doi: 10.1038/srep04924.

[175] F. Vasefi *et al.*, "Separating melanin from hemodynamics in nevi using multimode hyperspectral dermoscopy and spatial frequency domain spectroscopy," *J. Biomed. Opt.*, vol. 21, no. 11, p. 114001, Nov. 2016, doi: 10.1117/1.JBO.21.11.114001.

[176] Q. He, R. K. Wang, and R. K. Wang, "Analysis of skin morphological features and real-time monitoring using snapshot hyperspectral imaging," *Biomed. Opt. Express, Vol. 10, Issue 11, pp. 5625-5638*, vol. 10, no. 11, pp. 5625–5638, Nov. 2019, doi: 10.1364/BOE.10.005625.

[177] S. S. Mooldijk *et al.*, "Life expectancy with and without dementia in persons with mild cognitive impairment in the community," *J. Am. Geriatr. Soc.*, vol. 70, no. 2, pp. 481–489, Feb. 2022, doi: 10.1111/jgs.17520.

[178] World Health Organization, "WHO Guidelines - Risk Reduction for Cognitive Decline and Dementia," World Health Organization, 2019. [Online]. Available: https://www.who.int/publications/i/item/9789241550543

[179] L. Baillie and N. Thomas, "Personal information documents for people with dementia: Healthcare staff 's perceptions and experiences," *Dementia*, vol. 19, no. 3, pp. 574–589, Apr. 2020, doi: 10.1177/1471301218778907.

[180] B. Reisberg, S. H. Ferris, M. J. De Leon, and T. Crook, "The global deterioration scale for assessment of primary degenerative dementia," *Am. J. Psychiatry*, vol. 139, no. 9, pp. 1136–1139, 1982, doi: 10.1176/ajp.139.9.1136.

[181] B. Reisberg, "Functional Assessment Staging (FAST)," *Psychopharmacol. Bull.*, vol. 24, no. 4, pp. 653–659, 1988.

[182] J. C. Morris, "The clinical dementia rating (cdr): Current version and scoring rules," *Neurology*, vol. 43, no. 11, pp. 2412–2414, Nov. 1993, doi: 10.1212/wnl.43.11.2412-a.

[183] H. Hampel *et al.*, "Biomarkers for alzheimer's disease: Academic, industry and regulatory perspectives," *Nature Reviews Drug Discovery*, vol. 9, no. 7. Nature Publishing Group, pp. 560–574, Jul. 2010. doi: 10.1038/nrd3115.

[184] J. B. Pereira, E. Westman, and O. Hansson, "Association between cerebrospinal fluid and plasma neurodegeneration biomarkers with brain atrophy in Alzheimer's disease," *Neurobiol. Aging*, vol. 58, pp. 14–29, Oct. 2017, doi: 10.1016/j.neurobiolaging.2017.06.002.

[185] A. M. Fjell *et al.*, "CSF biomarkers in prediction of cerebral and clinical change in mild cognitive impairment and Alzheimer's disease," *J. Neurosci.*, vol. 30, no. 6, pp. 2088–2101, Feb. 2010, doi: 10.1523/JNEUROSCI.3785-09.2010.

[186] C. R. Jack *et al.*, "NIA-AA Research Framework: Toward a biological definition of Alzheimer's disease," *Alzheimer's Dement.*, vol. 14, no. 4, pp. 535–562, Apr. 2018, doi: 10.1016/j.jalz.2018.02.018.

[187] M. S. Fiandaca, M. E. Mapstone, A. K. Cheema, and H. J. Federoff, "The critical need for defining preclinical biomarkers in Alzheimer's disease," *Alzheimer's Dement.*, vol. 10, no. 3 SUPPL., pp. S196–S212, Jun. 2014, doi: 10.1016/j.jalz.2014.04.015.

[188] X. Hadoux *et al.*, "Non-invasive in vivo hyperspectral imaging of the retina for potential biomarker use in Alzheimer's disease," *Nat. Commun.*, vol. 10, no. 1, pp. 1–12, Dec. 2019, doi: 10.1038/s41467-019-12242-1.

[189] S. S. More, J. M. Beach, C. McClelland, A. Mokhtarzadeh, and R. Vince, "In Vivo Assessment of Retinal Biomarkers by Hyperspectral Imaging: Early Detection of Alzheimer's Disease," *ACS Chem. Neurosci.*, vol. 10, no. 11, pp. 4492–4501, Nov. 2019, doi: 10.1021/acschemneuro.9b00331.

[190] S. Lemmens *et al.*, "Combination of snapshot hyperspectral retinal imaging and optical coherence tomography to identify Alzheimer's disease patients," *Alzheimers. Res. Ther.*, vol. 12, no. 1, p. 144, Dec. 2020, doi: 10.1186/s13195-020-00715-1.

[191] H. Fabelo *et al.*, "Novel Methodology for Alzheimer's Disease Biomarker Identification in Plasma using Hyperspectral Microscopy," Nov. 2020. doi: 10.1109/DCIS51330.2020.9268654.

[192] Y. Sun, S. Duthaler, and B. J. Nelson, "Autofocusing in computer microscopy: Selecting the optimal focus algorithm," *Microsc. Res. Tech.*, vol. 65, no. 3, pp. 139–149, Oct. 2004, doi: 10.1002/jemt.20118.

[193] N. Subhash, J. R. Mallia, S. S. Thomas, A. Mathews, P. Sebastian, and J. Madhavan, "Oral cancer detection using diffuse reflectance spectral ratio R540/R575 of oxygenated hemoglobin bands," *J. Biomed. Opt.*, vol. 11, no. 1, p. 014018, 2006, doi: 10.1117/1.2165184.

[194] C. Fu *et al.*, "Rapid, label-free detection of cerebral ischemia in rats using hyperspectral imaging," *J. Neurosci. Methods*, vol. 329, p. 108466, Jan. 2020, doi: 10.1016/J.JNEUMETH.2019.108466.

[195] B. Martinez *et al.*, "Most Relevant Spectral Bands Identification for Brain Cancer Detection Using Hyperspectral Imaging," *Sensors*, vol. 19, no. 24, p. 5481, Dec. 2019, doi: 10.3390/s19245481.

[196] S. Prahl, "Optical absorption of hemoglobin," 1999. https://omlc.org/spectra/hemoglobin/

[197] F. Meng and A. I. Alayash, "Determination of extinction coefficients of human hemoglobin in various redox states," *Anal. Biochem.*, vol. 521, pp. 11–19, Mar. 2017, doi: 10.1016/j.ab.2017.01.002.

[198] L. Giannoni, F. Lange, and I. Tachtsidis, "Hyperspectral imaging solutions for brain tissue metabolic and hemodynamic monitoring: past, current and future developments," *J. Opt.*, vol. 20, no. 4, p. 044009, Apr. 2018, doi: 10.1088/2040-8986/aab3a6.

[199] L. Q Liu, "Non-invasive Technologies of Tissue Viability Measurement for Pressure Ulcer Prevention in Spinal Cord Injury," *Phys. Med. Rehabil. Disabil.*, vol. 1, no. 1, pp. 1–7, Nov. 2015, doi: 10.24966/PMRD-8670/100002.

[200] E. Johansson *et al.*, "CD44 Interacts with HIF-2α to Modulate the Hypoxic Phenotype of Perinecrotic and Perivascular Glioma Cells," *Cell Rep.*, vol. 20, no. 7, pp. 1641–1653, Aug. 2017, doi: 10.1016/j.celrep.2017.07.049.

[201] G. Florimbi *et al.*, "Accelerating the K-Nearest Neighbors Filtering Algorithm to Optimize the Real-Time Classification of Human Brain Tumor in Hyperspectral Images," *Sensors*, vol. 18, no. 7, p. 2314, Jul. 2018, doi: 10.3390/s18072314.

[202] G. Florimbi *et al.*, "Towards Real-Time Computing of Intraoperative Hyperspectral Imaging for Brain Cancer Detection Using Multi-GPU Platforms," *IEEE Access*, vol. 8, pp. 8485–8501, 2020, doi: 10.1109/ACCESS.2020.2963939.

[203] I. A. Cruz-Guerrero, R. Leon, D. U. Campos-Delgado, S. Ortega, H. Fabelo, and G. M. Callico, "Classification of Hyperspectral In Vivo Brain Tissue Based on Linear Unmixing," *Appl. Sci.*, vol. 10, no. 16, p. 5686, Aug. 2020, doi: 10.3390/app10165686.

[204] R. Mühle, H. Ernst, S. B. Sobottka, and U. Morgenstern, "Workflow and hardware for intraoperative hyperspectral data acquisition in neurosurgery," *Biomed. Eng. / Biomed. Tech.*, vol. 66, no. 1, pp. 31–42, Feb. 2021, doi: 10.1515/bmt-2019-0333.

[205] A. Patel and J. Chaudhary, "A Review on Infrared and Visible Image Fusion Techniques," in *Lecture Notes on Data Engineering and Communications Technologies*, vol. 33, Springer, 2020, pp. 127–144. doi: 10.1007/978-3-030-28364-3_12.

[206] B. Meher, S. Agrawal, R. Panda, and A. Abraham, "A survey on region based image fusion methods," *Inf. Fusion*, vol. 48, pp. 119–132, Aug. 2019, doi: 10.1016/J.INFFUS.2018.07.010.

[207] C. Ru, Z. Li, and R. Tang, "A Hyperspectral Imaging Approach for Classifying Geographical Origins of Rhizoma Atractylodis Macrocephalae Using the Fusion of Spectrum-Image in VNIR and SWIR Ranges (VNIR-SWIR-FuSI)," *Sensors*, vol. 19, no. 9, p. 2045, May 2019, doi: 10.3390/s19092045.

[208] P. Barnabé, G. Dislaire, S. Leroy, and E. Pirard, "Design and calibration of a two-camera (visible to near-infrared and short-wave infrared) hyperspectral acquisition system for the characterization of metallic alloys from the recycling industry," *J. Electron. Imaging*, vol. 24, no. 6, p. 061115, Nov. 2015, doi: 10.1117/1.JEI.24.6.061115.

[209] F. P. M. Oliveira and J. M. R. S. Tavares, "Medical image registration: a review," *Comput. Methods Biomech. Biomed. Engin.*, vol. 17, no. 2, pp. 73–93, Jan. 2014, doi: 10.1080/10255842.2012.670855.

[210] Y. M. Ahmad, S. Sahran, A. Adam, and - Syazarina, "Linear Intensity-Based Image Registration," *Int. J. Adv. Comput. Sci. Appl.*, vol. 9, no. 12, 2018, doi: 10.14569/IJACSA.2018.091231.

[211] E. Irmak, E. Erçelebí, and A. H. Ertaş, "Brain tumor detection using monomodal intensity based medical image registration and MATLAB," *Turkish J. Electr. Eng. Comput. Sci.*, vol. 24, pp. 2730–2746, 2016, doi: 10.3906/elk-1403-75.

[212] D. G. Lowe, "Distinctive Image Features from Scale-Invariant Keypoints," *Int. J. Comput. Vis.*, vol. 60, no. 2, pp. 91–110, Nov. 2004, doi: 10.1023/B:VISI.0000029664.99615.94.

[213] E. Rosten and T. Drummond, "Fusing points and lines for high performance tracking," in *Tenth IEEE International Conference on Computer Vision (ICCV'05) Volume 1*, 2005, pp. 1508-1515 Vol. 2. doi: 10.1109/ICCV.2005.104.

[214] C. Harris and M. Stephens, "A Combined Corner and Edge Detector," in *Procedings of the Alvey Vision Conference 1988*, 1988, pp. 23.1-23.6. doi: 10.5244/C.2.23.

[215] V. H. Gandhi, S. R. Panchal, and P. G. Student, "Feature Based Image Registration Techniques: An Introductory Survey," *Int. J. Eng. Dev. Res.*, vol. 2, no. 1, pp. 368–375, 2014, [Online]. Available: https://www.ijedr.org/papers/IJEDR1401064.pdf

[216] J. Zhao *et al.*, "Rapid Mosaicking of Unmanned Aerial Vehicle (UAV) Images for Crop Growth Monitoring Using the SIFT Algorithm," *Remote Sens.*, vol. 11, no. 10, p. 1226, May 2019, doi: 10.3390/rs11101226.

[217] P. Schwind, S. Suri, P. Reinartz, and A. Siebert, "Applicability of the SIFT operator to geometric SAR image registration," *Int. J. Remote Sens.*, vol. 31, no. 8, pp. 1959–1980, Apr. 2010, doi: 10.1080/01431160902927622.

[218] D. Mattes, D. R. Haynor, H. Vesselle, T. K. Lewellyn, and W. Eubank, "Nonrigid multimodality image registration," in *Medical Imaging 2001: Image Processing*, Jul. 2001, vol. 4322, pp. 1609–1620. doi: 10.1117/12.431046.

[219] B. Zitová and J. Flusser, "Image registration methods: A survey," *Image Vis. Comput.*, vol. 21, no. 11, pp. 977–1000, Oct. 2003, doi: 10.1016/S0262-8856(03)00137-9.

[220] P. H. S. Torr and A. Zisserman, "MLESAC: A new robust estimator with application to estimating image geometry," *Comput. Vis. Image Underst.*, vol. 78, no. 1, pp. 138–156, Apr. 2000, doi: 10.1006/cviu.1999.0832.

[221] H. Bay, T. Tuytelaars, and L. Van Gool, "SURF: Speeded up robust features," in *Lecture Notes in Computer Science (including subseries Lecture Notes in Artificial Intelligence and Lecture Notes in Bioinformatics)*, 2006, vol. 3951 LNCS, pp. 404–417. doi: 10.1007/11744023_32.

[222] J. Matas, O. Chum, M. Urban, and T. Pajdla, "Robust wide-baseline stereo from maximally stable extremal regions," in *Image and Vision Computing*, Sep. 2004, vol. 22, no. 10 SPEC. ISS., pp. 761–767. doi: 10.1016/j.imavis.2004.02.006.

[223] F. Manni *et al.*, "Hyperspectral Imaging for Skin Feature Detection: Advances in Markerless Tracking for Spine Surgery," *Appl. Sci.*, vol. 10, no. 12, p. 4078, Jun. 2020, doi: 10.3390/app10124078.

[224] S. Krig and S. Krig, "Interest Point Detector and Feature Descriptor Survey," in *Computer Vision Metrics*, Apress, 2014, pp. 217–282. doi: 10.1007/978-1-4302-5930-5_6.

[225] L. L. de Boer *et al.*, "Fat/water ratios measured with diffuse reflectance spectroscopy to detect breast tumor boundaries," *Breast Cancer Res. Treat.*, vol. 152, no. 3, pp. 509–518, Aug. 2015, doi: 10.1007/s10549-015-3487-z.

[226] S. Golovynskyi *et al.*, "Optical windows for head tissues in near-infrared and short-wave infrared regions: Approaching transcranial light applications," *J. Biophotonics*, vol. 11, no. 12, p. e201800141, Dec. 2018, doi: 10.1002/jbio.201800141.

[227] P. Liu, Z. Zhu, C. Zeng, and G. Nie, "Specific absorption spectra of hemoglobin at different PO2 levels: potential noninvasive method to detect PO2 in tissues," *J. Biomed. Opt.*, vol. 17, no. 12, p. 125002, Dec. 2012, doi: 10.1117/1.JBO.17.12.125002.

[228] C. C. Cooksey, B. K. Tsai, and D. W. Allen, "Spectral reflectance variability of skin and attributing factors," in *Radar Sensor Technology XIX; and Active and Passive Signatures VI*, 2015, vol. 9461, p. 94611M.

[229] K. Buijs and G. R. Choppin, "Near-Infrared Studies of the Structure of Water. I. Pure Water," *J. Chem. Phys.*, vol. 39, no. 8, pp. 2035–2041, Oct. 1963, doi: 10.1063/1.1734579.

[230] R. U. Gandhe and C. P. Bhave, "Intraoperative magnetic resonance imaging for neurosurgery - An anaesthesiologist's challenge.," *Indian J. Anaesth.*, vol. 62, no. 6, pp. 411–417, Jun. 2018, doi: 10.4103/ija.IJA_29_18.

[231] I. J. Gerard, M. Kersten-Oertel, K. Petrecca, D. Sirhan, J. A. Hall, and D. L. Collins, "Brain shift in neuronavigation of brain tumors: A review," *Medical Image Analysis*, vol. 35. pp. 403–420, 2017. doi: 10.1016/j.media.2016.08.007.

[232] N. Lakomkin and C. G. Hadjipanayis, "Fluorescence-guided surgery for high-grade gliomas," *J. Surg. Oncol.*, vol. 118, no. 2, pp. 356–361, Aug. 2018, doi: 10.1002/jso.25154.

[233] M. Schwake, S. Schipmann, M. Müther, M. Köchling, A. Brentrup, and W. Stummer, "5-ALA fluorescence–guided surgery in pediatric brain tumors—a systematic review," *Acta Neurochir. (Wien).*, vol. 161, no. 6, pp. 1099–1108, Jun. 2019, doi: 10.1007/s00701-019-03898-1.

[234] H. Fabelo *et al.*, "Dermatologic Hyperspectral Imaging System for Skin Cancer Diagnosis Assistance," in *2019 XXXIV Conference on Design of Circuits and Integrated Systems (DCIS)*, Nov. 2019, pp. 1–6. doi: 10.1109/DCIS201949030.2019.8959869.

[235] F. A. Kruse *et al.*, "The spectral image processing system (SIPS)—interactive visualization and analysis of imaging spectrometer data," *Remote Sens. Environ.*, vol. 44,

no. 2–3, pp. 145–163, May 1993, doi: 10.1016/0034-4257(93)90013-N.

[236] Y. Fujisawa *et al.*, "Deep-learning-based, computer-aided classifier developed with a small dataset of clinical images surpasses board-certified dermatologists in skin tumour diagnosis," *Br. J. Dermatol.*, vol. 180, no. 2, pp. 373–381, Feb. 2019, doi: 10.1111/bjd.16924.

[237] E. Song *et al.*, "Paired comparison of the sensitivity and specificity of multispectral digital skin lesion analysis and reflectance confocal microscopy in the detection of melanoma in vivo: A cross-sectional study," *J. Am. Acad. Dermatol.*, vol. 75, no. 6, pp. 1187-1192.e2, Dec. 2016, doi: 10.1016/j.jaad.2016.07.022.

[238] D. E. Elder, "Dysplastic naevi: an update," *Histopathology*, vol. 56, no. 1, pp. 112–120, Jan. 2010, doi: 10.1111/j.1365-2559.2009.03450.x.

[239] G. E. Dahl, T. N. Sainath, and G. E. Hinton, "Improving deep neural networks for LVCSR using rectified linear units and dropout," in *ICASSP, IEEE International Conference on Acoustics, Speech and Signal Processing - Proceedings*, Oct. 2013, pp. 8609–8613. doi: 10.1109/ICASSP.2013.6639346.

[240] G. E. Hinton, N. Srivastava, A. Krizhevsky, I. Sutskever, and R. R. Salakhutdinov, "Improving neural networks by preventing co-adaptation of feature detectors," Jul. 2012.

[241] P. Wan, C. Wu, Y. Lin, and X. Ma, "Optimal Threshold Determination for Discriminating Driving Anger Intensity Based on EEG Wavelet Features and ROC Curve Analysis," *Information*, vol. 7, no. 3, p. 52, Aug. 2016, doi: 10.3390/info7030052.

[242] D. Brutin, B. Sobac, B. Loquet, and J. Sampol, "Pattern formation in drying drops of blood," *J. Fluid Mech.*, vol. 667, pp. 85–95, Jan. 2011, doi: 10.1017/S0022112010005070.

[243] R. Chen, L. Zhang, D. Zang, and W. Shen, "Blood drop patterns: Formation and applications," *Adv. Colloid Interface Sci.*, vol. 231, pp. 1–14, May 2016, doi: 10.1016/j.cis.2016.01.008.

ULPGC
Universidad de
Las Palmas de
Gran Canaria